Reconstructing the Landscape Evolution of South Central Africa by Surface Exposure Dating of Waterfalls.

Spyros - Christos Olivotos

Dissertation

zur Erlangung des akademischen Grades
"doctor rerum naturalium"
(Dr. rer. nat.)
in der Wissenschaftsdisziplin "Geologie"

eingereicht an der
Mathematisch-Naturwissenschaftlichen Fakultät
Institut für Geowissenschaften
der Universität Potsdam

Ort und Tag der Disputation: Potsdam, 18.11.2022

1st supervisor: Prof. Dr. Jörg Erzinger
2nd supervisor: Dr. Samuel Niedermann
Co-supervisor: Dr. Silke Merchel

Reviewers:
Dr. Damien Delvaux, Royal Museum for Central Africa, Tervuren, Belgium.
Prof. Dr. Jörg Erzinger, Deutsches GeoForschungsZentrum GFZ, Potsdam, Germany.
Prof. Dr. Ralf Hetzel, Institute for Geology and Palaeontology, University of Münster, Münster, Germany.

https://doi.org/10.25932/publishup-60169
https://nbn-resolving.org/urn:nbn:de:kobv:517-opus4-601699

Table of Contents

Abstract

The East African Rift System (EARS) is a significant example of active tectonics, which provides opportunities to examine the stages of continental faulting and landscape evolution. The southwest extension of the EARS is one of the most significant examples of active tectonics nowadays, however, seismotectonic research in the area has been scarce, despite the fundamental importance of neotectonics. Our first study area is located between the Northern Province of Zambia and the southeastern Katanga Province of the Democratic Republic of Congo. Lakes Mweru and Mweru Wantipa are part of the southwest extension of the EARS. Fault analysis reveals that, since the Miocene, movements along the active Mweru-Mweru Wantipa Fault System (MMFS) have been largely responsible for the reorganization of the landscape and the drainage patterns across the southwestern branch of the EARS. To investigate the spatial and temporal patterns of fluvial-lacustrine landscape development, we determined in-situ cosmogenic ^{10}Be and ^{26}Al in a total of twenty-six quartzitic bedrock samples that were collected from knickpoints across the Mporokoso Plateau (south of Lake Mweru) and the eastern part of the Kundelungu Plateau (north of Lake Mweru). Samples from the Mporokoso Plateau and close to the MMFS provide evidence of temporary burial. By contrast, surfaces located far from the MMFS appear to have remained uncovered since their initial exposure as they show consistent ^{10}Be and ^{26}Al exposure ages ranging up to ~830 ka. Reconciliation of the observed burial patterns with morphotectonic and stratigraphic analysis reveals the existence of an extensive paleo-lake during the Pleistocene. Through hypsometric analyses of the dated knickpoints, the potential maximum water level of the paleo-lake is constrained to ~1200 m asl (present lake lavel: 917 m asl). High denudation rates (up to ~40 mm ka^{-1}) along the eastern Kundelungu Plateau suggest that footwall uplift, resulting from normal faulting, caused river incision, possibly controlling paleo-lake drainage. The lake level was reduced gradually reaching its current level at ~350 ka.

Parallel to the MMFS in the north, the Upemba Fault System (UFS) extends across the southeastern Katanga Province of the Democratic Republic of Congo. This part of our research is focused on the geomorphological behavior of the Kiubo Waterfalls. The waterfalls are the currently active knickpoint of the Lufira River, which flows into the Upemba Depression. Eleven bedrock samples along the Lufira River and its tributary stream, Luvilombo River, were collected. In-situ cosmogenic ^{10}Be and ^{26}Al were used in order to constrain the K constant of the Stream Power Law equation. Constraining the K constant allowed us to calculate the knickpoint retreat rate of the Kiubo Waterfalls at ~0.096 m a^{-1}. Combining the calculated retreat

rate of the knickpoint with DNA sequencing from fish populations, we managed to present extrapolation models and estimate the location of the onset of the Kiubo Waterfalls, revealing its connection to the seismicity of the UFS.

Deutsche Zusammenfassung

Die südwestliche Ausdehnung des Ostafrikanischen Grabenbruchsystems (East African Rift System, EARS) ist eines der bedeutendsten Beispiele aktiver Tektonik heutzutage, welches die Möglichkeit bietet, die Phasen der kontinentalen Verwerfung und der Landschaftsentwicklung zu untersuchen. Allerdings ist seismotektonische Forschung in diesem Gebiet trotz der fundamentalen Bedeutung der Neotektonik nur in geringem Umfang durchgeführt worden. Unser erstes Untersuchungsgebiet befindet sich zwischen der Nordprovinz Sambias und der Provinz Katanga im südöstlichen Teil der Demokratischen Republik Kongo. Die Seen Mweru und Mweru Wantipa sind Teil der südwestlichen Ausdehnung des EARS. Verwerfungsanalysen zeigen, dass seit dem Miozän Bewegungen entlang des aktiven Mweru–Mweru-Wantipa-Verwerfungssystems (MMFS) maßgeblich für die Reorganisation der Landschaft und der Entwässerungsmuster im südwestlichen Zweig des EARS verantwortlich sind. Um die räumlichen und zeitlichen Muster der fluvial-lakustrischen Landschaftsentwicklung zu untersuchen, haben wir in-situ kosmogenes ^{10}Be und ^{26}Al in insgesamt sechsundzwanzig Quarzit-Grundgesteinsproben bestimmt, die vorwiegend von Knickpunkten auf dem Mporokoso-Plateau (südlich des Mweru-Sees) und dem östlichen Teil des Kundelungu-Plateaus (nördlich des Mweru-Sees) gesammelt wurden. Proben vom Mporokoso-Plateau aus der Nähe des MMFS liefern Hinweise auf eine temporäre Bedeckung. Im Gegensatz dazu scheinen Oberflächen, die weit vom MMFS entfernt liegen, seit ihrer ersten Freilegung unbedeckt geblieben zu sein, da sie konsistente ^{10}Be- und ^{26}Al-Freilegungsalter bis zu ~830 ka aufweisen. Der Abgleich der beobachteten Bedeckungsmuster mit morphotektonischen und stratigraphischen Analysen zeigt die Existenz eines ausgedehnten Paläosees während des Pleistozäns. Durch hypsometrische Analysen der datierten Knickpunkte wird der potentielle maximale Wasserstand des Paläosees auf ~1200 m (heutige Seehöhe: 917 m) eingegrenzt. Hohe Denudationsraten (bis zu ~40 mm ka^{-1}) entlang des östlichen Kundelungu-Plateaus deuten darauf hin, dass die durch normale Verwerfungen hervorgerufene Hebung des Fußes einen Flusseinschnitt verursachte, der möglicherweise die Entwässerung des Paläosees kontrollierte. Der Seespiegel wurde allmählich abgesenkt und erreichte sein heutiges Niveau bei ~350 ka.

Parallel zum MMFS im Norden erstreckt sich das Upemba-Verwerfungssystem (UFS) über die südöstliche Katanga-Provinz der Demokratischen Republik Kongo. Dort konzentriert sich unsere Forschung auf das geomorphologische Verhalten der Kiubo-Wasserfälle. Diese Fälle sind der derzeit aktive Knickpunkt des Lufira-Flusses, der in die Upemba-Senke mündet. Elf

Gesteinsproben entlang des Lufira-Flusses und seines Nebenflusses, des Luvilombo-Flusses, wurden gesammelt. In-situ kosmogenes ^{10}Be und ^{26}Al wurden verwendet, um die K-Konstante der „Strom-Power-Law"-Gleichung einzuschränken. Die Eingrenzung der K-Konstante ermöglichte uns die Berechnung der Rückzugsrate der Kiubo-Wasserfälle auf ~0,096 m a^{-1}. Durch die Kombination der berechneten Rückzugsrate des Knickpunkts mit der DNA-Sequenzierung von Fischpopulationen konnten wir Extrapolationsmodelle formulieren und den Entstehungsort der Kiubo-Wasserfälle abschätzen. Diese Abschätzung legt einen Zusammenhang mit der Seismizität der UFS nahe.

Chapter 1

Introduction

1. Introduction

1.1. *The East African Rift System*

East Africa is known for its dynamic landscape and its geologic history. It is a key area for geomorphologic and tectonic studies, as it hosts one of the most classical examples of active intracontinental rifts, the East African Rift System (EARS; Chorowicz, 1989; Ebinger, 1989; Delvaux et al., 1992; Ring, 1994; Schlüter, 1997; Chorowicz, 2005; Braile et al., 2006; Stamps et al., 2008). Its size (> 3000 km long) and longevity (~25 Ma) provide a unique opportunity to study the evolution of continental rifting through time, from initial crustal break-up via normal faulting to oceanic rifting and, eventually, the opening of future oceans (Fig. 1.1). The EARS provides useful insight about the processes that have dominated the landscape evolution of eastern Africa during the last ~30 Ma. Rifting began around the early Miocene, while the seismic activity and the southward propagation of the fault system have continued until nowadays, following dispositions of Precambrian structures (Delvaux, 1991; Demissie, 2010). The rift forms two main features, the Eastern Branch and the Western Branch (WB), which run over a distance of ~2200 km and ~2100 km, respectively (Chorowicz, 2005).

A series of tectonic basins are aligned over several thousand kilometers along East Africa. These basins are controlled by faults forming narrow graben and trough structures accompanied by sedimentation and volcanic activity (Chorowicz, 2005). Lakes of various depths and sizes are developed along the graben structures of the EARS. The eastern part of Africa is characterized by more than 35 lakes, which are linked and controlled by tectonic structures, revealing a variety of morphological, geological and biological features (Tiercelin and Lezzar, 2002). These successions of tectonically controlled structures are usually delimited by two high parallel plateaus or mountain lines (Chorowicz, 2005). The Eastern Branch of the EARS is characterized by intense volcanism and comprises small and relatively shallow lakes due to semi-arid climatic conditions (Tiercelin and Lezzar, 2002). The WB is dominated by larger and deeper lakes with freshwater characteristics, mainly as a result of the more humid climate. The volcanic activity is not as intense as in the Eastern Branch and started around late Miocene (Tiercelin and Lezzar, 2002).

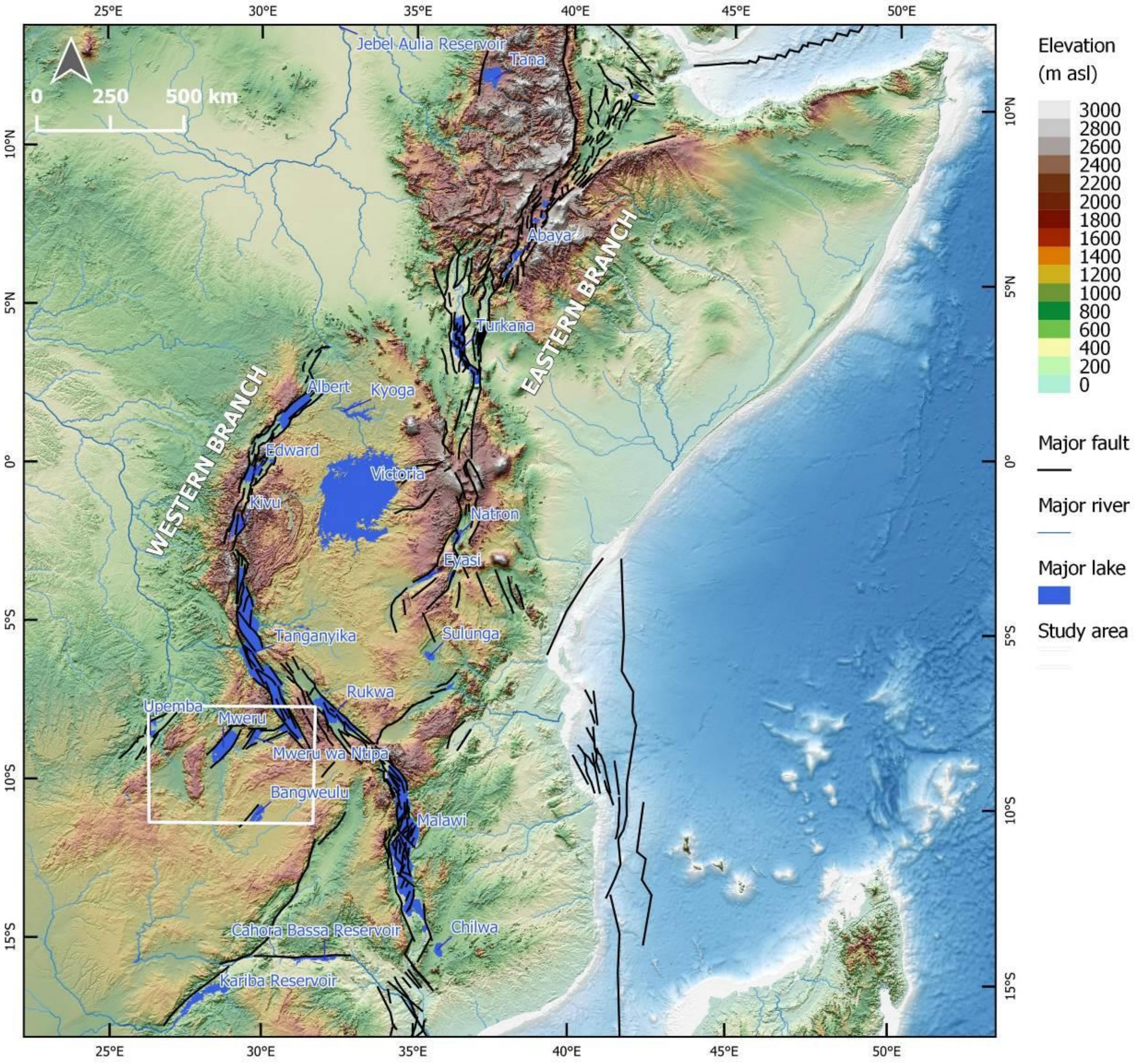

Figure 1.1.: Hypsographic DEM of the East African rift system. Black lines indicate major faults, blue lines indicate major rivers, while blue surfaces indicate major lakes. The white rectangular depicts the study area.

Lakes Tanganyika and Malawi are the deepest lakes of the WB, with maximum water depths of ~1470 and 770 m, respectively (Capart, 1949). The WB's extension rate is ~1 mm a^{-1} and together with the Eastern Branch, which extends at ~7 mm a^{-1}, it forms the EARS, one of the fastest spreading intracontinental rifts globally (Fernandes et al., 2004; Calais et al., 2006; Omenda et al., 2016). The southern arm of the upwelling African asthenospheric superplume beneath the Lake Victoria region (Kenya Dome) forces the continent to be raised hundreds of meters as the crustal lithosphere undergoes thinning processes (Ebinger and Sleep, 1998; Nyblade et al., 2000; Chakrabarti et al., 2009; Halldórsson et al., 2014; Koptev et al., 2015; Omenda et al., 2016). However, the crustal thickness along the Tanganyika Rift increases southwards, creating en echelon rift segments while transferring the extension towards the Rukwa Rift (Lavayssiere et al., 2019).

Uplift, drainage evolution, knickpoint migration and denudation processes are some of the features that are controlled by active tectonism and the climate. Despite the fact that active faulting controls and shapes the landscape southwest of the Tanganyika graben, detailed geomorphological and tectonic studies of the area remain scarce. Most of the existing studies have analyzed the first-order physiographic characteristics of these rifted valleys, deriving some tectonic correlations between these structures and the EARS (Mohr, 1974; Tiercelin et al., 1988; Mondeguer et al., 1989; Strecker et al., 1990; Delvaux, 1991; Chorowicz, 2005; Kipata et al., 2013). It has been established, for example, that the area was initially a Miocene basin, which was subsequently faulted during the Early Pleistocene (Dixey, 1944). Modern geomorphologists shifted their interest and studies towards tectonics and landscape evolution, recognizing the importance of discrete events, such as earthquakes, faulting, landslides and their relation with large-scale tectonic processes and climatic changes, using interdisciplinary tools to tackle challenging geologic issues (Brocklehurst, 2010). The work presented in this thesis focuses on the Western Branch (WB) of the EARS and specifically on the basin-and-range topography along the Mweru-Mweru Wantipa and Upemba Fault Systems (MMFS and UFS; Fig. 1.2).

It has been established that courses of the modern drainage system of the area, such as the Limpopo, Zambezi and Luapula rivers, are strongly controlled by ancient geological structures, which were established during the period of Gondwanaland as the continent underwent faulting and folding (Dixey, 1944; Dingle and Hendry, 1984; Moore, 1999; Cotterill 2004). Extensive peneplains and high plateaus are a result of a long period of denudation that initiated during the Mesozoic on Gondwanaland and lasted until the Miocene (Cotterill, 2004). These denudation patterns continued, while the arrival of the African Plume underneath Kenya forced the continent to be raised hundreds of meters as the crustal lithosphere underwent thinning processes (Cox, 1989; Ebinger and Sleep, 1998; Nyblade et al., 2000; Cotterill, 2004; Chorowicz, 2005; Chakrabarti et al., 2009; Nyblade, 2011; Halldórsson et al., 2014; Koptev et al., 2015). The drainage system of the Kalahari plateau has experienced profound rearrangements, leading to re-shaping and reversal of the main rivers and creating the modern courses of the Zambezi and its neighboring systems (Thomas and Shaw, 1990; Moore, 1999; Moore and Larkin, 2001; Moore et al., 2007; Cotterill and de Wit, 2011; Moore et al., 2012).

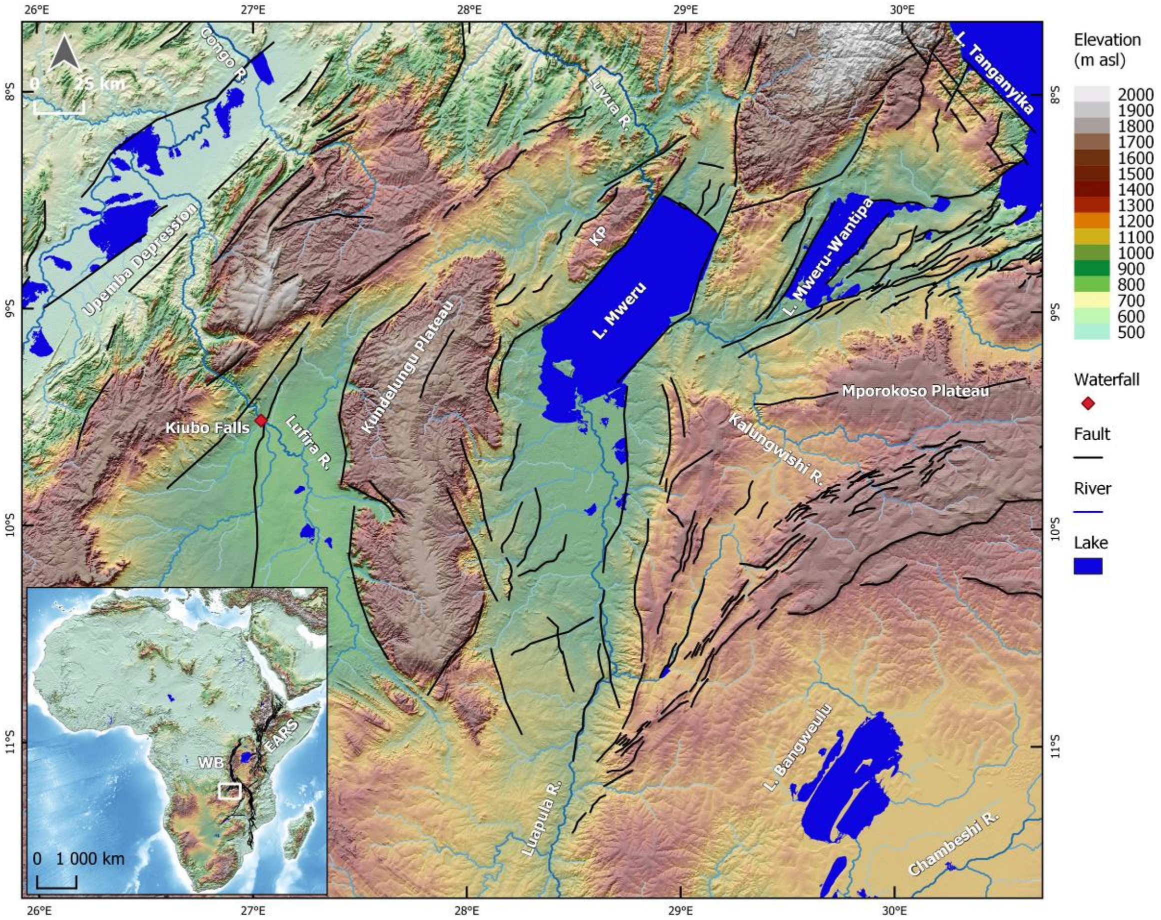

Figure 1.2.: Morphotectonic map of the Mweru-Mweru Wantipa and Upemba Fault Systems in the southern section of the Western Branch of the East African Rift System. Black lines indicate the main active normal faults in the area. Blue lines indicate major rivers, while blue surfaces indicate major lakes of the study area.

The successive rifting episodes did not only affect the courses of the drainage but also the morphology of the existing lakes. Evidence of paleo-lakes occurs all over the Western Branch, revealing a series of larger and deeper lakes (e.g. paleo-lakes Turkana, Edward-Albert, Bangweulu, Magadi, Thamalakane) along the EARS during the Plio-Pleistocene (Williamson, 1978; Hillaire-Marcel et al., 1986; Burrough and Thomas, 2008; Cotterill and de Wit, 2011; Cohen et al., 2016). Long-term lake fluctuations across east Africa during the Plio-Pleistocene have been recorded spanning time intervals from 2 to 20 ka (Masters et al., 1991; Gamrod, 2009; Shuman et al., 2009; Trauth et al., 2010). Intense volcanic activity together with tectonic movements and climatic variations initiated alteration between humid and arid periods impacting the landscape of eastern Africa (Delvaux, 1991; Tiercelin and Lezzar, 2002; Trauth et al., 2005; Mana et al., 2015). Strong evidence indicates that the original size of Lake Mweru was extended southwards of the present lake in the Northern Province of Zambia, forming a greater paleo-lake with a surface of ~40,000 km^2, which eventually was tapped by headwater retreat of the Luvua River (Dixey, 1944; Bos et al., 2006; Goodier et al., 2011; Cotterill and de Wit, 2011; this study). Despite the importance of the neotectonic activity of the area, geological studies are minimal. Nevertheless, remnants of lacustrine deposits and sands along the present-day Zambian shores of Lake Mweru provide evidence about the existence of the paleo-lake and indicate a different course of the Luapula River (Dixey, 1944; Bos et al., 1995, 2006). Repeated earthquakes (i.e. normal faulting, uplift) across the Kalahari Plateau caused the reorganization of the regional drainage system, forming new knickpoints (e.g. waterfalls) along the courses of the rivers (Ewiak et al., 2015). Knickpoints play a key role in tectonic geomorphology as they provide information about denudation processes and contribute to the identification of active faults (Howard et al., 1994; Brocklehurst, 2010). The evolution of knickpoints is not only correlated with tectonic activity (normal faulting) and lithologic differentiation but can also be associated with base-level change, uplift as well as sea-level variations, thus they provide a great communication link between the base level and the upstream catchment (Whipple and Tucker, 1999; Whipple et al., 2000). Scheingross et al. (2017) describe the relation of knickpoints with tectonic and climatic changes and the ability to reconstruct tectonic histories via river profiling. Knickpoints are also strong biogeographic indicators, as they control the fish fauna by creating natural barriers (Schwarzer et al., 2011). The biota population can be separated between upstream and downstream, creating divergent evolution (Schwarzer et al., 2011).

1.2. *Knickpoints and Waterfalls*

Geomorphology is one of the most fundamental fields of earth sciences which contribute to the understanding of active fault systems. Landscapes provide *"an important archive of the rates and spatial distribution of deformation"* (Kirby and Whipple, 2012). The relation of faults to folds, the reconstruction of paleoseismic events or even the determination of displacement rates along fault systems are some of the numerous contributions of geomorphology to tectonics (Kirby and Whipple, 2012). Tectonic geomorphology was born after the realization of the potential of the interactions between climate, surface processes, and tectonics (e.g. Molnar and England, 1990; Raymo and Ruddiman, 1992). One of the main problems that modern tectonic geomorphology faces is the dynamics of bedrock channel and knickpoint systems (Whipple and Tucker, 1999). Knickpoints offer profound evidence of the dynamic response of bedrock rivers.

A knickpoint is defined as the break in the slope of a fluvial longitudinal profile. The knickpoint face is the vertical surface which extends from the edge of the face to the base of the channel (Gardner, 1983; Crosby and Whipple, 2006). Knickpoints reflect localized bed incision (Crosby and Whipple, 2006). In most cases the high and steep knickpoints create a withdrawal reach where the water of the stream is oversteepened (waterfall). This effect is very important in the evolution of knickpoint morphology (Gardner, 1983). Differential erosion due to variation in lithology and alteration in shear stress may generate the break and/or steepening of the channel slope (Crosby and Whipple, 2006 and references therein). However, a knickpoint may also be formed after a relative decrease of the base level, which is often related to surface uplift or sea-level drop (Crosby and Whipple, 2006), making most knickpoints a connection link between the catchment and the base level (Whipple and Tucker, 1999; Whipple et al., 2000). In tectonically active landscapes, the bedrock channels are relief features which control the relationships between relief, elevation, and denudation (Howard et al., 1994). Understanding the behavior of knickpoints, and especially their retreat rates, is vital for understanding landscape evolution and catchment responses to perturbation (Bishop et al., 2005).

1.3. *Knickpoint Retreat*

The process of channel evolution is described by a mechanism of sudden slope alteration rather than gradual adjustments (Whipple and Tucker, 1999). The equilibrium between the upstream and downstream uplift rates is achieved by the knickpoint retreat, which is defined as the kinematic movement of the knickpoint face that progresses from downstream to upstream (Rosenbloom and Anderson, 1994; Whipple and Tucker, 1999; Bishop et al., 2005; Wobus et al., 2006). The retreat rate is defined as the ratio of the distance between the current position of the knickpoint and the supposed initial position to the time that passed between these two positions (Loget and Van Den Driessche, 2009). Knickpoint migration was initially described and explained by the presence of an erosion-resistant caprock above weaker rocks (Gilbert, 1877), but later generations of geomorphologists (e.g. Von Engeln, 1940; Young, 1985) discussed the retreat without the necessary existence of a caprock.

Retreat rates vary in general from 10^{-3} to 10^{-1} m a^{-1} (Van Heijst and Postma, 2001). Exceptionally high rates (>1 m a^{-1}) occur rarely in active orogens or for massive waterfalls such as the Niagara Falls (Philbrick, 1970; Tinkler et al., 1994; Wohl, 1998; Crosby and Whipple, 2006). Many field observations and experimental studies show that the migration rate is related to the upstream drainage area and the water discharge (Rosenbloom and Anderson, 1994; Bishop et al., 2005; Crosby and Whipple, 2006; Berlin and Anderson, 2007; Loget et al., 2009), while other studies revealed the connection of the migration rate to the bedrock strength and the transported sediments (Tucker, 2004; Crosby and Whipple, 2006; Gasparini et al., 2006; Hayakawa et al., 2008).

Both bedrock lithology and tectonic structure play an important role for knickpoint morphology and evolution (Miller, 1991; Alexandrowicz, 1994). Neither of them are essential, though, for the maintenance and propagation of the knickpoint (Young, 1985; Bishop and Goldrick, 1992). A strong example is the study of Hancock et al. (1998), which focuses on bedrock channel incision, while lithology is not among the fundamental parameters that control the rate of knickpoint retreat around the eastern Scotland rivers (Bishop et al., 2005). After a series of knickpoint retreat analyses at various locations and periods, Loget and Van Den Driessche (2009 and references therein) concluded that a) in alluvial rivers, the knickpoint retreat rate is two orders of magnitude higher than in bedrock rivers, for a constant drainage area; b) in bedrock rivers, climate can be responsible for a difference of one order of magnitude in the rate of knickpoint migration and c) a very low mean migration rate in bedrock rivers is possible due to the slow response time of the denudation processes which shape the landscape (Loget and Van Den Driessche, 2009).

Many studies have been done in order to predict river channel evolution. The most widely used approach is the Stream Power Law. It was developed following field experiments and observations carried out initially by Howard and Kerby (1983). It assumes steady, systematic flow, conditions in which sediment transport capacity exceeds sediment supply and that denudation rates are a function of either shear stress or stream power per unit area of channel bed (Berlin and Anderson, 2007; Croissant and Braun, 2014). In our study, the Stream Power Law is mainly used to calculate the knickpoint retreat rate and predict the knickpoint formation of the Kiubo Waterfalls in the Democratic Republic of Congo. More details about the knickpoint retreat analyses may be found in chapter 6.

1.4. *Terrestrial Cosmogenic Nuclides*

Surface exposure dating with terrestrial cosmogenic nuclides (TCN) is a geochronological method which allows to determine the exposure history of a rock surface. ^{3}He, ^{10}Be, ^{14}C, ^{21}Ne, ^{26}Al and ^{36}Cl are the six most common nuclides used. By measuring the concentrations of cosmogenic nuclides in a rock, surfaces can be directly dated (exposure age; Ivy-Ochs and Kober, 2008). Exposure ages which can be determined by the TCN method range from ~100 to 10^{7} years (Gosse and Phillips, 2001; Dunai, 2010).

Cosmic radiation constantly bombards the Earth’s atmosphere in the form of primary cosmic rays, which triggers nuclear reactions with atmospheric gas. These reactions produce the secondary cosmic rays which are composed of high energy nucleons, such as protons and neutrons, and mesons, e.g. muons (Gosse and Phillips, 2001; Darvill, 2013). As the secondary cosmic rays descend the atmosphere, absorption and scattering of the initial energy through further interactions and collisions result in a decrease of their intensity (Gosse and Phillips, 2001). This decrease of intensity is called attenuation and depends, to various degrees, on the material that the secondary cosmic rays traverse, i.e., on altitude. Furthermore, several additional factors influence the intensity of cosmic rays before they hit the Earth’s surface, such as the geomagnetic field, which creates a dependence on latitude (Dunai, 2010). Due to the variation of the primary cosmic rays according to latitude, the secondary cosmic rays vary, too. Therefore, the production rate of cosmogenic nuclides increases with altitude and latitude (Gosse and Phillips, 2001).

To establish production rates, surfaces already dated with various independent methods, such as radiocarbon-dated moraines (Putnam et al., 2010; Kaplan et al., 2011), Ar-Ar dated volcanic lavas (Dunai and Wijbrans, 2000; Foeken et al., 2012; Fenton et al., 2019) or inter-comparison between different nuclides (Balco and Shuster, 2009; Schimmelpfennig et al., 2011; Luna et al., 2018), have been used as cross-reference. Cosmogenic nuclide production rates are typically determined by measuring cosmogenic nuclide concentrations in surficial rocks with well-constrained exposure histories. Scaling factors are used in order to scale the production rate from the regional or global well-constrained rate to the local sampling site (Lal, 1991). In order to accomplish this scaling, theoretical and/or empirical models are used (Lifton et al., 2014). Based on this approach (atmospheric pressure, geomagnetic field, solar variability), seven main scaling models have been developed (Lal, 1991; Stone, 2000; Dunai, 2001; Desilets and Zreda, 2003; Lifton et al., 2005; Desilets et al., 2006; Lifton et., 2014). All scaling models are referenced to conditions at sea level and high geomagnetic latitude (SLHL; Ivy-Ochs and Kober, 2008).

When secondary cosmic ray particles hit a surface rock, a main reaction is triggered in the minerals, called *spallation* reaction, producing most of the cosmogenic nuclides (Darvill, 2013). Spallation sputters off fast and high energy neutrons, protons, alpha particles and other lighter nuclei (Niedermann, 2002). The second most important reaction that takes place is *negative muon capture*. Muons are heavier than electrons and are a decay product of pions (result of proton-proton or proton-neutron collisions; Niedermann, 2002). They are the most abundant particles at sea level (Lal, 1988; Niedermann, 2002). Secondary cosmic rays are further attenuated within a rock according to the depth below the surface, i.e., the production rate decreases as the sample depth increases. The extent to which the production rate decreases depends on the rock density and the cosmic ray attenuation length. Also, local obstacles, such as surrounding topography, and an inclination (angle from the horizon) of the studied surface reduce the cosmic ray flux with a non-linear dependence on the inclination angle at a particular site (Lal, 1991; Gosse et al., 1995; Dunne et al., 1999; Dunai and Wijbrans, 2000; Stone, 2000). This effect is called topographic shielding and should always be taken into consideration for the final calculations of the cosmogenic nuclide production together with the attenuation due to depth. Measurements in the field are fundamental (Dunai, 2010; Darvill, 2013).

^{10}Be and ^{26}Al are the most commonly used radionuclides for dating bedrock surfaces and/or sediments of various forms. The main targeted mineral for these analyses is quartz, which is a very resistant mineral and abundant in plenty of rock types. Furthermore, it can be reliably cleaned of meteoric ^{10}Be (produced in the atmosphere), whose presence would lead to age overestimation. ^{10}Be and ^{26}Al can both be extracted from a single quartz mineral separate, simplifying and facilitating the sample analyses, while providing more robust results. In addition to radionuclides, TCN methods can also be applied to noble gases. Stable ^{3}He and ^{21}Ne are used for age determination. Quartz can be used again as a target mineral for cosmogenic ^{21}Ne applications. In that case, the relative abundances of the three stable isotopes (^{20}Ne, ^{21}Ne and ^{22}Ne) are used in order to assess and correct for non-cosmogenic components (Hetzel et al., 2002; Niedermann, 2002).

For a rock that previously contained no cosmogenic nuclides and was suddenly brought to the surface and exposed to cosmic rays, TCN dating can be considered as surface exposure dating (e.g. glacier retreat, landslides or lava flows; Cerling and Craig, 1994; Gosse and Philips, 2001). One of the most common processes that reduce the amount of cosmogenic nuclides accumulating in a surface rock or sediment package is denudation. It removes the top layer of the studied surface and exposes a new surface layer that was previously partly shielded, leading to erroneous exposure ages if it is not taken into account. Two assumptions are applied in order to address this issue. In this way two ages can be determined. The first age is estimated under the assumption that no denudation has occurred, while the second one under a constant estimated denudation rate. This compromised and cautious approach is often applied to geologically (relatively) old surfaces, which can become extremely sensitive to denudation (Darvill, 2013). When a surface was exposed to cosmic radiation for a sufficient amount of time in order to accumulate a reserve of various cosmogenic nuclides and then was buried rapidly so that cosmogenic nuclide production essentially terminated, burial dating is possible instead of surface exposure dating (Granger and Muzikar, 2001). In the case of a complex exposure history (e.g. involving burial) of a surface, two or more nuclides with different half lives should be measured from a single sample.

The combination of several cosmogenic nuclides with different production rates and half-lives particularly increases the robustness of the interpretation, making the TCN technique powerful enough to provide information about exposure times and burial durations (Dehnert and Schlüchter, 2008). ^{10}Be and ^{26}Al are commonly used to unravel complex exposure histories based on their different half-lives (~1.4 and ~0.7 Ma respectively). A proper period of shielding/burial will allow ^{26}Al to decay faster (almost twice as fast compared to ^{10}Be), resulting in discordant exposure age estimates (Lal, 1991; Dehnert and Schlüchter, 2008). For more robust and reliable results it is possible to even measure three cosmogenic nuclides (^{10}Be, ^{26}Al and ^{21}Ne) from a single quartz separate (e.g. Hetzel et al., 2002; Kober et al., 2007). Combining these nuclides (^{10}Be/^{26}Al and ^{10}Be/^{21}Ne) allows us to check for scenarios that involve continuous exposures and/or complex histories with intermittent cover. When further information is lacking, minimum exposure or burial ages can always be determined, while maximum denudation rates are obtained by assuming that nuclide concentrations are in steady state (Ivy-Ochs and Kober, 2008). The TCN method is used to determine rates of tectonic activity, too. Dating landforms that are related to tectonic movements and faults or dating bedrock fault surfaces directly is achieved by using two radionuclides (^{10}Be and ^{26}Al) and especially the stable nuclide of ^{21}Ne, which theoretically is able to determine ages for surfaces that have been exposed for millions of years (Ivy-Ochs and Kober, 2008).

1.5. *Goal of the Study*

This study is part of an interdisciplinary project which aims at applying a novel approach to the reconstruction of landscape evolution by combining next generation DNA sequencing of carefully selected fish groups with surface exposure dating of key geomorphic landforms (river knickpoints). These landforms often result in divergent evolution between upstream and downstream populations of biota (Cotterill and de Wit, 2011; Schwarzer et al., 2011). Thus, a direct estimate of the age of the knickpoints can illustrate the details of landscape evolution and the evolution of the species. The genomic record residing in a species' history can in turn be applied more widely across a landscape, to resolve aspects of geomorphic evolution, particularly in situations where geochronological constraints are lacking (Cotterill and de Wit, 2011; Goodier, et al., 2011; van der Merwe, et al., 2021). By combining both phylogenetic and cosmogenic nuclide-based ages and analyzing the fault systems, a refined understanding of the timing and age of landscape changes may be achieved (Burridge et al., 2006; Cotterill and de Wit, 2011).

The focus of this study is to tackle fundamental issues referring to the understanding of the neo-tectonics, the drainage and river evolution and the level to which climatic variations have contributed to the geomorphological history of the area around the current Lakes Mweru and Upemba. The contribution of the general tectonic activity of the EARS is fundamental to the size and lifetime of the paleo-lakes. We attempt to constrain the extent and depth of the paleo-lake Mweru, while estimating its life span and describing possible mechanisms that resulted in the shrinking of this large lake during the Pleistocene. In addition, we discuss the contribution of cosmogenic nuclides in predicting knickpoint retreat rates, using as case study the Kiubo Waterfalls of the Lufira River, which are located in the Upemba Fault System (Fig. 1.2.). Due to the complex exposure scenarios, involving denudation and retreat of waterfalls, analysis of the radionuclides ^{10}Be and ^{26}Al was combined with measurements of stable ^{21}Ne.

Part of this research has been already published in the journal *Geomorphology* with the title “Quaternary landscape evolution in a tectonically active rift basin (paleo-lake Mweru, south-central Africa)” (Olivotos et al., 2021). It should be noted that chapters 4, 5 and 6 of this thesis are written as “stand alone” studies, therefore some aspects, such as parts of the Geological Setting and Methodology chapters, will be repeated in each one of them.

Chapter 2

Geological Setting

2. Geological Setting

2.1. *Lake Mweru and the Mweru-Mweru Wantipa Fault System*

Lake Mweru is part of the western branch of the EARS. Along with the Lakes Mweru-Wantipa and Bangweulu (Northern Province, Zambia), they shape a basin-and-range topography, controlled mostly by normal faults. Lake Mweru forms a half graben, which is part of the MMFS, and together with the Okavango rift they form the Southern Complex of the EARS (Tiercelin and Lezzar, 2002). The NE-SW trend of the MMFS intersects at high angles (~90°) the main EARS trend as a result of the rotation of the extension direction from ~E-W to NW-SE near the southern Lake Tanganyika (Mohr, 1974; Tiercelin et al., 1988; Mondeguer et al., 1989; Delvaux, 1991; Tiercelin and Lezzar, 2002; Chorowicz, 2005; Kipata et al., 2013; Saria et al., 2014). Gravimetric and heat flow anomalies witness the migration of the extensional activity to the southwest (Reeves, 1972; Ballard and Pollack, 1988; Tiercelin and Lezzar, 2002), making nowadays the Southern Complex an area of high seismicity (Shudofsky, 1985; Tiercelin and Lezzar, 2002).

The MMFS is ~400 km long and ~200 km wide and it can be separated in two parts. The eastern part of the fault zone is characterized by an elongated ENE-WSW trend, almost perpendicular to the NW-SE trend of the Mpulungu basin (southern Lake Tanganyika; Tiercelin and Lezzar, 2002). Small and parallel grabens form shallow depressions, which are typical to swamp environments (Mondeguer et al., 1989). To the west, the two major troughs with NNE-SSW trend form the two main shallow lakes (Lakes Mweru and Mweru-Wantipa). The majority of the faults are following the NNE-SSW trend, while few faults have a perpendicular trend of WNW-ESE mainly at the end of the basins (Mondeguer et al., 1989).

South of Lake Mweru, a large basin of sub horizontal sedimentary cover (Mporokoso Plateau) is developed on the Bangweulu Block (Mondeguer et al., 1989). The Bangweulu Block is mostly located in northern Zambia, but it also extends into the D. R. Congo and Tanzania. It is the tectonic foreland of the Irumidae orogenic belt (~1.8 Ga) and is composed of Archean and Paleoproterozoic crust, incorporated in the Paleoproterozoic Ubendian Belt as well (Hanson, 2003; De Waele and Fitzsimmons, 2007; De Waele et al., 2009). The Mporokoso Plateau comprises mostly undeformed fluvial and lacustrine sediments (De Waele and Fitzsimmons, 2007). The maximum age of this large metasedimentary and metavolcanic sequence (with a combined thickness of ca. 5000 m) was constrained to 1.8 Ga by Rb-Sr whole-rock dating of granites, which occur unconformably within the base of the plateau (De Waele and Fitzsimmons, 2007). Unrug (1984) characterized the Mporokoso Plateau as the pre-Katangan successions to the northwest and northeast of the Bangweulu Block.

A thick sedimentary rock succession, called Kundelungu Plateau, forms the half graben structure that delimits the lake to the north (Fig 1.2). The Kundelungu Plateau is a part of the larger Neoproterozoic Katangan Supergroup, together with the Roan and Nguba Groups, and it consists of carbonitic and siliciclastic sequences, which were deposited in a wider basin. This deposition corresponds to a major phase of extensional tectonics and normal faulting (Kampunzu et al., 1993; Batumike et al., 2007), and it is dated between <630 and ~500 Ma (Kampunzu and Cailteux, 1999; Cailteux et al., 2018).

The sedimentary rocks that are exposed at the northern margin of the plateau have horizontal to sub-horizontal bedding, while the ones exposed in the south are metamorphosed. These contrasting structural patterns between the two phases led to the division of the Katangan belt into a metamorphic zone (Lufilian Arc) in the south and an aulacogen structure (or paleo-graben) in the north (Unrug, 1988; Dumont and Hanon, 1997; Batumike et al., 2019). It was suggested that these two phases represent the transition from extensional to compressional tectonics in the Katangan basin (Kampunzu et al., 2000). Bedded red sandstones of the Kundelungu Plateau are exposed where Lake Mweru currently outflows into the Luvua River. This formation controls tectonically the development of the northwestern side of the half graben (Kipata et al., 2013).

Successive episodes of rifting since the late Miocene vastly reformed the ancient drainage network of Katanga and Northern Zambia, changing the course of major rivers and creating several paleo-lakes (Bangweulu, Lufira, Mweru and Upemba; Cotterill, 2004; Moore et al., 2007, 2012). Dixey (1944), Bos et al. (2006), Goodier et al. (2011) and Cotterill and de Wit (2011) support the idea that the original Lake Mweru formed a large impoundment that extended over the lower part of the Northern Province of Zambia. It is inferred that this high stand was eventually tapped by headwater retreat of the Luvua River, possibly in the Plio-Pleistocene (Fig. 1.2). The evidence for a “greater” Lake Mweru was primarily supported by lacustrine deposits (Dixey, 1944), whereas later Bos et al. (1995, 2006) suggested that sands along the present-day Zambian shores of Lake Mweru might indicate a different course of the Luapula River (Fig. 1.2). Nevertheless, no fieldwork has hitherto explored the precise extent and duration of such a paleo-lake.

2.2. *The Upemba Fault System*

The Upemba Depression is located in the Katanga Province of the DRC (Figure 1.2). It comprises around 50 lakes, including Lake Upemba. It is assumed that in earlier years the area was occupied by a single massive lake. Nowadays, it is covered by marshland (Symoens, 1963).

The geology of the Katanga Province (DRC) and Northern Zambia comprises Proterozoic formations influenced by a complex tectonic history (Porada and Berhorst, 2000), resulting in the intense topography of the Katanga Plateau and highlighting the Kamalondo and Lufira Depressions (Cotterill, 2005). The intense tectonic activity across Katanga and Northern Zambia (Mondeguer et al., 1989; Sebagenzi and Kaputo, 2002) led to substantial uplift events, which contributed to the formation of the characteristic features of the Biano, Kibara and Kundelungu Plateaus (Cotterill, 2005).

The Upemba Depression was initially described as a graben by Cornet (1912). An elongated fault system extends along its eastern side with a NE-SW strike. The Upemba Fault System (UFS) comprises the Biano and Kibara Plateaus (horsts) and the Kamalondo Depression (graben), which contains the Upemba swamps (Cotterill, 2005). One of the most dominant features that has contributed to the landscape formation is the Lufira River, which separates the two high plateaus (Cotterill, 2005). The catchement of the Lufira River is located in a broad depression to the south-east (Fig. 1.2). To the south-west, the Kundelungu Plateau delimits the northern edge of the Lufira Depression (Cotterill, 2005).

The UFS is a large subsidizing tectonic basin along the Kibaran margin, in the same way as the MMFS extends along the Kundelungu foreland (Sebagenzi and Kaputo, 2002). After the formation of the Neoproterozoic–Lower Paleozoic Lufilian Arc (Wendorff, 2005), both of these structures developed a NE-SW trending incipient rift branch. This propagation of the EARS into southern Africa is accompanied by moderate to intense seismicity (Calais et al., 2006; Craig et al., 2011) and thermo-mineral springs (Mondeguer et al., 1989; Sebagenzi and Kaputo, 2002; Kipata et al., 2013). The NE-SW trend of the UFS and the MMFS is a feature that can be found also in Bangweulu Lake, in the local drainage system of the Chambeshi River in Zambia and in the lowlands west of the Lufira River in the DRC. This distinct NE-SW orientation occurs across South East Africa (Dehandschutter and Lavreau, 1985) and suggests neotectonic reactivation, which can be seen even in the Neogene sediments and alluvium formations (Master et al., 2005). The cause of this lineament rejuvenation is related to the recent neotectonic activity of the EARS. Geophysical evidence of continental break-up in the south-eastern DRC and in north-western Zambia was reported from available gravitational, heat flow and seismological data (Sebagenzi and Kaputo, 2002), connecting the tectonic activity of the EARS to the most prominent seismotectonic features in the study area (Mavonga et al., 2010). The fundamental difference between the Upemba and Mweru Rift systems is the period of onset. The opening of the Upemba basin is connected to the breaking up of Gondwana during its crustal extension (Daly et al., 1989). The Mweru graben is related to the Cenozoic rifting episodes (Mondeguer et al., 1989). There is evidence that both of the rift systems are incipient arms of the EARS and still actively spreading (Fairhead and Girdler, 1972; Camelbeeck and Iranga, 1996).

As mentioned previously, neotectonic continental rifts usually follow pre-existing lineaments. The UFS is no exception, following the structures of the Kibaran belt. This Mesoproterozoic belt of supracrustal units is located in Central Africa and is part of the Kibaran orogeny. It comprises mostly metasedimentary rocks and minor metavolcanic rocks, which are S-type granitoids and mafic bodies. The Kibaran belt has around 1300 km length and trends NE-SW from the Katanga region in the DRC until southwest Uganda (Tack et al., 2010). Satellite imagery reveals two segments of the belt, KIB (Kibara belt sensu-stricto) in the Katanga region (Kokonyagi et al., 2004) and KAB (Katagwe-Ankole belt) in Rwanda-Burundi and its equivalent in Lake Kivu (Fernandez-Alonso et al., 2012). Btween the two belts there is a poorly defined deformation zone in which is superposed an elongated Karoo depression, which was reactivated during the late Cenozoic rifting (Fernandez-Alonso et al., 2012).

The thick supracrustal sedimentary sequence (>10,000 m) of the Kibaran belt is described as Kibara Supergroup and consists mainly of metamorphosed pelites, siltstones, sandstones and conglomerates, with minor carbonate rocks (Cahen et al., 1984). The metavolcanics intrude the metasedimentary succession as large felsic and mafic igneous bodies (Kampunzu et al., 1993). However, according to Cahen et al. (1984) both of the bedrock sequences were affected by two major compressional events between 1.4 and 1.0 Ga. The first event (1.4 to 1.25 Ga) is considered to be related to an active continental margin (Kampunzu et al., 1993). Between 1.25 and 1.0 Ga a continental collision occurred, generating the NE-SW trending isoclinal folds and thrusts, which in the future will become the host of the rift system (Cahen et al., 1984; Kampunzu et al., 1993). In addition, a Kibaran tectonothermal event across East Africa peaked around 1.3 Ga and is responsible for the NNE-SSW trending of the Kibaran belt (Meert et al., 1994; Van Daele et al., 2020; De Clercq et al., 2021)

Chapter 3

Methodology

3. Methodology

3.1. *Terrestrial Cosmogenic Nuclides*

Terrestrial cosmogenic nuclides (TCNs) are continuously produced in the Earth's uppermost layers (within a few meters from the ground-surface) by interactions of secondary cosmic rays with matter (Lal, 1988; Gosse and Phillips, 2001; Niedermann, 2002; Dunai, 2010; Section 1.4). Cosmogenic nuclides provide a means of determining the age of geomorphic features that were suddenly revealed by geological processes. However, any subsequent denudation of these surfaces decreases the nominal exposure age and only allows the determination of a minimum exposure age.

Geomorphic features that have been dated using this method include fluvial and marine terraces, alluvial fans, moraines, landslide deposits and exhumed fault planes (e.g. Brown et al., 1991; Granger et al., 1997; Kubik et al., 1998; Hancock et al., 1998; Schildgen et al., 2002; Saillard et al., 2011; Mouslopoulou et al., 2014). Local and catchment-wide denudation rates can be determined also (e.g. von Blanckenburg et al., 2004; Burbank and Anderson, 2013). Temporarily buried sedimentary deposits can be dated by combining two or more nuclides with different half-lives (e.g. Bierman et al., 1999; Matmon et al., 2003; Stock et al., 2004; Häuselmann et al., 2007; Matmon et al., 2014; Šujan et al., 2017). When production by cosmic rays stops, the concentration ratio of two radionuclides with different half-lives (e.g. ^{10}Be and ^{26}Al) or a radionuclide and a stable nuclide (e.g. ^{10}Be and ^{21}Ne) will progressively deviate from the production ratio as a function of time due to radioactive decay. Therefore, a decreased value of, e.g., ^{26}Al/^{10}Be can be explained by a period of temporary burial (e.g. Davis et al., 2014; Matmon et al., 2014). Such burial events add complexity to the exposure history of a land surface.

3.1.1. Sampling Procedure

About 50 samples of bedrock quartzites and sandstones across the Mporokoso Plateau (Zambia) and the Kundelungu Plateau (DRC), as well as from Kiubo and Luvilombo Waterfalls (DRC), were collected, mostly from vertical or subvertical (45-90°) surfaces, of which 36 were analyzed for their ^{10}Be, ^{26}Al and ^{21}Ne concentrations (Fig. 1.1 and 3.1). Most of the samples were taken downstream of the currently active knickpoint positions along the banks of the rivers. Where possible, samples were taken from the knickpoints (waterfalls) themselves to determine the minimum exposure age of the knickpoint at its current position. In order to determine maximum denudation rates, samples from horizontal surfaces (from above and below the knickpoints) were also collected. Three samples were collected directly from river beds, whileone sample was collected from a fault surface north of Lake.

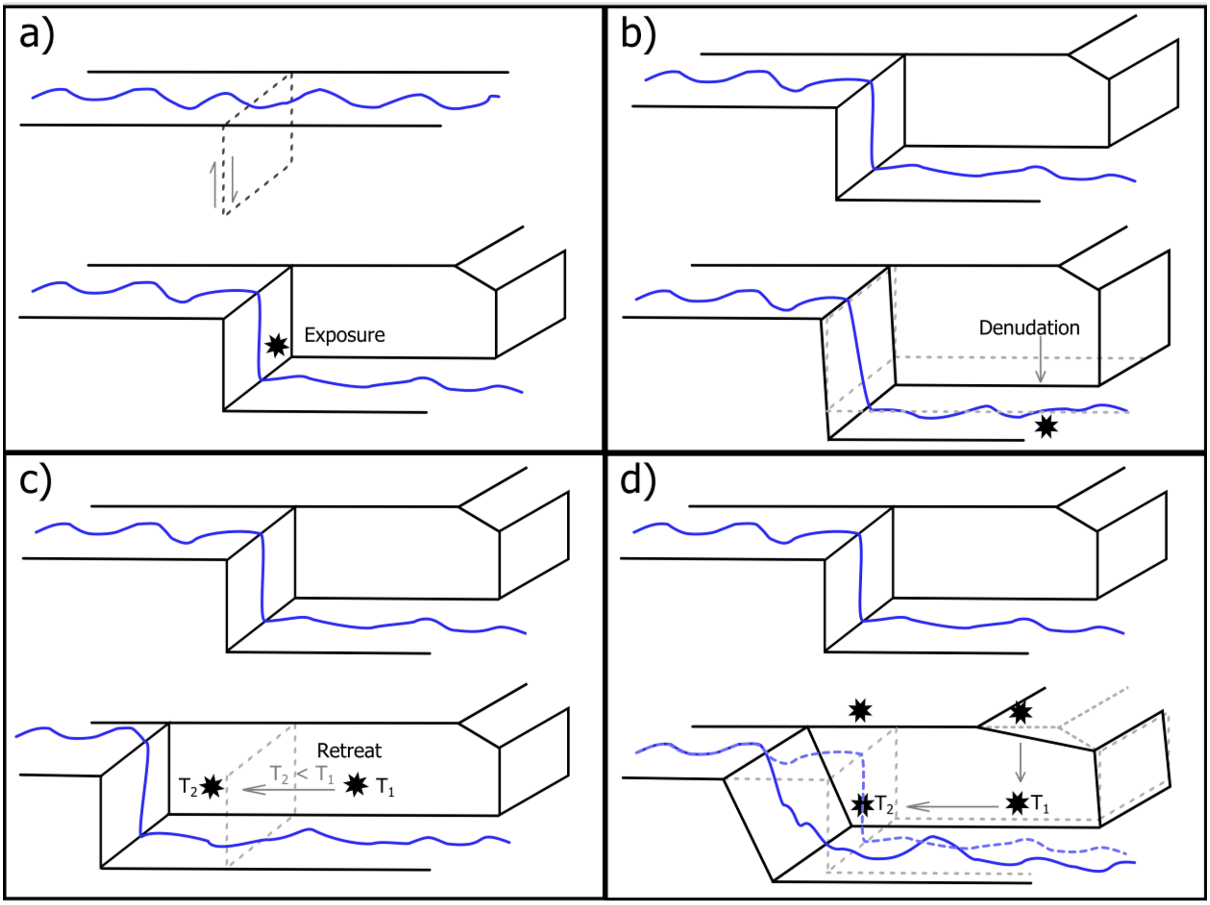

Figure 3.1: Graphic sketch of the terrestrial cosmogenic nuclide sampling process targeted on knickpoints. Black asterisks indicate sampling points. The potential minimum exposure ages of the samples are indicated as T_i. The blue line indicates the stream of the river.

Figure 3.1 presents the three sampling strategies used in this study. The blue line represents the stream of the river, while the star is the sampling location on the exposed surface. The first panel (a) describes an ideal case, the collection of a single sample directly on the vertical surface of the knickpoint. The upper sketch represents the initial surface prior the creation of the knickpoint, which was caused, in our case, by normal faulting. The direct sampling of the vertical surface is meant to date a rock surface that was not exposed to cosmic rays prior to the knickpoint formation. This exposure may occur through a fault for example and, ideally, a sample from this surface may provide the age of the knickpoint. The second case (b) presents the collection of a single horizontal surface sample from below the knickpoint. However, due to denudation such surfaces (river bed and/or horizontal channel bank) may not provide the actual exposure time but only a minimum age. The last two sketches (c and d) represent the collection of two sample sets from the vertical banks of the river channel. As the knickpoint retreats, the vertical banks of the channel are progressively exposed to cosmic radiation. Samples closer to the knickpoint (T2) should yield younger minimum exposure ages than the ones that are further downstream (T1; c). By combining both vertical bank and horizontal bank samples, a rate of knickpoint retreat may be determined and a comparison of both horizontal and vertical sample ages will indicate the main mechanism of knickpoint evolution (d).

3.1.2. Sample Processing, Analyses and Calculations

Thirty-six samples were crushed and sieved to 250–500 µm. The quartz grains were separated by the standard methods of heavy liquid and Frantz magnetic separation (Kohl and Nishiizumi, 1992). Preparation and processing of the samples took place following a modified version of the method described by Merchel and Herpers (1999) and the sample preparation manual of the UC Santa Barbara Cosmogenic Nuclide Preparation Facility (http://www.geog.ucsb.edu/~bodo/pdf/bookhagen_chemSeparation_UCSB.pdf), which is based on modifications of previous studies (e.g., Kohl and Nishiizumi, 1992; von Blanckenburg et al., 2004).

Different labs were used due to organizational and technical reasons. The labs used for sample preparation were Helmholtz-Zentrum Dresden-Rossendorf, Germany (HZDR), the HELGES laboratory of GFZ Potsdam, Germany and the University of Potsdam, Germany, while the radionuclide isotope ratio measurements were performed at the Accelerator Mass Spectrometers (AMS) of the DREAMS facility of HZDR, Dresden, Germany (Rugel et al., 2016), the National Laboratory of Age Determination of the Norwegian University of Science and Technology (NTNU), Trondheim, Norway (Seiler et al., 2018), the French national facility Accélérateur pour les Sciences de la Terre, Environnement, Risques (ASTER, CEREGE, Aix-en-Provence; Arnold et al., 2010; Sartégou et al., 2018) and the Institute of Nuclear Physics at the University of Cologne (Pascovici et al., 2013). ^{21}Ne determinations were carried out in the noble gas laboratory of the GFZ Potsdam, where the concentrations and isotopic compositions of He and Ne were measured using a static VG5400 noble gas mass spectrometer (Niedermann, 1997).

To calculate exposure ages and denudation rates, sea level high latitude (SLHL) spallogenic production rates of 4.01 atoms g^{-1} yr^{-1} for ^{10}Be, 27.93 atoms g^{-1} yr^{-1} for ^{26}Al (Borchers et al., 2016) and 17.51 atoms g^{-1} yr^{-1} for ^{21}Ne were used. This value is based on the total ^{10}Be production rate of 4.06 atoms g^{-1} a^{-1} (Borchers et al., 2016) and the ^{10}Be/^{21}Ne production ratio of 0.232 ± 0.009 (Goethals et al., 2009). Ages and denudation rates were calculated with

CosmoCalc 3.0 (Vermeesch, 2007), using Lal (1991) scaling factors and default values for all parameters except the SLHL production rates for the aforementioned nuclides. More details about sample processing, analyses and calculations of the final results will be found in the Chapters 4 and 6.

3.2. *Tectonic and Geomorphic Analyses*

Active faults across the Mweru-Mweru Wantipa Fault System (MMFS) and around the Upemba Fault System (UFS) were traced using an SRTM (Shuttle Radar Topography Mission) Digital Surface Model (30 m horizontal resolution) and analyzed with ArcGIS software (Fig. 3.2). Collecting attributes which are associated with the geometry and kinematics of the fault system (e.g. strike, fault traces, vertical maximum displacements, displacement rates and earthquake magnitudes) contributes to the detailed investigation of the regional tectonic deformation (Begg and Mouslopoulou, 2010). Lineament surface traces and landscape displacements represent active faults, and thus these features were used for the fault identification. Many faults may contain numerous fault traces that are either hard or soft linked (Walsh and Watterson, 1991). Cross-sections with general direction NW-SE and NNE-SSW were created, using the ArcGIS software, to analyze the tectonic evolution of the extended area of the MMFS.

Earthquake data of the last ~35 years (Fig. 3.2) were collected from forty-nine earthquakes across the MMFS and the UFS (Storchak et al., 2020). Seismic moments were calculated in order to analyze the current tectonic activity of the two fault systems.

Our digital topography analysis was based on selected domains of the 30-m NASADEM (NASA JPL, 2020). We have delineated the catchment of Lake Mweru using standard procedures implemented in TopoToolbox (Schwanghart and Scherler, 2014). Elevation lows (pits) were filled, a hydrological-corrected DEM was calculated, and the catchment extents were visually verified. Our catchment extent, using the higher resolution NASADEM data, is similar to that calculated in the HydroBASINs dataset (Lehner and Grill, 2013). Further, we identified river knickpoints using previously published approaches (Neely et al., 2017). More details about the tectonic and geomorphic analyses may be found in Chapter 5.

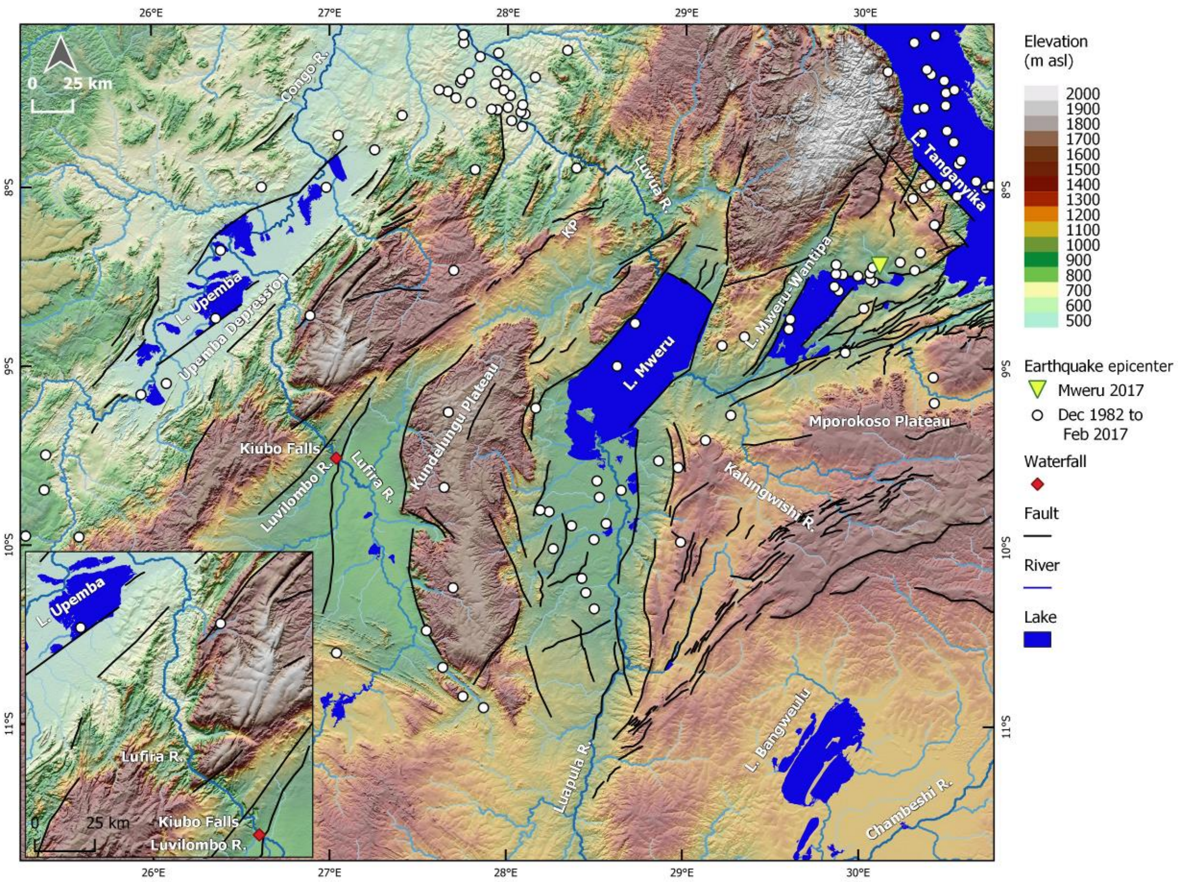

Figure 3.2: Morphotectonic map of the Mweru-Mweru Wantipa Fault System (MMFS) and the Upemba Fault System (inset) in the southern East African Rift System. Black lines indicate normal faults. White circles indicate earthquakes (December 1982 until February 2017).

Chapter 4

Quaternary Landscape Evolution of South-Central Africa: Cosmogenic Nuclides Identify the Paleo-Lake Mweru

4. Quaternary Landscape Evolution of South-Central Africa: Cosmogenic Nuclides Identify the Paleo-Lake Mweru

4.1. Introduction

The East African Rift System (EARS) represents one of the best studied active intracontinental rifts on Earth (Ebinger, 1989; Delvaux, 1991; Delvaux et al., 1992; Ring, 1994; Schlüter, 1997; Chorowicz, 2005; Braile et al., 2006; Stamps et al., 2008). The combination of the EARS's size, > 3000 km long, and longevity, active throughout the Neogene (~25 Ma), provides a unique opportunity to study the evolution of continental rifting, from initial crustal break-up (via normal faulting) to oceanic rifting and, finally, the opening of future oceans. Overall, the EARS may be considered the dominant control on the evolution of the landscape of eastern Africa during the last ~30 Ma (Chorowicz, 1989, 2005).

The study area is centered on Lake Mweru, a region that straddles the borders of the Democratic Republic of Congo (DRC; Katanga Province) and Zambia (Northern Province) (Fig. 4.1). This area, south-west of Lake Tanganyika, is part of the fast-spreading Western Branch (WB) of the EARS and is characterized by a basin-and-range topography, controlled by the normal faults of the Mweru-Mweru Wantipa Rift System (MMFS), which extends in almost perpendicular (ENE-WSW) trend to the Tanganyika Rift System. It is well known that the MMFS component of the WB consists of the most seismically active faults of central east Africa, which create typical horst and graben structures, hosting the two high-altitude lakes Mweru (917 m asl) and Mweru-Wantipa (932 m asl; Delvaux and Barth, 2010; Daly et al., 2020). The lakes are bounded by the two high plateaus of Mporokoso and Kundelungu, to the southeast and northwest, respectively (Fig. 4.1).

This study reports on, and interprets, new geologic data of an interdisciplinary project that combines molecular dating of select fish groups (through DNA sequencing) with surface exposure dating of key geomorphic landforms. By combining both phylogenetic and cosmogenic nuclide-based ages, a refined understanding of the timing and age of landscape changes may be achieved (Burridge et al., 2006; Goodier et al., 2011). Through the analysis of surface exposure dating on knickpoints, this paper contributes to the reconstruction of the landscape evolution of South-Central Africa.

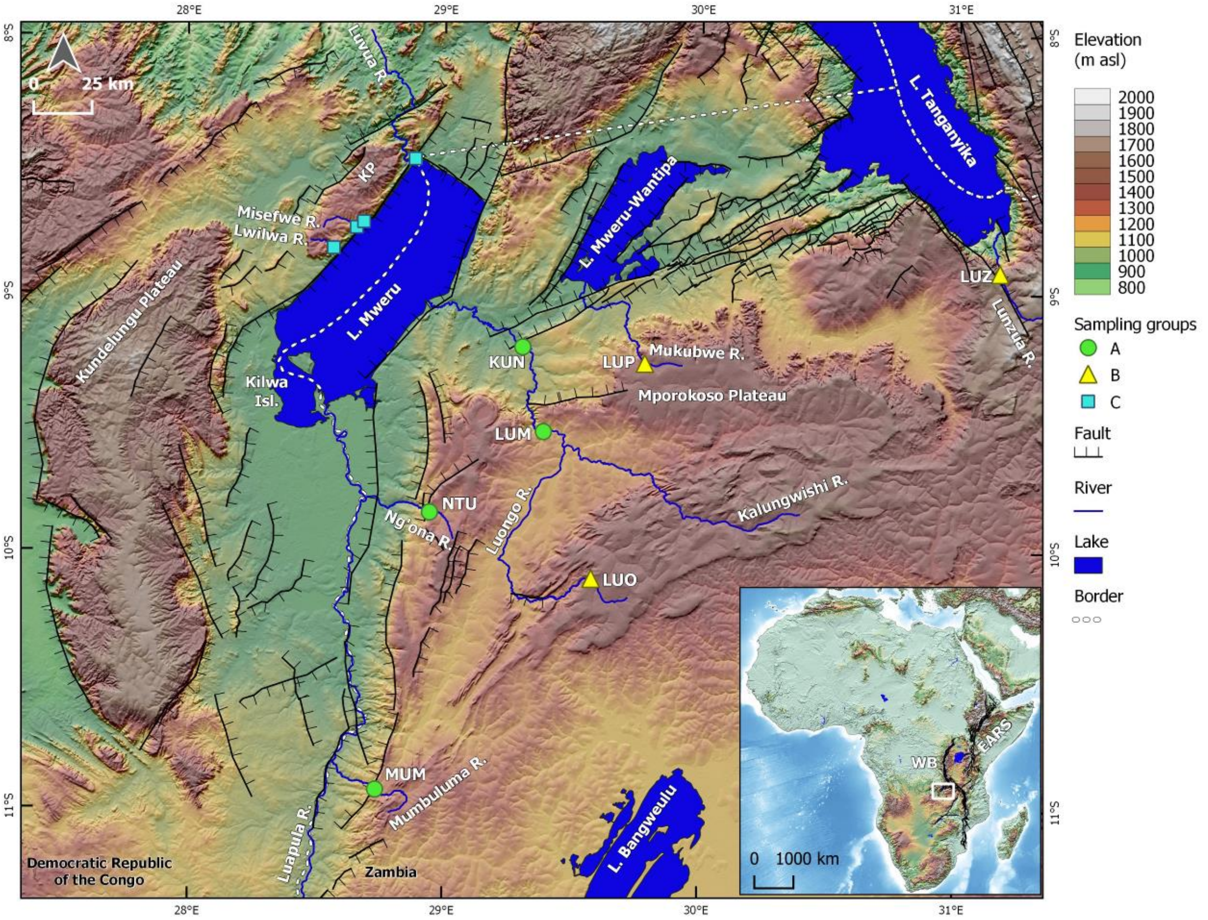

Figure 4.1: Morphotectonic map of the Mweru-Mweru Wantipa Fault System in the southern East African Rift System. Normal faults are indicated by black lines while ticks indicate downfaulted side. Green circles, yellow triangles and blue squares indicate sampling locations of the three different sampling groups (see section 4.3). Blue lines indicate major rivers. Inset shows location of study area in Africa. KUN: Kundabikwa Waterfalls; LUM: Lumangwe Waterfall; NTU: Ntumbachushi Waterfalls; MUM: Mumbuluma I Waterfalls; LUP: Lupupa Waterfall; LUO: Mumbuluma II Waterfall; LUZ: Lunzua Waterfalls.

Given the potential complex exposure scenarios, involving denudation and retreat of waterfalls, analysis of the radionuclides ^{10}Be and ^{26}Al was combined with measurements of stable ^{21}Ne in order to increase the robustness of the results.

Since geomorphological and geochronological data about the MMFS are scarce, our study aims to tackle fundamental issues referring to the understanding of the neo-tectonics, the drainage and river evolution and the level to which climatic variations have contributed to the geomorphological history of the area around the current Lake Mweru.

A secondary, but key consideration of this study is that knickpoints form important biogeographic controls, acting as natural barriers to species dispersal, especially of fish, and are often responsible for divergent evolution between upstream and downstream populations of biota (Schwarzer et al., 2011). Thus, knowing the age and timing of knickpoints (or the events that formed them) not only elucidates the evolution of the landscape but also the evolution of species that track these geomorphic features.

The existence of large and deep Plio-Pleistocene paleo-lakes within the WB (e.g. paleo-lakes Turkana, Edward-Albert (Obweruka), Bangweulu, Magadi, Thamalakane, Tanganyika) has already been described (Williamson, 1978; Hillaire-Marcel et al., 1986; Burrough and Thomas, 2008; Cotterill and de Wit, 2011; Danley et al., 2012; Cohen et al., 2016). In such fast-opening rift zones with stable velocities over the last 11 Ma, lake level fluctuations are mostly controlled by climatic variations (Lavayssiere et al., 2019). Evidence for a “greater” Lake Mweru is primarily found in lacustrine deposits, which are standing at ~1030 m asl (Dixey, 1944), about 100 m higher then present day lake levels. Other studies (Bos et al., 1995, 2006) suggest that sands along the present-day Zambian (southern and south-eastern) shores of Lake Mweru may be indicative of the migration of the course of the Luapula River (Fig. 4.1). Based on sedimentary deposits along the south-western shore of the lake, it is known that the Luapula River’s delta was more to the west than its current position (Bos et al., 1995). Several studies support the argument that the original Lake Mweru formed a large impoundment that extended over the lower part of the Northern Province of Zambia. It is inferred that this high stand was eventually tapped by headwater retreat of the Luvua River, possibly in the Plio-Pleistocene (Dixey, 1944; Bos et al., 2006; Goodier et al., 2011; Cotterill and de Wit, 2011; Fig. 4.1). Nevertheless, no fieldwork has hitherto confirmed the precise extent and duration of an inferred paleo-lake Mweru.

This chapter focuses on constraining the age of formation of the paleo-lake by dating key landfroms (knickpoints) across the two high plateaus (Mporokoso and Kundelungu Plateaus) which surround and delimit the current lake. An age determination of the onset of the paleo-lake contributes to the understanding of the landscape evolution of the southwestern part of the WB, while it reveals essential information about the drainage evolution of the Congo-Kalahari Watershed during the Pleistocene (Flügel et al., 2015; 2017). Furthermore, we will attempt to constrain the extent and depth of the paleo-lake Mweru, while estimating its life span and possible mechanisms that resulted in this large lake shrinking in size during the Pleistocene.

4.2. Geological Setting

The MMFS has a length of ~ 400 km, a width of ~ 200 km, and is divided into eastern and western parts. The eastern part is characterized by an elongated ENE-WSW trend, almost perpendicular to the NW-SE trend of the Mpulungu basin (southern Lake Tanganyika; Tiercelin and Lezzar, 2002). Small and parallel grabens form shallow depressions, characterized by wetland environments (Mondeguer et al., 1989). To the west, two major troughs with NNE-SSW trend form the two main shallow lakes (Lakes Mweru and Mweru Wantipa). The majority of the faults follow a NNE-SSW trend, while few faults that mainly confine the end of the basins have a vertical trend of WNW-ESE (Mondeguer et al., 1989). The deviation in the fault trend near the Mpulungu basin results from the competency contrast with the relatively stable Bangweulu Block (Mondeguer et al., 1989; Fig. 4.1). The rotation of the extension direction reactivated earlier dip-slip faults, since strain accumulated in the same pre-Pleistocene inherited crustal structures (Ring, 1994; Morley, 2002; Saria et al., 2014). Furthermore, earthquake fault plane solutions from the area indicate an extensional displacement around the WNW axis (Delvaux and Barth, 2010). Recent modeling studies suggest that the extension direction changes from ~60° to 90°, while a left-lateral motion is applied on two domains with NE-E oriented weaknesses in between them (Molnar et al., 2019 and references therein).

Lake Mweru (situated at ~9° S and ~29° E) forms part of the south-eastern extension of the Congo Basin, being fed from the south by the Luapula River and drained to the northwest by the Luvua River (Fig. 4.1). The drainage of the Lake Mweru sub-basin is mostly sub-dendritic, representing the interaction of rivers flowing on Precambrian basement and regional faulting (Deffontaines and Chorowicz, 1991; Flügel et al., 2015). The extensive delta of the Luapula River suggests rapid denudation of the high plateaus between Lake Mweru and Lake Bangweulu (Fig. 4.1). In addition, the accumulation of Quaternary sediments with a thickness of 400 m uncomformably overlying the Neoproterozoic basement (Bos et al., 2006; Daly et al., 2020) can be interpreted as further evidence of rapid denudation of the surrounding highlands. Quaternary sediments are absent from Kilwa Island, a Neoproterozoic clastic rock outcrop, north of the delta (Shudofsky, 1985; Tiercelin and Lezzar, 2002; Daly et al., 2020). In the north, the outflowing Luvua River runs through a steep valley path with several large waterfalls, suggesting rapid incision (Flügel et al., 2017). The Kalungwishi River, a major tributary, feeds Lake Mweru from the east. This river drains its own highland sub-basin and has several large knickpoints on its course. The inflowing rivers allow the lake to maintain a surface area of ~ 5100 km^2 year-round (Bos et al., 2006).

Southeast of Lake Mweru, a large basin of sub-horizontal sedimentary cover (Mporokoso Plateau) is developed onto the Archean-Paleoproterozoic cratonic Bangweulu Block

(Mondeguer et al., 1989; De Waele et al., 2009; Fig. 4.1). The Mporokoso Plateau consists mostly of undeformed fluvial and lacustrine sediments (De Waele and Fitzsimons, 2007). Unrug (1984) characterized the Mporokoso Plateau as the late Paleoproterozoic to late Mesoproterozoic pre-Katangan succession to the northwest and northeast of the Bangweulu Block. A thick sedimentary bedrock succession, called the Kundelungu Plateau, forms the half graben structure that delimits the lake to the northwest (Fig 4.1). The Kundelungu Plateau is a part of the larger Neoproterozoic (<883 Ma to ~573 Ma; Master et al., 2005) Katangan Supergroup, comprising carbonate and siliciclastic sequences, which were deposited in a wider basin. The bedded red sand- and siltstones of the Kundelungu Plateau are exposed at the northwest corner of Lake Mweru due to incision along the Luvua River (Kipata et al., 2013).

The interplay of faulting and erosion in the broader Lake Mweru region has resulted in two relatively flat but vertically offset surfaces: the Lake Mweru valley bottom and the surrounding plateaus. In general terms, the valley bottom (~ 900 m asl) is approximately 600 m lower than the flat plateau tops (~ 1500 m asl). The amagmatic character of the tectonism, combined with an indistinct sedimentation sequence across the southwestern extension of the EARS, does not allow precise dating of the initiation of faulting in the study area. The formation of the extended denudational surface of the Central African Plateau is estimated at around late Miocene to early Pliocene times (Daly et al., 2020). The absence of Neogene sedimentation across the Central African basin suggests that the tectonic activity must have been initiated after, or during, the uplift of the Central African Plateau, thereby constraining the onset of the MMFS to the late Pliocene - early Pleistocene (~2.6 Ma; Daly et al., 2020).

4.3. *Material and Methods*

4.3.1. *Sampling Process and Sample Grouping*

In order to ensure sufficient sample (quartz) to undertake dating, the field sampling mostly targeted bedrock quartzites due to their abundance in quartz. Sampling sites were located on or near waterfalls (knickpoints) as these are sites of exposed rock and considered key features in a river's development. Samples were taken from two broad areas, the Mporokoso and Kundelungu Plateaus (Fig 4.1). From across the Mporokoso Plateau, twenty-two samples from seven waterfalls were collected (Table 4.1), more than half of them from vertical or subvertical (45-90°) surfaces (Fig. 4.2a), downstream of the present-day knickpoint position, while, where possible, samples were also taken from the waterfalls themselves to determine the minimum exposure age of the knickpoint at its current position (Fig. 4.2b; 4.2c). Dating two samples with different distances from the present knickpoint enables us, in principle, to estimate knickpoint retreat rates (Fig. 3.1. In order to determine maximum denudation rates, samples from horizontal surfaces (from above and below the knickpoints) were also collected (Table 4.1; Fig. 4.2b).

Five additional quartz-rich samples were obtained from the northwest shore of Lake Mweru (Kundelungu Plateau): two of them derived from horizontal and two from vertical surfaces located along river channels (Fig. 4.2d) and one directly from the fault that bounds the MMFS to the north (Fig. 4.2e). Sample information may be found in Table 4.1 and more detailed description of the sampling process in Fig. 3.1.

Based on their location relative to the MMFS, we present our samples as three main groups: Group A samples are from south and southeast of Lake Mweru within the MMFS, Group B samples are also from southeast of Lake Mweru but situated outside the MMFS, and Group C samples derive from north of Lake Mweru, along the northern margin of the MMFS (Table 4.1; Fig. 4.1).

Table 4.1: Sampling details for samples from Northern Province, Zambia and Katanga Province, Democratic Republic of Congo. Total shielding factor includes surface dip, horizon shielding and self-shielding.

Name	Latitude ° S	Longitude ° E	Elevation (m)	Surface Dip (°)	Average Thickness (cm)	Total Shielding Factor
Kundabikwa Waterfalls, Kalungwishi River, Zambia						
KUN01	9.21207	29.30468	1037	90	2.5	0.49
KUN02	9.21201	29.30470	1043	0	2.5	0.97
KUN03	9.20947	29.30399	1043	0	2.5	0.98
KUN04	9.20949	29.30403	1039	90	2.5	0.49
KUN05	9.20824	29.30189	1034	0	7	0.94
KUN06	9.20849	29.30184	1030	90	2	0.49
KUN07	9.21781	29.30395	1030	0	2.5	0.98
Lumangwe Waterfall, Kalungwishi River, Zambia						
LUM02	9.54023	29.38688	1150	86	2.5	0.53
LUM03	9.54027	29.38696	1159	0	2.5	0.98
Ntumbachushi Waterfalls, Ngona River, Zambia						
NTU01	9.85439	28.94402	1157	75	2.5	0.65
NTU02	9.85421	28.94397	1157	5	2.5	0.88
NTU03	9.85481	28.94346	1167	90	2.5	0.49
Mumbuluma I Waterfalls, Mumbuluma River, Zambia						
MUM01	10.93031	28.73533	1182	90	2.5	0.49
MUM02	10.93544	28.73293	1178	0	2.5	0.98
MUM03	10.92980	28.73502	1177	90	8.5	0.46
MUM04	10.93012	28.73532	1186	0	2.5	0.98
Lupupa Waterfall, Mukubwe River, Zambia						
LUP01	9.27355	29.78074	1361	90	2.5	0.49
Mumbuluma II Waterfall, Luongo River, Zambia						
LUO01	10.10907	29.57566	1371	45	2.5	0.90
LUO02	10.10732	29.57449	1339	50	7.5	0.76
Lunzua Waterfalls, Lunzua River, Zambia						
LUZ01	8.91501	31.15994	1258	90	2.5	0.45
LUZ02	8.91686	31.16070	1303	90	2.5	0.48
Luvua River, D.R.Congo						
ME04	8.48340	28.88423	937	90	2	0.49
ME05	8.48366	28.88371	985	90	5	0.54
Musefwe River, D.R. Congo						
ME06	8.72807	28.68353	992	0	1	0.98
Lwilwa River, D.R. Congo						
ME09	8.82977	28.56613	1030	0	2	0.98
Fault scarp sample, D.R. Congo						
MWE01	8.74980	28.65532	1035	80	7.5	0.56

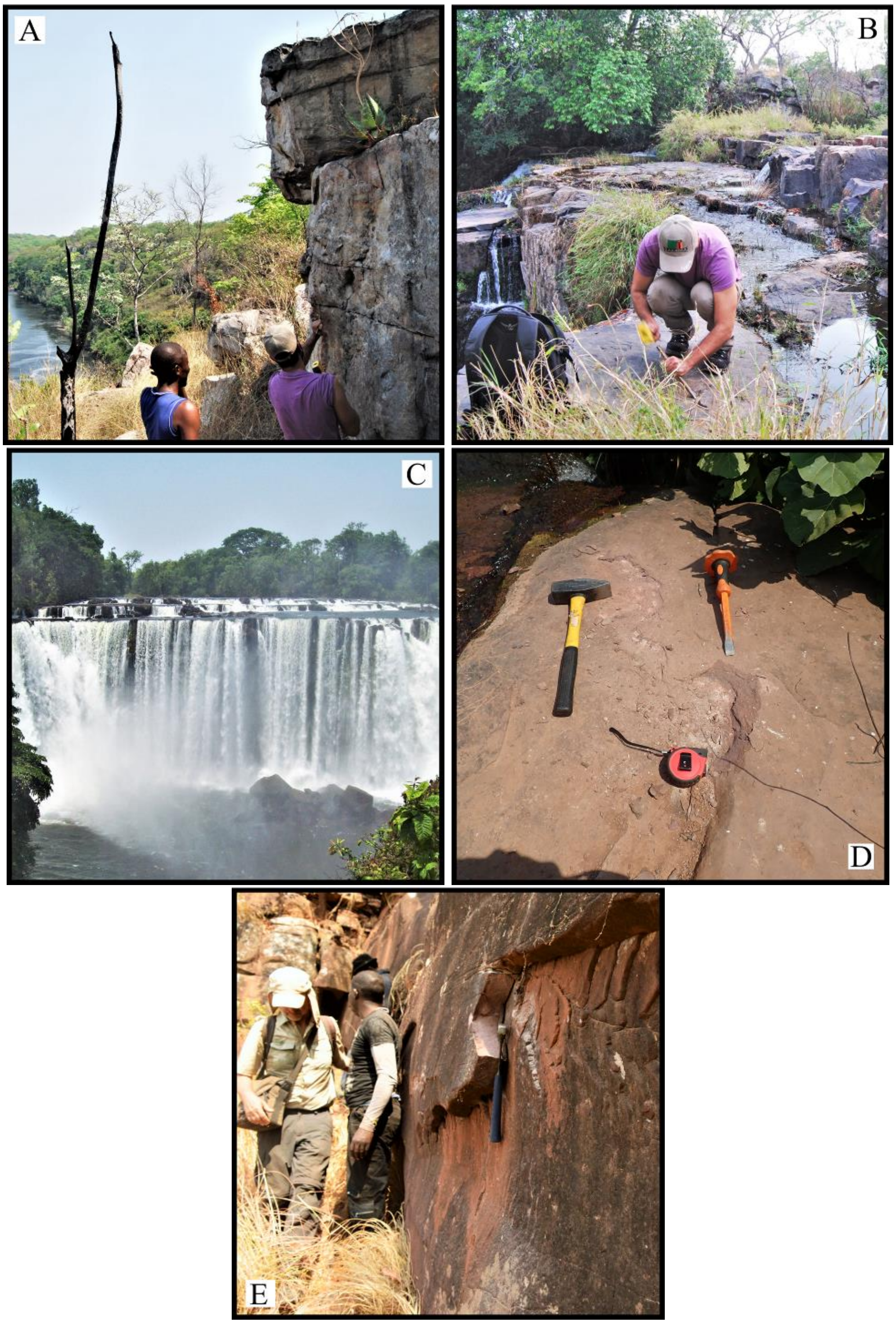

Figure 4.2: A) Sampling of KUN01 from a vertical face on the banks of Kalungwishi River, downstream of Kundabikwa Waterfalls, Zambia; B) Sampling of bedrock (MUM04) directly from the horizontal surface of the knickpoint at Mumbuluma I Waterfalls, Zambia; C) View of Lumangwe Waterfall, Zambia; D) Sample location of ME09, Lwilwa River, DRC; E) Sampling of MWE01 from the face of a fault, DRC.

Group A

The ~25 m high Kundabikwa Waterfalls (elevation ~1043 m asl) are carved into quartzitic bedrock and form one of the two main knickpoints along the Kalungwishi River. Three pairs of vertical and horizontal samples (KUN01/02, KUN03/04 and KUN05/06) were taken from the right bank at different distances from the present waterfalls. An additional sample (KUN07) was collected from the left river bank immediately above the waterfalls.

The Lumangwe Waterfall (~1159 m asl), located ca. 37 km upstream of the Kundabikwa Waterfalls, forms the most prominent knickpoint along the Kalungwishi River, with a height of ~40 m and a width of ~160 m (Fig. 4.2c). At Lumangwe Waterfall, the main bedrock is interbedded quartzite, with layers of red siltstones. Due to the vegetation density and the large volume of water, sampling this waterfall was challenging. Therefore, only one siltstone sample from a vertical face (LUM01) and a pair of quartzitic samples from vertical (LUM02) and horizontal (LUM03) surfaces were taken. Due to the very low amount of appropriately sized quartz grains, LUM01 could not be analyzed.

The cascade of the Ntumbachushi Waterfalls (~1160 m asl) is about 30 m high and is located on the Ng'ona River. Three samples were collected from these waterfalls, of which NTU01 and NTU03 were taken from the right vertical bank downstream of the current knickpoint, while NTU02 was collected above NTU01 from the corresponding horizontal bank.

The Mumbuluma Waterfalls (~1186 m asl) are situated on the Mumbuluma River and cascade down over two discrete steps. They will be denoted Mumbuluma I Waterfalls hereafter to distinguish them from the equally named waterfall on the Luongo River (section 4.3.1.1.). MUM01 and MUM04 were collected from a vertical and a horizontal surface, respectively, of the top cascade, while the samples MUM02 (horizontal) and MUM03 (vertical) were taken from the lower step of the waterfalls.

4.3.1.1. Group B

The Lupupa Waterfall is located on the Mukubwe River and has a height of approximately 90 m. The highest set of cascades is located at about 1360 m asl. Due to difficulties associated with the steepness of the waterfall, we only managed to collect one sample (LUP01) close to the top of the vertical cliff.

The Luongo River is one of the dominant rivers of the Northern Province in Zambia. We collected two samples (LUO01 and LUO02) from inclined surfaces of the Mumbuluma

Waterfall (hereafter denoted Mumbuluma II to distinguish it from the falls on the Mumbuluma River), which lies at ~1370 m asl with ~10 m height.

The Lunzua Waterfalls form a series of cascades along the Lunzua River. The waterfalls are close to the town of Mpulungu at the southern shore of Lake Tanganyika (Fig. 4.1) and are situated at ~1300 m asl. Two vertical samples (LUZ01 and LUZ02) were collected from the banks of the Lunzua River downstream of the cascades.

4.3.1.2. Group C

Due to the extreme inaccessibility of the waterfalls caused mainly by vegetation along the northwestern side of Lake Mweru, no samples from knickpoints were collected in that area. Rather, they were taken from river beds and banks comprising mostly of quartzitic bedrock. MWE01 derived from an almost vertical (80°) face that forms the surface expression of a normal fault scarp (Fig. 4.1; Fig. 4.2e). Two samples (ME04, ME05) were collected from the vertical walls of the gorge along the Luvua River, close to where it discharges from Lake Mweru (Fig. 4.1). The samples ME06 and ME09 were collected from horizontal bank surfaces along the Musefwe and Lwilwa rivers (Fig. 4.2d), two small tributaries northwest of Lake Mweru.

4.3.2. Sample Processing

Samples were crushed and sieved to 250–500 µm. Quartz grains were separated by the standard methods of heavy liquid and Frantz magnetic separation (Kohl and Nishiizumi, 1992). To dissolve all non-quartz minerals, samples were treated with dilute HCl and H_2SiF_6 (Brown et al., 1991). Afterwards, HF was used to remove any contribution of meteoric ^{10}Be by partially dissolving the quartz grains. A small fraction from each sample (~2 g) was kept for ^{21}Ne analyses, while the remaining ~25-50 g were used for ^{10}Be and ^{26}Al analyses. Further preparation and processing of the samples took place at the Helmholtz-Zentrum Dresden-Rossendorf (HZDR) following a modified version of the method described by Merchel and Herpers (1999) and at the University of Potsdam following the sample preparation manual of the UC Santa Barbara Cosmogenic Nuclide Preparation Facility (http://www.geog.ucsb.edu/~bodo/pdf/bookhagen_chemSeparation_UCSB.pdf), which is based on modifications of previous studies (e.g., Kohl and Nishiizumi, 1992; von Blanckenburg et al., 2004). The samples from the Kundabikwa Waterfalls (KUN) were prepared at HZDR, while the rest of the samples were prepared at University of Potsdam. For the radionuclide extraction, a known amount (~0.3 mg) of ^{9}Be carrier was added to each sample, whilst ~1 mg Al carrier was added only to the blank samples (Table 4.2). Samples that were prepared at HZDR were spiked with the ^{9}Be carrier “Phena DD” with a concentration of (3025 ± 9) µg g^{-1} (Merchel et al., 2008). As ^{27}Al carrier, a single element standard solution for ICP with an ^{27}Al concentration of 1000.5 mg l^{-1} and a density of 1.011 g cm^{-3}, made by ROTH, was used. For the samples that were prepared at University of Potsdam, the ^{9}Be carrier “Be 2 July 2016” with a concentration of (2511 ± 30) µg g^{-1} was used. The "Be 2 July 2016" carrier is an in-house carrier at the University of Potsdam that has been derived from Be-rich ores from a mine in Brazil. Furthermore, a Merck Certipur Aluminium ICP standard, traceable to NIST $Al(NO_3)_3$ in HNO_3 (2-3%), with a concentration of 10,000 mg l^{-1} Al was used. A complete Be and Al carrier data set is provided in the appendix (Tables A1 and A2). Concentrated HF was used for digestion of the samples. After evaporation of the HF and the addition of $HClO_4$, ICP-AES (Inductively Coupled Plasma Atomic Emission Spectroscopy) or ICP-MS (Inductively Coupled Plasma Mass Spectrometry) measurements were done from aliquots, which were dissolved in HCl, in order to quantify the total Al concentration (Table 4.2).

Be and Al were separated via ion exchange columns and precipitated as hydroxides. The last step before the target pressing was the ignition to oxides (900-1000 °C). Be isotope ratios were measured by Accelerator Mass Spectrometry (AMS) at the DREAMS facility of HZDR (Rugel et al., 2016; Table 4.2) and the National Laboratory of Age Determination of the Norwegian University of Science and Technology (NTNU), Trondheim (Seiler et al., 2018; Table 4.2). Al isotope ratio measurements were performed at HZDR (Rugel et al., 2016; Table 4.2) and at the French national facility Accélérateur pour les Sciences de la Terre, Environnement, Risques (ASTER, CEREGE, Aix-en-Provence; Arnold et al., 2010; Sartégou et al., 2018; Table 4.2).

^{21}Ne analyses were carried out in the noble gas laboratory of the GFZ Potsdam. The samples were initially purified using heavy liquids and magnetic separation, while in some cases, due to the small amount of the sample, hand-picking under a binocular microscope of non-quarzitic minerals was necessary. The material was also etched with diluted HCl and a mixture of diluted HF (1-4%) and HNO_3. The concentrations of the stable noble gas nuclides were measured using a static VG5400 noble gas mass spectrometer (Niedermann et al., 1997). About 0.7 g of clean quartz per sample were wrapped in Al foil and heated in four steps (400 °C, 600 °C, 800 °C and 1200 °C). A series of purification techniques, such as the combination of cryogenic traps and heated getters, were applied before and during the measurement in order to avoid implications from interfering compounds (e.g. CO_2, water vapor and heavy noble gases; Ivy-

Ochs and Kober, 2008). In addition, ~1 g aliquots of most samples were crushed in vacuum to determine the isotopic composition of Ne trapped in fluid inclusions (Niedermann 2002; Hetzel et al., 2002).

Table 4.2: Measured ^{10}Be/^{9}Be and ^{26}Al/^{27}Al ratios and ^{27}Al concentration in samples and blanks. Processing blanks are indicated with SOBLx (x=number of batch analyzed). All uncertainties presented are 1σ. Uncertainty for all ICP-MS (D) and ICP-OES (P) measurements of ^{27}Al concentrations is 3%. Labs used: D= HZDR, Dresden, Germany; T= NTNU, Trondheim, Norway; C= ASTER, CEREGE, Aix-en-Provence, France; P=University of Potsdam, Germany.

Name	^{10}Be/^{9}Be (10^{-13})	AMS	^{26}Al/^{27}Al (10^{-13})	AMS	^{27}Al (μg g^{-1})	ICP
KUN01	25.97±0.53	*D*	27.28±0.61	*D*	66	*D*
KUN02	16.81±0.34	*D*	17.99±0.46	*D*	73	*D*
KUN03	39.69±0.80	*D*	43.18±0.96	*D*	60	*D*
KUN04	30.75±0.62	*D*	31.60±0.86	*D*	80	*D*
KUN05	34.56±0.69	*D*	34.02±0.75	*D*	100	*D*
KUN06	5.60±0.13	*D*	5.48±0.20	*D*	103	*D*
KUN07	35.72±0.72	*D*	35.14±0.77	*D*	103	*D*
SOBL1	0.0142±0.0032	*D*	0.151±0.059	*D*	-	*D*
MUM01	2.082±0.056	*D*	3.05±0.15	*C*	184	*P*
MUM02	11.68±0.24	*D*	17.31±0.63	*C*	131	*P*
MUM03	3.421±0.081	*D*	4.72±0.27	*C*	112	*P*
MUM04	7.06±0.16	*D*	8.92±0.30	*C*	122	*P*
NTU01	0.900±0.033	*D*	1.02±0.10	*C*	177	*P*
LUP01	1.517±0.041	*D*	1.304±0.075	*C*	246	*P*
NTU03	3.120±0.076	*D*	3.73±0.26	*C*	116	*P*
SOBL2	0.0168±0.0038	*T*	0.031±0.014	*C*	-	*P*
LUO02	31.58±0.30	*T*	35.3±1.3	*C*	263	*P*
LUZ02	2.854±0.072	*T*	8.26±0.25	*C*	116	*P*
SOBL3	0.0185±0.0054	*T*	0.021±0.015	*C*	-	*P*
LUO01	1.539±0.049	*T*	9.39±0.29	*C*	146	*P*
NTU02	18.15±0.27	*T*	26.3±1.2	*C*	178	*P*
LUM02	2.178±0.067	*T*	1.326±0.087	*C*	1233	*P*
LUM03	10.44±0.15	*T*	13.13±0.40	*C*	237	*P*
LUZ01	11.58±0.16	*T*	21.40±0.72	*C*	165	*P*
SOBL5	0.0267±0.0065	*T*	0.044±0.044	*C*	-	*P*
ME04	0.335±0.023	*T*	0.378±0.038	*C*	275	*P*
ME05	0.331±0.022	*T*	0.370±0.032	*C*	320	*P*
ME06	2.026±0.061	*T*	2.465±0.088	*C*	264	*P*
ME09	2.150±0.057	*T*	2.19±0.12	*C*	347	*P*
MWE01	0.240±0.019	*T*	0.89±0.10	*C*	91	*P*
SOBL6	0.0329±0.0072	*T*	0.081±0.025	*C*	-	*P*

4.3.3. Calculations

Waterfalls are dynamic systems that undergo geomorphological changes through time. The rate at which knickpoints migrate upstream along a river is dependent on a combination of lithology, elevation, morphology, climatic conditions, and tectonic activity (Howard et al., 1994; Whipple and Tucker, 1999; Whipple et al., 2000; Brocklehurst, 2010). Their complexity means waterfalls can be a challenge to date, even with cosmogenic nuclides. Nevertheless, useful parameters such as denudation rates, periods of burial, minimum exposure ages and sequential exposure can be estimated for knickpoints and their surrounding landscape.

To calculate exposure ages and denudation rates, sea level high latitude (SLHL) spallogenic production rates of 4.01 atoms g^{-1} a^{-1} for ^{10}Be and 27.93 atoms g^{-1} a^{-1} for ^{26}Al were used (Borchers et al., 2016). Minimum ages and maximum denudation rates were calculated with CosmoCalc 3.0 (Vermeesch, 2007), using Lal (1991) scaling factors and default values for all parameters except the SLHL production rates. The density used for the calculations is 2.65 g cm^{-3} for all samples. Values were corrected according to sample thickness (1-10 cm) and geometric shielding. All ^{10}Be/^{9}Be ratios were normalized to the in-house standard material "SMD-Be-12" with a weighted mean value of $(1.704\pm0.030)\times10^{-12}$ (Akhmadaliev et al., 2013). The "SMD-Be-12" has been cross-calibrated to the NIST SRM 4325 standard, which has a ^{10}Be/^{9}Be ratio of $(2.79 \pm0.03)\times10^{-11}$ (Nishiizumi et al., 2007). ^{26}Al/^{27}Al ratios measured at DREAMS were normalized to the in-house standard "SMD-Al-11", with a ^{26}Al/^{27}Al ratio of $(9.66 \pm 0.14)\times10^{-12}$ (Rugel et al., 2016), while the Al ratios measured at ASTER were normalized to "SM-Al-11" with a ^{26}Al/^{27}Al ratio of $(7.401\pm0.064)\times10^{-12}$ (Arnold et al., 2010). Both Al standards are traceable via cross-calibration to the same primary standards (MB04-A, MB04-B, MB04-D) from a ^{26}Al round-robin exercise (Merchel and Bremser, 2004). For samples with ^{10}Be and ^{26}Al ages agreeing within error limits, error-weighted mean ages were also calculated.

To calculate minimum ^{21}Ne exposure ages, a sea level high latitude (SLHL) production rate of 17.51 atoms g^{-1} a^{-1} was used. This value is based on the total ^{10}Be production rate of 4.06 atoms g^{-1} a^{-1} (Borchers et al., 2016) and the ^{10}Be/^{21}Ne production ratio of 0.232 ± 0.009 (Goethals et al., 2009).

Since the attenuation length of terrestrial cosmogenic nuclide (TCN) production is smaller at low angles than in a vertical direction (Dunne et al., 1999), the TCN concentration decreases faster perpendicularly beneath an inclined surface than beneath a horizontal surface. This must be taken into account when calculating denudation rates of inclined or vertical surfaces and, therefore, a slope dependent correction (Hermanns et al., 2004) was applied to such surfaces.

In general, discordance between ^{10}Be and ^{26}Al ages may be due to long exposure (when ^{26}Al production equals decay, i.e., after a few ^{26}Al half-lives), denudation which has not been taken into account, or shielding from cosmic rays after initial exposure (e.g., Lal, 1991; Gosse and Phillips, 2001; Goethals et al., 2009). To reveal complex exposure histories, ^{10}Be concentrations can be plotted against ^{26}Al/^{10}Be ratios. In such two-nuclide plots, samples which lie between the "steady state denudation line" and the "constant exposure line" have experienced simple exposure histories, i.e., a combination of surface exposure and denudation. In contrast, samples plotting beneath the steady state field indicate burial after initial exposure. The calculation of burial ages (Lal, 1991) is based on the assumption that a surface has once been irradiated by cosmic rays up to steady state and was later buried until the present. This assumption is obviously not correct in our study, as all samples were taken from presently exposed surfaces. If such samples indicate burial, they must have been re-exposed sometime in the past, and only minimum burial ages can be calculated from them.

4.4. <u>Results</u>

4.4.1. ^{21}Ne Results

Total ^{21}Ne excesses were calculated relative to the ^{21}Ne/^{20}Ne ratio of Ne trapped in fluid inclusions as determined by crushing extractions (Table 4.3); their origin can be either cosmogenic or nucleogenic. Some samples have high ^{4}He concentrations and show substantial contributions of excess ^{21}Ne extracted at temperatures >800 °C (Table 4.3). Since the production of radiogenic ^{4}He is accompanied by that of nucleogenic ^{21}Ne and since cosmogenic ^{21}Ne is quantitatively degassed below 800 °C (Niedermann, 2002), both observations indicate the presence of high amounts of nucleogenic ^{21}Ne, and it is likely that some of the excess ^{21}Ne extracted below 800 °C from these samples is nucleogenic also. The positions of data in the three-isotope plots may also indicate the presence of nucleogenic Ne (Niedermann, 2002), though this is less evident for our sample suite (Fig. 4.3). Nevertheless, even for samples with little ^{21}Ne excess in the highest heating step and relatively small ^{4}He concentrations, the calculated ^{21}Ne exposure ages (Table 4.3) are much higher than the ^{10}Be and ^{26}Al ages (Section 4.4.2).

Despite the fact that ^{10}Be and ^{26}Al indicate extended periods of burial for many samples (Fig. A2; see section 4.5), there is no straightforward way to interpret the Ne data under the usual assumption that all excess ^{21}Ne up to an extraction temperature of 800 °C is cosmogenic, except by assuming very complex or unlikely scenarios. It remains unclear why Ne did not work in our study area, but it may be related to the old (~1.8 Ga) rocks of the Mporokoso Plateau, which have high U and Th concentrations (Unrug, 1984; De Waele and Fitzsimons, 2007). A complete Ne data set is provided in the appendix, including all three-isotope plots and two examples of two-nuclide plots (Appendix Table A3, A4 and Fig. A1, A2).

Table 4.3: ^{21}Ne excess concentrations (calculated relative to the ^{21}Ne/^{20}Ne ratio of the gas trapped in fluid inclusions as determined by crushing extractions of quartz sample aliquots; shown separately for the 400-800°C and 1200°C heating steps, respectively), ^{4}He concentrations (as another indicator for nucleogenic Ne contribution), and nominal minimum exposure ages T_{21} calculated from $^{21}Ne_{ex}$(400-800°C). Asterisk (*) indicates samples collected from vertical or subvertical surfaces. Number sign (#) indicates sample with final heating temperature 1000°C. All errors presented are 1σ. All samples were analyzed at GFZ Potsdam.

Name	$^{21}Ne_{ex}$(400-800°C) (10^6 atoms g^{-1})	$^{21}Ne_{ex}$(1200°C) (10^6 atoms g^{-1})	^{4}He (10^{-8} cm^3 STP g^{-1})[1]	T_{21} (ka)
KUN01*	24.2±1.1	1.734±0.069	45.89±0.72	2143±96
KUN02	25.81±0.84	1.389±0.082	23.26±0.34	1149±43
KUN03	28.33±0.90	1.778±0.066	53.56±0.82	1251±49
KUN04*	28.9±1.0	2.185±0.087	45.35±0.68	2556±92
KUN05	27.22±0.90	1.93±0.12	61.90±0.95	1267±42
KUN06*	24.85±0.94	1.53±0.13	51.14±0.84	2205±83
KUN07	27.12±0.88	3.10±0.10	48.96±0.76	1209±44
LUM02*	20.8±1.5	2.41±0.11	124.0±2.0	1550±110
LUM03	17.2±1.1	1.12±0.21	18.05±0.23	698±45
MUM01*	29.3±1.3	1.51±0.18#	31.06±0.42	2301±99
MUM02	36.0±1.4	1.99±0.17	30.88±0.50	1425±55
MUM03*	30.2±1.1	1.267±0.085	31.13±0.51	2523±91
MUM04	28.8±6.4	1.07±0.17	22.58±0.35	1130±250
LUO01	23.0±1.0	0.764±0.069	17.07±0.25	870±39
LUO02	30.9±1.3	1.89±0.13	64.36±0.97	1408±61
LUP01*	26.9±1.2	5.07±0.21	423.6±7.5	1885±87
NTU01	18.9±2.1	1.53±0.11	54.72±0.91	1150±130
NTU02	24.0±1.6	2.52±0.13	21.29±0.33	1084±73
NTU03	6.9±2.0	2.54±0.16	45.08±0.67	560±160

[1] 10^{-8} cm^3 STP = 2.687×10^{11} atoms

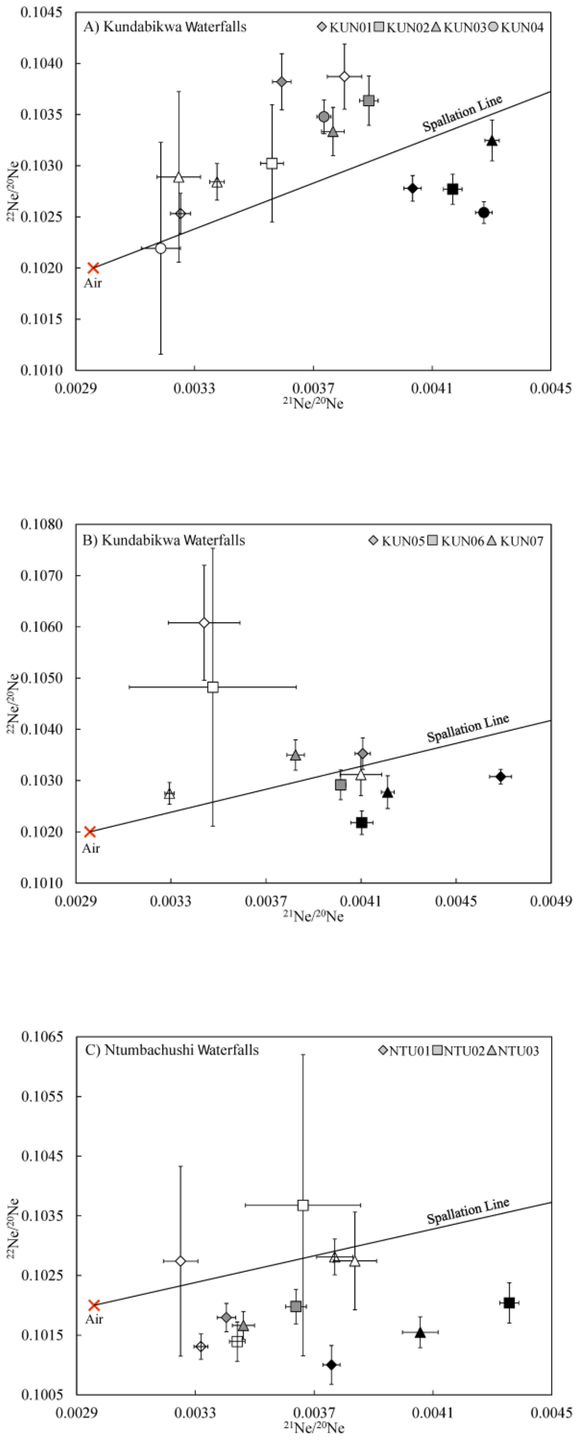

Figure 4.3: Examples of neon three-isotope diagrams showing ^{21}Ne/^{20}Ne versus ^{22}Ne/^{20}Ne. Colors indicate different heating steps (white: 400°C, gray: 600°C, black: 800°C; 1200°C data would plot out of the field shown). Crushing extractions are shown in transparent. The air value is indicated with a red cross. The spallation line is the mixing line between air and cosmogenic Ne (Niedermann et al., 1993). a) Kundabikwa Waterfalls (KUN01-KUN04); b) Kundabikwa Waterfalls (KUN05-KUN07); c) Ntumbachushi Waterfalls (NTU01-NTU03).

4.4.2. ^{10}Be and ^{26}Al Minimum Exposure Ages

Below we present the ^{10}Be and ^{26}Al results (shown in Table 4.4) by sample groups.

Table 4.4: ^{10}Be and ^{26}Al concentrations and minimum exposure ages (T_{10}, T_{26}) based thereon. Asterisk (*) indicates samples collected from vertical or subvertical surfaces. All uncertainties presented are 1σ. They include: measurement uncertainty (statistical), standard uncertainty (certification), reproducibility of standard analyses, carrier uncertainties. Age uncertainties do not include errors of production rates and scaling. See text for details on production rates and scaling method used. AMS labs where analyses were performed: D= HZDR, Dresden, Germany; T= NTNU, Trondheim, Norway; C= ASTER, CEREGE, Aix-en-Provence, France.

Name	^{10}Be (10^6 atoms g^{-1})	T_{10} (ka)	^{10}Be AMS	^{26}Al (10^6 atoms g^{-1})	T_{26} (ka)	^{26}Al AMS
Group A						
KUN01*	1.178±0.024	514±11	*D*	4.03±0.15	244.0±9.1	*D*
KUN02	0.725±0.015	145.1±3.0	*D*	2.91±0.11	82.1±3.2	*D*
KUN03	1.751±0.035	367.3±7.4	*D*	5.81±0.22	169.2±6.3	*D*
KUN04*	1.305±0.027	577±12	*D*	5.63±0.23	360±15	*D*
KUN05	1.491±0.030	326.5±6.6	*D*	7.59±0.28	240.9±9.0	*D*
KUN06*	0.2400±0.0055	94.6±2.2	*D*	1.256±0.060	70.2±3.3	*D*
KUN07	1.570±0.032	329.3±6.7	*D*	8.07±0.30	360±13	*D*
LUM02*	0.657±0.025	225.4±8.6	*T*	3.64±0.26	181±13	*C*
LUM03	1.074±0.028	198.2±5.1	*T*	6.93±0.30	186.9±8.0	*C*
NTU01*	0.0820±0.0032	21.70±0.85	*D*	0.525±0.056	19.6±2.1	*C*
NTU02	1.754±0.046	376.0±9.8	*T*	10.43±0.58	335±19	*C*
NTU03*	0.2806±0.0076	100.4±2.7	*D*	1.52±0.12	77.3±5.9	*C*
MUM01*	0.1986±0.0059	68.9±2.0	*D*	1.25±0.07	61.5±3.5	*C*
MUM02	1.479±0.035	271.1±6.5	*D*	8.77±0.41	236±11	*C*
MUM03*	0.3054±0.0082	113.8±3.0	*D*	1.91±0.12	101.8±6.5	*C*
MUM04	0.643±0.016	112.8±2.8	*D*	3.78±0.17	94.6±4.3	*C*
Group B						
LUP01*	0.1385±0.0041	42.5±1.3	*D*	0.957±0.062	41.6±2.7	*C*
LUO01	0.484±0.019	81.0±3.2	*T*	3.06±0.13	72.7±3.1	*C*
LUO02	3.441±0.080	830±19	*T*	20.72±0.97	844±40	*C*
LUZ01*	1.306±0.033	533±13	*T*	7.88±0.36	499±23	*C*
LUZ02*	0.309±0.010	102.6±3.4	*T*	2.128±0.091	101.5±4.3	*C*
Group C						
ME04*	0.0292±0.0024	12.1±1.0	*T*	0.216±0.023	12.6±1.4	*C*
ME05*	0.0294±0.0024	10.72±0.88	*T*	0.258±0.024	13.2±1.2	*C*
ME06	0.2136±0.0080	42.8±1.6	*T*	1.506±0.071	42.7±2.0	*C*
ME09	0.2270±0.0079	44.5±1.5	*T*	1.69±0.10	46.9±2.9	*C*
MWE01*	0.0249±0.0026	7.89±0.81	*T*	0.173±0.020	7.67±0.90	*C*

4.4.2.1. Group A

Vertical samples KUN01 and KUN04 from Kundabikwa Waterfalls yield ^{10}Be minimum ages of ~510 and ~580 ka, respectively, while ^{26}Al minimum ages are younger, ~240 and ~360 ka. The horizontal samples KUN03, KUN05 and KUN07 show consistently younger minimum ^{10}Be ages than the vertical samples (~320-370 ka) and ^{26}Al minimum ages in a similar range (~170-360 ka). The horizontal KUN02 (^{10}Be: ~150 ka; ^{26}Al: ~80 ka) and vertical KUN06 (^{10}Be: ~90 ka; ^{26}Al: ~70 ka) samples show much younger minimum ages compared to the other

Kundabikwa samples. The Lumangwe Waterfall samples LUM02 and LUM03 yielded minimum ^{10}Be ages of ~230 and ~200 ka, respectively, and minimum ^{26}Al ages of ~180 and ~190 ka. One vertical sample from Ntumbachushi Waterfall (NTU01) yielded a very young minimum ^{10}Be and ^{26}Al mean age of ~20 ka. The ^{10}Be minimum age of the horizontal sample NTU02 is similar to those derived from the horizontal surface proximal to the Kundabwika Waterfalls (~380 ka) while its ^{26}Al age (~340 ka) is slightly younger. NTU03, which was derived from a vertical surface, returns much younger ^{10}Be and ^{26}Al minimum ages of ~110 and ~100 ka, respectively. The samples MUM01 (vertical) and MUM04 (horizontal) from the top cascade of the Mumbuluma I Waterfalls yield minimum ^{10}Be ages of ~70 and ~110 ka, respectively, while ^{26}Al minimum ages are slightly younger (~60 and ~90 ka). The horizontally positioned sample MUM02 shows minimum ages of ^{10}Be (~270 ka) and ^{26}Al (~240 ka) which are older than for the vertical sample MUM03 (~110 and ~100 ka, respectively).

4.4.2.2. Group B

For the single sample collected from Lupupa Waterfall, the minimum ^{10}Be and ^{26}Al ages are in excellent agreement at a mean of 42.4±1.1 ka. The Mumbuluma II Waterfall sample LUO01 yields a minimum ^{10}Be and ^{26}Al mean age of 76.8±2.2 ka, which is an order of magnitude younger than the exceptionally old minimum mean age of LUO02 of 833±17 ka. Sample LUZ01, taken within a narrow river gorge of the Lunzua River, shows a minimum ^{10}Be and ^{26}Al mean age of 524±12 ka. LUZ02 was collected only about 2.4 m below the top surface and yields a mean age of 102.2±2.7 ka.

4.4.2.3. Group C

Sample MWE01 yielded minimum ^{10}Be and ^{26}Al ages which are in agreement at 7.79±0.60 ka. Samples ME04 and ME05 return minimum ^{10}Be and ^{26}Al mean ages of 12.29±0.81 ka and 11.56±0.72 ka, respectively, while ME06 and ME09 yielded minimum ^{10}Be and ^{26}Al mean ages of 42.8±1.6 and 45.7±2.0 ka, respectively.

4.4.3. Maximum Denudation Rates

For several samples that derive from Groups B and C, maximum denudation rates are also reported (Table 4.5). Samples from the eastern part of the Kundelungu Plateau yield maximum denudation rates ranging from ~15 to ~40 mm ka^{-1} (samples MWE01, ME04, ME05, ME06 and ME09), while denudation rates associated with the Mporokoso Plateau are much lower and range from ~0.4 to ~6 mm ka^{-1} (samples LUO01, LUO02, LUZ01 and LUZ02). Even though the denudation rates reported in this study are local ones, they indicate general differences in the denudation history of both studied plateaus.

Table 4.5: ^{10}Be and ^{26}Al maximum denudation rates (ε_{10}, ε_{26}) obtained for samples of Groups B and C. All uncertainties presented are 1σ.

Name	Dip angle (°)	ε_{10} (mm ka^{-1})	ε_{26} (mm ka^{-1})
LUO01	45	5.65±0.22	6.39±0.27
LUO02	50	0.4016±0.0094	0.317±0.015
LUZ01	90	0.3906±0.0099	0.375±0.017
LUZ02	90	2.367±0.079	2.40±0.10
ME04	90	22.6±1.9	22.6±2.4
ME05	90	25.4±2.1	21.3±2.0
ME06	0	15.96±0.60	16.42±0.77
ME09	0	15.26±0.53	14.79±0.91
MWE01	80	39.2±4.0	41.9±4.9

4.5. Reconstructed Scenarios for the Principal Sets of TCN Results

Most of the samples from Group A indicate burial (Fig. 4.1; Fig. 4.4). A few significant age discrepancies arising from samples collected from a single waterfall are also evident (Table 4.4). The fact that all waterfalls in Group A are located within the MMFS and at elevations <1200 m asl (that is, significantly lower than Group B samples, which are all located >1200 m asl) indicates that faulting and uplift may have played an important role in the burial of the landscape.

As discussed earlier (Section 4.1), stratigraphic evidence suggests that during the Pleistocene the study area hosted an enlarged lake, approximately 130 km wide and 300 km long (~40,000 km^2), centered around the (much smaller) present-day Lake Mweru (~5000 km^2). TCN production is completely blocked (except for some minor production by muons) when a surface is ≥10 m below the lake level. Therefore, interpreting the Plio–Pleistocene tectonic history of south-central Africa, we suggest that the burial patterns recorded by our samples most likely reflect the existence of a paleo-lake that inundated a much larger depocenter. Below we discuss separately the likely exposure scenarios for each waterfall in Group A.

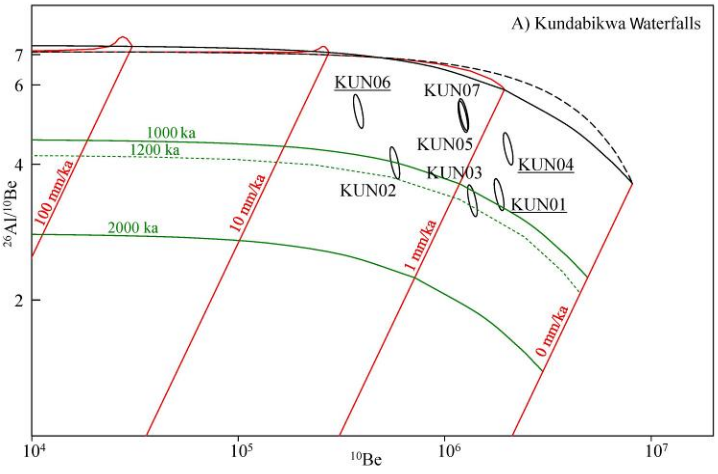

A) Kundabikwa Waterfalls
KUN06
KUN07
KUN05
KUN04
KUN03
KUN02
KUN01
1000 ka
1200 ka
2000 ka
100 mm/ka
10 mm/ka
1 mm/ka
0 mm/ka
²⁶Al/¹⁰Be
7
6
4
2
10⁴
10⁵
¹⁰Be
10⁶
10⁷

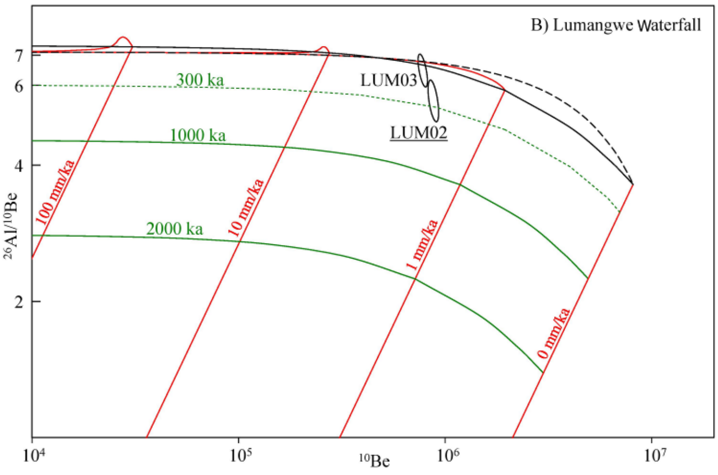

B) Lumangwe Waterfall
LUM03
LUM02
300 ka
1000 ka
2000 ka
100 mm/ka
10 mm/ka
1 mm/ka
0 mm/ka
²⁶Al/¹⁰Be
7
6
4
2
10⁴
10⁵
¹⁰Be
10⁶
10⁷

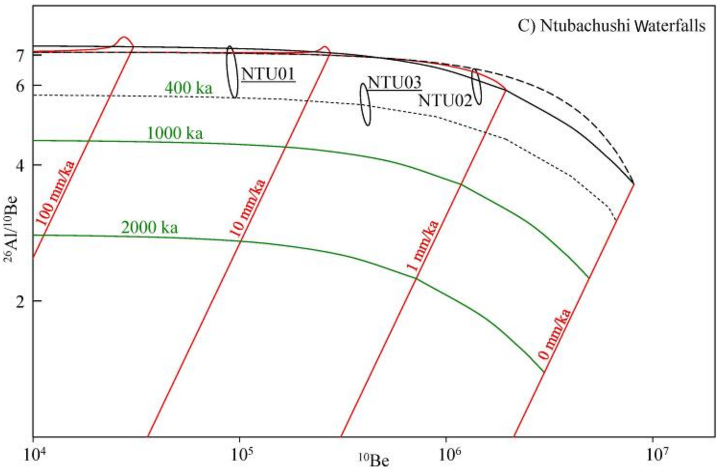

C) Ntubachushi Waterfalls
NTU01
NTU03
NTU02
400 ka
1000 ka
2000 ka
100 mm/ka
10 mm/ka
1 mm/ka
0 mm/ka
²⁶Al/¹⁰Be
7
6
4
2
10⁴
10⁵
¹⁰Be
10⁶
10⁷

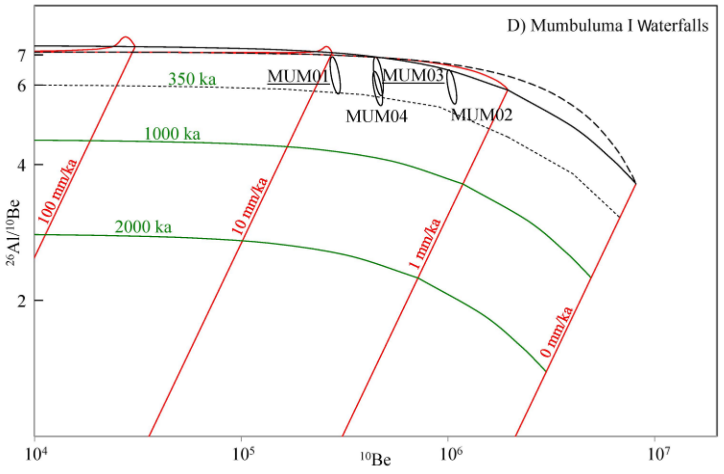

Figure 4.4: Two-nuclide diagrams showing ^{10}Be concentrations (atoms/g, corrected for total shielding and scaled to common elevation) versus ^{26}Al/^{10}Be ratios for samples of Group A. The black dashed line indicates the “constant exposure line” and the solid black line the “steady state denudation line” (e.g. Lal, 1991). Red lines show the temporal evolution of data at constant denudation rates and subsequent burial. Green lines indicate duration of burial under the assumption that samples were first exposed and later completely buried until present. Samples are indicated with black error ellipses (1σ shown). Underlined labels indicate samples taken from vertical surfaces. A) Kundabikwa Waterfalls; B) Lumangwe Waterfall; C) Ntumbachushi Waterfalls; D) Mumbuluma I Waterfalls.

4.5.1. Group A

4.5.1.1. Kundabikwa Waterfalls

Samples from the Kundabikwa Waterfalls indicate burial of at least 250 ka (Fig. 4.6A). The significantly younger minimum exposure ages of samples KUN02 and KUN06 (Table 4.4) probably indicate enhanced surface denudation or rockfalls/landslides (e.g., mechanical failure of exposed rock outcrop leading to fresh exposure). In addition, two of the three pairs of samples (KUN01/KUN02 and KUN03/KUN04) indicate older ^{10}Be and ^{26}Al minimum ages (Table 4.4) for the vertical face compared to the top horizontal surface. The fact that the top horizontal surface (KUN02, KUN03 and KUN05) of the area is younger than the vertical sections (KUN01, KUN04) is intriguing and requires further examination.

Based on the relative ^{10}Be and ^{26}Al minimum age estimates, we reconstruct the complex exposure-burial history of Kundabikwa Waterfalls and paleo-lake Mweru over six sequential stages (Fig. 4.5). The pre-lake stage (T1) represents the initial state of the river. In order to record a burial signal, the studied surfaces must have been exposed prior to burial. Thus, the knickpoint must have already existed during stage T1. The vertical faces of the banks are gradually exposed through sequential knickpoint retreat. During this stage, channel denudation dominates. The denudation rate is relatively low on the top-horizontal surface. Most geomorphologic characteristics from this stage are assumed to have been erased by today. The second stage (T2) is defined by the onset of the lake-level rise (flooding). Water starts to cover the vertical river banks. Denudation decreases as the base-level increases, leading to slower knickpoint migration. Denudation is minimal (but probably not zero) as the top horizontal surfaces are flooded and lake sedimentation initiates. During T3, the lake reaches its greatest depth. Water and sediments now shield the sampled surfaces from cosmic ray irradiation, entirely blocking ^{10}Be and ^{26}Al production. Lacustrine sedimentation occurs mostly on the horizontal surfaces. The lake-level is now the base-level, resulting in the interruption of denudation.

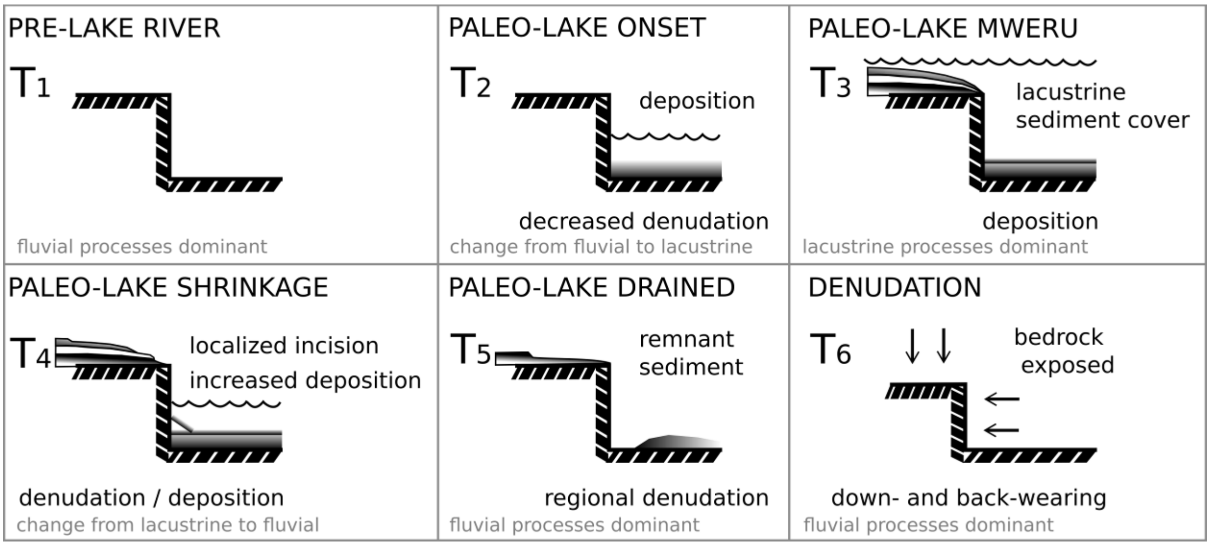

Figure 4.5: Schematic figure of successive landscape stages of Kalungwishi River at Kundabikwa Waterfalls and paleo-lake Mweru. T1: Initial river state with waterfall already in place. T2: Onset of paleo-lake Mweru below Kundabikwa Waterfalls. Areas downstream of the knickpoint are covered with water and sediment, while denudation at and upstream of the waterfalls is reduced due to lower energy environment. T3: Full establishment of paleo-lake Mweru resulting in water cover and sediment deposition on top horizontal surfaces. T4: Drainage of the paleo-lake, resulting in exposure of areas above the knickpoint with concomitant incision of lacustrine sediments at the waterfalls and deposition of these sediments into the remaining lake below the waterfalls. T5: Paleo-lake Mweru is completely drained and sediments deposited during T3 and T4 are removed through regional denudation, resulting in differential bedrock exposure. T6: Present day river course with limited sedimentary cover and ongoing down- and backwearing through increased denudation.

Denudation recommences with the onset of lake drainage and associated drop of the water-level (stage T4). Localized denudation occurs on the sediment-covered horizontal surfaces while the vertical faces remain under water, with TCN production still being absent for all submerged areas. Consequent to paleo-lake outflow (T5) via the Luvua River, regional denudation of the sediments that blanket the horizontal surfaces occurs. This period of new equilibrium may have been characterized by low energy environments, which can be described, for example, as a changing complex of small wetlands, oxbow lakes and meandering channel systems, similar to the current situation in the upper reaches of present-day Lake Mweru. Lacustrine sediments are now confined to the top horizontal banks, as in the channel the sediments are eroded. The subsequent lowering of base level as the lake drains sees the rejuvenation of the waterfalls. In the last stage (T6), most of the lacustrine sediments have been removed from all surfaces and the top horizontal surfaces are re-exposed and TCN production resumes. Back- and downwearing of the vertical bank faces leads to further denudation of the bedrock surfaces. We note that gradual rising and lowering of the lake's water-level between stages T2 and T4 should have lasted thousands or even tens of thousands of years in order to induce a detectable difference between the cosmogenic nuclide concentrations of different (horizontal vs. vertical) sampled surfaces. Indeed, previous studies of other paleo-lakes have revealed long-term lake fluctuations spanning time-intervals from 2 to >20 ka (Masters et al., 1991; Gamrod, 2009; Shuman et al., 2009; Trauth et al., 2010).

4.5.1.2. Lumangwe Waterfall

According to Figure 4.4B, sample LUM03 does not show an unequivocal burial signal, in contrast to LUM02 that clearly underwent a complex exposure history. One possible explanation is that LUM02 (1150 m asl) was covered by lake water, while LUM03 (1159 m asl) was not (or it was only slightly covered so the cosmogenic nuclide production did not stop completely). Such a scenario implies that the Lumangwe cascades marked the eastern shore of the paleo-lake. Another possibility is that the LUM02 rock face was covered by a recent landslide or rockfall. However, no physical evidence of such an event can be found, suggesting that if it did occur, the Kalungwishi River has subsequently removed any such debris. A minimum burial time of 300 ka is estimated for LUM02 (Fig. 4.6B).

4.5.1.3. Ntumbachushi Waterfalls

Samples NTU01 and NTU02 do not indicate a clear burial signal. The weathered profile of the NTU01 surface and the very young minimum ^{10}Be and ^{26}Al mean age (~20 ka) most likely indicate a recent rockfall. Although NTU03 does indicate burial of ~400 ka (Fig. 4.4C), this age is questionable due to the young minimum ^{10}Be and ^{26}Al ages (~100 and ~80 ka, respectively) that derive from the same sample and which, coupled with the highly weathered and fractured nature of the sampled surface, make it unlikely to record an ancient pre-lake stage.

4.5.1.4. *Mumbuluma I Waterfalls (Mumbuluma River)*

All results from the Mumbuluma I falls indicate a clear burial signal at 1σ confidence level, though not at 2σ (Fig. 4.4D). The top cascade yields younger minimum ^{10}Be ages (MUM01, MUM04) than the second cascade downstream (MUM02, MUM03), suggesting that the lower waterfall formed before the top one. Also, the top horizontal surface (MUM04; minimum ^{10}Be age 113 ka) seems to have undergone more intense denudation than the lower surface (MUM02; 271 ka). A rockfall may explain the young minimum ^{10}Be age of the vertical sample MUM01 (~70 ka). The approximate minimum burial time of the area is ~350 ka (Fig. 4.4D), an age which is in good agreement with the duration of burial recorded at the Lumangwe falls.

4.5.2. Group B

Samples in Group B date waterfalls which are situated outside the MMFS (Fig. 4.1). ^{10}Be and ^{26}Al minimum ages are in good agreement for most samples, indicating that these surfaces have not been buried since their initial exposure (Fig. 4.6). Thus, it appears that these locations were not flooded by the paleo-lake. Minimum exposure ages and maximum denudation rates within this group are discussed below.

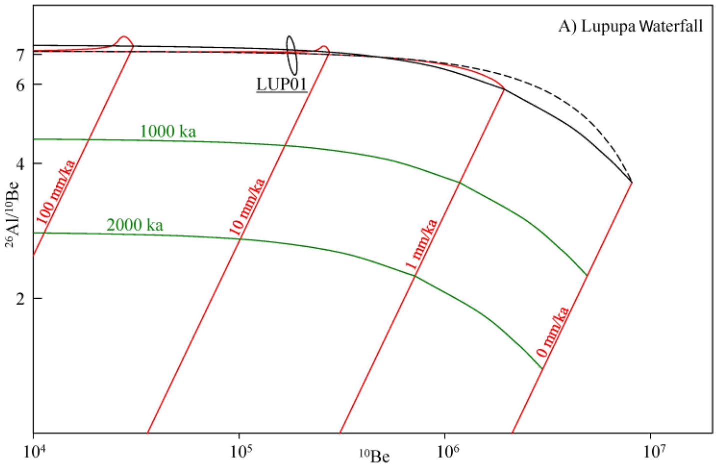

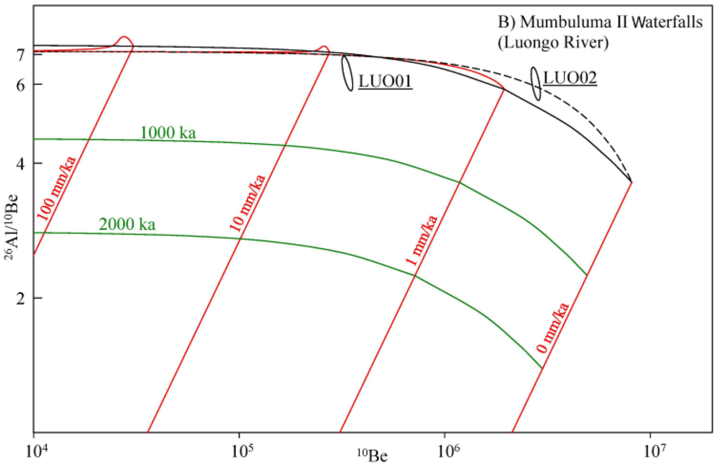

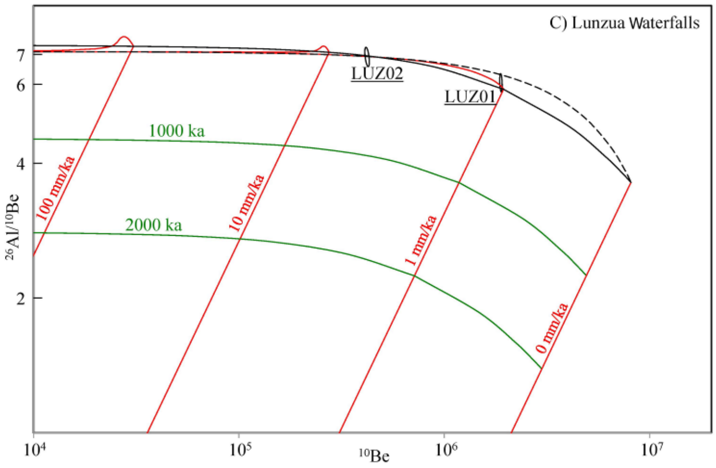

Figure 4.6 Two-nuclide diagrams showing ^{10}Be concentrations (atoms/g) versus ^{26}Al/^{10}Be ratios for samples of Group B. See Figure 4.6 for explanations. A) Lupupa Waterfall; B) Mumbuluma II Waterfall (Luongo River); C) Lunzua Waterfalls.

4.5.2.1. Lupupa Waterfall

LUP01 shows very young minimum ^{10}Be and ^{26}Al ages (42.5±1.3 and 41.6±2.7 respectively), which probably do not reflect the actual age of the waterfall but a rockfall event. For such recent events, no burial signal is expected (Fig. 4.6A).

4.5.2.2. Mumbuluma II Waterfall (Luongo River)

Both samples from the Luongo’s Mumbuluma II Waterfall are from sub-vertical (45°-50°) surfaces and show no clear ^{10}Be-^{26}Al burial signal (Fig. 4.6B). This cascade was formed on a bedrock contact between quartzites and sandstones. The development of the cascade is clearly controlled by differential denudation between the overlying softer sandstone and the harder quartzite. Maximum denudation rates of ~6 mm ka^{-1} for the sandstone (LUO01) and of ~0.4 mm ka^{-1} for the quartzite (LUO02) are calculated (Table 4.5). The large difference in the denudation rates of the two lithologies further highlights the role of differential denudation in the formation of this cascade. Sample LUO02 plots exactly on the no denudation line in Figure 4.6B, indicating a minimum ^{10}Be and ^{26}Al mean exposure age of 833±17 ka. This age, which is the oldest recorded minimum exposure age among the studied waterfalls, indicates a very old formation age of the Mumbuluma II knickpoint. It is worth mentioning that this is an exceptionally old age for an inclined surface located within the zone of an actively incising river channel.

4.5.2.3. Lunzua Waterfalls

Both samples from Lunzua Waterfalls show no ^{10}Be-^{26}Al burial signal (Fig. 4.6C). LUZ01 yields a very old minimum age for a vertical surface, which indicates that it was constantly exposed since at least 524±12 ka. In terms of a steady denudation rate, this age would correspond to a local rate of receding of the rock face (in horizontal direction) of ~0.4 mm ka^{-1}. LUZ02 yields a much younger minimum ^{10}Be and ^{26}Al mean age (102.2±2.7 ka). It is unclear whether the age difference between the two samples reflects the retreat of the waterfall or is just due to more intense denudation near the top.

4.5.3. Group C

Samples from the northwest side of Lake Mweru (Group C) were located at lower elevations than those from groups A and B, and their minimum ^{10}Be and ^{26}Al ages are distinctly younger and more comparable to one another (Table 4.4). The sample that derives from a vertical surface of the fault (MWE01; Fig. 4.1) implies a fast but steady denudation rate of ~40 mm ka^{-1} (Table 4.5) or a rockfall on the fault surface <10 ka ago. Additionally, two further samples (ME04, ME05) from vertical sections along the Luvua River show rather young minimum ^{10}Be and ^{26}Al mean ages (12.29±0.81 and 11.56±0.72 ka, respectively). As the paleo-lake Mweru was drained via the Luvua River during the Pleistocene (Cotterill and de Wit, 2011), it is possible that these young ages reflect rockfall events or steady and fast incision, but obviously they do not represent the age of paleo-lake drainage. Fast denudation of the northeastern section of the Kundelungu Plateau is further supported by two samples which were collected from horizontal surfaces along the Musefwe and Lwilwa rivers (ME06 and ME09; Fig. 4.1), yielding maximum ^{10}Be denudation rates of ~16 mm ka^{-1} (Table 4.5). In summary, Group C samples show no ^{10}Be-^{26}Al burial signals and relatively young minimum ages due to recent rockfalls and/or fast eroding surfaces (Fig. 4.7; Tables 4.4, 4.5). However, these young ages do not contradict the assumed extension of the paleo-lake Mweru over this section of the Kundelungu Plateau. Rather, they suggest that pre paleo-lake surfaces have not been preserved due to faster denudation. Such rates could be related to a potential uplifting caused by tectonic activity. Further investigation of this activity is required.

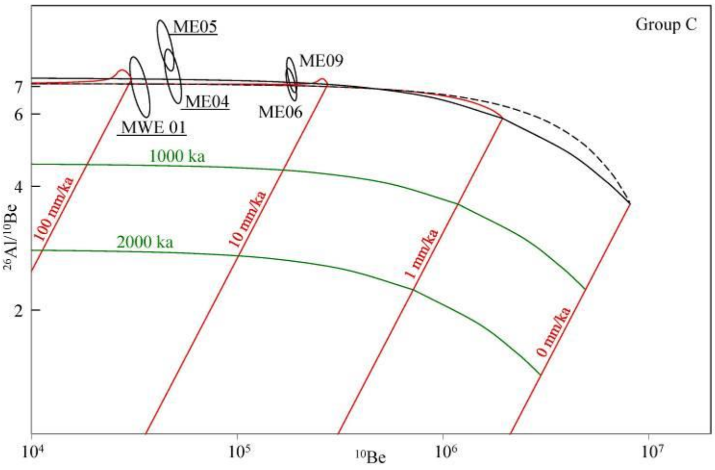

Figure 4.7: Two-nuclide diagram showing ^{10}Be concentration (atoms/g) versus $^{26}Al/^{10}Be$ ratios for samples of Group C. See Figure 4.6 for explanations.

4.6. Discussion

4.6.1. The Drainage of Paleo-Lake Mweru

At Kundabikwa Waterfalls, three samples (KUN01, 02, 03) yield burial ages of ~1 Ma (Fig. 4.4A). The minimum burial ages of the other four samples (KUN04, 05, 06, 07) are lower (~500 ka). This may be explained by a higher contribution of post-burial production, which shifts data points in the two-nuclide plot (Fig. 4.4A) from the burial area towards the steady-state field again. Therefore, it is the oldest burial age among all samples that provides a minimum estimate for the time the Kundabikwa Waterfalls have been covered, i.e. >1 Ma. Indeed, it is possible that the paleo-lake Mweru existed much longer than that. If the lake (including the various lake fluctuations) actually lasted more than ~2 Ma, essentially all ^{26}Al present in a sample today would have been produced after the drainage of the paleo-lake (as the half-life of ^{26}Al is 705 ka and after three half-lives almost 90% will have decayed; Norris et al., 1983). Under such an assumption, the highest minimum ^{26}Al age of all samples showing burial would provide a time constraint for when the paleo-lake was drained to a level below the elevation of the waterfalls. Sample KUN04 of the Kundabikwa Waterfalls records the highest ^{26}Al minimum age among all samples that indicate burial, constraining the timing of lake drainage to ~350 ka (i.e. middle Pleistocene). Variable denudation and tectonic rates within the study area can explain the observed variations in minimum ages between different locations. Nevertheless, all samples from Group A are consistent with an inferred lake drainage at ~200-400 ka, with age differences most likely representing lake level fluctuations.

Dramatic lake level fluctuations, which are related to tectonic factors and/or aridification periods, have been reported throughout the late Pleistocene (14-450 ka) across Lake Tanganyika, Lake Malawi and the southwest extension of the EARS (Danley et al., 2012; Ivory et al., 2016). From 450 to 350 ka, a regional lowering of the temperature and global sea level is directly correlated with the low stand of the lake levels across the Western Branch (Bakker and Mercer, 1986). In addition, a major dry period across the Congo basin occurred between ~270 and 180 ka, resulting in an additional lowering of the water level (Gasse et al., 1989). The evidence for the drainage of paleo-lake Mweru based on ^{10}Be and ^{26}Al data, together with tectonic analyses (see Chapter 5) and the evidence for intensive climatic variation during the Pleistocene, indicate a gradual shrinking of the paleo-lake rather than a sudden tectonic event. The outflow of the paleo-lake through the Luvua River was most likely one of the main events that drained the lake (Dixey, 1944; Bos et al., 2006; Goodier et al., 2011; Cotterill and de Wit, 2011; Fig. 4.1). However, evaporation, especially in arid periods, may have further accelerated contraction of the paleo-lake, notably across the vast, shallow depression located between the two sections of the Kundelungu Plateau (Fig. 4.1).

4.6.2. Paleo-Lake Mweru During the Quaternary

Assuming that the paleo-lake Mweru existed for a minimum of ~2 Ma, the burial ages constrain its formation to the late Pliocene-early Pleistocene. This assumption is supported by the high species endemism of the extant fish fauna of Lake Mweru (Cotterill, 2005; Meier et al., 2019). More specifically, recent molecular clock analyses have estimated respective timings of origin of several radiations of endemic fish clades (Family Cichlidae) confined within Lake Mweru. Four of these clades have evolved diverse species flocks, whose origins are estimated at 270–350, 430–560, 270–940, and 720–940 ka, constrained by a molecular clock calibrated for the Cichlidae (Meier et al., 2019). Thus, depending on the applied calibration scheme, the mean genetic divergence of the most common recent ancestors provides a date of 0.27-1.04 Ma and their actual speciation dates (i.e. timing of completed lineage divergence) was likely more recent (Meier et al., 2019). The second line of geobiotic evidence comprises the "Mweru Complex" of killifishes, genus *Nothobranchius*. The timing of radiation of its seven species is significant, because their ecology confines them within the floodplains that formed after the shrinkage of the larger lake. The independently constrained molecular clock of *Nothobranchius* estimates the origin of this complex between 0.48 and 1.01 Ma (van der Merwe et al., 2021).

Our data inform a schematic map that estimates the maximum size of the paleo-lake Mweru through the Pleistocene (Fig. 4.8). The maximum lake level is constrained via TCN dating at 1200 m asl, while the minimum level should be the elevation of the Kundabikwa Waterfalls (~1050 m asl). The estimate of a 1200 m asl lake level is supported by the hypsometric and knickpoint analysis (~1180 m asl), which will be described in detail in Chapter 5. The Lumangwe and Ntumbachushi Waterfalls are assumed to represent the eastern shorelines of this paleo-lake. The southern border of the paleo-lake likely coincided closely with the Mumbuluma I waterfalls which, together with preliminary molecular phylogenetic analyses (Cotterill, 2004, 2005), suggest that the southern section of the Kundelungu Plateau was connected with the Mporokoso Plateau during the Pliocene (and prior to the formation of the Luapula River; Tack et al., 2003; Cotterill and de Wit, 2011; Guillocheau et al., 2015).

Red siltstones from the Kundelungu Plateau are possibly correlated with the upper red beds of the Luapula Beds, implying that the Luapula River eroded the once connected Kundelungu and Mporokoso Plateaus (Abraham, 1959; Thieme, 1971). The western bank of the paleo-lake is defined by the Kundelungu Plateau that rises to ~1700 m asl. Paleo-lake Mweru was likely connected to the Mweru Wantipa wetlands as suggested by the relationships of *Pseudocrenilabrus* (Family Cichlidae) species from these two waterbodies (Egger et al., 2015). However, it appears unlikely that it was linked with the Mpulungu graben of Lake Tanganyika due to the highly distinct fish fauna of these two lakes. This is in agreement with Dixey (1944, 1946), who proposed that the Lakes Mweru and Mweru Wantipa were once connected, a hypothesis re-affirmed by Cotterill and de Wit (2011). Finally, the northern banks are defined by the edge of the extensive plateau between the Mweru Wantipa wetlands and Lake Tanganyika (Fig. 4.8).

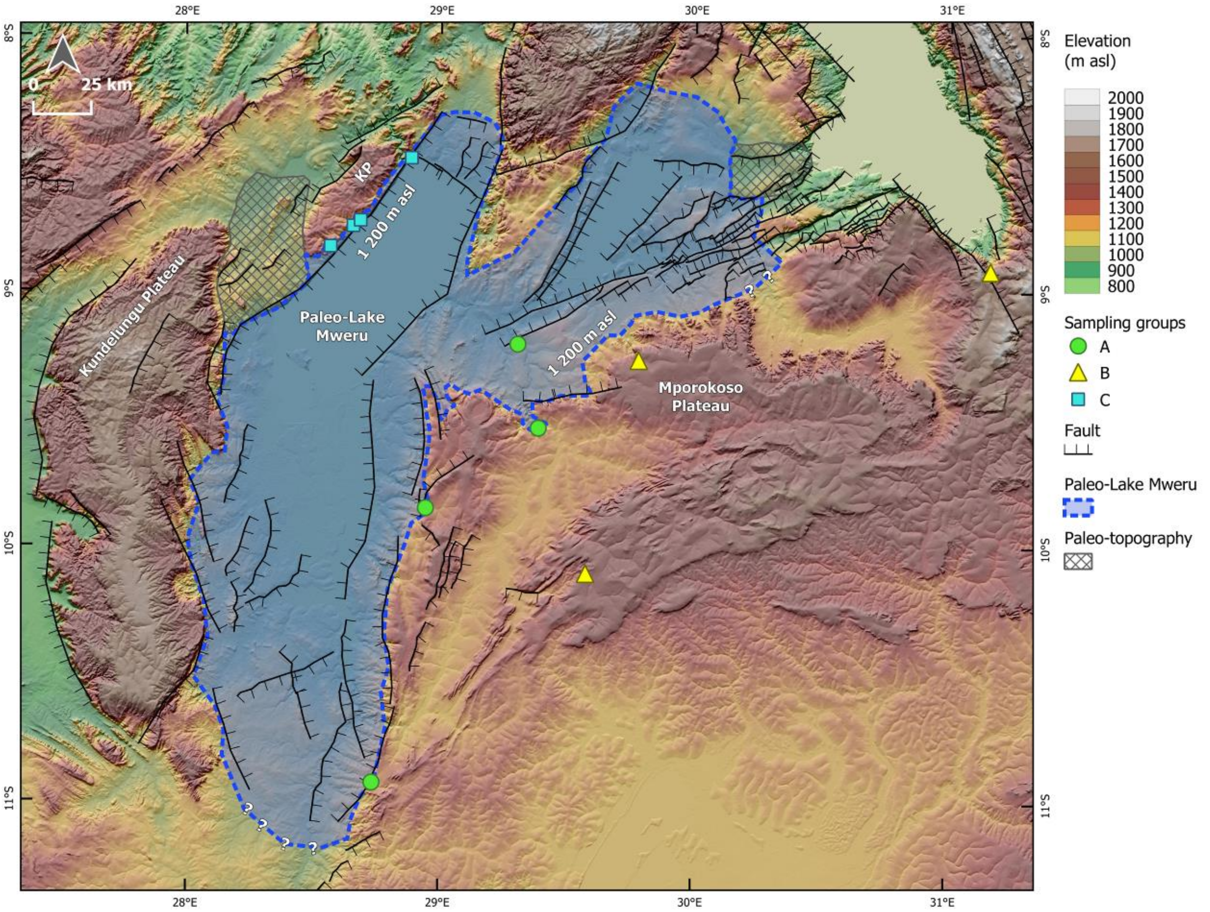

Figure 4.8: Schematic representation of the possible maximum extent of paleo-lake Mweru during the Plio-Pleistocene (see blue contour at 1200 m asl). Shaded areas represent possible reconstructed paleo-topography that was present during the Plio-Pleistocene.

4.7. <u>Conclusions</u>

Two exceptionally old, consistent minimum ^{10}Be and ^{26}Al exposure ages were obtained from vertical/sub-vertical surfaces besides active river courses, possibly reflecting the actual exposure ages of these surfaces. The sample LUZ01 (Lunzua Waterfalls) yielded a minimum exposure age of 524 ka, while LUO02 (Mumbuluma II Waterfalls) showed an even older minimum exposure age of 833 ka. On the other hand, burial signals from key knickpoints around the Mweru-Mweru Wantipa fault zone provide strong evidence for the existence of a greater paleo-lake Mweru, which extended over around 40 000 km^2 with a maximum water level at ~1200 m asl. TCN results support the phylogenetic molecular clock analyses that also constrain the formation of the paleo-lake during the late Pliocene - early Pleistocene based on the divergence age estimates of the four cichlid radiations endemic to Lake Mweru. The deepening/flooding of the paleo-lake, which was probably due to the active extension and associated normal faulting, continued at least until the Middle Pleistocene (~0.36 Ma), resulting in the complex exposure histories of the knickpoints on the Mporokoso Plateau.

Chapter 5

Tectonic and Geomorphological Evolution of the Paleo-Lake Mweru

5. Tectonic and Geomorphological Evolution of the Paleo-Lake Mweru

5.1. *Introduction*

The Western Branch (WB) of the East African Rift System (EARS) is mostly dominated by elongated active rift systems related to mechanical rifting, while the extension is concentrated along border faults which bound each system (Hinz et al., 2018). Its extension rate is 1-2 mm a^{-1} and together with the Eastern Branch, which extends with 5.2-1 mm a^{-1}, the EARS is one of the fastest spreading intracontinental rifts globally (Fernandes et al., 2004; Calais et al., 2006; Saria et al., 2014). The southern arm of the upwelling asthenospheric African superplume under the Lake Victoria region (Kenya Dome) forces the continent to be raised hundreds of meters as the crustal lithosphere undergoes thinning processes (Ebinger and Sleep, 1998; Nyblade et al., 2000; Chakrabarti et al., 2009; Halldórsson et al., 2014; Koptev et al., 2015).

Our study area lies southwest of Lake Tanganyika, where the tectonic complex of the Mweru-Mweru Wantipa Rift System (MMFS) extends in an almost perpendicular (ENE-WSW) trend to the Tanganyika Rift System. It is well known that the MMFS consists of the most seismically active faults of central east Africa, which create typical horst and graben structures, hosting the two high-altitude lakes Mweru (917 m asl) and Mweru-Wantipa (932 m asl) (Delvaux and Barth, 2010; Kipata et al., 2013; Daly et al., 2020). The lakes are bounded by the two high reliefs of the Mporokoso and Kundelungu plateaus, to the southeast and northwest, respectively.

While the role of active faulting in controlling river patterns and shaping the landscapes of the southwest Tanganyika graben has been investigated, detailed geomorphological and tectonic studies of the area remain scarce. Much of the existing literature analyzes only first-order physiographic characteristics of these rifted valleys, deriving some tectonic correlations between these structures and the EARS (Mohr, 1974; Tiercelin et al., 1988; Mondeguer et al., 1989; Strecker et al., 1990; Delvaux, 1991; Chorowicz, 2005; Kipata et al., 2013). The active tectonism continues to deform the old erosional surfaces until today, controlling large topographic features and the regional drainage system. The initial drainage system of the Central African Plateau has experienced profound rearrangements, due to repeated faulting and differential vertical movements (i.e. normal faulting, uplift). Several flexural models suggest the extent of the Chambeshi drainage system is directly controlled by the footwall uplift of the Mporokoso Plateau, which has led to the re-shaping and reversal of the main rivers, creating numerous knickpoints and new courses (Thomas and Shaw, 1990; Cotterill and de Wit, 2011; Moore et al., 2012; Daly et al., 2020). The creation of knickpoints is not only correlated with tectonic activity (normal faulting) and differential erosion but can also be associated with base-level change as well as sea-level and climatic variations (Whipple and Tucker, 1999; Whipple et al., 2000). These factors control the size of the tectonic-developed lakes, which are aligned over several thousand kilometers along the EARS.

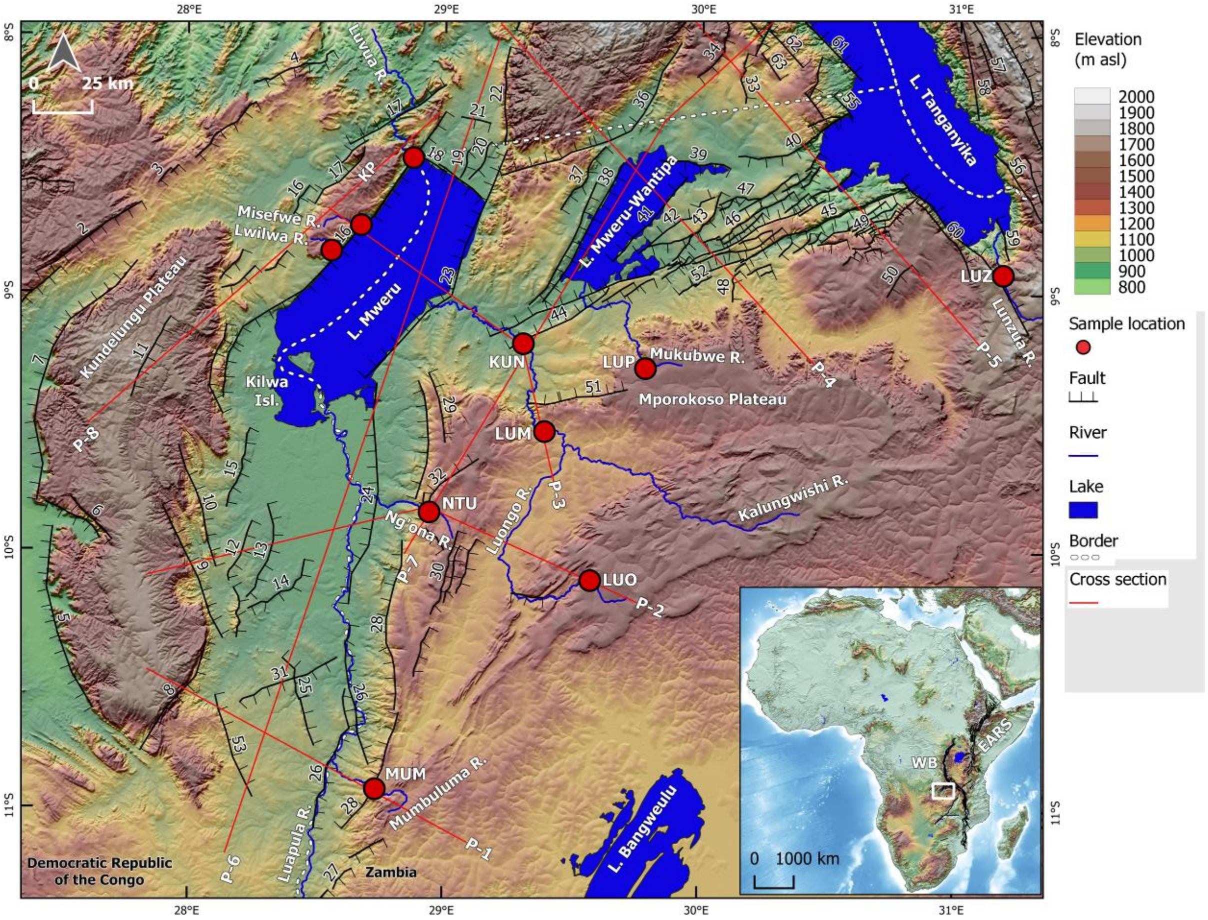

Figure 5.1: Morphotectonic map of the Mweru-Mweru Wantipa Fault System in the southern East African Rift System. Normal faults are indicated by black lines while ticks indicate downfaulted side. Numbers next to each fault correspond to entries in Table 5.1. Red lines indicate topographic profiles presented in Figures 5.5, 5.6 and 5.7. Red circles indicate terrestrial cosmogenic nuclide sampling locations (see Chapter 4). Inset shows location of study area in Africa. KUN: Kundabikwa Waterfalls; LUM: Lumangwe Waterfall; NTU: Ntumbachushi Waterfalls; MUM: Mumbuluma I Waterfalls; LUP: Lupupa Waterfall; LUO: Mumbuluma II Waterfall; LUZ: Lunzua Waterfalls.

The Plio-Pleistocene paleo-lakes within the WB (e.g. paleo-lakes Turkana, Edward-Albert (Obweruka), Bangweulu, Magadi, Thamalakane, Tanganyika, Kivu, Rukwa and Malawi) were consisted by a series of large and deep lakes (Williamson, 1978; Hillaire-Marcel et al., 1986; Burrough and Thomas, 2008; Cotterill and de Wit, 2011; Danley et al., 2012;

Cohen et al., 2016). In such fast-opening rift zones with stable velocities over the last 11 Ma, lake level variations are mostly controlled by climatic variations (Lavayssiere et al., 2019). According to Trauth et al. (2005), East Africa experienced three major humid periods (2.7-2.5 Ma, 1.9-1.7 Ma and 1.1-0.9 Ma) contributing to the water level instability of the paleo-lakes during the Pleistocene.

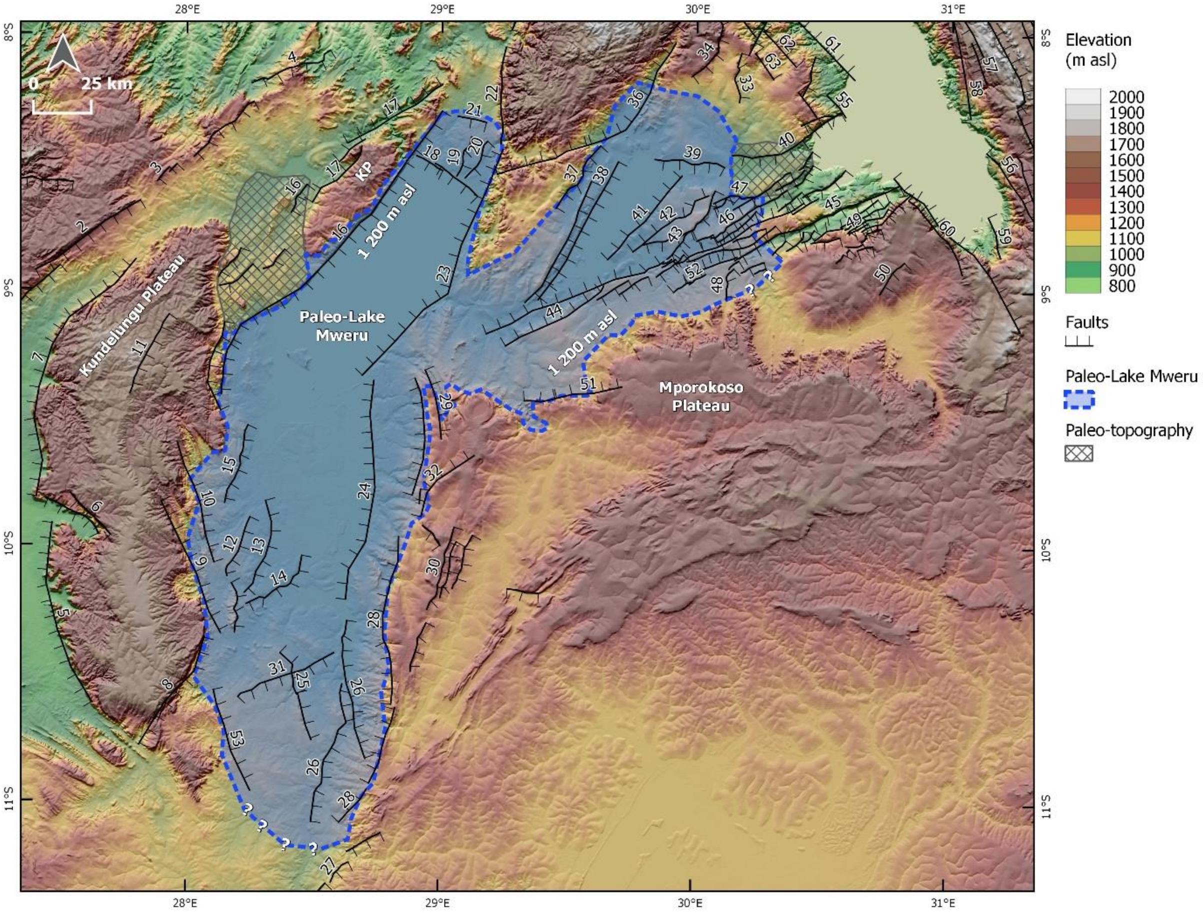

Figure 5.2: Schematic representation of the possible maximum extent of paleo-lake Mweru during the Plio-Pleistocene (see blue contour at ~1200 m asl). Hatched areas represent reconstructed paleo-topography that was present during the Plio-Pleistocene (see Chapter 4).

Terrestrial cosmogenic nuclide (TCN) dating of key knickpoints (waterfalls) across the Mporokoso and Kundelungu plateaus combined with morphotectonic analysis suggests the existence of the paleo-lake Mweru during the Pleistocene (Chapter 4; Fig. 5.2; Olivotos et al., 2021). Our previous chapter (Chapter 4) indicates an extended period of burial and subsequent re-exposure (Olivotos et al., 2021). The study presented in this chapter aims to quantify the contribution of normal faulting to the formation and shrinking of the paleo-lake and assess its spatial and temporal evolution during the Pleistocene. We achieve this by combining active fault and digital topography analysis with TCN ages on key geomorphic features.

5.2. *Geological Setting*

Lakes Mweru and Mweru-Wantipa occur in a half graben structure that forms part of the MMFS, and together with the Okavango rift they form the Southern Complex of the WB (Tiercelin and Lezzar, 2002). Lake Mweru is fed from the south by the Luapula River, whose extensive delta suggests rapid erosional activity of the high plateaus between Lake Mweru and Lake Bangweulu (Fig. 5.1). North of the delta and inside the lake lies Kilwa Island, which consists of Neoproterozoic clastic rocks (Shudofsky, 1985; Tiercelin and Lezzar, 2002; Daly et al., 2020). The stratigraphy of the lake is thought to be a 400 m Quaternary sediment sequence unconformably overlying the Neoproterozoic basement (Bos et al., 2006; Daly et al., 2020). Lake Mweru drains northwest, via the Luvua River through a steep meander-like path, into the Lualaba (Congo) River. Along the eastern shore of the lake, an ~10 m high beach terrace indicates an actively uplifted coastline controlled by a long major fault line across the southern borders of the Kundelungu Plateau (Daly et al., 2020). The southeastern border of the lake is delimited by a major fault parallel to the trend of the Mporokoso Plateau, creating the deepest part of the lake, which is 27 m (Bos et al., 2006).

The MMFS extends over a length of ~400 km and a width of ~200 km and can be separated in two parts. The eastern part of the fault zone is characterized by an elongated ENE-WSW trend, almost perpendicular to the NW-SE trend of the Mpulungu basin (southern Lake Tanganyika) (Tiercelin and Lezzar, 2002). Small and parallel grabens form shallow depressions, which are typical to swamp environments (Mondeguer et al., 1989). To the west, the two major troughs with NNE-SSW trend form the two main shallow lakes (Lakes Mweru and Mweru-Wantipa). The majority of the faults follow the NNE-SSW trend, while few faults have a vertical trend of WNW-ESE and mainly confine the end of the basins (Mondeguer et al., 1989). The deviation of the trend near the Mpulungu basin (south Lake Tanganyika) results from the difference of competency of the relatively stable Bangweulu block (Mondeguer et al., 1989; Fig. 5.1). This rotation of the extension direction reactivated earlier dip-slip faults, since strain accumulated in the same pre-Pleistocene inherited crustal structures (Ring, 1994; Morley, 2002; Saria et al., 2014). Furthermore, earthquake fault plane solutions from the area indicate an extensional displacement around the WNW axis (Delvaux and Barth, 2010). Recent modeling studies suggest that the extension direction changes by ~60° to 90° while a left-lateral motion is applied on two domains with NE-E oriented weaknesses in between them (Molnar et al., 2019).

South of Lake Mweru, a large basin of sub horizontal sedimentary cover (Mporokoso Plateau) is developed on the Archean-Paleoproterozoic craton called Bangweulu block (Mondeguer et al., 1989; Fig. 5.1). It is the tectonic foreland of the Irumides orogenic belt (~1.8 Ga) and is composed of Archean and Paleoproterozoic crust, incorporated in the Paleoproterozoic Ubendian Belt as well (Hanson, 2003; De Waele and Fitzsimons, 2007; De Waele et al., 2009). The Mporokoso Plateau comprises mostly undeformed fluvial and lacustrine sediments (De Waele and Fitzsimons, 2007). The maximum age of this large metasedimentary and metavolcanic sequence (with a combined thickness of ca. 5 000 m) was constrained to 1.8 Ga by Rb-Sr whole-rock dating of granites, which occur unconformably within the base of the plateau (De Waele and Fitzsimons, 2007). Unrug (1984) characterized the Mporokoso Plateau as the pre-Katangan successions to the northwest and northeast of the Bangweulu Block.

A thick sedimentary rock succession, called Kundelungu Plateau, forms the half graben structure that delimits the lake to the northwest (Fig 5.1). Together with the Roan and Nguba Groups, the Kundelungu Plateau is a part of the larger Neoproterozoic Katangan Supergroup and consists of carbonitic and siliciclastic sequences, which were deposited in a wider basin. This deposition corresponds to a major phase of extensional tectonics and normal faulting (Kampunzu et al., 1993; Batumike et al., 2007), and it is dated between <630 and ∼500 Ma (Kampunzu and Cailteux, 1999; Cailteux et al., 2018). Bedded red sandstones of the Kundelungu Plateau are exposed where Lake Mweru currently outflows into the Luvua River. This formation controls tectonically the development of the western side of the lake (Kipata et al., 2013).

The amagmatic character of the tectonism, combined with an indistinct sedimentation sequence across the Southern Complex, make the precise dating of the initiation of the fault activity in our study area difficult. The formation of the extended erosional surface of the Central African Plateau is estimated around late Miocene to early Pliocene (Daly et al., 2020). The absence of Mio-Pliocene sedimentation across the basin suggests that the tectonic activity must have been initiated after, or during, the uplift of the Central African Plateau, thereby constraining the onset of the MMFS to the late Pliocene - early Pleistocene (~2.6 Ma; Daly et al., 2020).

The southeastern border of the lake is delimited by a major fault (Fault 23 in Fig. 5.1) parallel to the trend of the Mporokoso Plateau (Bos et al., 2006). This rectangular lake is surrounded by uplifted rift margins, with the lake geometry and bathymetry being controlled by basin subsidence. The structural control of this setting is described in further detail in section 5.5.

5.3. Material and Methods

5.3.1. Fault and Tectonic Analyses

We used a Shuttle Radar Topography Mission (SRTM) digital surface model (DSM), Google Earth^{TM} imagery, and the ArcGIS software (version 10.6) to map the traces of 63 normal faults in the area, from west of Lake Mweru to the southern shorelines of Lake Tanganyika (Fig. 5.1). This area largely includes faults of the MMFS, while at its eastern edge it comprises elements of the EAR (Fig. 5.1).

We focused our analysis on two fault parameters that, collectively, provide important information on the fault system's activity and growth: the fault length (L) and the fault displacement (D). Fault length represents an important parameter in estimating the seismic potential (including earthquake magnitude and single-event displacement) on each studied fault (Wells and Coppersmith, 1994; Wesnousky, 2008). It should be noted that several of the identified faults contain numerous parallel or sub-parallel strands (e.g. faults 30, 38, 44, 46, 49, etc. in Fig. 5.1) or along-strike segments (e.g. 1, 2, 7, 16, 43, etc.), which are either hard or soft linked (Walsh and Watterson, 1991). Here, these elements are thought to represent a single coherent fault that ruptures along its entirety; however, it remains possible that individual earthquakes rupture these faults or fault segments only partially. The maximum vertical displacement (or throw) on each normal fault derives by averaging numerous (>10) scarp height measurements from fault perpendicular topographic profiles collected proximal to the fault's center. Fault lengths and displacements represent direct measurements drawn on the DSM and are presented in Table 5.1 together with the faults' geometries. Indirect earthquake attributes (e.g. earthquake magnitude, average recurrence interval, etc.) associated with each studied fault derive from Wells and Coppersmith's (1994) and Wesnousky's (2008) empirical relations and are shown in Table 5.2.

Measurement of active fault lengths and displacements can be subject to significant uncertainties (Wesnousky, 2008; Mouslopoulou et al., 2012; Nicol et al., 2016a). This is because fault scarps are prone to erosion and burial, especially at fault tips where displacements are often too small to be detected with conventional mapping methods (such as aerial photo or DSM analysis, field mapping, etc.) where vertical resolution is usually > 2 m. In this study, as fault scarps of < 2 m are not resolvable on the available DSM, and also because fault scarps of any size may be partly or entirely modified by erosion and/or burial, the fault lengths/displacements presented should be considered as minimum values. The rifting in this section of the WB of the EARS where the MMFS extends is thought to have initiated about 2.6 Ma (late Pliocene-early Pleistocene; Tiercelin and Lezzar, 2002; Molnar et al., 2019; Daly et al., 2020). Thus, fault displacement rates are here calculated using the maximum displacement measured on each fault and dividing it by the time-interval of 2.6 Ma.

Table 5.1: Fault parameters since the onset of the Mweru-Mweru Wantipa Fault system (2.6 Ma). Single Event Displacement (SED) indicates the maximum offset produced by a fault during a single earthquake.

Fault ID	Strike	Dip	Length (km)	Maximum Displacement[1] (m)	Displacement Rate (mm a^{-1})	SED[2] (m)
Mweru-Mweru Wantipa Fault System						
1	NNE-SSW	E-SE	140	60	0.02	12.6
2	NE-SW	SE	71	250	0.10	6.4
3	NE-SW	SE	55	150	0.06	5.0
4	NE-SW	SE	39	80	0.03	3.5
5	NNW-SSE	W	83	400	0.15	7.5
6	NW-SE	SW	32	700	0.27	2.9
7	NNE-SSW	W	120	450	0.17	10.8
8	NE-SE	SE	55	500	0.19	5.0
9	NNW-SSE	E	62	450	0.17	5.6
10	NNW-SSE	E	55	200	0.08	5.0
11	NNE-SSW	SE	34	50	0.02	3.1
12	NE-SW	SE	54	110	0.04	4.9
13	NE-SW	SE	43	35	0.01	3.9
14	NE-SW	SE	35	50	0.02	3.2
15	NNE-SSW	SE	35	80	0.03	3.2
16	NE-SW	SE	168	510	0.20	15.1
16A	NE-SW	SE	57	200	0.08	5.1
17	NE-SW	NW	101	400	0.15	9.1
18	NW-SE	SW	35	45	0.02	3.2
19	NNE-SSW	SE	18	25	0.01	1.6
20	NNE-SSW	SE	19	40	0.02	1.7
21	W-E	S	12	20	0.01	1.1
22	NNE-SSW	E	77	200	0.08	6.9
23	NE-SW	NW	118	200	0.08	10.6
24	N-S	W	97	90	0.04	8.7
25	NNW-SSE	NE	33	60	0.02	3.0
26	N-S	E	61	40	0.02	5.5
27	NNE-SSW	SE	40	60	0.02	3.6
28	N-S	W	130	200	0.08	11.7
29	NNW-SSE	NE	30	100	0.04	2.7
30	NNE-SSW	SE	65	150	0.06	5.9
31	NNE-SSW	SE	46	30	0.01	4.1
32	NE-SW	NW	40	140	0.05	3.6

Fault ID	Strike	Dip	Length (km)	Maximum Displacement[1] (m)	Displacement Rate (mm a^{-1})	SED[2] (m)
33	N-S	E	22	80	0.03	2.0
34	NE-SW	SE	55	220	0.09	5.0
35	NE-SW	SE	33	200	0.08	3.0
36	NE-SW	NW	102	250	0.10	9.2
37	NE-SW	SE	34	70	0.03	3.1
38	NE-SW	SE	73	200	0.08	6.6
39	E-W	S	29	60	0.02	2.6
40	ENE-WSW	SSE	52	500	0.19	4.7
41	NE-SW	NW	48	120	0.05	4.3
42	NE-SW	NW	42	30	0.01	3.8
43	NE-SW	SE	38	180	0.07	3.4
44	NE-SW	NW	82	180	0.07	7.4
45	NE-SW	SE	84	80	0.03	7.6
46	NE-SW	NW/SE	81	460	0.18	7.3
47	NE-SW	NW	31	120	0.05	2.8
48	NE-SW	SE	94	300	0.12	8.5
49	NE-SW	SE	60	420	0.16	5.4
50	NNE-SSW	SE	17	10	0.003	1.5
51	E-W	N	42	150	0.06	3.8
52	ENE-WSW	N	40	250	0.10	3.6
53	NNW-SSE	ENE	32	100	0.04	2.9
Tanganyika Rift System						
54	NNW-SSE	ENE	100	130	0.05	9.0
55	NNW-SSE	ENE	162	300	0.12	14.6
56	NNW-SSE	ENE	56	200	0.08	5.0
57	NNW-SSE	WNW	54	80	0.03	4.9
58	NNW-SSE	WNW	49	400	0.15	4.4
59	NNW-SSE	ENE	18	250	0.10	1.6
60	NNW-SSE	NE	133	600	0.23	12.0
61	NNW-SSE	NE	52	200	0.08	4.7
62	NNW-SSE	SE	45	150	0.06	4.1
63	NNW-SSE	NE	57	200	0.08	5.1

[1] Displacement Rate = [Maximum Displacement]/2600 ka
[2] SED = 0.09*[Fault Length] (Wesnousky, 2008)

Table 5.2: Fault Parameters since the onset of the Mweru-Mweru Wantipa Fault system (2.6 Ma) continued. ERI stands for Earthquake Recurrence Interval.

Fault ID	ERI[1] (ka)	Earthquake Magnitude[2] (Mw)	Number of events[3] [the last 350 ka]	Throw[4] (m) [the last 350 ka]	Number of events[5] [the last 2.6 Ma]	Throw[6] (m) [the last 2.6 Ma]
Mweru-Mweru Wantipa Fault System						
1	546	7.13	1	8	5	60
2	66	6.99	5	34	39	250
3	86	6.94	4	20	30	150
4	114	6.87	3	11	23	80
5	49	7.02	7	54	54	400
6	11	6.83	33	94	243	700
7	62	7.10	6	61	42	450
8	26	6.94	14	67	101	500
9	32	6.96	11	61	81	450
10	64	6.94	5	27	40	200
11	159	6.84	2	7	16	50
12	115	6.93	3	15	23	110
13	287	6.89	1	5	9	35
14	164	6.85	2	7	16	50
15	102	6.85	3	11	25	80
16	77	7.17	5	69	34	510
16A	67	6.95	5	27	39	200
17	59	7.06	6	54	44	400
18	182	6.85	2	6	14	45
19	168	6.71	2	3	15	25
20	111	6.72	3	5	23	40
21	140	6.63	3	3	19	20
22	90	7.01	4	27	29	200
23	138	7.09	3	27	19	200
24	252	7.05	1	12	10	90
25	129	6.83	3	8	20	60
26	357	6.96	1	5	7	40
27	156	6.87	2	8	17	60
28	152	7.11	2	27	17	200
29	70	6.81	5	14	37	100
30	101	6.97	4	20	26	150
31	359	6.90	1	4	7	30
32	67	6.87	5	19	39	140
33	64	6.75	5	11	40	80
34	59	6.94	6	27	44	220
35	39	6.83	9	27	67	200
36	95	7.06	4	34	27	250
37	114	6.84	3	9	23	70
38	85	7.00	4	27	30	200
39	113	6.81	3	8	23	60
40	24	6.93	14	67	107	500
41	94	6.91	4	16	28	120

Fault ID	ERI[1] (ka)	Earthquake Magnitude[2] (Mw)	Number of events[3] [the last 350 ka]	Throw[4] (m) [the last 350 ka]	Number of events[5] [the last 2.6 Ma]	Throw[6] (m) [the last 2.6 Ma]
42	328	6.88	1	4	8	30
43	49	6.86	7	24	53	180
44	107	7.02	3	24	24	180
45	246	7.02	1	11	11	80
46	41	7.02	9	62	63	460
47	60	6.82	6	16	43	120
48	73	7.05	5	40	35	300
49	33	6.96	11	57	78	420
50	398	6.70	1	1	7	10
51	66	6.88	5	20	40	150
52	37	6.87	9	34	69	250
53	75	6.83	5	14	35	100
Tanganyika Rift System						
54	180	7.06	2	18	14	130
55	126	7.16	3	40	21	300
56	66	6.94	5	27	40	200
57	158	6.93	2	11	16	80
58	29	6.91	12	54	91	400
59	17	6.71	21	34	154	250
60	52	7.12	7	81	50	600
61	61	6.93	6	27	43	200
62	70	6.90	5	20	37	150
63	67	6.95	5	27	39	200

[1] ERI= SED/[Displacement Rate]
[2] Earthquake Magnitude = 6.12+0.47*log[Fault Length] (Wells and Coppersmith, 1994)
[3] Number of events [over the last 350 ka] = 350 ka /ERI
[4] Throw [over the last 350 ka] = [Number of events]*SED
[5] Number of events [over the last 2.6 Ma] = (2600 ka)/ERI
[6] Throw [over the last 2.6 Ma] = [Number of events]*SED

5.3.2. Digital Topography Analysis

We analyzed selected domains of the 30-m NASADEM (NASA JPL, 2020). We have delineated the catchment of Lake Mweru using standard procedures implemented in TopoToolbox (Schwanghart and Scherler, 2014). Elevation lows (pits) were filled, a hydrological-corrected DEM was calculated, and the catchment extents were visually verified. Our catchment extent, using the higher resolution NASADEM data, is similar to that calculated in the HydroBASINs dataset (Lehner and Grill, 2013). The catchment extent was used to extract the hypsometric curve, showing the surface area for each elevation bin. Further, we identified river knickpoints using previously published approaches (Neely et al., 2017). This entailed deriving longitudinal river profiles, converting them to Chi coordinates, and identifying knickpoint lips and bases based on positive or negative distance above a best-fit Chi profile (Neely et al., 2017). Chi profiles are area-normalized profiles where the distance coordinate has been normalized by an averaged river profile following an exponential function (Perron and Royden, 2012). The resulting profile, when in steady state, will follow a straight line. We analyze profile deviation above and below an averaged line to identify knickpoints. More detailed analysis steps are described in Neely et al. (2017). To avoid small knickpoints and remove noise inherent in the DEM, we focus on knickpoints with magnitudes (i.e., deviations from the average Chi profile line) exceeding 30 m. Field observations suggest that major waterfalls associated with past lake-level highstands are generally higher than 30 m.

5.4. Results

5.4.1. Tectonic Analysis

5.4.1.1. Fault Geometries and Kinematics

We mapped 63 lineaments that we interpreted to represent the surface expressions of active normal faulting at depth (Fig. 5.1; Table 5.1). Fifty-three faults are located within the MMFS, while ten are located within the Mpulungu basin (southern Lake Tanganyika). The faults in the southern MMFS strike NE-SW while the northeast section of the fault system swings its strike clockwise to an ENE-WSW orientation (Table 5.1), intersecting, at high angles (~90°), the NW to SE trending normal faults around Lake Tanganyika. Fault lengths (L) in our dataset range from 12 km to 168 km, whereas maximum vertical fault displacements (D) range from 10 m to 700 m (Fig. 5.3A). Fault displacement rates (DR) are typically low, ranging from 0.004 mm a^{-1} to 0.27 mm a^{-1} (Fig. 5.3C). This, in turn, corresponds to an average earthquake recurrence for the faults in the MMFS of ~120 ka (Table 5.2). In order to understand the impact of normal faulting on the formation of the past and current landscape proximal to Lake Mweru, we explore the D-L relationship on the 53 normal faults in the MMFS (Table 5.2).

The D-L relation may provide important information on the growth and scaling properties of faults (Fig. 5.3; Walsh and Watterson, 1988; Bilham and Bodin, 1992; Cowie and Scholz, 1992; Schlische et al., 1996; Kim and Sanderson, 2005; Schultz et al., 2008; Nicol et al., 2010, 2020a). The graphs in Figures 5.3A and 5.3C indicate positive D-L and DR-L relationships for the faults in the MMFS, suggesting that larger faults have accommodated more displacement and have moved faster than smaller faults (Nicol et al., 1997, 2005). Similar graphs which indicate positive relationships between fault displacements/displacement rates and length have been recorded on several other active and inactive fault systems globally (Kim and Sanderson, 2005; Mouslopoulou et al., 2009; Nicol et al., 2020a, b). Despite the overall positive D-L trend for most fault systems globally, the D values at a given L value and the slope of the best-fit line in these graphs may vary between fault systems (but also between different sampling periods in the same fault system), with the slope typically ranging from 0.5 to 1.5 (Schlische et al., 1996; Kim and Sanderson, 2005; Nicol et al., 2010; Torabi and Berg, 2011, Nicol et al., 2020b). This variability in the D-L scaling may be due to biases arising from the time-window of observation, the age of the faulted horizons, the strain accommodated by each fault system, the mechanical properties of the faulted rocks and/or the degree of fault interactions (Watterson et al., 1996; Bailey et al., 2005; Mouslopoulou et al., 2009; Nicol et al., 2010;).

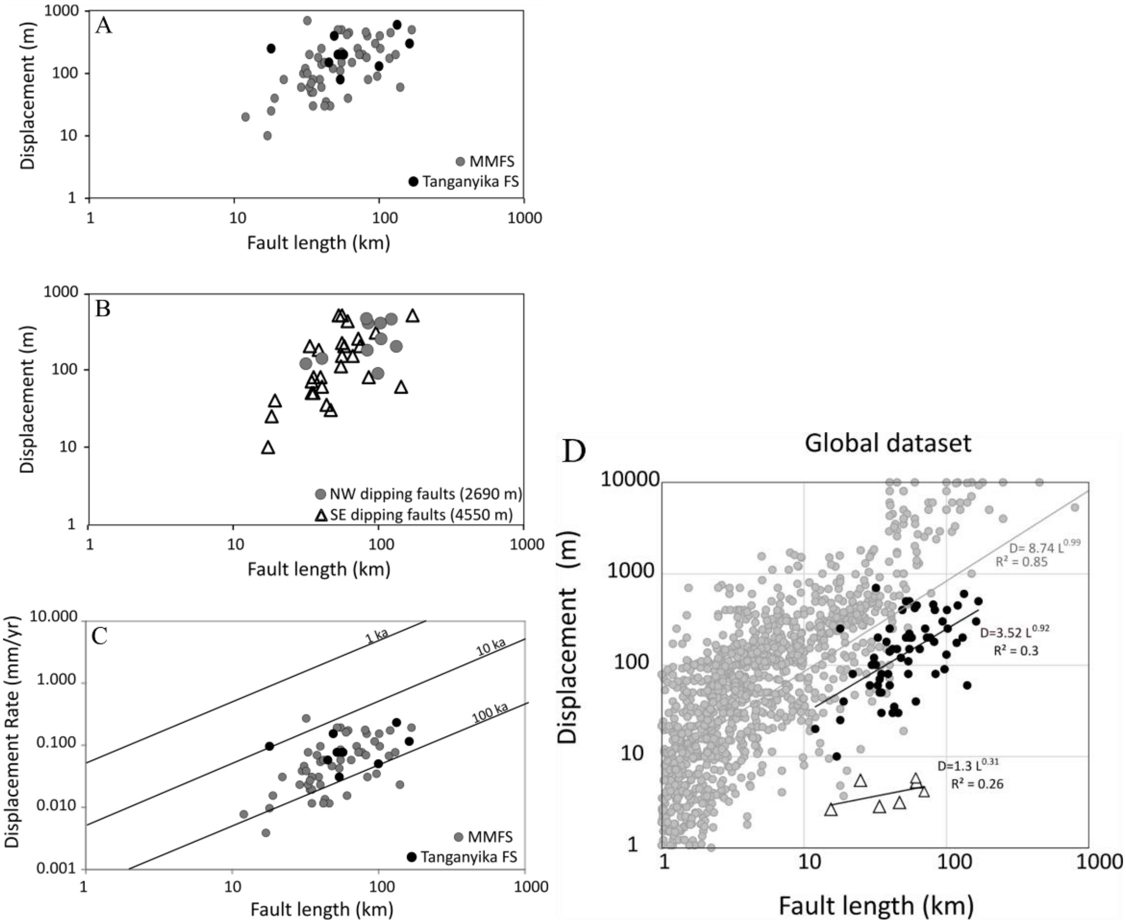

Figure 5.3: A) Log-log plot illustrating the relationship between topographic fault length and total displacement for the faults in the MMFS (gray circles) and the Mpulungu basin (southern Tanganyika Fault System; black circles). B) Same as (a) but illustrating separately the NW dipping (circles) and the SE dipping (triangles) faults in the MMFS. C) Log-log plot illustrating the relationship between topographic fault length and the displacement rate for the faults in the MMFS (gray circles) and the Mpulungu basin (black circles). D) Global dataset of displacement vs. fault length (shaded area; Nicol et al., 2016c). Black circles show data for the same faults as in Figure 5.3A while white triangles represent single-event displacement rupture lengths for historical earthquakes (Wesnousky, 2008). Least squares lines of best fit and R^2 values are also indicated for each dataset.

To better understand the growth of the faults in the MMFS with respect to other fault systems globally, we have plotted their D-L trend against a global dataset of inactive normal faults (Fig. 5.3D; Nicol et al., 2016c and references therein). Comparison shows that the faults in the MMFS plot in agreement with the global dataset occupying, however, the lower part of the global population (exponents ~0.92 vs. ~0.99, respectively; Fig. 5.3D). To explore further the growth of the faults in Africa, we have also plotted in Figure 5.3D the single-event displacement rupture lengths from a global compilation of historic normal fault earthquakes (Wesnousky, 2008). As expected, single earthquakes clearly plot below the average trend of the global dataset (including the MMFS); their slope is significantly less than 1 (~0.3) and their scatter greater than that of the global dataset (R^2 values of 0.26 vs. 0.85; Fig. 5.3D). These features collectively suggest that each fault in the MMFS has accommodated numerous earthquakes, the number of which scales with fault length.

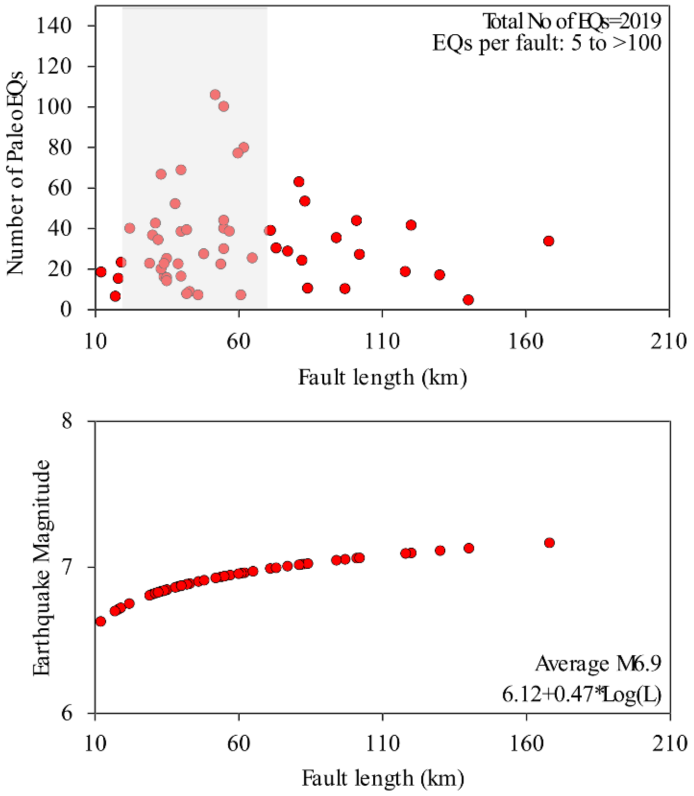

Figure 5.4: Correlation between fault length and the number of paleo-earthquakes (EQs) per fault (upper panel) and earthquake magnitude (lower panel), respectively. The number of earthquakes per fault ranged from 5 to more than 100, with an average magnitude of M6.9.

The approximate number of earthquakes accommodated by each fault in the MMFS, together with their earthquake magnitude and recurrence interval, has been calculated using Wesnousky's (2008) scaling relationships (Table 5.2). First, we calculate the Single Event Displacement (SED) for each fault in the MMFS from the fault length (L) and subsequently the Earthquake Recurrence Interval (ERI) on each fault (Table 5.2). The ERI is subsequently used, in conjunction with the displacement rate (e.g. maximum displacement of a fault divided by the time-period that rifting is thought to have initiated – 2.6 Ma; Daly et al., 2020; Chapter 4) to estimate the number of earthquakes accommodated by each fault (Table 5.2 and Fig. 5.4). We find that the faults in the MMFS are likely to have accommodated ~2,000 ground-rupturing earthquakes since the rift's onset (~35 events per fault), with earthquake magnitudes ranging from M6.7 to M7.2 (Table 5.2 and Fig. 5.4).

5.4.1.2. Faulted Topography

To explore the relationship between the faulted topography, the available TCN ages and the current extents of Lakes Mweru and Mweru Wantipa, we generated five rift-perpendicular topographic profiles (profiles 1-5; Fig. 5.5) and one rift-parallel profile (profile 6; Fig. 5.6; see Fig. 5.1 for location of profiles). The profiles 1-3, across the southern MMFS and the modern Lake Mweru, reveal a strongly asymmetric rift (Fig. 5.5). To characterize the distribution of strain along the rift, we have calculated the cumulative throw across the five profiles illustrated in Figure 5.5. Furthermore, to better visualize the landscape when rifting in the area was about to commence, we subtracted from the identified faults the throw measured along all topographic profiles (profiles 1-8; Fig. 5.7), that is the displacement accrued on each fault since the initiation of faulting at 2.6 Ma.

Our analysis shows a three-fold increase in the cumulative throw, trending northeastwards along the rift (from ~800 m across profile 1 to ~2180 m across profile 5), with the southeast dipping faults having accommodated almost twice as much displacement (4550 m) compared to the northwest dipping faults (2690 m; Fig. 5.5). The dominance of the southeast dipping faults is persistent along the entire length of the MMFS, where these faults appear to have locally (e.g., see profile 5) accommodated up to 4 times more throw compared to the northwest dipping faults. The northeastward increase in extension, which is manifested by the greater number of active faults and the more confined rift axis, is not surprising as the MMFS at its northernmost extension approaches (and intersects) the fast spreading (~1 mm a^{-1}) EARS (Fig. 1; Fernandes et al., 2004: Calais et al., 2006; Omenda et al., 2016).

Topographic analysis suggests that the faults which are largely responsible for the formation of the modern landscape within the MMFS are faults 8, 9, 16, 17, 23 and 28 in the south, and faults 38, 40, 46 and 48 in the north. The profile along Lake Mweru (profile 6; Fig. 5.6) reveals a shallow topographic basin (within <100 m from the modern lake) which is bounded at its northern side by the Kundelungu Plateau and to the south by steep hilly country formed by sediments of the Luapula River's delta. Profile 7 runs along Lake Mweru Wantipa and displays the high topographic relief between the Mporokoso Plateau and the Mpulungu basin, while profile 8 reveals the impact of normal faulting on the landscape associated with the Kundelungu Plateau (Fig. 5.7). These profiles are discussed in detail in Section 5.5.

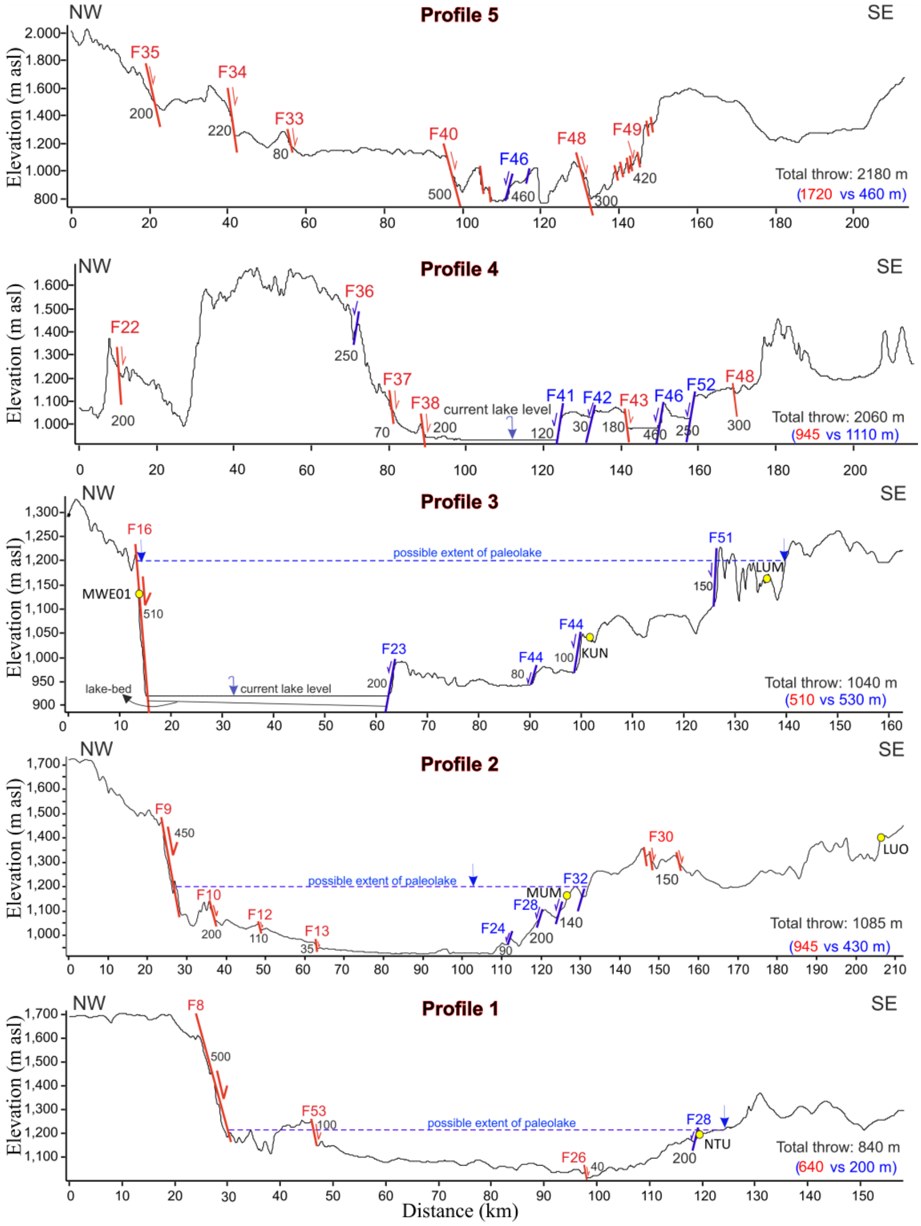

Figure 5.5: Five topographic profiles approximately perpendicular to the trend of the MMFS (for location of the profiles see Figure 5.1). The SE dipping faults are indicated with red lines while the NW dipping faults with blue lines. Sample locations are indicated with yellow circles. Numbers with F next to faults correspond to numbered faults in Figure 5.1 and entries in Table 5.1. Plain numbers next to the faults indicate the throw (m) of the respective fault. The total fault throw as well as the throw of the NW (blue) and SE (red) dipping faults are indicated on each profile. Blue dashed line indicates the potential water level of the paleo-lake Mweru.

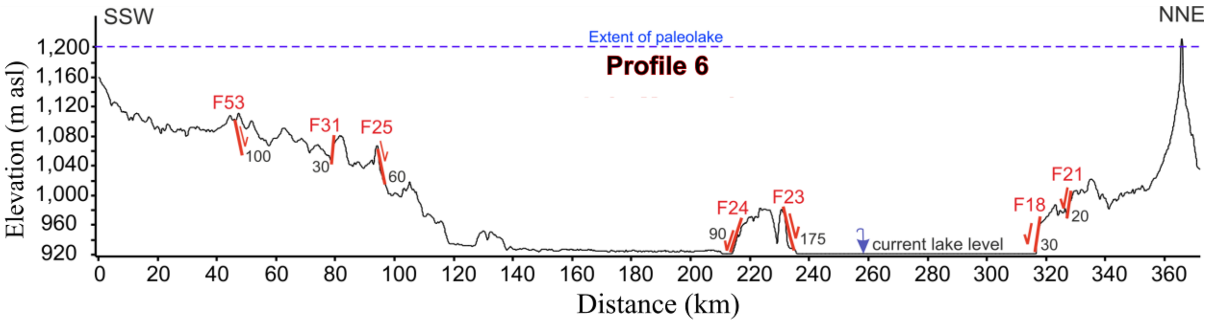

Figure 5.6: Topographic profile along the trend of the MMFS. See Figure 5.1 for profile location and Figure 5.5 for explanations.

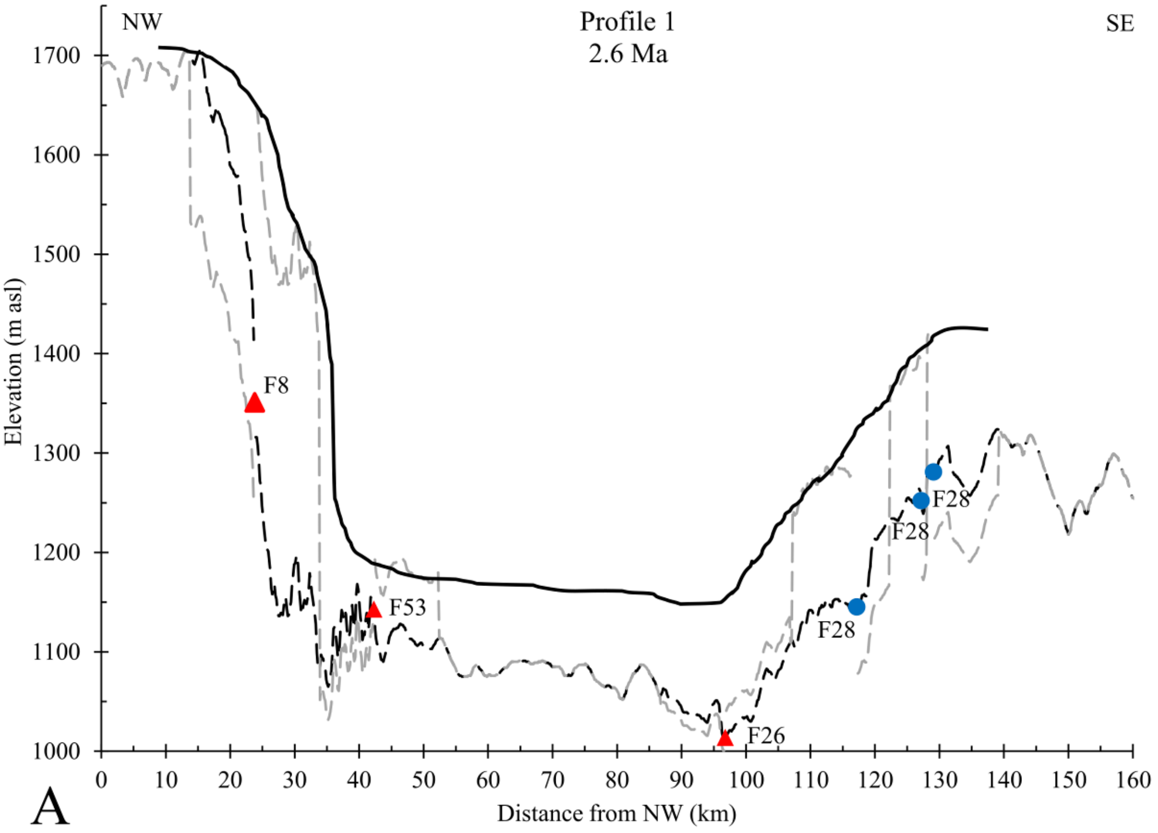

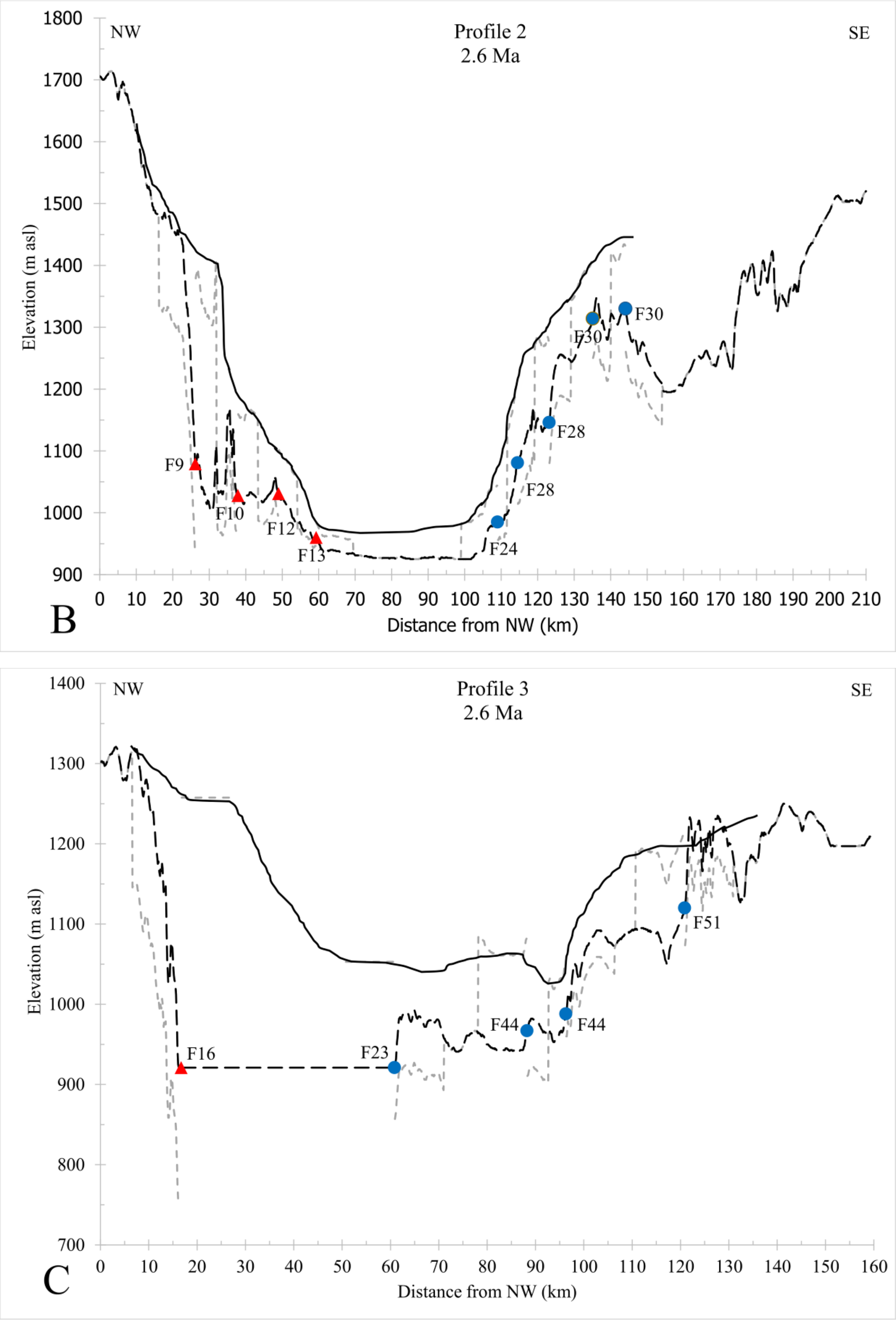
Profile 2
2.6 Ma
NW
SE
Elevation (m asl)
1800
1700
1600
1500
1400
1300
1200
1100
1000
900
F9
F10
F12
F13
F24
F28
F28
F30
F30
0
10
20
30
40
50
60
70
80
90
100
110
120
130
140
150
160
170
180
190
200
210
Distance from NW (km)
B
Profile 3
2.6 Ma
NW
SE
Elevation (m asl)
1400
1300
1200
1100
1000
900
800
700
F16
F23
F44
F44
F51
0
10
20
30
40
50
60
70
80
90
100
110
120
130
140
150
160
Distance from NW (km)
C

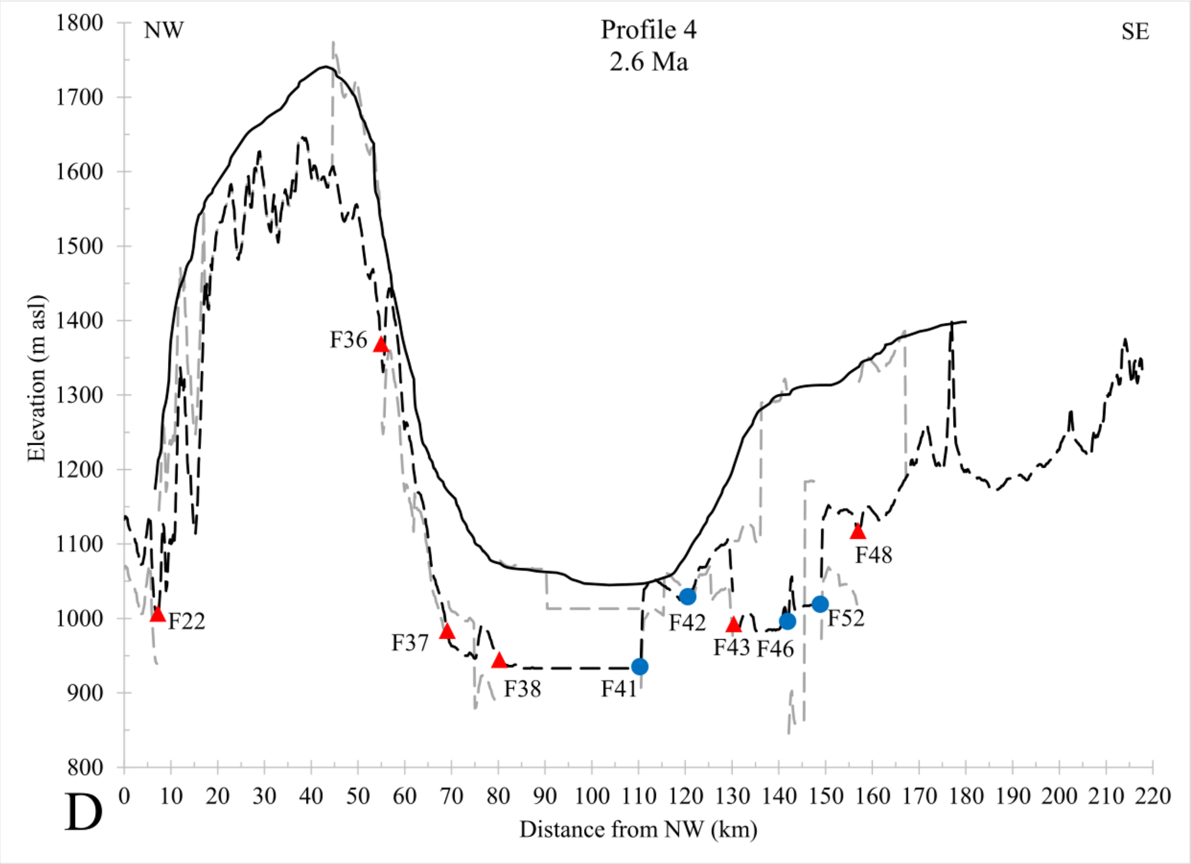
NW
Profile 4
2.6 Ma
SE
Elevation (m asl)
1800
1700
1600
1500
1400
1300
1200
1100
1000
900
800
F36
F22
F37
F38
F41
F42
F43
F46
F52
F48
0
10
20
30
40
50
60
70
80
90
100
110
120
130
140
150
160
170
180
190
200
210
220
Distance from NW (km)
D

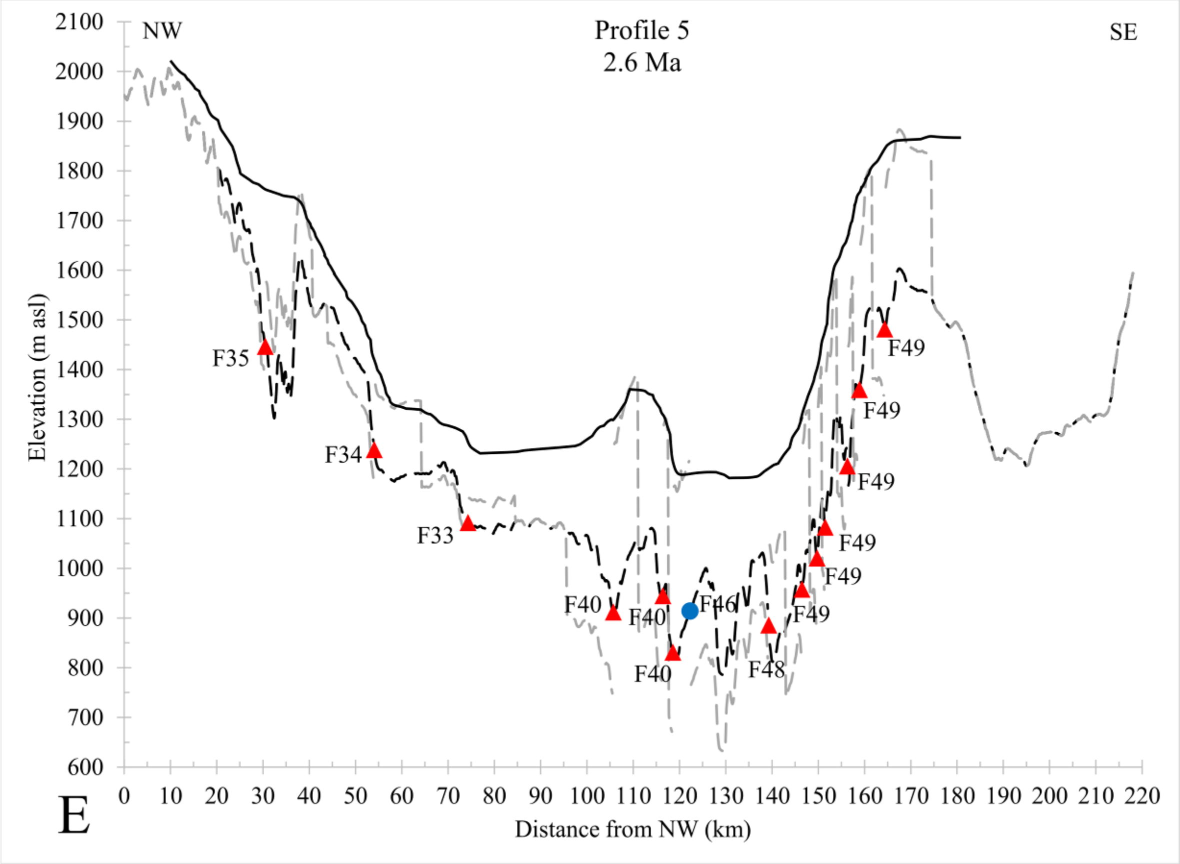
NW
Profile 5
2.6 Ma
SE
Elevation (m asl)
2100
2000
1900
1800
1700
1600
1500
1400
1300
1200
1100
1000
900
800
700
600
F35
F34
F33
F40
F40
F40
F46
F48
F49
F49
F49
F49
F49
F49
0
10
20
30
40
50
60
70
80
90
100
110
120
130
140
150
160
170
180
190
200
210
220
Distance from NW (km)
E

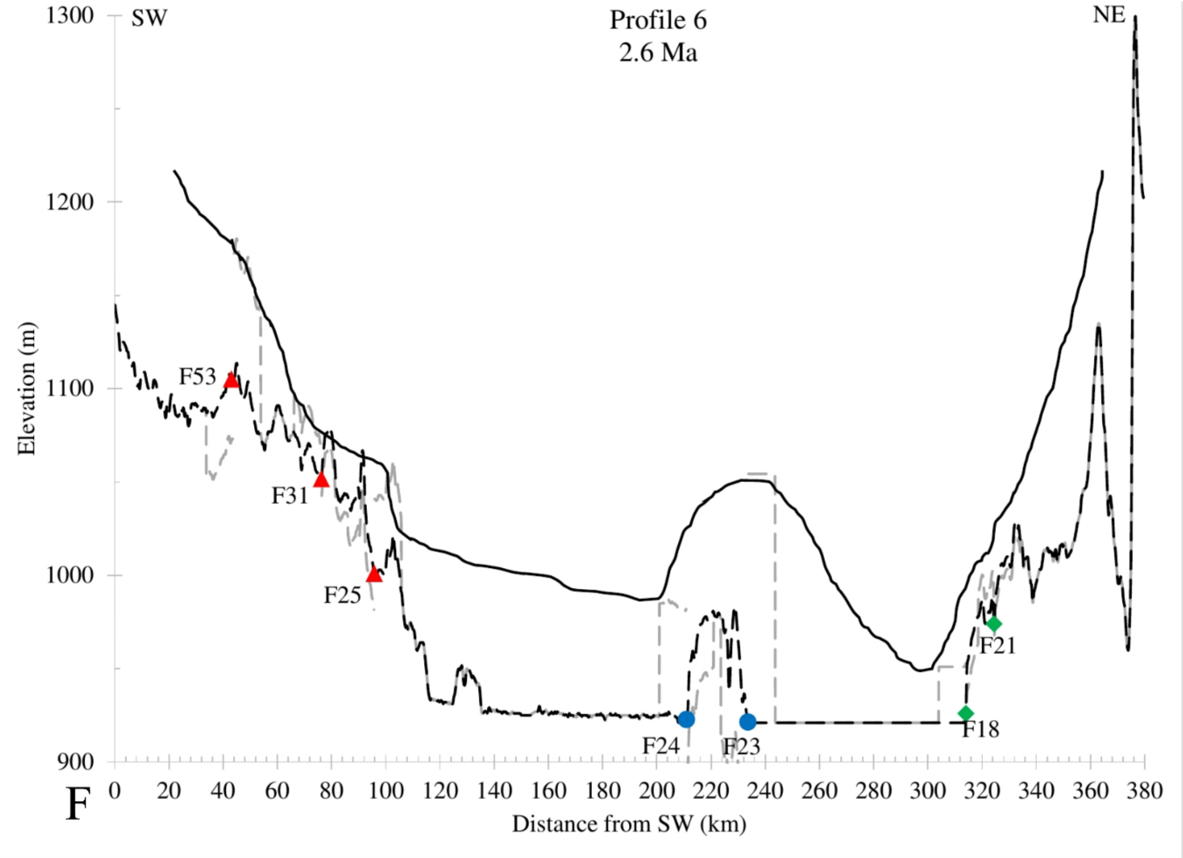
Profile 6
2.6 Ma
SW
NE
Elevation (m)
1300
1200
1100
1000
900
F53
F31
F25
F24
F23
F21
F18
0
20
40
60
80
100
120
140
160
180
200
220
240
260
280
300
320
340
360
380
Distance from SW (km)
F

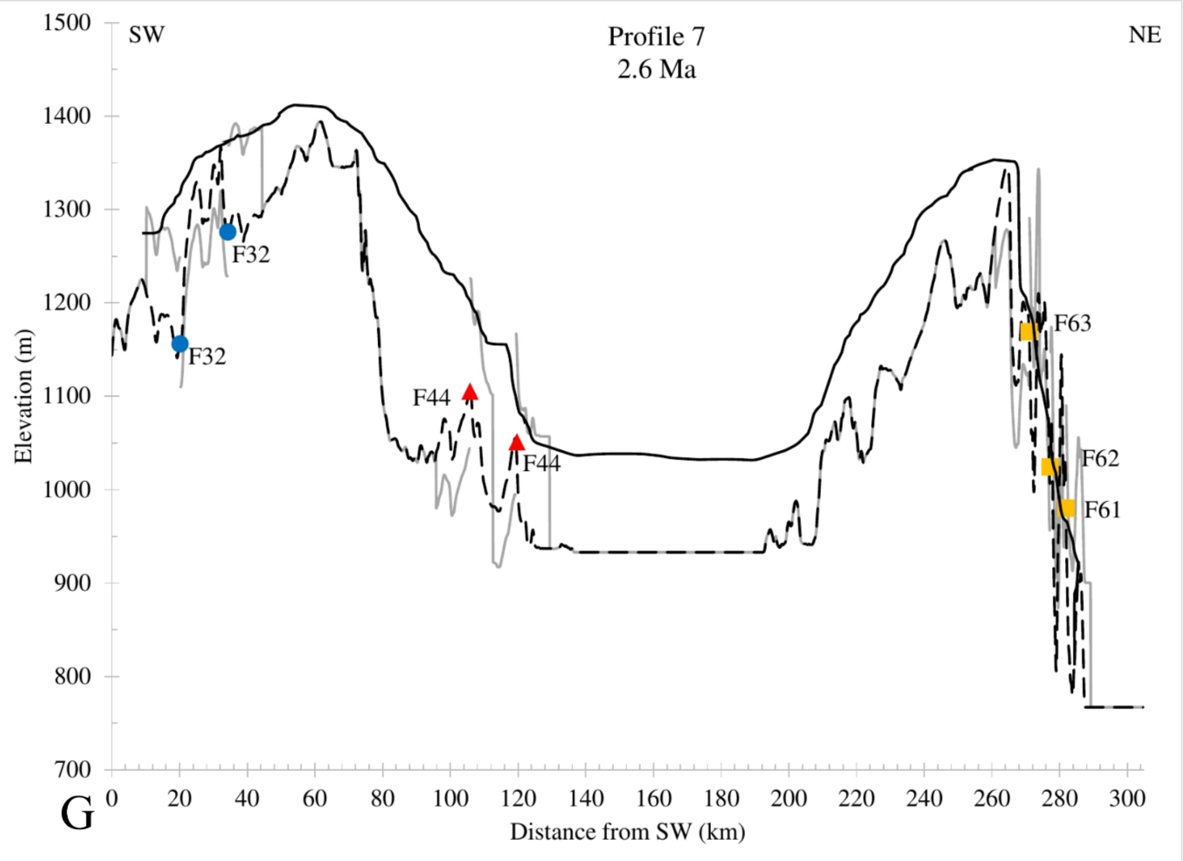
Profile 7
2.6 Ma
SW
NE
Elevation (m)
1500
1400
1300
1200
1100
1000
900
800
700
F32
F32
F44
F44
F63
F62
F61
0
20
40
60
80
100
120
140
160
180
200
220
240
260
280
300
Distance from SW (km)
G

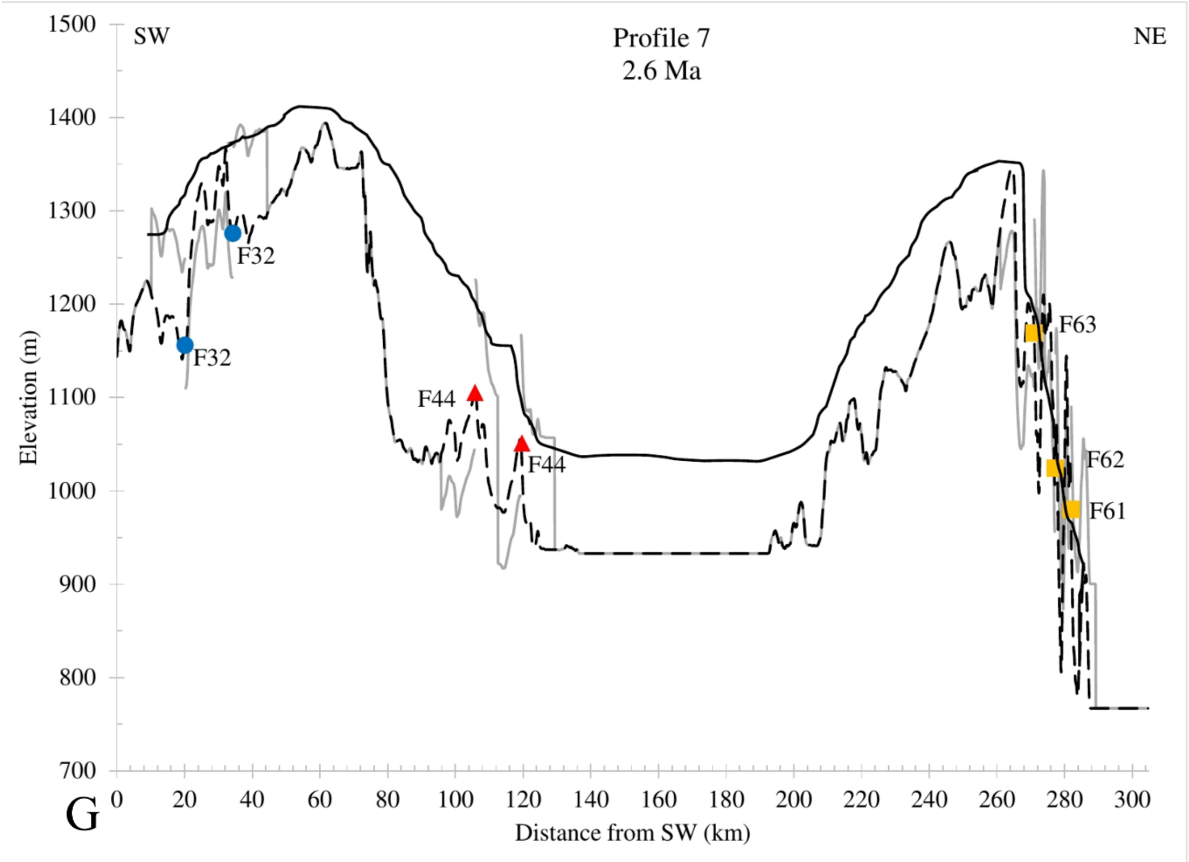

Figure 5.7: Reconstructed landscape at 2.6 Ma based on the topographic profiles presented in Figures 5.5 and 5.6 and two additional profiles (Profiles 7 and 8) which are depicted in Figure 5.1. Subtracted throw resulted assuming a constant fault displacement rate (see Table 5.1 for values) during the last 2.6 Ma. Dashed black lines represent the current landscape. Gray dashed line indicates the approximate elevation of the reconstructed landscape about 2.6 Ma (rift's onset), while black solid line is the average elevation of the reconstructed landscape. The SE dipping faults are indicated by red triangles while blue circles indicate the NW dipping faults. The SW dipping faults are presented as green rhombuses, while yellow squares show the NE dipping faults.

5.4.2. Geomorphic Analysis

We identified a total of 61 river knickpoints from individual stream profiles that corroborate the paleo-shoreline observation (Fig. 5.8A). In a second step, we analyzed the hypsometry of the Lake Mweru catchment to delineate the impact of paleo-lake Mweru on the elevation distribution. The hypsometric curve of the catchment (Fig. 5.8B, blue and black lines) reveals large areas characterized by gentle slopes, which we interpret to correspond to areas confining the paleo-lake Mweru. They all lie at elevations between 920-930 m asl, 990-1100 m asl and 1170-1190 m asl, which align with the sampled waterfalls at 1050 and 1160 m asl. We observe additional areas with low slopes at varying elevations, but focus our analyses on the most prominent elevations. We have furthermore excluded slope angles above 3° to better show terrain associated with lake-erosion processes (Fig. 5.8B, blue line). In the same elevation framework, we plot the number of knickpoints observed at a specific elevation. Knickpoints cluster at specific elevations and delineate the remnant paleo-shorelines in a more refined spatial pattern, indicating three abandoned shorelines at elevations of ~925 m asl, ~1000 m asl and ~1180 m asl, respectively (Fig. 5.8B).

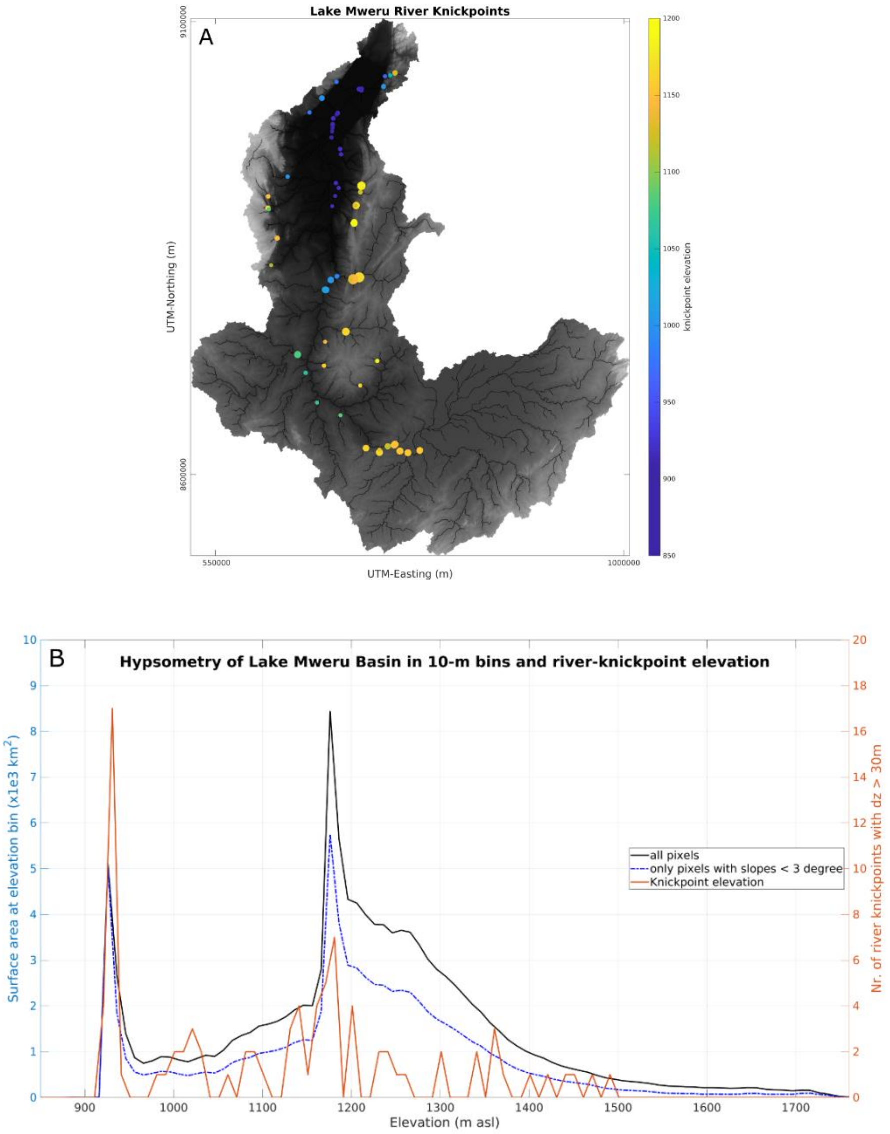

Figure 5.8: A) Locations of river knickpoints for the Lake Mweru catchment. Symbol colors indicate knickpoint elevations and symbol sizes show knickpoint magnitudes (lip minus base elevation). Only river knickpoints with elevations between 900 and 1200 m asl are shown. Note the clustering of river knickpoints at ~925 (dark blue), ~1000 (light blue), and ~1180 (yellow) m asl that correspond to paleo-shorelines of paleo-lake Mweru. B) Hypsometric curve of Lake Mweru derived from a 30 m SRTM DEM (NASA JPL, 2020). All grid cells within the Lake Mweru catchment were binned into 10 m elevation bins and their respective surface areas were calculated (black line). The elevations were filtered to only show hillslope angles < 3° (blue line). Note the two distinctive peaks at ~925 m asl and ~1180 m asl that show the approximate elevations of the current and paleo-lake Mweru respectively. Knickpoint elevation shows a

high number of river knickpoints at paleo-lake shorelines (only river knickpoints with at least 30 m offset are shown).

5.5. Discussion

Our results explore the landscape evolution of the Mweru rift system, the southwest extension of the EARS, since the late Neogene. The establishment of paleo-lake Mweru initiated a new drainage network, feeding the paleo-lake until the penultimate capture of this depocenter by an Upper Congo headwater. Here we discuss the implications of these new insights with respect to the southward and westward propagation of rifting.

5.5.1. Onset of Active Faulting and the Formation of the Paleo-Lake Mweru

Rifting in the study area is thought to have commenced by at least ~2.6 Ma (Tiercelin and Lezzar, 2002; Decrée et al., 2010; Molnar et al., 2019; Daly et al., 2020). Overall, analysis of the faulted topography within the MMFS reveals that individual faults have played a pivotal role in forming the two depressions that host the Lakes Mweru and Mweru Wantipa. Active faulting and associated footwall uplift are also responsible for the wide ridge that extends today between the two lakes (Fig. 5.1). The landscape reconstruction through subtraction of the 2.6 Ma fault throws (Fig. 5.7) displays a mild relief across the extended area of the MMFS, revealing that the landscape was similar to the flat East African erosion surface. During the early Pleistocene, the average topographic altitude was formerly higher, though it is possible that the relative height difference between the Kundelungu and Mporokoso Plateaus has not changed significantly since the onset of rifting. A low energy environment such as a shallow wetland and associated meandering rivers probably extended over this landscape, which was related to the extensive and relatively long-lived paleo-Chambeshi drainage system (Cotterill, 2005).

The southern part of the MMFS (profiles 1 and 6; Fig. 5.7A, 5.7F) hosts deltaic deposits associated with the Luapula River (Fig. 5.1). The primary faults that bound the depression that hosts present-day Lake Mweru to the west are (from south to north) faults 8, 9, 10 and 16 (Fig. 5.1). The total throw on these southeast dipping faults is ~640 m as opposed to the 200 m of cumulative throw recorded on the northwest dipping faults (i.e., 23 and 28) that bound this depression to the southeast. This geometry reveals a highly asymmetric rift tilted to the southeast. Profiles in Figure 5.7A and 5.7F suggest that faults 8 and 23 contributed drastically to the lowering of the landscape between the two horsts by a total throw of ~700 m. During the early Pleistocene, the southern part of the Mporokoso Plateau was about 250 m lower than the Kundelungu Plateau. It is known that during this period, the Luapula River captured the paleo-

Chambeshi River, which led to the present-day linkage between the Bangweulu and Mweru lakes (Cotterill, 2005). This interpretation, which is not described by the tectonic analysis presented here, suggests that the proto-Luapula River was flowing southward towards Lake Bangweulu (as suggested previously; Cotterill, 2005, 2006; Cotterill and de Wit, 2011; Moore et al., 2012). The onset of tectonic activity, together with the southward knickpoint retreat of the proto-Luapula River, may have contributed to the separation of the previously topographically connected Mporokoso and Kundelungu Plateaus.

Moving northwards, to profiles 2 and 6 (Figs. 5.7B, 5.7F), the elevation difference between the two shoulders of the rift is more distinct. The southeast dipping faults of the Kundelungu Plateau sum a total throw of almost 800 m, while faults along the Mporokoso Plateau have a total throw of ~300 m. It appears that the Mporokoso Plateau stood around 1400-1500 m asl during the late Pliocene. The basement of the lake was clearly higher than today, standing at ~1000 m asl, while the Kundelungu Plateau maintained its high elevation at ~1700 m asl. Faults 9, 16, 23, 24, 28 and 32 were the main contributors of downfaulting. In this area, the wetland was deeper (Kilwa Island did not exist) and the clastic bedrock was the main dominant rock type of the wetland's bottom. According to profiles 3 and 6 (Figs. 5.7C, 5.7F), the local average altitude of the landscape was lower, reaching the highest point of ~1350 m asl on the Kundelungu Plateau. The maximum altitude of the Mporokoso Plateau was ~1250 m asl, minimizing the elevational difference between the two shoulders of the rift. The total throw of the southeast dipping faults is ~500 m, while the northwest dipping faults' total displacement is 400 m, creating an almost symmetric section in a generally asymmetric structure. Considering Figure 5.7C, the reconstructed landscape during the early Pleistocene had a relatively low relief. Both these plateaus seem to have had an approximately similar local height (~1400 m asl), and the lowest point was probably close to the present-day location of the Kundabwika Waterfalls, which was controlled by fault 44.

Cotterill (2006) discussed the possibility that part of the Kalungwishi River, today flowing north, was redirected from the south, as the Kalungwishi River was formerly a major headwater of the proto-Luongo River (Fig. 5.1). Geobiological estimates of evolutionary events can be applied from the genomic record of extant fishes. These estimates of speciation events confer an independent chronology of these drainage links (Cotterill and de Wit, 2011). A pertinent example is the Early Pleistocene speciation of a killifish, *Nothobranchius ostergaardi*, confined within the eastern Mweru Wantipa basin; this species diverged from 0.46 to 1.11 Ma from its closest living relatives, which today occur south of the Congo-Zambezi watershed (van der Merwe et al., 2021). Their origin is attributed to the breakup of the paleo-Chambeshi River, and this event overlaps with independent pulses of fish speciation within the Mweru graben, as well as TCN dates constraining the tenure of paleo-lake Mweru. The onset of the MMFS (deepening of the paleo-lake Mweru) then disrupted the paleo-drainage of the Luongo-Kalungwishi system, contributing gradually to its disconnection from the paleo-Chambeshi drainage (Cotterill, 2006; Cotterill and de Wit, 2011).

Compared to Lake Mweru (917 m asl), Lake Mweru Wantipa stands at a higher elevation (932 m asl), and it is characterized by a high relief landscape. According to profiles 4 and 5 (Fig. 5.5), the total throw of the southeast dipping faults along the Kundelungu Plateau reaches up to 1720 m, while the northeast dipping faults have a maximum total throw of 460 m. Despite the approximately four-fold difference of the throw measured on the southeast and northwest faults, the rift here does not appear to be strongly asymmetric. This can be rationalized if we consider that the former faults are distributed across a distance of ~140 km whereas the latter ones span only 10 km across the rift’s shoulder. From a geomorphological perspective, the Mweru Wantipa depression hosts the seismically most active structures of the Southwestern Extension of the EARS (Daly et al., 2020). This is also supported by the DEM fault analysis that suggests a denser fault network of fresh discontinuous traces between the Lakes Mweru Wantipa and Tanganyika. The extended landscape around the modern Lake Mweru Wantipa during the early Pleistocene was also characterized by high relief, while the base of the wetland was standing at ~1150 m asl (Fig. 5.7D). The Kundelungu Plateau was standing at a maximum altitude of > 2000 m asl, while the Mporokoso Plateau had a maximum elevation of ~1900 m asl (Fig. 5.7E). The modern lowlands (cross hatching in the east in Fig. 5.2) on the borders between Lake Mweru Wantipa and the Mpulungu basin have currently an average elevation <1200 m asl. During the Pleistocene (Fig. 5.7G), the elevation was just ~50 m higher, with the lowest point ~1200 m asl. However, this elevation difference was sufficient to prevent the merging of paleo-lake Mweru and paleo-lake Tanganyika and suggests that these lakes have never been linked.

The western margin of the paleo-lake was defined by the long and high Kundelungu Plateau. The depression (cross hatching in the west in Fig. 5.2) that separates the main part of the plateau from its eastern continuity did not exist during the Pleistocene. Based on Figure 5.7H, the two parts of the plateau were connected, and the average elevation of the linking crest was ~1400 m. Faults 16a and 17 downfaulted the intervening landscape by ~200 m, resulting in the separation of the southwestern and northeastern sections of the Kundelungu Plateau.

There is no evidence of a sudden tectonic event that created this depression, so we assume that it was dominated by gradual lowering of the landscape due to normal faulting and intense denudation activity across the Kundelungu Plateau, as implied also by the TCN data.

Interestingly, the transition from Pliocene to Pleistocene (2.6 Ma) is characterized by a major climatic change in the southern hemisphere, from warm and humid conditions to aridification until 1.8 Ma, which is invoked as a driver of contraction and expansion of the lakes (Cohen et al., 1997). The lakes that were already flooded since ~3.6 Ma experienced contractions around 1.1 Ma (Cohen et al., 1997). Lavayssiere et al. (2019) reported that Lake Tanganyika dried down to the point it was divided into three contracted paleo-lakes, limited within the sub basins of the rift, which possibly caused fish speciation. The lake levels were restored gradually until 550 ka, while fluctuations in levels occurred, possibly linked to alterations in Pleistocene paleoclimates (Cohen et al., 1997; Trauth et al., 2005, 2010; Lavayssiere et al., 2019). Indeed, TCN dating suggests water level fluctuations across the paleo-lake Mweru during the Pleistocene (Section 5.2), which attests to complex interactions between past climates and tectonics.

5.5.2. The Destruction of the Paleo-Lake at ~350 ka

Terrestrial cosmogenic nuclide dating suggests that the paleo-lake was tapped about 350 ka (see Chapter 4). All samples which indicate temporary burial are consistent with an inferred lake drainage at ~200-400 ka, with age differences most likely representing lake level fluctuations (see Chapter 4). The reconstruction of key features that formed the landscape at ~350 ka is required to determine potential waterways allowing for the drainage, and consequent lowering, of the paleo-lake. To achieve this, we calculated, assuming constant displacement rates over these timescales (Mouslopoulou et al., 2009), the throw accrued on each fault since 350 ka and we subsequently subtracted it from its total displacement (Table 5.2). The modified faulted topography is assessed via profiles 1-6 (cross sections in Fig. 5.1), the results of which are illustrated in Figure 5.9. The restored topography at 350 ka reveals minor, albeit crucial, readjustments that appear to have impacted on the size of the paleo-lake.

Profile 1 displays the southern part of the paleo-lake, where the modern delta of the Luapula River lies (Fig. 5.9A). There is minimal information about Luapula River and its delta during this period, while it is known that the link between Lake Mweru and Lake Bangweulu existed prior the destruction of the paleo-lake Mweru (Cotterill, 2005). However, the reduction of the lake level around 350 ka probably forced the reversal of the river’s flow and the creation of the new deltaic feature at the southern margin of the lake (Cotterill, 2003, 2005). The key knickpoint of interest in this area is Mumbuluma I Waterfalls (Mumbuluma River; Fig. 5.9A), which was located relatively close to the southern shores of the paleo-lake (Cotterill and de Wit, 2011). It was directly affected by the lake level fluctuations that intensively took place during the Pleistocene due to their position close to the paleo-lake level (>1185 m asl). According to Profile 6, the southern section of the bottom of the paleo-lake (0-70 km from SW in Profile 6; Fig. 5.9F) had a maximum elevation of ~1150 m asl.

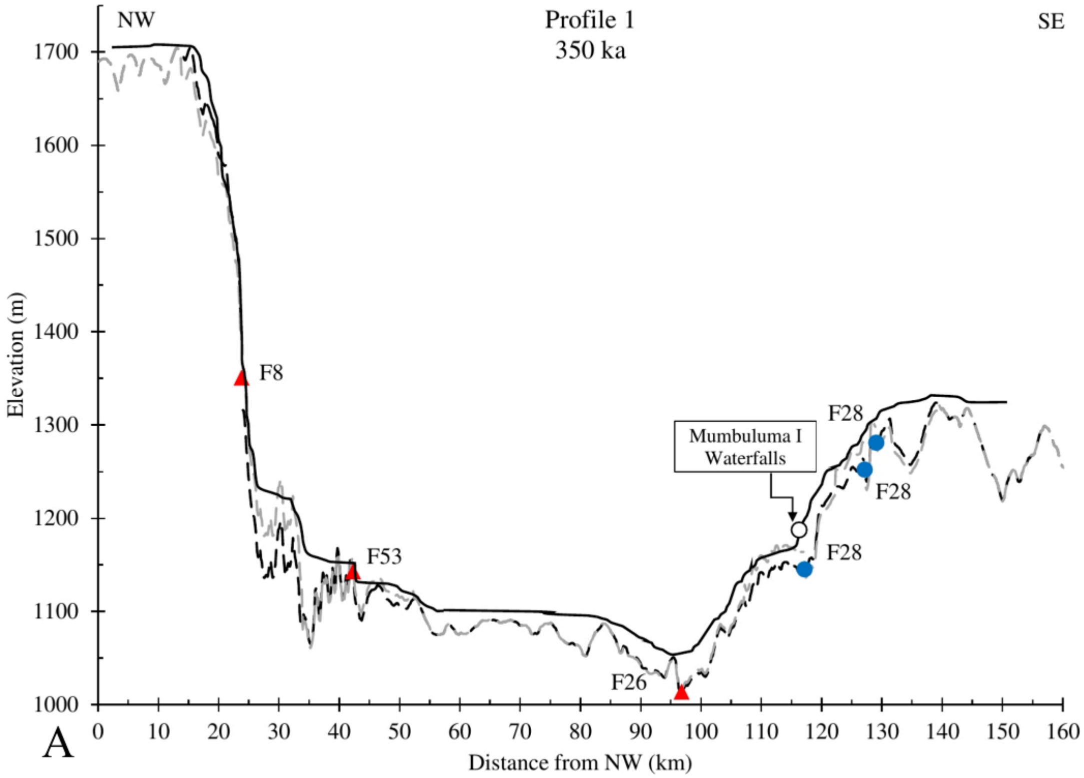

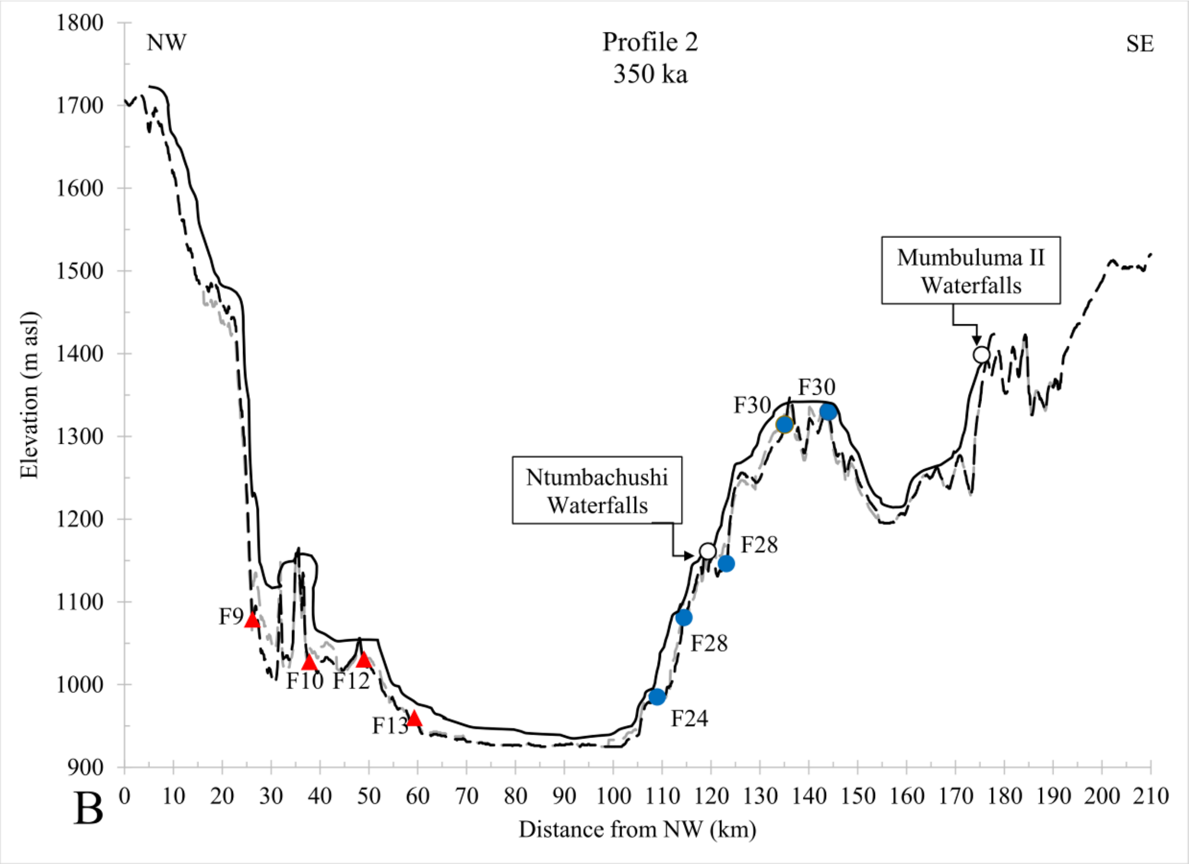
Profile 2
350 ka
NW
SE
Elevation (m asl)
1800
1700
1600
1500
1400
1300
1200
1100
1000
900
Mumbuluma II Waterfalls
Ntumbachushi Waterfalls
F9
F10
F12
F13
F24
F28
F28
F30
F30
B
0 10 20 30 40 50 60 70 80 90 100 110 120 130 140 150 160 170 180 190 200 210
Distance from NW (km)

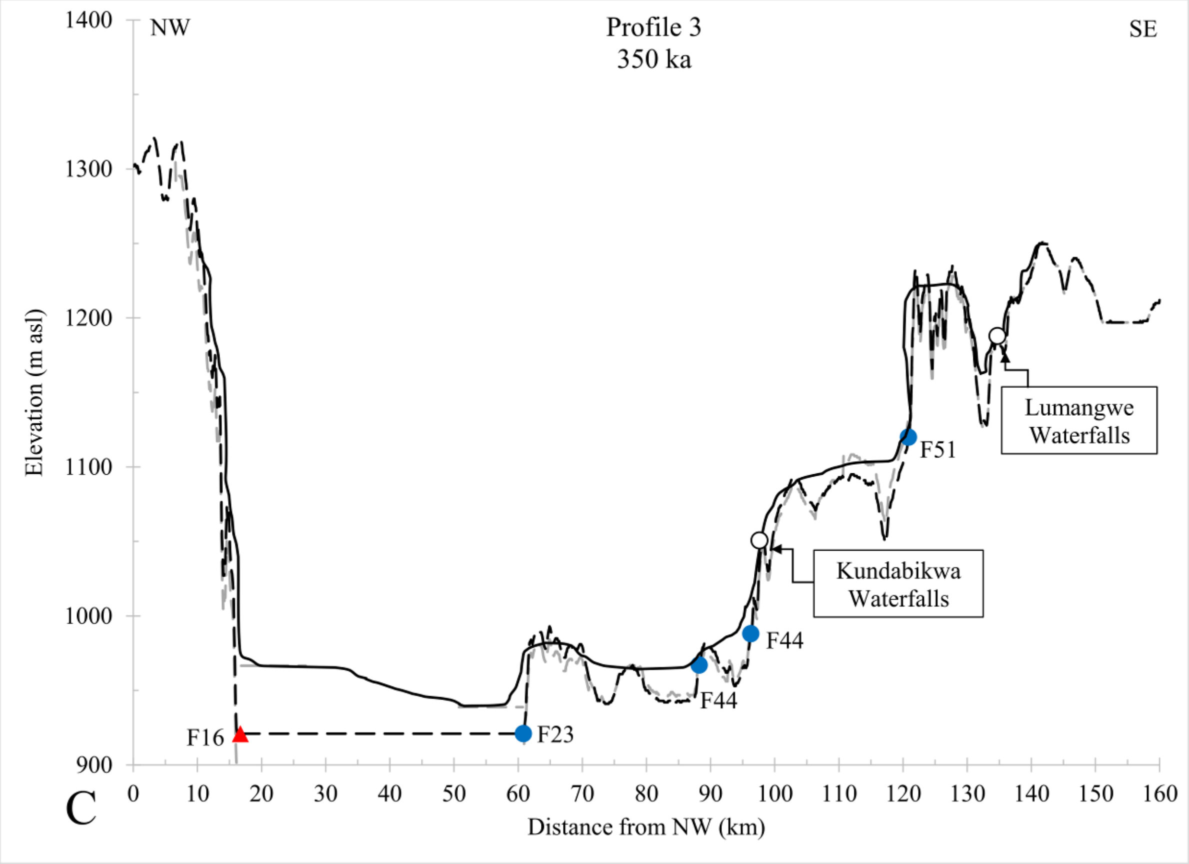
Profile 3
350 ka
NW
SE
Elevation (m asl)
1400
1300
1200
1100
1000
900
Lumangwe Waterfalls
Kundabikwa Waterfalls
F51
F44
F44
F16
F23
C
0 10 20 30 40 50 60 70 80 90 100 110 120 130 140 150 160
Distance from NW (km)

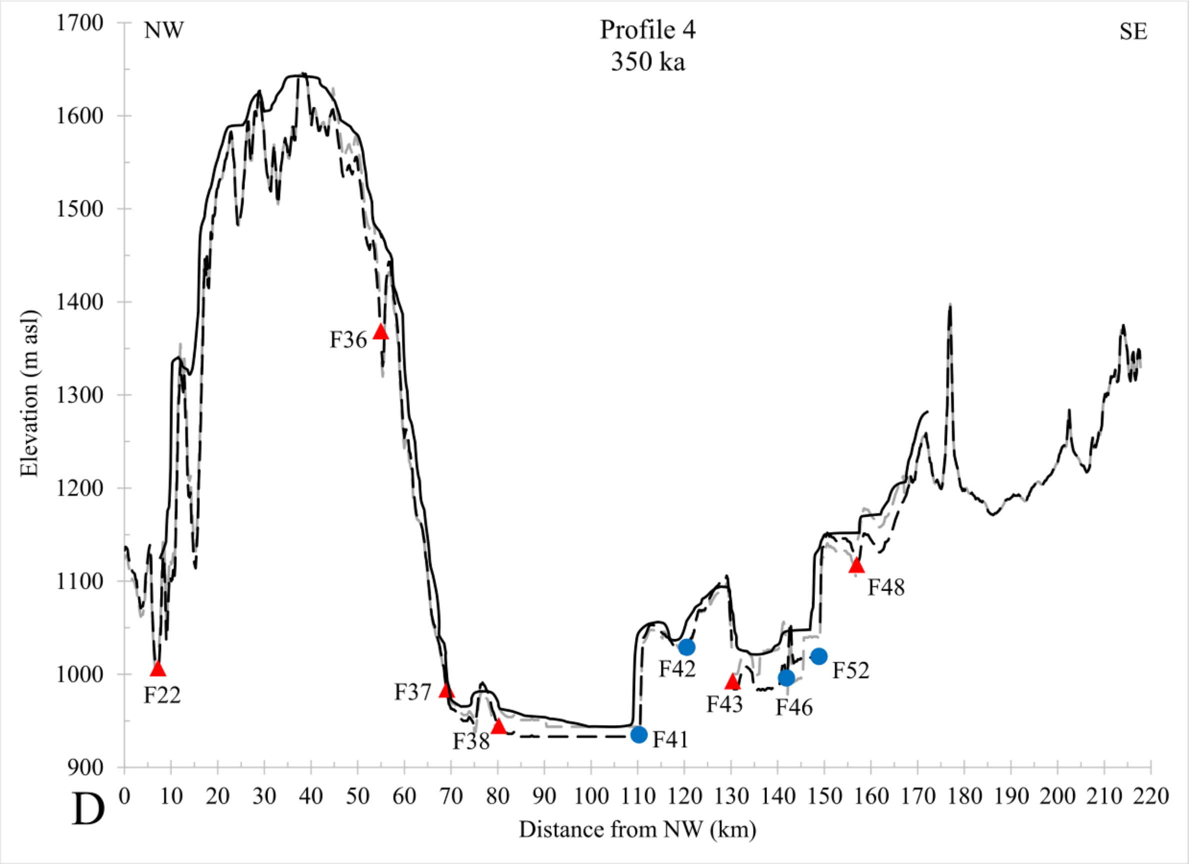
Profile 4
350 ka
NW
SE
Elevation (m asl)
1700
1600
1500
1400
1300
1200
1100
1000
900
F22
F36
F37
F38
F41
F42
F43
F46
F52
F48
0 10 20 30 40 50 60 70 80 90 100 110 120 130 140 150 160 170 180 190 200 210 220
Distance from NW (km)
D

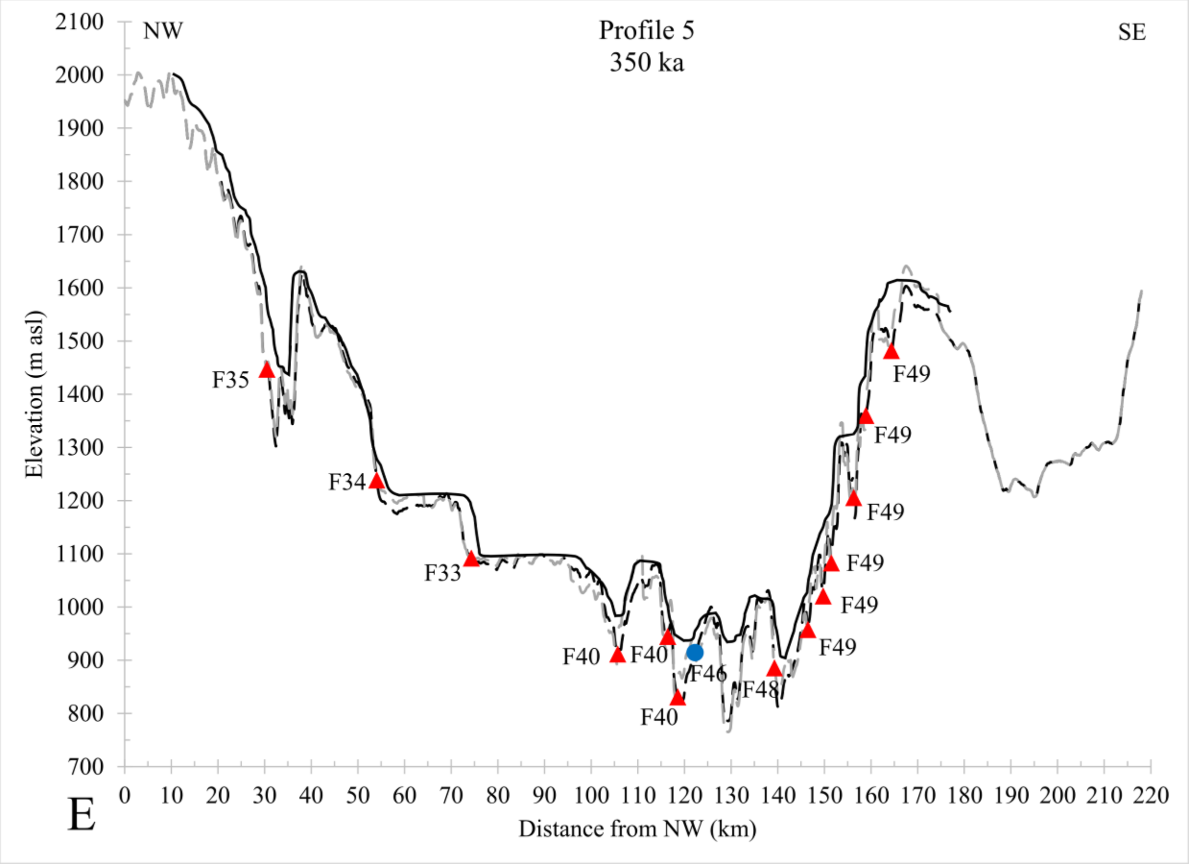
Profile 5
350 ka
NW
SE
Elevation (m asl)
2100
2000
1900
1800
1700
1600
1500
1400
1300
1200
1100
1000
900
800
700
F35
F34
F33
F40
F40
F40
F46
F48
F49
F49
F49
F49
F49
F49
0 10 20 30 40 50 60 70 80 90 100 110 120 130 140 150 160 170 180 190 200 210 220
Distance from NW (km)
E

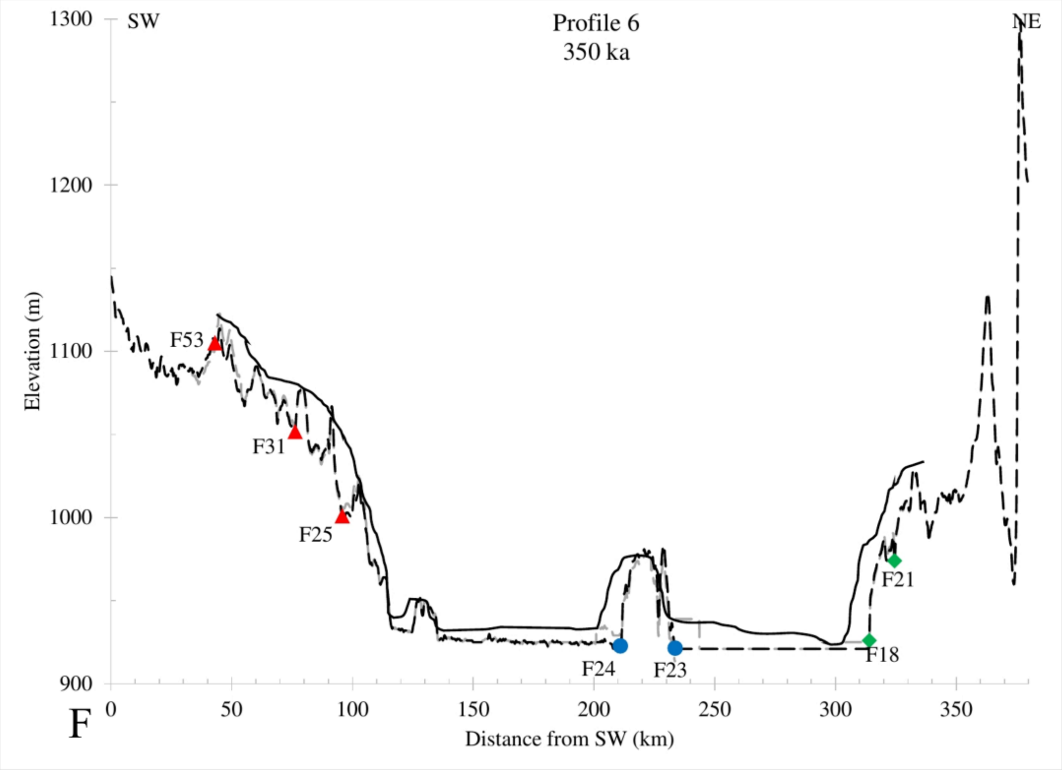

Figure 5.9: Reconstructed landscape profiles of the elevational sections (Figures 5.5 and 5.6) at 350 ka, based on the displacement rate of the mapped faults within the MMFS. Black dashed line represents the current landscape. Gray dashed line indicates the reconstructed landscape at 350 ka, while black solid line is the corrected estimation of the reconstructed landscape. The SE dipping faults are indicated by red triangles. Blue circles show the NW dipping faults. The SW dipping faults are presented with green rhombuses.

The paleo-lake was deeper northwards, where the bottom of the lake was at ~930 m asl (Profiles 2, 6; Figs. 5.9B and 5.9F). Ntumbachushi Waterfalls were standing at 1160 m asl, representing the eastern part of the paleo-lake’s shoreline (see Chapter 4). TCN data recorded the climate-driven fluctuations, which affected the waterfalls due to their position close to the possible maximum paleo-lake level. Mumbuluma II Waterfall (Luongo River) was probably never covered by the paleo-lake, providing a minimum formation age of ~830 Ma (see Chapter 4). Lumangwe Waterfalls, which are located south of the Kundabikwa Waterfalls on Kalungwishi River, were possibly placed close to the eastern border of the paleo-lake. According to the profiles in Figure 5.5, faults 8, 9 and 16 were the largest displacement faults that formed the asymmetrical half-graben structure that hosted the paleo-lake. Faults 16a and 17 also contributed to the formation of the depression west of present-day Lake Mweru and across the Kundelungu Plateau (Fig. 5.9C). This depression may have played a key role in the lowering of the paleo-lake's water level as it aided its tapping to the west (Fig. 5.2). Faster denudation rates on the Kundelungu Plateau (~40 mm ka^{-1}) compared to the Mporoskoso Plateau (~6 mm ka^{-1}) were forced by footwall uplift across Fault 16, resulting in fast incision along the northward flowing Luvua River (Fig. 5.1).

Dramatic lake level fluctuations have been reported throughout the late Pleistocene (14-450 ka) across Lake Tanganyika, Lake Malawi and the southwest extension of the EARS, which are related to tectonic factors and/or aridification periods (Danley et al., 2012; Ivory et al., 2016). From 450 to 350 ka, a regional lowering of the temperature and global sea level is directly correlated with the low stand of the lake levels across the Western Branch (Bakker and Mercer, 1986). In addition, a major dry period across the Congo basin occurred between ~270 and 180 ka, resulting in an additional lowering of the water level (Gasse et al., 1989). The evidence for the drainage of paleo-lake Mweru based on ^{10}Be and ^{26}Al data, together with tectonic analyses and the evidence for intensive climatic variation during the Pleistocene, indicate a gradual shrinking of the paleo-lake rather than a sudden tectonic event. The outflow of the paleo-lake through the Luvua River was most likely one of the main events that drained the lake (Dixey, 1944; Bos et al., 2006; Goodier et al., 2011; Cotterill and de Wit, 2011; Fig. 5.1). However, evaporation, especially in arid periods, may have further accelerated contraction of the paleo-lake, notably across the vast, shallow depression located between the two sections of the Kundelungu Plateau (Fig. 5.2).

5.6. Conclusions

Tectonic and digital topographic analyses confirm the existence of a large paleo-lake Mweru, which was revealed via terrestrial cosmogenic nuclide dating (see Chapter 4). This paleo lake exceeded the sizes of the present-day Lakes Mweru and Mweru Wantipa. As estimated previously, our results indicate the onset of the paleo-lake at around 2.6 Ma.

The timing of lake existence is consistent with the phylogenetic molecular clock analyses of endemic fish species, which also constrain the formation of the paleo-lake at the late Pliocene - early Pleistocene. Formation of this lake is correlated with the onset of the Mweru-Mweru Wantipa Fault System in the Early Pleistocene and likely established an estimated maximum shoreline at ~1200 m asl. The extent of the paleo-lake was also identified by river knickpoint and hypsometric analysis to constrain its paleo-shorelines at ~1180 m.

Intense normal faulting and associated footwall uplift at the northwestern paleo-lake boundary must have forced fast river incision in the eastern section of the Kundelungu Plateau. The deepening/flooding of the paleo-lake, which was probably due to the active extension and the climatic changes, started since the onset of the Mweru-Mweru Wantipa Fault System (~2.6 Ma), resulting in complex exposure histories observed at the knickpoints on the Mporokoso Plateau. The lake level decreased gradually and eventually the lake reached its current level at ~350 ka.

Chapter 6

Knickpoint Evolution Constrained by Cosmogenic Nuclides: A Case Study from the Kiubo Waterfalls, DRC

6. Knickpoint Evolution Constrained by Cosmogenic Nuclides: A Case Study from the Kiubo Waterfalls, DRC

6.1. *Introduction*

In the past few decades, many studies have been dedicated to our understanding of the interactions between tectonics and denudation. By studying cases that indicate landscape disequilibrium, the geomorphic conditions and processes which determine the landscape evolution can be described. Among the features that geomorphologists study in order to investigate and tackle this issue are knickpoints along a fluvial profile. Knickpoints are defined as sudden changes in the slope along a longitudinal profile and may be represented by obvious waterfalls, but also by more subtle features that are not easily recognizable without the analysis of river slope data (Gardner, 1983; Hayakawa and Matsukura, 2003; Bishop et al., 2005; Hayakawa and Oguchi, 2006; Crosby and Whipple, 2006). The mechanism by which a stream network responds to any fluctuation of the base level is upstream retreat of the knickpoint (Berlin and Anderson, 2007).

The knickpoint retreat rate is one of the most controversial subjects of modern geomorphology. Understanding the mechanisms of river bed incision provides vital information about the landscape and drainage evolution of the study area. Tectonically active landscapes are often characterized by steep structures in bedrock channels, which were triggered by regional uplift, denudation and knickpoint migration, which can set the lower boundary condition for adjacent hillslopes (Whipple and Tucker, 1999; Whipple, 2004). Analyzing the knickpoint movement through time provides useful insights regarding the communication between the base level and the upstream catchment (Bishop et al., 2005). Quantifying geomorphological and tectonic characteristics such as uplift and/or incision/denudation is still very challenging, due to many unknown parameters and links between our topographic observations and the actual rates of surface processes (Burbank et al., 1996). Knickpoint retreat rates and their retreat processes have been investigated using field observations (e.g., Young, 1985; Miller, 1991; Seidl et al., 1996; Weissel and Seidl, 1998; Hayakawa and Matsukura, 2003), physical modeling (‘sand-box’) (e.g. Holland and Pickup, 1976; Gardner, 1983), or large-scale numerical modeling (van der Beek et al., 2001).

Crosby and Whipple (2006) studied the predictability of the position of a knickpoint through the fluvial network. They tested two numerical models, the first of which describes the knickpoint retreat mechanism as a power function of drainage area and the second one predicts knickpoint formation as soon as a certain threshold drainage area is reached (Berlin and Anderson, 2007). The first model is described as the Stream Power Law (Howard and Kerby, 1983; Whipple and Tucker, 1999). It has provided remarkable results on the prediction of the knickpoint position through reverse retreat. The knickpoint retreat modeling of the Roan Plateau in western Colorado (USA) by Berlin and Anderson (2007) is an exceptional example. The success of this case study indicated that the drainage area is the most important controlling factor of the knickpoint retreat, for long timescale processes. Despite the simple formulation of the Stream Power Law, its power lies in its capacity to reproduce many of the characteristic features of natural systems (the concavity of a river profile, the propagation of knickpoints, etc.; Croissant and Braun, 2014). However, a better constraint on the corresponding erodibility constant (K) would provide a better insight and generate more robust results by constraining the timing of the incision (Berlin and Anderson, 2007; Croissant and Braun, 2014).

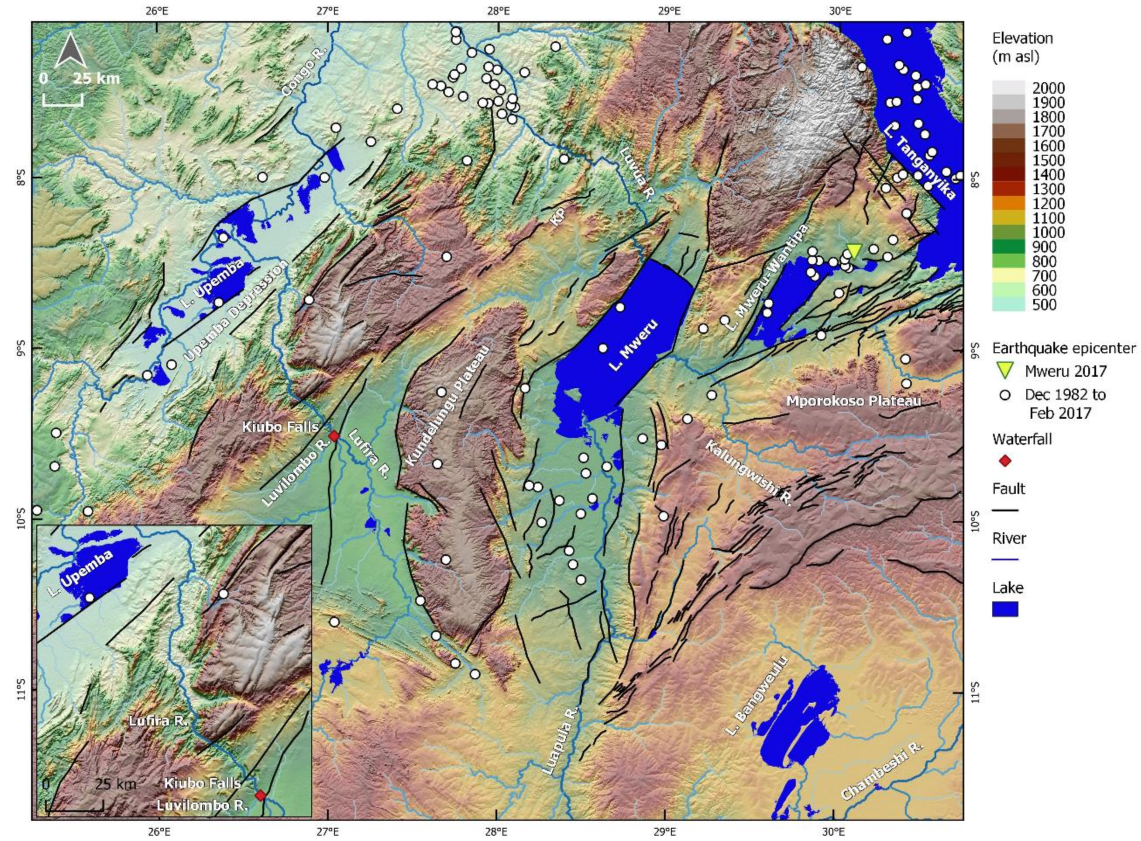

Figure 6.1: Morphotectonic map of the Upemba and the Mweru-Mweru Wantipa Fault Systems. The study area of this chapter is the Kiubo Waterfalls which are enlarged in the inset of the map. Normal faults are indicated by black lines. Red diamond indicates the position of the Kiubo Waterfalls. White circles indicate earthquake locations across the Upemba and the Mweru-Mweru Wantipa Fault Systems. The yellow triangle indicates the recent earthquake event which took place at the Mweru Wantipa Lake in February 2017.

The aim of this study is to potentially constrain the K constant in the Stream Power Law by introducing age restrictions from terrestrial cosmogenic nuclide (TCN) dating on bedrock samples from the Lufira and Luvilombo Rivers in the Katanga Province of the Democratic Republic of Congo (DRC; Fig. 6.1). The radionuclides ^{10}Be and ^{26}Al were used in combination with the stable isotope ^{21}Ne in order to retrieve robust results. The uncertainty of the state of a waterfall challenges the TCN dating of knickpoints (Howard and Kerby, 1983; Whipple and Tucker, 1999; Whipple et al., 2000; Brocklehurst, 2010). Nevertheless, useful parameters such as denudation rates, periods of burial and minimum exposure ages can be estimated for knickpoints and their surrounding landscape. Constraining the K constant will provide an opportunity to calculate an average knickpoint retreat rate of the Lufira River and estimate the initial formation point of the Kiubo Waterfalls. In addition, tectonic analyses have been applied in order to investigate the activity of the Upemba Fault System (UFS) and its correlation with the formation of the Kiubo Waterfalls. The importance of these waterfalls is represented on the one hand by the biodiversity of the fish population and their distribution based on the behavior of the knickpoint, and on the other hand by the direct relation of the waterfall's knickpoint to the active tectonism of the UFS.

6.2. *Geology and Geomorphology of the Study Area*

Lufira River is an ~650 km long stream and flows into the Upemba Depression (Fig. 6.1). It has a general curvilinear shape and two major zones of elevation drop. The first zone is related to two artificial dam walls, including the dam known as Lac Tashangalele (aka Lac Lufira), that occurs as two dams, with the first major dam wall situated at 1118 m asl and the second at 1014 m asl. The first zone also includes a series of downstream waterfalls and cascades, approximately 220 km away from the headwaters (Flugel, 2014). There, a total drop of around 100 m occurs over a distance of 30 km. The second zone is situated around 430 km downstream from the headwaters of the Lufira River (Fig. 6.2). In that area, the middle course of the Lufira River flows through the extensive Kundelungu Swamps (889 to 870 m asl), whose end is marked by the Kiubo Falls. This second drop, 80 m over 40 km, is formed due to a difference of lithology, and starts with the active knickpoint of the Kiubo Waterfalls (Fig. 6.3). Downstream from the Kiubo Waterfalls, the river flows into the Upemba Depression (~ 576 m asl) while passing through steep valleys which progressively widen downstream (Flugel, 2014). Knickpoint analyses of the Lufira River reveal 11 main knickpoints, 9 of which occur in relatively sudden elevation drops and are related to lithographic changes (Fig. 6.2; Flugel, 2014). Lufira River is the eastern tributary stream of the Lualaba River, which is affected by the tectonic activity of the Mweru-Mweru Wantipa Rift System (Tack et al., 2003). Luvilombo River, a tributary stream of the main Lufira River, merges immediately below the close-by Kiubo and Luvilombo Waterfalls (2 km northwest of the Kundelungu National Park-West; Fig. 6.1).

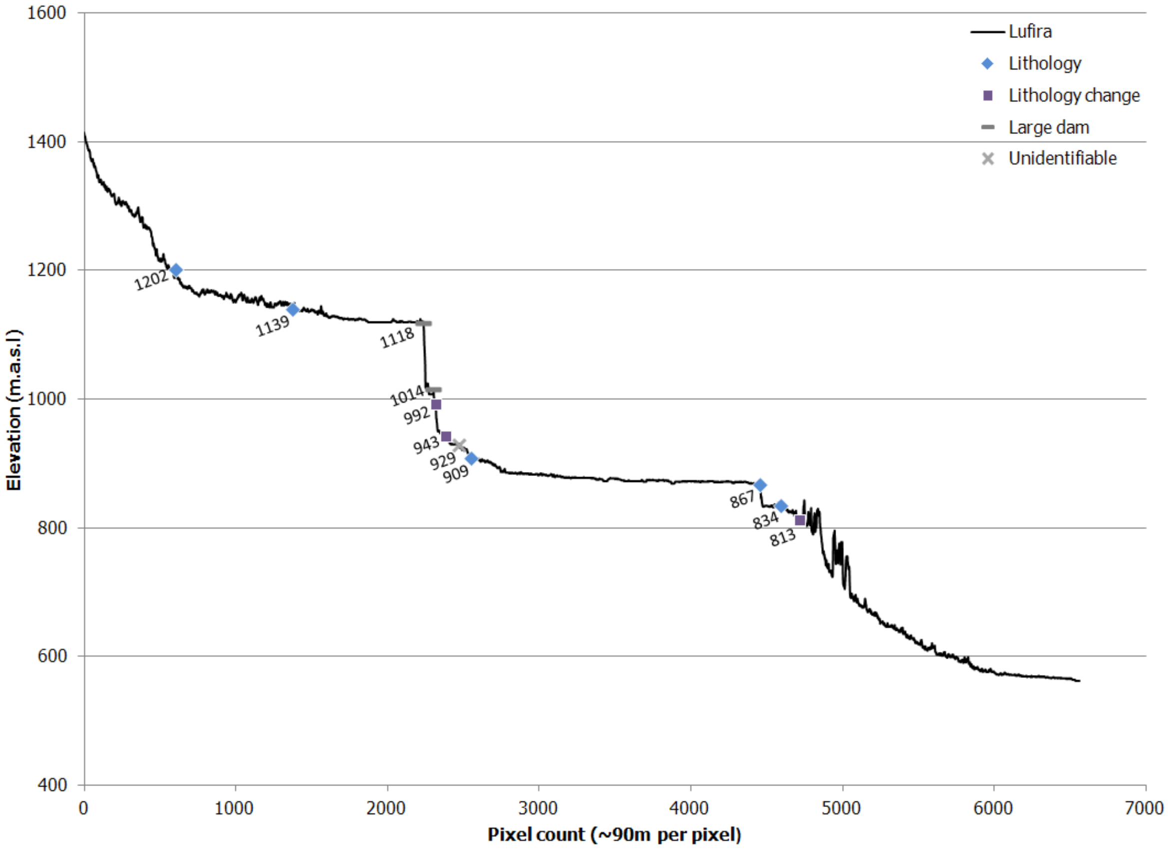

Figure 6.2: Longitudinal profile of the Lufira River. There are 11 main knickpoints identified, whose causes are resistant lithology (blue rhombus; n = 5), a change in lithology (yellow square; n = 3), artificial dam wall (gray dash; n = 2) and a singular knickpoint whose cause remains unresolved (green cross). Figure based on Flugel (2014).

The Upemba Depression is part of a major rift system, which is related to a large extensional fault that penetrated deep into Gondwana (Klerkx et al., 1998). Its trend is parallel to the NE-SW trend of the MMFS. The basin consists of a fairly complete stratigraphic succession from Late Carboniferous to Early Jurassic sediments (Delvaux, 2001), which succeed basal tillites and Cenozoic blocks (Villeneuve, 1983). These formations are known as the bedrock basement of the UFS and their age is correlated to the Kibaran belt (Sebagenzi and Kaputo, 2002; Villeneuve et al., 2019). To the northwest, the UFS is bounded by the Archean/Paleoproterozoic Congo craton, while a mosaic of older crustal rocks amalgamated prior to the Kibaran orogeny extends to the southeast (Kapenda et al., 1998). The UFS trends accordingly to the direction of the main folds of the Kibaran belt, which is one of the most well-preserved Mesoproterozoic belts in the world (Kampunzu et al., 2001). Due to the lack of modern tectonic, petrological, geochemical and precise geochronological data, the orogenic history of this belt is poorly described (Kokonyangi et al., 2004). The UFS runs over 700 km with an average width of 300 km, while the complete Kibaran orogenic system of central and southern Africa extends over 3 000 km. The presence of a large volume of granitoids suggests that they were emplaced along a previous plate convergent margin, leading to the onset of the extensional rifting (Kampunzu et al., 2001).

Figure 6.3: Kiubo Waterfalls, Lufira River, Democratic Republic of Congo.

As a part of the UFS, the Lufira River flows on top of fine-grained brick quartzite and shale, which are interbeded with brownish sandstones and red and white banded shales, including a few thin beds of dolomite. This sequence is named the Lufira Beds (or Nzilo Group) and has a thickness ranging from 2700 to 7000 m (DeWaele et al., 2016). The Kiubo Waterfalls is the most important knickpoint along the Lufira River, with an absolute height of 40 m and a width of 90 m (Fig. 6.3). The waterfalls extend over the Kiubo Group, which consists of stratified shales, silty shales and sandstones with occasional irregular bedding (de Magnée and François, 1988). The top of the Kiubo Group is related to a major tectonic unconformity. This feature represents the basal thrust-faults of the nappes, and is locally overlain by the breccias that form the base of these nappes (Cailteux et al., 2018).

6.3. Material and Methods

6.3.1. Sampling

Eleven bedrock samples were collected from vertical (~90°) and horizontal surfaces along the Luvilombo and Lufira Rivers (Fig. 6.4; Table 6.1). As mentioned in previous sections of this thesis (Chapter 3), the preferred rock type was quartzite, due to its abundance in quartz. In the Kiubo Waterfalls area however, where quartzites are absent, the dominant lithology is brownish sandstones, consisting of enough quartz to allow for a successful TCN analysis, too. The sampled rock belongs to the Kiubo Group, which is part of the Kibaran Belt. The first five samples (LUV01-05) were taken close to the knickpoint of Luvilombo Waterfalls and along the left banks of the Luvilombo River downstream (Fig. 6.5A). The second group (LUF01-LUF06) was taken close to the Kiubo Waterfalls and downstream along both banks of the Lufira River (Figs. 6.5B, C). The aim of this sampling strategy was to determine knickpoint retreat rates by dating several samples from different distances downstream of the present knickpoint. Two samples (LUF01 and LUF06) were taken directly from the Kiubo Waterfalls knickpoint in order to potentially determine the minimum exposure age of the current waterfalls (Fig. 6.5C).

Figure 6.4: Sample locations along the Luvilombo (left tributary stream) and Lufira Rivers (main stream). Samples which were collected from a vertical surface are indicated with blue rhombus, while the samples that were collected from horizontal surfaces are shown as red rhombus.

Figure 6.5: Photos of sampling locations: A) Luvilombo Waterfalls, Luvilombo River; B) Downstream of the Kiubo Waterfalls, on the left bank of the Lufira River; C) Current knickpoint of the Kiubo Waterfalls, Lufira River.

Table 6.1: Sampling details for samples from the Katanga Province, Democratic Republic of Congo. Total shielding factor includes surface dip, horizon shielding and self-shielding.

Name	Latitude ° S	Longitude ° E	Elevation (m)	Surface Dip (°)	Average Thickness (cm)	Total Shielding Factor
Luvilombo Waterfalls, Luvilombo River, D.R. Congo						
LUV01	9.52217	27.03917	840	90	2.0	0.48
LUV02	9.52227	27.03918	847	0	4.0	0.94
LUV03	9.51849	27.03462	848	90	5.0	0.48
LUV04	9.51902	27.03503	852	90	2.5	0.49
LUV05	9.51823	27.03432	864	0	2.0	0.98
Kiubo Waterfalls, Lufira River, D.R. Congo						
LUF01	9.51557	27.03738	836	90	7.5	0.56
LUF02	9.51410	27.03335	844	90	9.0	0.45
LUF03	9.51179	27.03303	858	0	5.0	0.48
LUF04	9.51388	27.02957	858	90	5.0	0.48
LUF05	9.51388	27.02952	863	0	5.0	0.48
LUF06	9.51767	27.03720	860	90	4.5	0.48

6.3.2. Sample Processing

The sample processing for the ^{10}Be and ^{26}Al analyses was applied according to Kohl and Nishiizumi (1992) and the UC Santa Barbara Cosmogenic Nuclide Preparation Facility protocol (http://www.geog.ucsb.edu/~bodo/pdf/bookhagen_chemSeparation_UCSB.pdf), which is based on modifications of previous studies (e.g., Kohl and Nishiizumi, 1992; von Blanckenburg et al., 2004). The samples were crushed and sieved down to 250-500 μm, and quartz grains were separated via the standard methods of heavy liquid and Frantz magnetic separation. All samples were etched in diluted HCl, H_2SiF_6 and HF in order to dissolve all non-quartz minerals and remove any contribution of meteoric ^{10}Be.

Sample LUF03 was not processed due to the low amount of quartz grains. Fractions of ~10-30 g of pure quartz from the 10 remaining samples were used for ^{10}Be and ^{26}Al analysis (Table 6.2). The preparation and processing of the samples took place at the HELGES laboratory (Helmholtz Laboratory for the Geochemistry of the Earth Surface) of GFZ Potsdam and at the University of Potsdam. Samples that were prepared at HELGES were spiked with a ^{9}Be carrier with a concentration of 779.4±13.4 µg g^{-1}. ^{27}Al carrier was used only for the blank samples, as the rest of the samples contained enough native ^{27}Al. A single element standard solution for ICP-MS/OES with a ^{27}Al concentration of 1002 mg ml^{-1} was used. For the samples that were prepared at the University of Potsdam, the ^{9}Be carrier “Be 2 July 2016” with a concentration of 2511±30 µg g^{-1} was used. The "Be 2 July 2016" carrier is an in-house carrier at the University of Potsdam that has been derived from Be-rich ores from a mine in Brazil. A Merck Certipur Aluminium ICP standard with an Al concentration of 10,000 mg l^{-1} was used.

Total dissolution and digestion were obtained by using concentrated HF. After total dissolution, aliquots were taken in order to quantify the total Al concentration in the samples (Table 6.2). The determination of the Al amount was done by ICP-OES measurements at University of Potsdam and GFZ Potsdam. Be and Al were separated via ion exchange columns and precipitated as hydroxides. Before the last step of target pressing, the samples were heated up to 1000 °C. This ignition step transformed the sample solutions to Be and Al oxides. Due to technical and organizational issues, the samples were measured at different Accelerator Mass Spectrometers (AMS). Specifically, the Be measurements of the LUV sample series (except for LUV03) and LUF06 took place at the National Laboratory of Age Determination of the Norwegian University of Science and Technology (NTNU), Trondheim, Norway (Seiler et al., 2018; Table 6.2), while the Al measurements of the same series were performed at the French national facility Accélérateur pour les Sciences de la Terre, Environnement, Risques (ASTER, CEREGE, Aix-en-Provence; Arnold et al. 2010; Sartégou et al., 2018; Table 6.2). Both Be and Al measurements for the LUF series (except LUF06) and the sample LUV03 took place at the Institute of Nuclear Physics at the University of Cologne (Pascovici et al., 2013; Table 6.2). All sample and blank values are provided in Table 6.2.

Table 6.2: Measured $^{10}Be/^{9}Be$ and $^{26}Al/^{27}Al$ ratios and ^{27}Al concentrations in samples and blanks. Processing blanks are indicated with SOBLx (x=number of batch analyzed). All uncertainties presented are 1σ. Uncertainty for all ICP-OES measurements of ^{27}Al concentrations at University of Potsdam is 3% and at GFZ Potsdam is 5%. Labs used: T= NTNU, Trondheim, Norway; A= ASTER, CEREGE, Aix-en-Provence, France; P=University of Potsdam, Germany; C= University of Cologne, Germany; G= GFZ Potsdam, Germany.

Name	$^{10}Be/^{9}Be$ (10^{-13})	AMS	$^{26}Al/^{27}Al$ (10^{-13})	AMS	^{27}Al (μg g^{-1})	ICP
LUV01	0.247±0.020	*T*	0.696±0.080	*A*	106	*P*
LUV02	0.799±0.047	*T*	2.255±0.098	*A*	180	*P*
LUV04	0.710±0.038	*T*	1.900±0.076	*A*	145	*P*
LUV05	1.666±0.062	*T*	4.48±0.14	*A*	129	*P*
LUF06	0.176±0.018	*T*	0.386±0.038	*A*	120	*P*
SOBL4	0.0185±0.0054	*T*	0.021±0.015	*A*	-	*P*
LUF01	0.835±0.050	*C*	0.270±0.032	*C*	345	*G*
LUF02	0.72±0.11	*C*	0.221±0.039	*C*	414	*G*
LUF04	1.101±0.065	*C*	0.879±0.077	*C*	192	*G*
LUF05	3.70±0.15	*C*	4.07±0.23	*C*	140	*G*
LUV03	1.159±0.083	*C*	0.65±0.15	*C*	191	*G*
SOBL7	0.089±0.013	*C*	0.146±0.049	*C*	-	*G*

^{21}Ne analyses were carried out in the noble gas laboratory of the GFZ Potsdam. Heavy liquids and magnetic separation were used as first step in order to purify the samples, as it was described in the beginning of this chapter. The next step was to etch the material with diluted HCl and a mixture of diluted HF (1-4%) and HNO_3. In some cases, due to the small amount of the sample, additional hand-picking of non-quarzitic minerals under a binocular microscope was necessary. The concentrations of the stable noble gas nuclides were measured using a static VG5400 noble gas mass spectrometer (Niedermann et al., 1997). An amount of 0.7 g of clean quartz per sample was wrapped in Al foil and heated in four steps (400 °C, 600 °C, 800 °C and 1200 °C). This procedure facilitates an assessment of contributions of non-cosmogenic components (nucleogenic or trapped). In addition, ~1 g aliquots of three samples (LUV01, LUV04 and LUF06) were crushed in vacuum to determine the isotopic composition of Ne trapped in fluid inclusions (Niedermann, 2002; Hetzel et al., 2002). More details about the ^{21}Ne measurements can be found in section 4.3.2 of chapter 4.

6.3.3. *TCN Calculations*

Exposure ages were calculated using the sea level high latitude (SLHL) spallogenic production rates of 4.01 atoms g^{-1} a^{-1} for ^{10}Be and 27.93 atoms g^{-1} a^{-1} for ^{26}Al (Borchers et al., 2016). To calculate minimum ^{21}Ne exposure ages, a SLHL production rate of 17.51 atoms g^{-1} a^{-1} was used. This value is based on the total ^{10}Be production rate of Borchers et al (2016) and the ^{10}Be/^{21}Ne production ratio of 0.232 ± 0.009 (Goethals et al., 2009). All ages were calculated with CosmoCalc 3.0 (Vermeesch, 2007), using Lal (1991) scaling factors and default values for all parameters except the SLHL production rates for the aforementioned nuclides. A density of 2.65 g cm^{-3} was used for all calculations. In addition, all values were corrected based on sample thickness (1-10 cm) and geometric shielding.

6.3.4. *Stream Power Law Calculations*

In order to determine the knickpoint migration rate of Kiubo Waterfalls, we used the equation of the Stream Power Law as Whipple and Tucker (1999) described it:

$$1)\quad \varepsilon = KA^m S^n$$

where ε is the knickpoint retreat rate, m and n are positive constants reflecting basin hydrology, hydraulic geometry, and erosion processes, and K is a dimensional coefficient of denudation (its dimensions are dependent on the values of m and n) that combines the effects of lithology, climate, and sediment load. A is the drainage area above the knicpoint, which appears as a proxy for discharge, while S is the knickpoint's slope[1] (Whipple and Tucker, 1999; Berlin and Anderson, 2007). The knickpoint retreat rate can also be expressed as a function of the horizontal velocity (v) times the slope of the knickpoint:

$$2)\quad \varepsilon = vS$$

Combining equations (1) and (2) provides the Stream Power Law for one single knickpoint:

$$3)\quad v = KA^m S^{n-1}$$

---

[1] $S = {}^{\Delta z}/_{\Delta x}$

where S is the knickpoint's slope, Δz is the elevation difference between the two points that define the surface of the knickpoint and Δx is the distance between these two points.

We combined the Stream Power Law with the average velocity equation. We assume that the knickpoint behaves as a single point in space:

$$4)\quad v = {}^{\Delta L}/_{\Delta t}$$

where velocity (v) is a vector quantity that measures displacement (or change in position, ΔL) over the change in time (Δt).

If we assume that the velocity is the migration rate of the knickpoint, the equations 2, 3 and 4 combined provide useful insight for the dimensional coefficient of denudation K:

$$5)\quad K = \frac{\Delta L}{\Delta t}\frac{1}{A^m S^{n-1}}$$

6.3.5. *Seismic Analysis*

The direct relation of the knickpoints to the active tectonism of the UFS is reflected by the earthquake patterns that occur across the study area. Our earthquake dataset spans a time period of ~35 years, from 09/12/1982 (time 0 on x axis in Fig. 6.6) until 24/02/2017, when the large Mweru Mw 5.7 earthquake occurred (indicated by yellow triangle in Fig. 6.1). All the recorded earthquake data were collected from the ISC-GEM Global Instrumental Earthquake Catalogue (Giacomo et al., 2018) and are presented in Table 6.3.

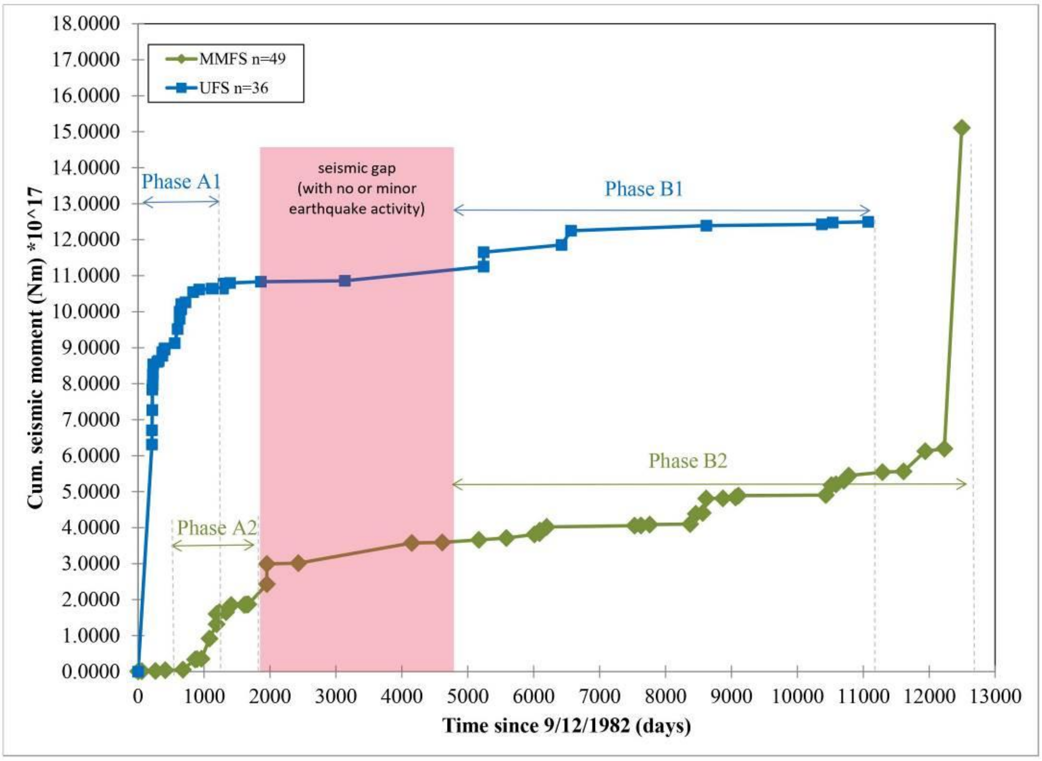

Figure 6.6: Plot illustrates the cumulative seismic moment (Mo) released within the MMFS and the UFS during the last 35 years. All earthquake data is included in Table 6.3.

Table 6.3: Earthquake data base of the Mweru-Mweru Wantipa and Upemba Fault Systems. The data were collected from the ISC-GEM Global Instrumental Earthquake Catalogue. Over a nearly 35 year period (9/12/1982 – 24/02/2017), 85 earthquakes were recorded (49 at MMFS and 36 at UFS).

Magnitude (Mw)	Date recorded	Time (Days since 9/12/1982)	Seismic Moment (10^{17} Nm)	Cumulative Moment (10^{17} Nm)
Mweru-Mweru Wantipa Fault System				
3.9	09/12/1982	0	0.0089	0.0089
3.7	02/02/1983	55	0.0045	0.013
3.8	30/08/1983	264	0.0063	0.020
4.1	27/01/1984	413	0.018	0.037
4.1	21/10/1984	681	0.018	0.055
4.9	23/04/1985	866	0.28	0.34
3.9	20/05/1985	893	0.0089	0.35
4.0	28/07/1985	962	0.013	0.36
5.1	28/11/1985	1085	0.56	0.92
5.0	14/03/1986	1190	0.40	1.3
4.9	14/03/1986	1190	0.28	1.6
4.4	28/04/1986	1236	0.050	1.7
3.4	04/08/1986	1334	0.0016	1.7
4.8	21/10/1986	1412	0.20	1.9

Magnitude (Mw)	Date recorded	Time (Days since 9/12/1982)	Seismic Moment (10^{17} Nm)	Cumulative Moment (10^{17} Nm)
3.6	10/05/1987	1613	0.0032	1.9
3.9	04/06/1987	1638	0.0089	1.9
3.6	28/06/1987	1661	0.0032	1.9
3.5	07/07/1987	1671	0.0022	1.9
5.1	16/04/1988	1955	0.56	2.4
5.1	16/04/1988	1955	0.56	3.0
4.1	05/08/1989	2431	0.018	3.0
5.1	24/04/1994	4153	0.56	3.6
4.1	30/07/1995	4615	0.018	3.6
4.5	04/02/1997	5171	0.071	3.7
4.4	28/03/1998	5588	0.050	3.7
4.6	25/05/1999	6011	0.10	3.8
4.3	11/08/1999	6088	0.035	3.9
4.5	17/08/1999	6095	0.071	3.9
4.6	27/11/1999	6197	0.10	4.0
4.3	24/07/2003	7531	0.035	4.1
3.7	30/10/2003	7629	0.004	4.1
4.2	09/03/2004	7761	0.025	4.1
4.1	11/11/2005	8373	0.018	4.1
4.9	06/02/2006	8460	0.28	4.4
4.2	22/05/2006	8564	0.025	4.4
5.0	13/07/2006	8616	0.40	4.8
3.9	24/03/2007	8871	0.009	4.8
4.2	30/09/2007	9061	0.025	4.8
4.4	15/11/2007	9106	0.050	4.9
4.0	01/07/2011	10431	0.013	4.9
4.9	25/09/2011	10517	0.28	5.2
4.1	04/12/2011	10586	0.018	5.2
4.6	31/03/2012	10704	0.10	5.3
4.7	14/06/2012	10780	0.14	5.5
4.6	07/11/2013	11291	0.10	5.5
4.1	24/09/2014	11612	0.018	5.6
5.1	19/08/2015	11941	0.56	6.1
4.5	03/06/2016	12230	0.071	6.2
5.9	24/02/2017	12495	8.91	15.1
Upemba Fault System				
5.8	07/07/1983	210	6.31	6.3
5	07/07/1983	210	0.40	6.7
5.1	12/07/1983	215	0.56	7.3
5.1	12/07/1983	215	0.56	7.8
4.7	19/07/1983	221	0.14	8.0
4.9	23/07/1983	226	0.28	8.3
4.9	27/07/1983	230	0.28	8.5
4.5	29/09/1983	294	0.071	8.6

Magnitude (Mw)	Date recorded	Time (Days since 9/12/1982)	Seismic Moment (10^{17} Nm)	Cumulative Moment (10^{17} Nm)
4.2	18/10/1983	313	0.025	8.6
4.7	11/12/1983	367	0.14	8.8
4.6	12/12/1983	367	0.10	8.9
4.5	14/01/1984	401	0.071	8.9
4.3	14/01/1984	401	0.035	9.0
4.7	18/06/1984	557	0.14	9.1
5.0	31/07/1984	600	0.40	9.5
4.9	30/08/1984	630	0.28	9.8
4.8	30/08/1984	630	0.20	10.0
4.5	24/09/1984	655	0.071	10.1
4.7	25/09/1984	656	0.14	10.2
4.4	28/11/1984	719	0.050	10.3
4.9	24/03/1985	835	0.28	10.5
4.5	21/06/1985	925	0.071	10.6
4.2	28/12/1985	1114	0.025	10.6
3.4	20/06/1986	1289	0.0016	10.6
4.7	28/06/1986	1297	0.14	10.8
4	07/10/1986	1397	0.013	10.8
4.3	15/01/1988	1862	0.035	10.8
4.2	13/07/1991	3138	0.025	10.9
5.0	15/04/1997	5241	0.40	11.3
5.0	15/04/1997	5241	0.40	11.7
4.8	10/07/2000	6423	0.20	11.9
5.0	02/12/2000	6567	0.40	12.3
4.7	15/07/2006	8619	0.14	12.4
4.3	02/05/2011	10370	0.035	12.4
4.4	15/10/2011	10537	0.050	12.5
4.1	05/04/2013	11075	0.02	12.5

6.4. Results and Discussion

6.4.1. Seismic Analysis

Understanding the seismic activity of the UFS will provide us with clear insights about the tectonic intensity of the fault system and the impact that this activity might have on the Kiubo Waterfalls. Geomorphologic and seismotectonic research in the area has been scarce, despite the fundamental importance of neotectonics, which controls and radically reshapes all landscapes southwest of the Western Branch of the EARS. Our analysis of the seismicity patterns recorded within the MMFS and the UFS during the last 35 years provides indications for earthquake interactions (Fig. 6.6; Table 6.3). Collectively, more than 80 earthquakes ($3.4<Mw<5.9$) were recorded (UFS: n=36, MMFS: n=49). Indeed, their activity appears to be interrelated, with bursts of earthquakes being approximately coeval in the two fault systems.

We can distinguish two main phases (Phases A and B; Fig. 6.6). The UFS started rupturing (Phase A1) and towards the end of its burst the MMFS was activated (Phase A2). Then they both underwent a period of no (or little) seismicity before they both went into a more intense phase (Phase B). Our analyses provide proof of the intense tectonic activity of the UFS, which continues to the present and affects the surrounding landscapes and the evolution of the knickpoints.

6.4.2. Terrestrial Cosmogenic Nuclides

6.4.2.1. ^{21}Ne Results

Ne results are provided in the Appendix (Table A3, 4 and Fig. A1, 2). The calculated ^{21}Ne exposure ages are much higher than the ^{10}Be and ^{26}Al ages. They are based on the total ^{21}Ne excesses of the 400-800°C heating steps and were calculated relative to the ^{21}Ne/^{20}Ne ratio of Ne trapped in fluid inclusions as determined by crushing extractions (Table A4). However, the data in the three-isotope plots and the unusual degassing patterns (highest excesses in the 600 and 800°C steps) suggest the presence of nucleogenic Ne (Fig. A1; Niedermann, 2002). Since there is no indication of a complex exposure scenario in our study area, which could explain higher ^{21}Ne/^{10}Be and ^{21}Ne/^{26}Al ratios, a contribution of nucleogenic ^{21}Ne is the most likely explanation for the apparent age discrepancy. Therefore, the ^{21}Ne results will not be included in our interpretations and discussion. Below we present the ^{10}Be and ^{26}Al results.

6.4.2.2. ^{10}Be and ^{26}Al Results

The low quartz quality of the quartz-rich brownish sandstone samples made the purification process more demanding and time consuming, resulting in a limited amount of pure quartz grains available for the TCN analysis. LUV03, LUF01 and LUF02 samples yielded unrealistically low ^{26}Al concentrations compared to their ^{10}Be concentrations. While it is not quite clear why the ^{26}Al ages are lower than the ^{10}Be ages, we assume that many of the quartz grains were so fine that they fell apart during the acid treatment, which affected the final ^{26}Al age determination. Based on the results of the rest of the samples (Table 6.4), ^{10}Be ages are considered more trustworthy than the ^{26}Al ones.

Samples from the Luvilombo River indicate Be and Al exposure ages from ~10 to ~40 ka (Table 6.4). Specifically, the vertical sample LUV01 yielded a minimum mean age of 10.32±0.73 ka while the top horizontal sample LUV02 yielded an older mean age of 20.14±0.77 ka. Moving downstream, the sample LUV03 yielded a minimum ^{10}Be exposure age of ~30 ka, while the low ^{26}Al exposure age of ~17 ka is due to the technical issues mentioned above (Table 6.4). The ^{10}Be and ^{26}Al minimum ages of the sample LUV04 are in agreement, resulting in a minimum mean exposure age of this surface of 36.0±1.3 ka. The top horizontal sample taken close to LUV03 and LUV04 (i.e. LUV05) yielded a minimum mean age of 39.9±1.0 ka (Table 6.4).

Table 6.4: ^{10}Be and ^{26}Al concentrations and minimum exposure ages (T_{10}, T_{26}) based thereon. Asterisk (*) indicates samples collected from vertical surfaces. "Mean T" indicates the error-weighted mean of the ^{10}Be and ^{26}Al minimum exposure ages. All uncertainties presented are 1σ. They include: measurement uncertainty (statistical), standard uncertainty (certification), reproducibility of standard analyses, carrier uncertainties. Age uncertainties do not include errors of production rates and scaling. AMS labs where analyses were performed: T= NTNU, Trondheim, Norway; A= ASTER, CEREGE, Aix-en-Provence, France; C= University of Cologne, Cologne, Germany. Samples with problematic ^{26}Al results are indicated with *italics*.

Name	^{10}Be (10^6 atoms	T_{10} (ka)	^{10}Be	^{26}Al (10^6 atoms g$^-$	T_{26} (ka)	Mean T	^{26}Al
LUV01*	0.0224±0.0020	10.26±0.91	*T*	0.162±0.020	10.4±1.2	10.32±0.73	*A*
LUV02	0.0817±0.0047	19.0±1.1	*T*	0.654±0.035	21.4±1.1	20.14±0.77	*A*
*LUV03**	0.0637±0.0050	29.8±2.3	*C*	0.261±0.063	16.7±4.0	-	*C*
LUV04*	0.0755±0.0040	33.7±1.8	*T*	0.612±0.031	38.6±1.9	36.0±1.3	*A*
LUV05	0.1788±0.0059	39.7±1.3	*T*	1.284±0.055	40.3±1.7	39.9±1.0	*A*
*LUF01**	0.0700±0.0049	34.9±2.4	*C*	0.184±0.027	12.5±1.8	-	*C*
*LUF02**	0.063±0.011	28.0±5.0	*C*	0.179±0.037	11.4±2.4	-	*C*
LUF04*	0.0510±0.0034	22.4±1.5	*C*	0.364±0.035	23.1±2.2	22.6±1.2	*C*
LUF05	0.2155±0.0091	48.8±2.0	*C*	1.259±0.082	39.7±2.5	45.3±1.6	*C*
LUF06*	0.0168±0.0020	7.51±0.87	*T*	0.101±0.011	6.37±0.67	6.79±0.53	*A*

LUF01 and LUF06 are the two samples that were collected from the Kiubo Waterfalls directly. However, they provided different ages. LUF01 indicates a minimum ^{10}Be age of ~35 ka and a (problematic) ^{26}Al age of ~13 ka. The sample LUF06 yielded the youngest mean age of all samples, which is 6.79±0.53 ka (Table 6.4). The samples from the river banks downstream of the Kiubo Waterfalls show older ages. On the right river bank, the sample LUF02 yielded a ^{10}Be age of ~28 ka, while the ^{26}Al age of ~11 ka is again problematic due to the processing issues mentioned above. On the left bank, the vertical sample LUF04 yielded a mean minimum age of 22.6±1.2 ka, while the top horizontal sample LUF05 has a minimum mean age of 45.3±1.6 ka (Table 6.4).

6.4.3. Stream Power Law and Knickpoint Retreat Rates

Due to the inconsistent minimum exposure ages that the LUF series yielded, we decided to exclude these samples from the process. The significantly young minimum age of LUF06 is probably not related to the real exposure age of the Kiubo Waterfalls, but more likely represents enhanced surface denudation or a rockfall/landslide event caused by the strong flow of the Lufira River. Furthermore, due to technical issues during the chemical processing of the samples LUF01 and LUF02 (see section 6.4.2.2), their ^{26}Al ages are possibly lower than the real exposure ages. The only vertical sample that was collected from the Kiubo Waterfalls and provided robust ^{26}Al results is LUF04, which is excluded as well, as its minimum age is smaller than the minimum ages of the LUV series despite its position further downstream. Due to the fact that the results of the LUF series did not show the expected trend of increasing ages with increasing distance from the knickpoint, we attempted to constrain the K constant for the Luvilombo River by estimating the knickpoint retreat rate of the Luvilombo Waterfalls via equation (4).

Three sampling points along the Luvilombo River as well as the current knickpoint position of the Luvilombo Waterfall (four points in total) were used as reference points to estimate the knickpoint retreat rate using a least squares regression line. In a plot of distance versus age (Fig. 6.7), the retreat rate is given by the inverse slope of the regression line. The current position of the knickpoint was included as the point zero of the equation (origin of the graph). The three samples LUV01, LUV03 and LUV04 were chosen due to their analytical robustness and their direct correlation with the river incision processes as they are samples from the vertical river bank. LUV03 was included in our regression model, despite its young minimum ^{26}Al exposure age. We believe that the minimum ^{10}Be age of LUV03 is trustworthy as it is in agreement with the minimum ages of the rest of the LUV series. All horizontal samples (LUV02 and LUV05) were excluded as their relation to incision processes is indirect at best. The ages of the horizontal samples are consistently older than for the vertical samples. Horizontal surfaces were also affected by the channel incision as the knickpoint was retreating upstream. However, they might have been exposed prior to the knickpoint's arrival on the former shallow valley bottom and thus they would have already accumulated some cosmogenic nuclides, resulting in ages older than the age of the incision process (Table 6.4).

The estimated retreat rate of the Luvilombo Waterfalls is ~0.030 m a^{-1} (Fig. 6.7). Constraining the K value of the Luvilombo Waterfalls allows us to calculate the retreat rate of the Kiubo Waterfalls as well. The K constant of the Luvilombo River (A_{Luv}=3245 km^2) is calculated at 1.57×10^{-6} m^{1-2m} a^{-1} using the Stream Power Law equation (5). In our study we use the values 1 and 0.45 for the positive constants n and m, respectively (Croissant and Braun, 2014). By assuming n=1, the calculation becomes independent of the slope value. Assuming that the K value is constant throughout the same lithology, climate and sediment load, we can use the value estimated for the Luvilombo River and apply it to the Kiubo Waterfalls, using the drainage area of the Lufira River above the Kiubo knickpoint (A_{Luf}=42571 km^2) instead. Like that, the knickpoint retreat rate of the Kiubo Waterfalls is estimated via equation (1) at around 0.096 m a^{-1}. These knickpoint migration rates also reflect the difference of the power between the two drainage systems. The Lufira River yields a faster knickpoint retreat rate than the smaller tributary Luvilombo River.

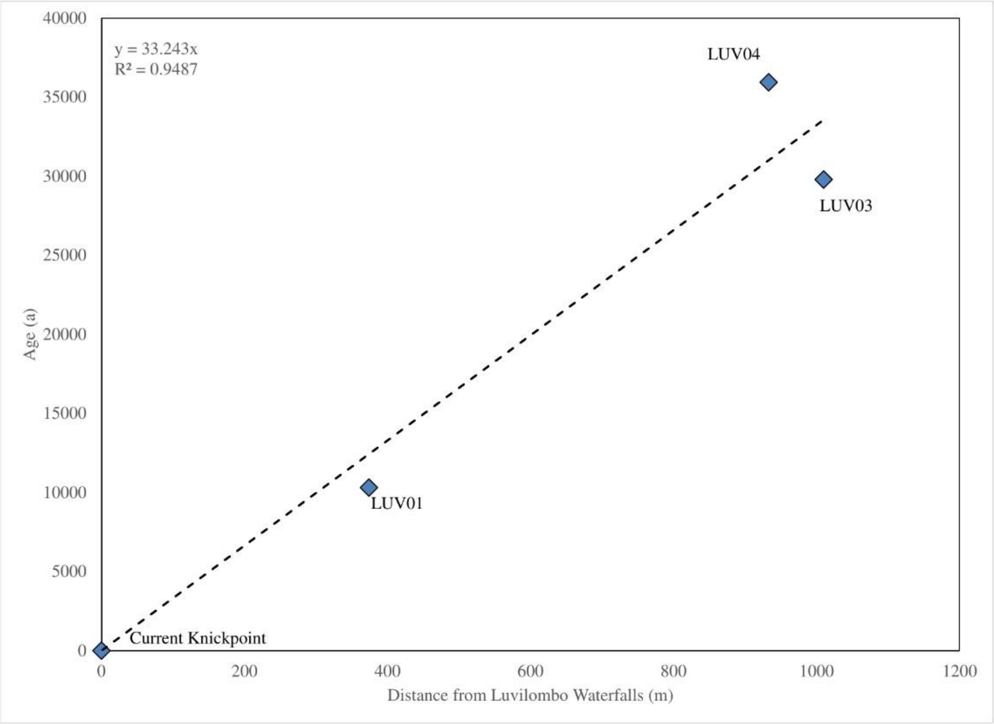

Figure 6.7: Plot illustrating the relation of the distance of the LUV01, LUV03 and LUV04 samples from the Luvilombo Waterfalls to their minimum exposure age. The black dashed line represents the least square regression line, which is forced through the origin (i.e., the current falls at age 0). The inverted slope of the line corresponds to the knickpoint retreat rate.

6.4.4. *Extrapolation of the Knickpoint*

Determining the knickpoint retreat rate of the Kiubo Waterfalls by constraining the K constant provides helpful information about the development of the knickpoint and contributes insights about the evolution and the origin of the waterfalls. Recent DNA sequencing analysis on the fish species of *Nothobranchius* (*N. hassoni*, *N. flagrans*, *N. polli* and *N.brieni*) at the Kiubo Waterfalls reveal that a separation of the fish groups is well constrained at ~3.52 Ma (2.96 – 4.15 Ma; van der Merwe et al., 2021). Assuming that the knickpoint retreat rate has been stable through time and based on the fish separation dates, we can extrapolate the current position of the waterfall back in time and estimate the possible onset location of the knickpoint. In section 6.4.3, the knickpoint retreat rate of the Kiubo Waterfalls was calculated to be around

0.096 m a^{-1}. Three extrapolation models were attempted in relation to the minimum, maximum and mean possible fish separation dates (2.96, 3.52 and 4.15 Ma) in order to investigate the best fitting scenario.

The extrapolation reaches were calculated via equation (4). The first model (2.96 Ma) indicates that the potential formation point of the Kiubo Waterfall was 283 km downstream the current knickpoint. The middle separation date 3.52 Ma yields a distance of about 336 km, while the oldest age yields a 396 km distance from the current knickpoint. It is necessary to mention that our models include uncertainties from the TCN dating method and the Stream Power Law. These uncertainties are difficult to be determined in this study, thus the aforementioned values are just representing potential approximate reaches.

Figure 6.8 depicts the potential locations where the Kiubo Waterfalls were created. Figure 6.8A shows the distance (~213 km) of the Upemba Lake from the current knickpoint. Figure 6.8B indicates the results of the first model. Based on the minimum age of the DNA sequencing analysis, the knickpoint should have been formed 283 km downstream the Kiubo Waterfalls. The possible reach extends beyond the Upemba Depression and terminates in a small wetland area. It is worth mentioning that the termination area is near a fault that is part of the UFS, leaving open a possible relation of the formation of the knickpoint to the tectonic activity of the UFS. In Figure 6.8C (~3.52 Ma), the 336 km reach of the Kiubo Waterfalls extends approximately half the way to the conjunction of the Lualaba and Luvua rivers, and terminates in a wetland environment, not close to any mapped tectonic feature. Figure 6.8D represents the 396 km reach of the waterfalls based on the maximum fish seperation date of 4.15 Ma. This reach extends to the conjunction of the Lualaba and Luvua rivers. In this scenario, the formation of the knickpoint is related to a non-tectonic event, but it reveals its possible correlation with the confluence of these two rivers. However, taking into consideration that the exposure ages which were used to calculate the retreat rate are minimum ages, the retreat rate will be a maximum rate. The combination of a maximum rate with a maximum fish separation age will therefore yield an extreme maximum reach. Since the current landscape between the Luvua-Lualaba confluence and the UFS consists of a series of flat wetland settings with no obvious incised valley and since no large Luvua River may have existed prior to the drainage of paleo-lake Mweru, this knickpoint retreat scenario does not seem very likely.

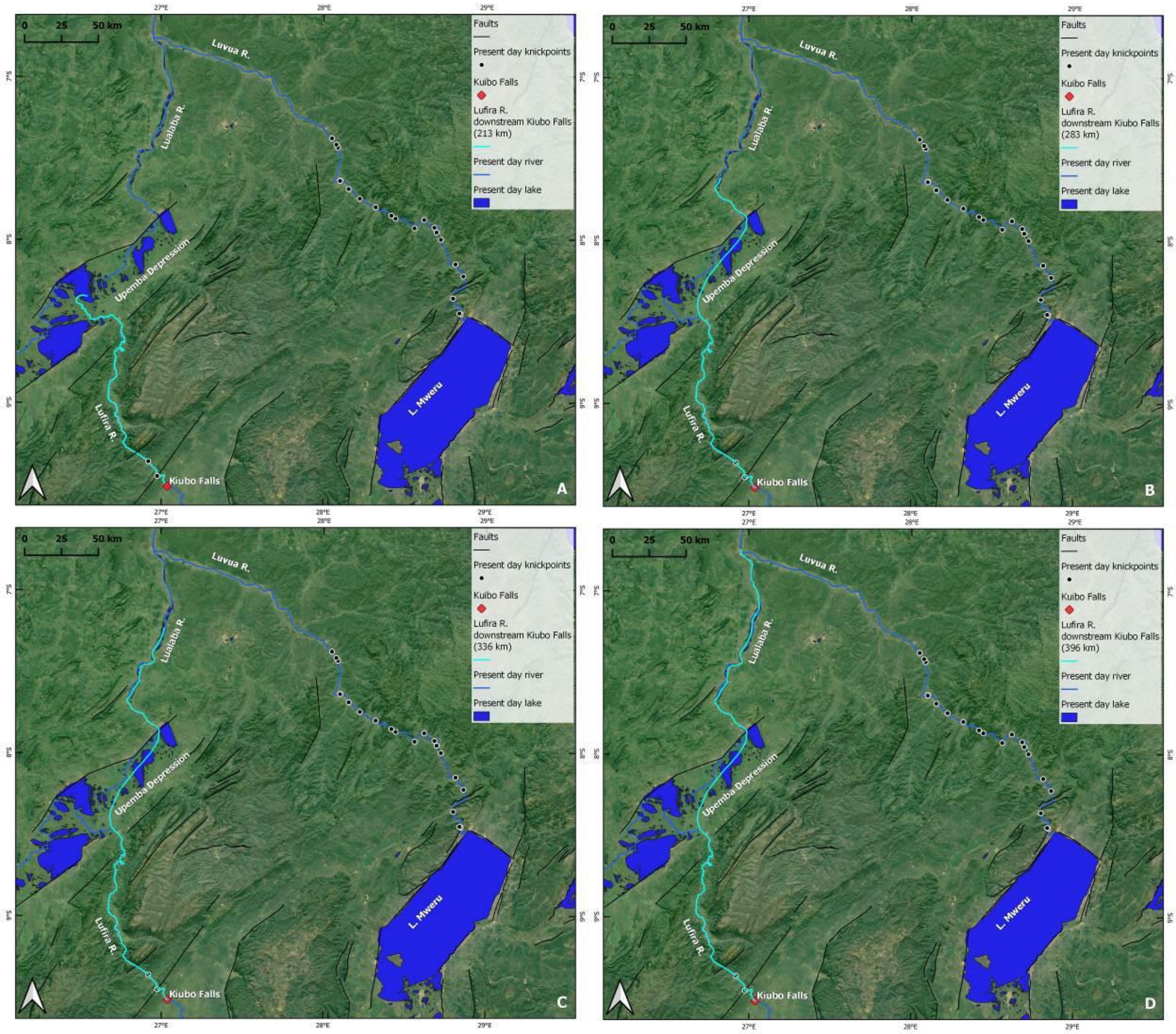

Figure 6.8: Schematic representations of the possible formation locations of the Kiubo Waterfalls. Light blue line indicates the extrapolation path of the knickpoint. Black lines indicate faults, while white circles indicate knickpoints along Luvua River. The red rhombus indicates the Kiubo Waterfalls. A) Present day reach of the Lufira River (213 km) below Kiubo Waterfalls; B) Calculated 283 km reach of the Lufira River at 2.96 Ma; C) Calculated 336 km reach of the Lufira River at 3.52 Ma; D) Calculated 396 km reach of the Lufira River at 4.15 Ma.

Based on the present day understanding of this part of the African landscape, the most likely model is the first one (283 km; Fig. 6.8B), due to the profound connection of knickpoint formation to a major local geological feature, which is the tectonic activity of the UFS during the late Pliocene. Due to the nature of the waterfalls, the lithology across the Lufira River, which determines the shape and geometry of the knickpoint, and the upstream knickpoint retreat, the fish groups above and below have remained separated, with no known occurrences of *N. brieni* upstream of Kiubo Waterfalls (van der Merwe et al., 2021). The study area reveals a highly complex landscape which has been strongly affected by active tectonics and intense denudation. Detailed geological and fish sampling will be necessary in order to investigate thoroughly all scenarios presented here and the possible correlation of the Kiubo Waterfalls to a major geologic event during the Pliocene.

6.5. *Conclusions*

Terrestrial cosmogenic nuclide dating can provide a fundamental aid to the geomorphological issue of constraining the K constant of the Stream Power Law. There is an ongoing debate about the exact value of K that should be applied in different locations/landscapes, while many researchers have tried to model the connection between the bedrock geology, the climate and the K constant. However, determining this value via terrestrial cosmogenic nuclide dating has never been attempted before.

In this study we managed to constrain the K constant of the Stream Power Law by using the terrestrial cosmogenic nuclide dating method at the Luvilombo Waterfalls, DRC. This knickpoint yields a K constant value of $1.57\times10^{-6}\ m^{1-2m}\ a^{-1}$ ($m=0.45$). Using this K constant, we were able to calculate the knickpoint retreat rate of the Kiubo Waterfalls at 0.096 $m\ a^{-1}$. Assuming that the knickpoint migration rate is stable through time and by combining terrestrial cosmogenic nuclide dating with the Stream Power Law and the DNA sequencing from fish populations, we managed to present possible extrapolation models and estimate the location of the onset of the Kiubo Waterfalls, revealing a possible connection of the knickpoint to the tectonic activity of the Upemba Fault System.

Even if our case study is simplistic and is based on several assumptions and uncertainties, the results are interesting as we believe them to be the first age constraint for the K constant in the region. We thus provide insight about the development of the Lufira River through the knickpoint evolution of the Kiubo and Luvilombo Waterfalls, and introduce intriguing concepts for future research.

Chapter 7

Conclusions and Outlook

7. Conclusions and Outlook

Lake Mweru, located between the Northern Province of Zambia and the south-eastern Katanga Province of the Democratic Republic of Congo, is part of the southwest extension of the East African Rift System (EARS). In this study we described the existence of a greater paleo-lake Mweru during the Pleistocene. Terrestrial cosmogenic nuclide dating of samples around the current Lake Mweru supports the phylogenetic molecular clock analyses of fish that also constrain the formation of the paleo-lake at the early Pleistocene. Elevational analyses of the dated knickpoints constrain the level of the paleo-lake to around 1200 m asl and its area to around 40000 km^2. Water level fluctuations were recorded by ^{10}Be and ^{26}Al, caused by intense climate variations documented across southeastern Africa. Calculated high denudation rates (up to ~40 mm ka^{-1}) along the eastern Kundelungu Plateau suggest that active rifting along the Mweru-Mweru Wantipa Fault System contributed to the gradual drainage of the paleo-lake. The shrinkage of the paleo-lake is placed around 0.36 Ma. Further research is needed to investigate in depth and constrain with more accuracy the extent of the paleo-lake and determine its borders. More dense and targeted sampling around the potential borders of the paleo-lake, which our study suggests, is essential for tackling this issue. In addition, two exceptionally old minimum ^{10}Be and ^{26}Al exposure ages (524 and 833 ka) were obtained from two waterfalls that are located south of the Mweru-Mweru Wantipa Fault System, possibly reflecting the actual exposure ages of these knickpoints and attesting to low denudation rates on the Mporokoso Plateau.

Our tectonomorphic analyses show the relation of the paleo-lake Mweru with the tectonic activity of the Mweru-Mweru Wantipa Fault System during the Pleistocene. We present the first detailed tectonic map of the fault system. The analysis reveals a NW-SE rotation of the extension field of the EARS as the main mechanism of the Mweru-Mweru Wantipa Fault System formation. The majority of the faults are characterized by medium length and displacement, creating pull-apart valleys and horst-graben structures. Tectonic and geomorphic analyses confirm the existence of the large paleo-lake Mweru, which was revealed by terrestrial cosmogenic nuclide dating. The onset of the rift system is constrained around 2.6 Ma, which is also consistent with the timing of the paleo-lake. Hypsometric analysis supports the terrestrial cosmogenic nuclide dating results, constraining its paleo-shorelines at ~1180 m. Landscape reconstruction via subtraction of the measured throws of the identified major faults across the fault system was used to analyze the tectonomorphic conditions during the rifting commencement. The normal faulting and the associated uplift at the northwestern paleo-lake boundary indeed contributed to the gradual decrease of the lake level until eventually the lake reached its current level at ~0.35 Ma. Further field work will be necessary to explore in depth the tectonic characteristics of the Mweru-Mweru Wantipa Fault System. Moreover, river profiles of the main streams that feed Lake Mweru are important to recognize the types of knickpoints and their connection to the bedrock geology, active rifting, climatic variations and the change of the base level, in order to thoroughly investigate the drainage evolution of the study area in relation to the evolution of the paleo-lake Mweru.

Last but not least, we studied the evolution of the Kiubo Waterfalls, which are located in the southern Katanga Province of the Democratic Republic of Congo. Through terrestrial cosmogenic nuclide dating we attempted to constrain the K constant of the main knickpoint evolution model of the Stream Power Law. Even though many researchers have tried to model the connection between bedrock geology, climate and K constant, an optimization of the value via terrestrial cosmogenic nuclide dating has never been attempted before. In this study we managed to constrain the K constant at $\sim 1.57 \times 10^{-6}\ m^{1-2m}\ a^{-1}$ ($m=0.45$). Our simplistic approach was based on the assumption that the knickpoint migration rate was stable through time and the K constant is stable throughout the same lithology, climate and sediment load. Combining terrestrial cosmogenic nuclide dating with the Stream Power Law and the DNA sequencing from fish populations of the Lufira River, we managed to extrapolate and predict the formation of the Kiubo Waterfalls, which potentially occurred near the Upemba Fault System during the Pliocene. Further dense and targeted sampling around Kiubo Waterfalls will be necessary to gather more terrestrial cosmogenic nuclide data in order to verify our preliminary results and investigate the behavior of the knickpoint since its onset.

Acknowledgements

This study is part of the interdisciplinary project “Exploiting the Genomic Record of Living Biota to Reconstruct the Landscape Evolution of South Central Africa” funded by the Volkswagen Foundation (VolkswagenStiftung). This project would not have been successful without the contribution of several people from different institutes.

From GFZ Potsdam, I would like to thank first and foremost my advisor Samuel Niedermann for all the scientific support and mentoring. His guidance in all the TCN analyses, the fieldwork and sampling, the discussion of the results and in general his contribution in every step of our research was vital. Prof. Jörg Erzinger is also acknowledged for his help and supervision during my research. A great thank you to Vasiliki Mouslopoulou, whom I would count as an unofficial supervisor, for guiding me through all the tectonic and seismologic part of this research. Her mentoring was of significant importance on a scientific as well as on a personal level. I would also like to thank Enzio Schnabel, Heike Rothe, Sabine Tonn, Hertmut Liep, Johannes Glodny and Hella Wittmann for their help and assistance with laboratory processes and analyses.

From the University of Potsdam, I would like to thank Bodo Bookhagen for his help with all the Be and Al analyses, the discussion of the results and in general his great support thoughout my journey. Daniel Gorzawski, Antje Musiol, Julia Artel and Konstanze Stübner are thanked for their help and assistance with laboratory processes and analyses too. Special thanks to Milena Wöller and Anna Rosner for lab assistance, moral support and all the fun we had during my time at the University of Potsdam.

Parts of this research were carried out at the Ion Beam Centre (IBC) at the Helmholtz-Zentrum Dresden-Rossendorf e.V., a member of the Helmholtz Association. I am grateful for all the help I received from my third advisor Silke Merchel. Her insight in the chemistry lab was a school for me on so many levels. Furthermore, I thank Sabrina Beutner for the ICP-MS measurements and the DREAMS operator team, specifically Georg Rugel, Andy Gärtner and Andreas Scharf for their assistance with the AMS measurements.

The ASTER team (Régis Braucher, Georges Aumaître, Didier Bourlès and Karim Keddadouche) at at CEREGE, Aix-en-Provence, France and the National Laboratory for Age Determination team (Marie-Josée Nadeau and Martin Seiler) at NTNU University Museum, Trondheim, Norway are acknowledged for assistance with AMS measurements during the time that the AMS at Helmholtz-Zentrum Dresden-Rossendorf was not operational.

I am also grateful to all the colleagues of our project: To Tryel Flugel for all the assistance with the geomorphological part of the study and for all the long scientific, philosophical and personal discussions. Without his support and help, this thesis would not have been possible. In addition, I would like to thank Fenton ‘Woody’ Cotterill for his insight on the geomorphology, DNA sequencing information and in general for supervising the entire project. I thank Frederic ‘Fredi’ Schedel for his moral support and discussion about the fish results. I sincerely thank Christian Mwabanua Mutabi, Bauchet Manda, Boniface, George and Kelvin for their enthusiastic assistance in the field.

Finally, I would like to thank my family and friends who have always been there for me, especially my mother and brother for encouraging and supporting me throughout the whole process. A big thank you also to my good friends Stamatis Flemetakis, Voula Ioannidi and Anna Malci who supported me emotionally and scientifically too.

References

Abraham, D. (1959). The stratigraphical and structural relationship of the Kundelungu System, Plateau Series and basement rocks in the Mid-Luapula valley, Northern Rhodesia. D. Phil. Thesis, Univ. Leeds, 152 pp.

Akhmadaliev, S., Heller, R., Hanf, D., Rugel, G. and Merchel, S. (2013). The new 6 MV AMS-facility DREAMS at Dresden. Nuclear Instruments and Methods in Physics Research Section B: Beam Interactions with Materials and Atoms, 294, 5-10. https://doi.org/10.1016/j.nimb.2012.01.053

Alexandrowicz, Z. (1994). Geologically controlled waterfall types in the outer Carpathians. Geomorphology 9, 155–165.

Arnold, M., Merchel, S., Bourlès, D. L., Braucher, R., Benedetti, L., Finkel, R. C., Aumaître, G., Gottdang, A. and Klein, M. (2010). The French accelerator mass spectrometry facility ASTER: improved performance and developments. Nuclear Instruments and Methods in Physics Research Section B: Beam Interactions with Materials and Atoms, 268(11-12), 1954-1959. https://doi.org/10.1016/j.nimb.2010.02.107

Bailey, W. R., Walsh, J. J. and Manzocchi, T. (2005). Fault populations, strain distribution and basement fault reactivation in the East Pennines Coalfield, UK. Journal of Structural Geology, 27(5), 913-928. https://doi.org/10.1016/j.jsg.2004.10.014

Bakker, E. M. V. Z. and Mercer, J. H. (1986). Major late Cainozoic climatic events and palaeoenvironmental changes in Africa viewed in a worldwide context. Palaeogeography, Palaeoclimatology, Palaeoecology, 56(3-4), 217-235. https://doi.org/10.1016/0031-0182(86)90095-7

Balco, G. and Shuster, D. L. (2009). Production rate of cosmogenic ^{21}Ne in quartz estimated from ^{10}Be, ^{26}Al, and ^{21}Ne concentrations in slowly eroding Antarctic bedrock surfaces. Earth and Planetary Science Letters, 281(1-2), 48-58. https://doi.org/10.1016/j.epsl.2009.02.006

Ballard, S. and Pollack, H. N. (1988). Modern and ancient geotherms beneath southern Africa. Earth and Planetary Science Letters, 88(1-2), 132-142. https://doi.org/10.1016/0012-821X(88)90052-0

Batumike, M. J., Belousova, E., Griffin, W. L., Lubala, T. R., Chabu, M., Kaseti, P. K., Djuma, B. A. and Ferrière, L. (2019). Petrography and perovskite U-Pb age of the Katuba kimberlite, Kundelungu Plateau (DR Congo): Implications for regional tectonism and mineralisation. Journal of African Earth Sciences, 156, 35-43. https://doi.org/10.1016/j.jafrearsci.2019.04.014

Batumike, M. J., Cailteux, J. L. H. and Kampunzu, A. B. (2007). Lithostratigraphy, basin development, base metal deposits, and regional correlations of the Neoproterozoic Nguba and Kundelungu rock successions, central African Copperbelt. Gondwana Research, 11(3), 432-447. https://doi.org/10.1016/j.gr.2006.04.012

Begg, J. G. and Mouslopoulou, V. (2010). Analysis of late Holocene faulting within an active rift using lidar, Taupo Rift, New Zealand. Journal of Volcanology and Geothermal Research, 190(1-2), 152-167. https://doi.org/10.1016/j.jvolgeores.2009.06.001

Berlin, M. M. and Anderson, R. S. (2007). Modeling of knickpoint retreat on the Roan Plateau, western Colorado. Journal of Geophysical Research: Earth Surface, 112(F3). https://doi.org/10.1029/2006JF000553

Bierman, P. R., Marsella, K. A., Patterson, C., Davis, P. T. and Caffee, M. (1999). Mid-Pleistocene cosmogenic minimum-age limits for pre-Wisconsinan glacial surfaces in southwestern Minnesota and southern Baffin Island: a multiple nuclide approach. Geomorphology, 27(1-2), 25-39. https://doi.org/10.1016/S0169-555X(98)00088-9

Bilham, R. and Bodin, P. (1992). Fault zone connectivity: Slip rates on faults in the San Francisco Bay area, California. Science, 258(5080), 281-284. https://doi.org/10.1126/science.258.5080.281

Bishop, P. and Goldrick, G. (1992). Morphology, processes and evolution of two waterfalls near Cowra, New South Wales. The Australian Geographer, 23(2), 116-121. https://doi.org/10.1080/00049189208703061

Bishop, P., Hoey, T. B., Jansen, J. D. and Artza, I. L. (2005). Knickpoint recession rate and catchment area: the case of uplifted rivers in Eastern Scotland. Earth Surface Processes and Landforms, 30(6), 767-778. https://doi.org/10.1002/esp.1191

Borchers, B., Marrero, S., Balco, G., Caffee, M., Goehring, B., Lifton, N., Nishiizumi, K., Phillips, F., Schaefer, J. and Stone, J. (2016). Geological calibration of spallation production rates in the CRONUS-Earth project. Quaternary Geochronology, 31, 188-198. https://doi.org/10.1016/j.quageo.2015.01.009

Bos, A. R., Kapasa, C. K. and van Zwieten, P. A. (2006). Update on the bathymetry of Lake Mweru (Zambia), with notes on water level fluctuations. African Journal of Aquatic Science, 31(1), 145-150. https://doi.org/10.2989/16085910609503882

Bos, A. R., van Zwieten, P. A. M. and Ngula, E. S. (1995). A limnological survey on Lake Mweru, Zambia. DoF/ML/Report No. 27, Department of Fisheries, Nchelenge, Zambia, 90 pp.

Braile, L. W., Keller, G. R., Wendlandt, R. F., Morgan, P. and Khan, M. A. (2006). The East African rift system. In Developments in Geotectonics (Elsevier), Vol. 25, 213-III. https://doi.org/10.1016/S0419-0254(06)80013-3

Brocklehurst, S. H. (2010). Tectonics and geomorphology. Progress in Physical Geography, 34(3), 357-383. https://doi.org/10.1177/0309133309360632

Brown, E. T., Edmond, J. M., Raisbeck, G. M., Yiou, F., Kurz, M. D. and Brook, E. J. (1991). Examination of surface exposure ages of Antarctic moraines using in situ produced ^{10}Be and ^{26}Al. Geochimica et Cosmochimica Acta, 55(8), 2269-2283. https://doi.org/10.1016/0016-7037(91)90103-C

Burbank, D. W. and Anderson, R. S. (2013). Tectonic geomorphology, Second Edition. Environmental and Engineering Geoscience, 19(2), 198–200. https://doi.org/10.2113/gseegeosci.19.2.198

Burbank, D., Meigs, A. and Brozović, N. (1996). Interactions of growing folds and coeval depositional systems. Basin Research, 8(3), 199-223. https://doi.org/10.1046/j.1365-2117.1996.00181.x

Burridge, C. P., Craw, D. and Waters, J. M. (2006). River capture, range expansion, and cladogenesis: the genetic signature of freshwater vicariance. Evolution, 60(5), 1038-1049. https://doi.org/10.1111/j.0014-3820.2006.tb01181.x

Burrough, S. L. and Thomas, D. S. G. (2008). Late Quaternary lake-level fluctuations in the Mababe Depression: Middle Kalahari palaeolakes and the role of Zambezi inflows. Quaternary Research, 69(3), 388-403. https://doi.org/10.1016/j.yqres.2008.02.003

Cahen, L., Snelling, N. G., Delhal, G. and Vail, J. R. (1984). The Geochronology and Evolution of Africa. Clarendon Press, Oxford. 512 pp.

Cailteux, J. L., Muchez, P., De Cuyper, J., Dewaele, S. and De Putter, T. (2018). Origin of the megabreccias in the Katanga Copperbelt (DR Congo). Journal of African Earth Sciences, 140, 76-93. https://doi.org/10.1016/j.jafrearsci.2017.12.029

Calais, E., Ebinger, C., Hartnady, C. and Nocquet, J. M. (2006). Kinematics of the East African Rift from GPS and earthquake slip vector data. Geological Society, London, Special Publications, 259(1), 9-22. https://doi.org/10.1144/GSL.SP.2006.259.01.03

Camelbeeck, T. and Iranga, M. D. (1996). Deep crustal earthquakes and active faults along the Rukwa trough, eastern Africa. Geophysical Journal International, 124(2), 612-630. https://doi.org/10.1111/j.1365-246X.1996.tb07040.x

Capart, A. (1949). Sondages et carte bathymétrique. Exploration hydrobiologique du Lac Tanganyika, v.2 (2), 681. Institut Royal des Sciences Naturelles de Belgique, Brussels.

Cerling, T. E. and Craig, H. (1994). Geomorphology and in-situ cosmogenic isotopes. Annual Review of Earth and Planetary Sciences, 22(1), 273-317. https://doi.org/10.1146/annurev.ea.22.050194.001421

Chakrabarti, R., Basu, A. R., Santo, A. P., Tedesco, D. and Vaselli, O. (2009). Isotopic and geochemical evidence for a heterogeneous mantle plume origin of the Virunga volcanics, Western rift, East African Rift system. Chemical Geology, 259(3-4), 273-289. https://doi.org/10.1016/j.chemgeo.2008.11.010

Chorowicz, J. (1989). Transfer and transform fault zones in continental rifts: examples in the Afro-Arabian rift system. Implications of crust breaking. Journal of African Earth Sciences (and the Middle East), 8(2-4), 203-214. https://doi.org/10.1016/S0899-5362(89)80025-9

Chorowicz, J. (2005). The East African rift system. Journal of African Earth Sciences, 43(1-3), 379-410. https://doi.org/10.1016/j.jafrearsci.2005.07.019

Cohen, A. S., Lezzar, K. E., Tiercelin, J. J. and Soreghan, M. (1997). New palaeogeographic and lake-level reconstructions of Lake Tanganyika: implications for tectonic, climatic and biological evolution in a rift lake. Basin Research, 9(2), 107-132. https://doi.org/10.1046/j.1365-2117.1997.00038.x

Cohen, A.S., Gergurich, E.L., Kraemer, B.M., McGlue, M.M., McIntyre, P.B., Russell, J.M., Simmons, J.D. and Swarzenski, P.W. (2016). Climate warming reduces fish production and benthic habitat in Lake Tanganyika, one of the most biodiverse freshwater ecosystems. Proceedings of the National Academy of Sciences, 113(34), 9563-9568. https://doi.org/10.1073/pnas.1603237113

Cornet, J. (1912). Tremblements de terre au Congo. Annales de la Société géologique de Belgique.

Cotterill, F. P. (2006). The Evolutionary History and Taxonomy of the Kobus leche species complex of south-central Africa in the context of Palaeo-Drainage Dynamics (Doctoral dissertation, Stellenbosch: Stellenbosch University).

Cotterill, F. P. D. (2004). Drainage evolution in south-central Africa and vicariant speciation in swamp-dwelling weaver birds and swamp flycatchers. The Honeyguide, 25(1), 7-25.

Cotterill, F. P. D. (2005). The Upemba lechwe, *Kobus anselli*: an antelope new to science emphasizes the conservation importance of Katanga, Democratic Republic of Congo. Journal of Zoology, 265(2), 113-132. https://doi.org/10.1017/S0952836904006193

Cotterill, F. P. D. and de Wit, M. J. (2011). Geoecodynamics and the Kalahari epeirogeny: linking its genomic record, tree of life and palimpsest into a unified narrative of landscape evolution. South African Journal of Geology, 114(3-4), 489-514. https://doi.org/10.2113/gssajg.114.3-4.489

Cowie, P. A. and Scholz, C. H. (1992). Displacement-length scaling relationship for faults: data synthesis and discussion. Journal of Structural Geology, 14(10), 1149-1156. https://doi.org/10.1016/0191-8141(92)90066-6

Cox, K. G. (1989). The role of mantle plumes in the development of continental drainage patterns. Nature, 342(6252), 873-877. https://doi.org/10.1038/342873a0

Craig, A. J., Hasson, M., Jordaens, K., Breman, F. C. and Louette, M. (2011). Range extension of the Lufira Masked Weaver Ploceus ruweti, endemic to Katanga province, Democratic Republic of Congo. Ostrich, 82(1), 77-78. https://doi.org/10.2989/00306525.2010.523018

Croissant, T. and Braun, J. (2014). Constraining the stream power law: a novel approach combining a landscape evolution model and an inversion method. Earth Surface Dynamics, 2(1), 155-166. https://doi.org/10.5194/esurf-2-155-2014

Crosby, B. T. and Whipple, K. X. (2006). Knickpoint initiation and distribution within fluvial networks: 236 waterfalls in the Waipaoa River, North Island, New Zealand. Geomorphology, 82(1-2), 16-38. https://doi.org/10.1016/j.geomorph.2005.08.023

Daly, M. C., Chorowicz, J. and Fairhead, J. D. (1989). Rift basin evolution in Africa: the influence of reactivated steep basement shear zones. Geological Society, London, Special Publications, 44(1), 309-334. https://doi.org/10.1144/GSL.SP.1989.044.01.17

Daly, M. C., Green, P., Watts, A. B., Davies, O., Chibesakunda, F. and Walker, R. (2020). Tectonics and Landscape of the Central African Plateau and their Implications for a Propagating Southwestern Rift in Africa. Geochemistry, Geophysics, Geosystems, 21(6), e2019GC008746. https://doi.org/10.1029/2019GC008746

Danley, P. D., Husemann, M., Ding, B., DiPietro, L. M., Beverly, E. J. and Peppe, D. J. (2012). The impact of the geologic history and paleoclimate on the diversification of East African cichlids. International Journal of Evolutionary Biology, 2012, Article ID 574851. https://doi.org/10.1155/2012/574851

Darvill, C. M. (2013). Cosmogenic nuclide analysis. Chapter 4 in Geomorphological Techniques. British Society for Geomorphology, London, UK, 364-388.

Davis, M., Matmon, A., Placzek, C. J., McIntosh, W., Rood, D. H. and Quade, J. (2014). Cosmogenic nuclides in buried sediments from the hyperarid Atacama Desert, Chile. Quaternary Geochronology, 19, 117-126. https://doi.org/10.1016/j.quageo.2013.06.006

De Clercq, S., Chew, D., O'Sullivan, G., De Grave, J. and Dewaele, S. (2021). Characterisation and geodynamic setting of the 1 Ga granitoids of the Karagwe-Ankole belt (KAB), Rwanda. Precambrian Research, 10-13.
https://doi.org/10.1016/j.precamres.2021.106124

De Magnée, I. and François, A. (1988). The origin of the Kipushi (Cu, Zn, Pb) deposit in direct relation with a Proterozoic salt diapir. Copperbelt of Central Africa, Shaba, Republic of Zaire. In Base metal sulfide deposits in sedimentary and volcanic environments, 74-93.

De Magnée, I. and François, A. (1988). The origin of the Kipushi (Cu, Zn, Pb) deposit in direct relation with a Proterozoic salt diapir. Copperbelt of Central Africa, Shaba, Republic of Zaire. In Base metal sulfide deposits in sedimentary and volcanic environments. 74-93. Springer, Berlin, Heidelberg.

De Waele, B. and Fitzsimons, I. C. W. (2007). The nature and timing of Palaeoproterozoic sedimentation at the southeastern margin of the Congo Craton; zircon U–Pb geochronology of plutonic, volcanic and clastic units in northern Zambia. Precambrian Research, 159(1-2), 95-116. https://doi.org/10.1016/j.precamres.2007.06.004

De Waele, B., Fitzsimons, I. C. W., Wingate, M. T. D., Tembo, F., Mapani, B. and Belousova, E. A. (2009). The geochronological framework of the Irumide Belt: a prolonged crustal history along the margin of the Bangweulu Craton. American Journal of Science, 309(2), 132-187. https://doi.org/10.2475/02.2009.03

Decrée, S., Deloule, É., Ruffet, G., Dewaele, S., Mees, F., Marignac, C., Yans, J. and De Putter, T. (2010). Geodynamic and climate controls in the formation of Mio–Pliocene world-class oxidized cobalt and manganese ores in the Katanga province, DR Congo. Mineralium Deposita, 45, 621-629. https://doi.org/10.1007/s00126-010-0305-8

Deffontaines, B. and Chorowicz, J. (1991). Principles of drainage basin analysis from multisource data: application to the structural analysis of the Zaire Basin. Tectonophysics, 194(3), 237-263. https://doi.org/10.1016/0040-1951(91)90263-R

Dehandschutter, J. and Lavreau, J. (1985). Lineaments and extensional tectonics: examples from Shaba (Zaire) and NE Zambia. Bulletin de la Société Belge de Géologie, 94, 209-221.

Dehnert, A. and Schlüchter, C. (2008). Sediment burial dating using terrestrial cosmogenic nuclides. E&G Quaternary Science Journal, 57(1/2), 210-225. https://doi.org/10.3285/eg.57.1-2.8

Delvaux, D. (1991). The Karoo to Recent rifting in the western branch of the East-African Rift System: A bibliographical synthesis. Mus. Roy. Afr. Centr., Tervuren (Belg.), Dépt. Géol. Min., Rapp. ann. 1989–1990, 63–83.

Delvaux, D. and Barth, A. (2010). African stress pattern from formal inversion of focal mechanism data. Tectonophysics, 482(1-4), 105-128. https://doi.org/10.1016/j.tecto.2009.05.009

Delvaux, D., Levi, K., Kajara, R. and Sarota, J. (1992). Cenozoic paleostress and kinematic evolution of the Rukwa-North Malawi rift valley (East African rift system). Bulletin des Centres de Recherche Exploration-Production Elf-Aquitaine, 16(2), 383-406.

Delvaux, T., Buekens, P., Godin, I. and Boutsen, M. (2001). Barriers to prenatal care in Europe. American journal of preventive medicine, 21(1), 52-59.

Demissie, G. (2010). Mantle Influence, Rifting and Magmatism in the East African Rift System (EARS): A Regional View of the Controls on Hydrothermal Activity. In Proceedings World Geothermal Congress, Bali, Indonesia, 25-29.

Desilets, D. and Zreda, M. (2003). Spatial and temporal distribution of secondary cosmic-ray nucleon intensities and applications to in situ cosmogenic dating. Earth and Planetary Science Letters, 206(1-2), 21-42. https://doi.org/10.1016/S0012-821X(02)01088-9

Desilets, D., Zreda, M. and Prabu, T. (2006). Extended scaling factors for in situ cosmogenic nuclides: new measurements at low latitude. Earth and Planetary Science Letters, 246(3-4), 265-276. https://doi.org/10.1016/j.epsl.2006.03.051

Dewaele, S., Hulsbosch, N., Cryns, Y., Boyce, A., Burgess, R. and Muchez, P. (2016). Geological setting and timing of the world-class Sn, Nb–Ta and Li mineralization of Manono-Kitotolo (Katanga, Democratic Republic of Congo). Ore Geology Reviews, 72, 373-390.

Dingle, R. V. and Hendry, Q. B. (1984). Late Mesozoic and Tertiary sediment supply to the eastern Cape Basin (SE Atlantic) and palaeo-drainage systems in southwestern Africa. Marine Geology, 56(1-4), 13-26. https://doi.org/10.1016/0025-3227(84)90003-3

Dixey, F. (1944). The geomorphology of northern Rhodesia. South African Journal of Geology, 47 (Transactions 1944), 9-45.

Dixey, F. (1946). Erosion and tectonics in the East African rift system. Quarterly Journal of the Geological Society, 102(1-4), 339-388. https://doi.org/10.1144/GSL.JGS.1946.102.01-04.16

Dorsey, R. J., O'Connell, B., McDougall, K. and Homan, M. B. (2018). Punctuated sediment discharge during early Pliocene birth of the Colorado River: Evidence from regional stratigraphy, sedimentology, and paleontology. Sedimentary Geology, 363, 1-33. https://doi.org/10.1016/j.sedgeo.2017.09.018

Dumont, P. and Hanon, M. (1997). Le Plateau des Kundelungu, paléograben ou aulacogène? In: Gisements stratiformes de cuivre et minéralisations associées, 51-69. International Cornet Symposium, 1997.

Dunai, T. J. (2001). Influence of secular variation of the geomagnetic field on production rates of in situ produced cosmogenic nuclides. Earth and Planetary Science Letters, 193(1-2), 197-212. https://doi.org/10.1016/S0012-821X(01)00503-9

Dunai, T. J. (2010). Cosmogenic Nuclides: Principles, concepts and applications in the Earth surface sciences. Cambridge University Press.

Dunai, T. J. and Wijbrans, J. R. (2000). Long-term cosmogenic ^{3}He production rates (152 ka–1.35 Ma) from ^{40}Ar/^{39}Ar dated basalt flows at 29ºN latitude. Earth and Planetary Science Letters, 176(1), 147-156. https://doi.org/10.1016/S0012-821X(99)00308-8

Dunne, J., Elmore, D. and Muzikar, P. (1999). Scaling factors for the rates of production of cosmogenic nuclides for geometric shielding and attenuation at depth on sloped surfaces. Geomorphology, 27, 3-11. https://doi.org/10.1016/S0169-555X(98)00086-5

Ebinger, C. J. (1989). Tectonic development of the western branch of the East African rift system. Geological Society of America Bulletin, 101(7), 885-903. https://doi.org/10.1130/0016-7606(1989)101<0885:TDOTWB>2.3.CO;2

Ebinger, C. J. and Sleep, N. H. (1998). Cenozoic magmatism throughout east Africa resulting from impact of a single plume. Nature, 395(6704), 788-791. https://doi.org/10.1038/27417

Egger, B., Klaefiger, Y., Indermaur, A., Koblmüller, S., Theis, A., Egger, S., Näf, T., Van Steenberge, M., Sturmbauer, C., Katongo, C. and Salzburger, W. (2015). Phylogeographic and phenotypic assessment of a basal haplochromine cichlid fish from Lake Chila, Zambia. Hydrobiologia, 748(1), 171-184.

Ewiak, O., Victor, P. and Oncken, O. (2015). Investigating multiple fault rupture at the Salar del Carmen segment of the Atacama Fault System (northern Chile): Fault scarp morphology and knickpoint analysis. Tectonics, 34(2), 187-212.

Fairhead, J. D. and Girdler, R. W. (1972). The seismicity of the East African rift system. Tectonophysics, 15(1-2), 115-122. https://doi.org/10.1016/0040-1951(72)90056-X

Fenton, C. R., Niedermann, S., Dunai, T. and Binnie, S. A. (2019). The SPICE project: Production rates of cosmogenic ^{21}Ne, ^{10}Be, and ^{14}C in quartz from the 72 ka SP basalt flow, Arizona, USA. Quaternary Geochronology, 54, 101019. https://doi.org/10.1016/j.quageo.2019.101019

Fernandes, R. M. S., Ambrosius, B. A. C., Noomen, R., Bastos, L., Combrinck, L., Miranda, J. M. and Spakman, W. (2004). Angular velocities of Nubia and Somalia from continuous GPS data: implications on present-day relative kinematics. Earth and Planetary Science Letters, 222(1), 197-208. https://doi.org/10.1016/j.epsl.2004.02.008

Fernandez-Alonso, M., Cutten, H., De Waele, B., Tack, L., Tahon, A., Baudet, D. and Barritt, S. D. (2012). The Mesoproterozoic Karagwe-Ankole Belt (formerly the NE Kibara Belt): The result of prolonged extensional intracratonic basin development punctuated by two short-lived far-field compressional events. Precambrian Research, 216, 63-86. https://doi.org/10.1016/j.precamres.2012.06.007

Flugel, T. J. (2014). The evolution of the Congo-Kalahari Watershed: African mega-geomorphology. Ph.D. thesis University of Cape Town. http://hdl.handle.net/11427/8695

Flügel, T. J., Eckardt, F. D. and Cotterill, F. P. (2015). The present day drainage patterns of the Congo river system and their Neogene evolution. In Geology and Resource Potential of the Congo Basin, 315-337. Springer, Berlin, Heidelberg.

Flügel, T. J., Eckardt, F. D. and Cotterill, W. F. P. (2017). The geomorphology and river longitudinal profiles of the Congo-Kalahari Watershed. The African Neogene-Climate, Environments and People: Palaeoecology of Africa 34, 31-52. https://doi.org/10.1201/9781315161808-4.

Foeken, J. P., Stuart, F. M. and Mark, D. F. (2012). Long-term low latitude cosmogenic ^{3}He production rate determined from a 126 ka basalt from Fogo, Cape Verdes. Earth and Planetary Science Letters, 359, 14-25. https://doi.org/10.1016/j.epsl.2012.10.005

Gamrod, J. L. (2009). Paleolimnological records of environmental change preserved in Paleo-Lake Mababe, northwest Botswana. Doctoral dissertation, Oklahoma State University.

Gardner, T. W. (1983). Experimental study of knickpoint and longitudinal profile evolution in cohesive, homogeneous material. Geological Society of America Bulletin, 94(5), 664-672. https://doi.org/10.1130/0016-7606(1983)94<664:ESOKAL>2.0.CO;2

Gasparini, N. M., Bras, R. L. and Whipple, K. X. (2006). Numerical modeling of non–steady-state river profile evolution using a sediment-flux-dependent incision model. Special Papers - Geological Society of America, 398, 127-141.

Gasse, F., Stabell, B., Fourtanier, E. and van Iperen, Y. (1989). Freshwater diatom influx in intertropical Atlantic: relationships with continental records from Africa. Quaternary Research, 32(2), 229-243. https://doi.org/10.1016/0033-5894(89)90079-3

Giacomo, D. D., Engdahl, E. R. and Storchak, D. A. (2018). The ISC-GEM Earthquake Catalogue (1904–2014): status after the extension project. Earth System Science Data, 10(4), 1877-1899. https://doi.org/10.5194/essd-10-1877-2018

Gilbert, G. K. (1877). Report on the geology of the Henry Mountains (Utah). In: U.S. Geographical and Geological Survey of the Rocky Mountain Region: Washington, D.C., U.S. Gov. Printing Office.

Goethals, M.M., Hetzel, R., Niedermann, S., Wittmann, H., Fenton, C.R., Kubik, P.W., Christl, M. and von Blanckenburg, F. (2009). An improved experimental determination of cosmogenic ^{10}Be/^{21}Ne and ^{26}Al/^{21}Ne production ratios in quartz. Earth and Planetary Science Letters, 284(1-2), 187-198. https://doi.org/10.1016/j.epsl.2009.04.027

Goodier, S. A., Cotterill, F. P., O'Ryan, C., Skelton, P. H. and de Wit, M. J. (2011). Cryptic diversity of African tigerfish (Genus *Hydrocynus*) reveals palaeogeographic signatures of linked Neogene geotectonic events. Plos One, 6(12), e28775. https://doi.org/10.1371/journal.pone.0028775

Gosse, J. C. and Phillips, F. M. (2001). Terrestrial in situ cosmogenic nuclides: theory and application. Quaternary Science Reviews, 20(14), 1475-1560. https://doi.org/10.1016/S0277-3791(00)00171-2

Gosse, J. C., Evenson, E. B., Klein, J., Lawn, B. and Middleton, R. (1995). Precise cosmogenic ^{10}Be measurements in western North America: Support for a global Younger Dryas cooling event. Geology, 23(10), 877-880. https://doi.org/10.1130/0091-7613(1995)023<0877:PCBMIW>2.3.CO;2

Granger, D. E. and Muzikar, P. F. (2001). Dating sediment burial with in situ-produced cosmogenic nuclides: theory, techniques, and limitations. Earth and Planetary Science Letters, 188(1-2), 269-281. https://doi.org/10.1016/S0012-821X(01)00309-0

Granger, D. E., Kirchner, J. W. and Finkel, R. C. (1997). Quaternary downcutting rate of the New River, Virginia, measured from differential decay of cosmogenic ^{26}Al and ^{10}Be in cave-deposited alluvium. Geology, 25(2), 107-110. https://doi.org/10.1130/0091-7613(1997)025<0107:QDROTN>2.3.CO;2

Guillocheau, F., Chelalou, R., Linol, B., Dauteuil, O., Robin, C., Mvondo, F., Callec, Y. and Colin, J. P. (2015). Cenozoic landscape evolution in and around the Congo Basin: constraints from sediments and planation surfaces. In: Geology and Resource Potential of the Congo Basin. Springer, Berlin, Heidelberg, 271-313. https://doi.org/10.1007/978-3-642-29482-2_14

Halldórsson, S. A., Hilton, D. R., Scarsi, P., Abebe, T. and Hopp, J. (2014). A common mantle plume source beneath the entire East African Rift System revealed by coupled helium-neon systematics. Geophysical Research Letters, 41(7), 2304-2311. https://doi.org/10.1002/2014GL059424

Hancock, G. S., Anderson, R. S., Whipple, K. X., Tinkler, K. J. and Wohl, E. E. (1998). Beyond power: Bedrock river incision process and form. Geophysical Monograph-American Geophysical Union, 107, 35-60.

Hanson, R. E. (2003). Proterozoic geochronology and tectonic evolution of southern Africa. Geological Society, London, Special Publications, 206(1), 427-463. https://doi.org/10.1144/GSL.SP.2003.206.01.20

Häuselmann, P., Fiebig, M., Kubik, P. W. and Adrian, H. (2007). A first attempt to date the original "Deckenschotter" of Penck and Brückner with cosmogenic nuclides. Quaternary International, 164, 33-42. https://doi.org/10.1016/j.quaint.2006.12.013

Hayakawa, Y. and Matsukura, Y. (2003). Recession rates of waterfalls in Boso Peninsula, Japan, and a predictive equation. Earth Surface Processes and Landforms, 28(6), 675-684. https://doi.org/10.1002/esp.519

Hayakawa, Y. S. and Oguchi, T. (2006). DEM-based identification of fluvial knickzones and its application to Japanese mountain rivers. Geomorphology, 78(1-2), 90-106. https://doi.org/10.1016/j.geomorph.2006.01.018

Hayakawa, Y. S., Yokoyama, S. and Matsukura, Y. (2008). Erosion rates of waterfalls in post-volcanic fluvial systems around Aso volcano, southwestern Japan. Earth Surface Processes and Landforms, 33(5), 801-812. https://doi.org/10.1002/esp.1615

Hermanns, R. L., Niedermann, S., Ivy-Ochs, S. and Kubik, P. W. (2004). Rock avalanching into a landslide-dammed lake causing multiple dam failure in Las Conchas valley (NW Argentina) – evidence from surface exposure dating and stratigraphic analyses. Landslides, 1(2), 113-122. https://doi.org/10.1007/s10346-004-0013-5

Hetzel, R., Niedermann, S., Ivy-Ochs, S., Kubik, P. W., Tao, M. and Gao, B. (2002). ^{21}Ne versus ^{10}Be and ^{26}Al exposure ages of fluvial terraces: the influence of crustal Ne in quartz. Earth and Planetary Science Letters, 201(3-4), 575-591. https://doi.org/10.1016/S0012-821X(02)00748-3

Hillaire-Marcel, C., Carro, O. and Casanova, J. (1986). ^{14}C and Th/U dating of Pleistocene and Holocene stromatolites from East African paleolakes. Quaternary Research, 25(3), 312-329. https://doi.org/10.1016/0033-5894(86)90004-9

Hinz, N., Cumming, B. and Sussman, D. (2018). Exploration of fault-related deep-circulation geothermal resources in the western branch of the East African Rift System: examples from Uganda and Tanzania. In Proceedings, 7th African Rift Geothermal Conference.

Holland, W. N. and Pickup, G. (1976). Flume study of knickpoint development in stratified sediment. Geological Society of America Bulletin, 87(1), 76-82. https://doi.org/10.1130/0016-7606(1976)87<76:FSOKDI>2.0.CO;2

Howard, A. D. and Kerby, G. (1983). Channel changes in badlands. Geological Society of America Bulletin 94: 739–752.

Howard, A. D., Dietrich, W. E. and Seidl, M. A. (1994). Modeling fluvial erosion on regional to continental scales. Journal of Geophysical Research: Solid Earth, 99(B7), 13971-13986. https://doi.org/10.1029/94JB00744

Ivory, S. J., Blome, M. W., King, J. W., McGlue, M. M., Cole, J. E. and Cohen, A. S. (2016). Environmental change explains cichlid adaptive radiation at Lake Malawi over the past 1.2 million years. Proceedings of the National Academy of Sciences, 113(42), 11895-11900. https://doi.org/10.1073/pnas.1611028113

Ivy-Ochs, S. and Kober, F. (2008). Surface exposure dating with cosmogenic nuclides. E&G Quaternary Science Journal, 57(1/2), 179-209. https://doi.org/10.3285/eg.57.1-2.7, 2008.

Kampunzu, A. B. and Cailteux, J. (1999). Tectonic evolution of the Lufilian Arc (Central Africa Copper Belt) during Neoproterozoic Pan African orogenesis. Gondwana Research, 2(3), 401-421. https://doi.org/10.1016/S1342-937X(05)70279-3

Kampunzu, A. B., Armstrong, R. A., Kokonyangi, J. and Ngulube, D. A. (2001). Kibaran geochronology, timing of orogenic events and petrogenetic implications for the source of the Kibaran tin granites. In: Abstracts, IGCP 418 4th Field Meeting, Durban.

Kampunzu, A. B., Kanika, M., Kapenda, D. and Tshimanga, K. (1993). Geochemistry and geotectonic setting of late Proterozoic Katangan basic rocks from Kibambale in Central Shaba (Zaire). Geologische Rundschau, 82(4), 619-630. https://doi.org/10.1007/BF00191489

Kampunzu, A. B., Tembo, F., Matheis, G., Kapenda, D. and Huntsman-Mapila, P. (2000). Geochemistry and tectonic setting of mafic igneous units in the Neoproterozoic Katangan Basin, Central Africa: implications for Rodinia break-up. Gondwana Research, 3(2), 125-153. https://doi.org/10.1016/S1342-937X(05)70093-9

Kapenda, D., Kampunzu, A. B., Cabanis, B., Namegabe, M. and Tshimanga, K. (1998). Petrology and geochemistry of post–kinematic mafic rocks from the Paleoproterozoic Ubendian belt, NE Katanga (Democratic Republic of Congo). Geologische Rundschau, 87(3), 345-362. https://doi.org/10.1007/s005310050214

Kaplan, M. R., Strelin, J. A., Schaefer, J. M., Denton, G. H., Finkel, R. C., Schwartz, R., Putnam, A. E., Vandergoes, M. J., Goehring, B. M. and Travis, S. G. (2011). In-situ cosmogenic ^{10}Be production rate at Lago Argentino, Patagonia: implications for late-glacial climate chronology. Earth and Planetary Science Letters, 309(1-2), 21-32. https://doi.org/10.1016/j.epsl.2011.06.018

Kim, Y. S. and Sanderson, D. J. (2005). The relationship between displacement and length of faults: a review. Earth-Science Reviews, 68(3-4), 317-334. https://doi.org/10.1016/j.earscirev.2004.06.003

Kipata, M. L., Delvaux, D., Sebagenzi, M. N., Cailteux, J. and Sintubin, M. (2013). Brittle tectonic and stress field evolution in the Pan-African Lufilian arc and its foreland (Katanga, DRC): from orogenic compression to extensional collapse, transpressional inversion and transition to rifting. Geologica Belgica, 16(1), 1-17.

Kirby, E. and Whipple, K. X. (2012). Expression of active tectonics in erosional landscapes. Journal of Structural Geology, 44, 54-75. https://doi.org/10.1016/j.jsg.2012.07.009

Klerkx, J., Theunissen, K. and Delvaux, D. (1998). Persistent fault controlled basin formation since the Proterozoic along the Western Branch of the East African Rift. Journal of African Earth Sciences, 26(3), 347-361. https://doi.org/10.1016/S0899-5362(98)00020-7

Kober, F., Ivy-Ochs, S., Schlunegger, F., Baur, H., Kubik, P. W. and Wieler, R. (2007). Denudation rates and a topography-driven rainfall threshold in northern Chile: Multiple cosmogenic nuclide data and sediment yield budgets. Geomorphology, 83(1-2), 97-120. https://doi.org/10.1016/j.geomorph.2006.06.029

Kohl, C. P. and Nishiizumi, K. (1992). Chemical isolation of quartz for measurement of in-situ-produced cosmogenic nuclides. Geochimica et Cosmochimica Acta, 56(9), 3583-3587. https://doi.org/10.1016/0016-7037(92)90401-4

Kokonyangi, J., Armstrong, R., Kampunzu, A. B., Yoshida, M. and Okudaira, T. (2004). U–Pb zircon geochronology and petrology of granitoids from Mitwaba (Katanga, Congo): implications for the evolution of the Mesoproterozoic Kibaran belt. Precambrian Research, 132(1-2), 79-106. https://doi.org/10.1016/j.precamres.2004.02.007

Koptev, A., Calais, E., Burov, E., Leroy, S. and Gerya, T. (2015). Dual continental rift systems generated by plume–lithosphere interaction. Nature Geoscience, 8(5), 388-392. https://doi.org/10.1038/ngeo2401

Kubik, P. W., Ivy-Ochs, S., Masarik, J., Frank, M. and Schlüchter, C. (1998). ^{10}Be and ^{26}Al production rates deduced from an instantaneous event within the dendro-calibration curve, the landslide of Köfels, Ötz Valley, Austria. Earth and Planetary Science Letters, 161(1-4), 231-241. https://doi.org/10.1016/S0012-821X(98)00153-8

Lal, D. (1988). In situ-produced cosmogenic isotopes in terrestrial rocks. Annual Review of Earth and Planetary Sciences, 16(1), 355-388. https://doi.org/10.1146/annurev.ea.16.050188.002035

Lal, D. (1991). Cosmic ray labeling of erosion surfaces: in situ nuclide production rates and erosion models. Earth and Planetary Science Letters, 104(2-4), 424-439. https://doi.org/10.1016/0012-821X(91)90220-C

Lavayssiere, A., Drooff, C., Ebinger, C., Gallacher, R., Illsley-Kemp, F., Oliva, S. J. and Keir, D. (2019). Depth extent and kinematics of faulting in the southern Tanganyika rift, Africa. Tectonics, 38(3), 842-862. https://doi.org/10.1029/2018TC005379

Lehner, B. and Grill, G. (2013). Global river hydrography and network routing: baseline data and new approaches to study the world's large river systems. Hydrological Processes, 27(15), 2171-2186. https://doi.org/10.1002/hyp.9740

Lifton, N. A., Bieber, J. W., Clem, J. M., Duldig, M. L., Evenson, P., Humble, J. E. and Pyle, R. (2005). Addressing solar modulation and long-term uncertainties in scaling secondary cosmic rays for in situ cosmogenic nuclide applications. Earth and Planetary Science Letters, 239(1-2), 140-161. https://doi.org/10.1016/j.epsl.2005.07.001

Lifton, N., Sato, T. and Dunai, T. J. (2014). Scaling in situ cosmogenic nuclide production rates using analytical approximations to atmospheric cosmic-ray fluxes. Earth and Planetary Science Letters, 386, 149-160. https://doi.org/10.1016/j.epsl.2013.10.052

Loget, N. and Van Den Driessche, J. (2009). Wave train model for knickpoint migration. Geomorphology, 106(3-4), 376-382. https://doi.org/10.1016/j.geomorph.2008.10.017

Luna, L. V., Bookhagen, B., Niedermann, S., Rugel, G., Scharf, A. and Merchel, S. (2018). Glacial chronology and production rate cross-calibration of five cosmogenic nuclide and mineral systems from the southern Central Andean Plateau. Earth and Planetary Science Letters, 500, 242-253. https://doi.org/10.1016/j.epsl.2018.07.034

Mana, S., Furman, T., Turrin, B. D., Feigenson, M. D. and Swisher III, C. C. (2015). Magmatic activity across the East African North Tanzanian divergence zone. Journal of the Geological Society, 172(3), 368-389. https://doi.org/10.1144/jgs2014-072

Master, S., Rainaud, C., Armstrong, R. A., Phillips, D. and Robb, L. J. (2005). Provenance ages of the Neoproterozoic Katanga Supergroup (Central African Copperbelt), with implications for basin evolution. Journal of African Earth Sciences, 42(1-5), 41-60. https://doi.org/10.1016/j.jafrearsci.2005.08.005

Masters, L. S., Burkhardt, J. W. and Tausch, R. (1991). The geomorphic process: effects of base level lowering on riparian management. Rangelands Archives, 13(6), 280-284.

Matmon, A., Bierman, P. R., Larsen, J., Southworth, S., Pavich, M. and Caffee, M. (2003). Temporally and spatially uniform rates of erosion in the southern Appalachian Great Smoky

Mountains. Geology, 31(2), 155-158. https://doi.org/10.1130/0091-7613(2003)031<0155:TASURO>2.0.CO;2

Matmon, A., Fink, D., Davis, M., Niedermann, S., Rood, D. and Frumkin, A. (2014). Unraveling rift margin evolution and escarpment development ages along the Dead Sea fault using cosmogenic burial ages. Quaternary Research, 82(1), 281-295. https://doi.org/10.1016/j.yqres.2014.04.008

Mavonga, T., Kavotha, S. K., Lukaya, N., Etoy, O., Mifundu, W., Bizimungu, R. K. and Durieux, J. (2010). Some aspect of seismicity prior to the 27 November 2006 eruption of Nyamuragira volcano and its implication for volcano monitoring and risk mitigation in the Virunga area, Western Rift Valley of Africa. Journal of African Earth Sciences, 58(5), 829-832. https://doi.org/10.1016/j.jafrearsci.2010.02.002

Meert, J. G., Hargraves, R. B., Van der Voo, R., Hall, C. M. and Halliday, A. N. (1994). Paleomagnetic and ^{40}Ar/^{39}Ar studies of late Kibaran intrusives in Burundi, East Africa: implications for late Proterozoic supercontinents. The Journal of Geology, 102(6), 621-637. https://doi.org/10.1086/629708

Meier, J. I., Stelkens, R. B., Joyce, D. A., Mwaiko, S., Phiri, N., Schliewen, U. K., Selz, O.M., Wagner, C.E., Katongo, C. and Seehausen, O. (2019). The coincidence of ecological opportunity with hybridization explains rapid adaptive radiation in Lake Mweru cichlid fishes. Nature Communications, 10(1), 1-11. https://doi.org/10.1038/s41467-019-13278-z

Merchel, S. and Bremser, W. (2004). First international ^{26}Al interlaboratory comparison–Part I. Nuclear Instruments and Methods in Physics Research Section B: Beam Interactions with Materials and Atoms, 223, 393-400. https://doi.org/10.1016/j.nimb.2005.05.051

Merchel, S. and Herpers, U. (1999). An update on radiochemical separation techniques for the determination of long-lived radionuclides via accelerator mass spectrometry. Radiochimica Acta, 84(4), 215-220. https://doi.org/10.1524/ract.1999.84.4.215

Merchel, S., Braucher, R., Benedetti, L., Grauby, O. and Bourlès, D. L. (2008). Dating carbonate rocks with in-situ produced cosmogenic ^{10}Be: Why it often fails. Quaternary Geochronology, 3(4), 299-307. https://doi.org/10.1016/j.quageo.2008.01.008

Miller, J. R. (1991). The influence of bedrock geology on knickpoint development and channel-bed degradation along downcutting streams in south-central Indiana. The Journal of Geology, 99(4), 591-605. https://doi.org/10.1086/629519

Mohr, P. A. (1974). ENE-trending lineaments of the African rift system. Proc. First Int. Conf. New Basement Tectonics, Utah. Geol. Ass. Publ., 5 (1974), 327-336.

Molnar, N. E., Cruden, A. R. and Betts, P. G. (2019). Interactions between propagating rifts and linear weaknesses in the lower crust. Geosphere, 15(5), 1617-1640. https://doi.org/10.1130/GES02119.1

Molnar, P. and England, P. (1990). Late Cenozoic uplift of mountain ranges and global climate change: chicken or egg? Nature, 346(6279), 29-34. https://doi.org/10.1038/346029a0

Mondeguer, A., Ravenne, C., Masse, P. and Tiercelin, J. J. (1989). Sedimentary basins in an extension and strike-slip background; the "South Tanganyika troughs complex", East African Rift. Bulletin de la Société Géologique de France, 3, 501-522. https://doi.org/10.2113/gssgfbull.V.3.501

Moore, A. E. (1999). A reappraisal of epeirogenic flexure axes in southern Africa. South African Journal of Geology, 102(4), 363-376. https://hdl.handle.net/10520/EJC-942c6e6ad

Moore, A. E. and Larkin, P. A. (2001). Drainage evolution in south-central Africa since the breakup of Gondwana. South African Journal of Geology, 104(1), 47-68. https://doi.org/10.2113/104.1.47

Moore, A. E., Cotterill, F. P. D. and Eckardt, F. D. (2012). The evolution and ages of Makgadikgadi palaeo-lakes: consilient evidence from Kalahari drainage, evolution south-central Africa. South African Journal of Geology, 115(3), 385-413. https://doi.org/10.2113/gssajg.115.3.385

Moore, A. E., Cotterill, F. P., Main, M. P. and Williams, H. B. (2007). The Zambezi River. Large rivers: Geomorphology and Management, 311-332.

Morley, C. K. (2002). Evolution of large normal faults: Evidence from seismic reflection data. AAPG bulletin, 86(6), 961-978. https://doi.org/10.1306/61EEDBFC-173E-11D7-8645000102C1865D

Mouslopoulou, V., Moraetis, D., Benedetti, L., Guillou, V., Bellier, O. and Hristopulos, D. (2014). Normal faulting in the forearc of the Hellenic subduction margin: Paleoearthquake history and kinematics of the Spili Fault, Crete, Greece. Journal of Structural Geology, 66, 298-308. https://doi.org/10.1016/j.jsg.2014.05.017

Mouslopoulou, V., Nicol, A., Walsh, J. J., Begg, J. G., Townsend, D. B. and Hristopulos, D. T. (2012). Fault-slip accumulation in an active rift over thousands to millions of years and the importance of paleoearthquake sampling. Journal of Structural Geology, 36, 71-80. https://doi.org/10.1016/j.jsg.2011.11.010

Mouslopoulou, V., Walsh, J. J. and Nicol, A. (2009). Fault displacement rates on a range of timescales. Earth and Planetary Science Letters, 278(3-4), 186-197. https://doi.org/10.1016/j.epsl.2008.11.031

NASA JPL (2020). NASADEM Merged DEM Global 1 arc second V001 [Data set]. NASA EOSDIS Land Processes DAAC. Last accessed September 2020. https://doi.org/10.5067/MEaSUREs/NASADEM/NASADEM_HGT.001

Neely, A. B., Bookhagen, B. and Burbank, D. W. (2017). An automated knickzone selection algorithm (KZ-Picker) to analyze transient landscapes: Calibration and validation. Journal of Geophysical Research: Earth Surface, 122(6), 1236-1261. https://doi.org/10.1002/2017JF004250

Nicol, A., Childs, C., Walsh, J.J., Manzocchi, T. and Schöpfer, M.P.J. (2016c). Interactions and growth of faults in an outcrop-scale system. In: The Geometry and Growth of Normal Faults. (Edited by Childs, C., Holdsworth, R. E., Jackson, C. A.-L., Manzocchi, T., Walsh, J. J. & Yielding, G.). Geological Society of London, Special Publication, 439. https://doi.org/10.1144/SP439.9

Nicol, A., Mouslopoulou, V., Begg, J. and Oncken, O. (2020a). Displacement accumulation and sampling of paleoearthquakes on active normal faults of Crete in the eastern Mediterranean. Geochemistry, Geophysics, Geosystems, 21(11), e2020GC009265. https://doi.org/10.1029/2020GC009265

Nicol, A., Robinson, R., Van Dissen, R. J. and Harvison, A. (2016b). Variability of recurrence interval and single-event slip for surface-rupturing earthquakes in New Zealand. New Zealand

Journal of Geology and Geophysics, 59(1), 97-116. https://doi.org/10.1080/00288306.2015.1127822

Nicol, A., Van Dissen, R., Stirling, M. and Gerstenberger, M. (2016a). Completeness of the paleoseismic active fault record in New Zealand. Seismological Research Letters, 86, 1299-1310. https://doi.org/10.1785/0220160088

Nicol, A., Walsh, J. J., Villamor, P., Seebeck, H. and Berryman, K. R. (2010). Normal fault interactions, paleoearthquakes and growth in an active rift. Journal of Structural Geology, 32(8), 1101-1113. https://doi.org/10.1016/j.jsg.2010.06.018

Nicol, A., Walsh, J. J., Watterson, J. and Underhill, J. R. (1997). Displacement rates of normal faults. Nature, 390(6656), 157-159. https://doi.org/10.1038/36548

Nicol, A., Walsh, J., Berryman, K. and Nodder, S. (2005). Growth of a normal fault by the accumulation of slip over millions of years. Journal of Structural Geology, 27(2), 327-342. https://doi.org/10.1016/j.jsg.2004.09.002

Nicol, A., Walsh, J., Childs, C. and Manzocchi, T. (2020b). The growth of faults. In Understanding Faults (pp. 221-255). Elsevier. https://doi.org/10.1016/B978-0-12-815985-9.00006-0

Niedermann, S. (2002). Cosmic-ray-produced noble gases in terrestrial rocks: dating tools for surface processes. Reviews in Mineralogy and Geochemistry, 47(1), 731-784. https://doi.org/10.2138/rmg.2002.47.16

Niedermann, S., Bach, W. and Erzinger, J. (1997). Noble gas evidence for a lower mantle component in MORBs from the southern East Pacific Rise: Decoupling of helium and neon isotope systematics. Geochimica et Cosmochimica Acta, 61(13), 2697-2715.

Niedermann, S., Graf, T. and Marti, K. (1993). Mass spectrometric identification of cosmic-ray-produced neon in terrestrial rocks with multiple neon components. Earth and Planetary Science Letters, 118(1-4), 65-73.

Nishiizumi, K., Imamura, M., Caffee, M. W., Southon, J. R., Finkel, R. C. and McAninch, J. (2007). Absolute calibration of ^{10}Be AMS standards. Nuclear Instruments and Methods in Physics Research Section B: Beam Interactions with Materials and Atoms, 258(2), 403-413. https://doi.org/10.1016/j.nimb.2007.01.297

Norris, T. L., Gancarz, A. J., Rokop, D. J. and Thomas, K. W. (1983). Half-life of ^{26}Al. Journal of Geophysical Research: Solid Earth, 88(S01), B331-B333. https://doi.org/10.1029/JB088iS01p0B331

Nyblade, A. A. (2011). The upper-mantle low-velocity anomaly beneath Ethiopia, Kenya, and Tanzania: Constraints on the origin of the African superswell in eastern Africa and plate versus plume models of mantle dynamics. Geological Society of America Special Papers, 478, 37-50.

Nyblade, A. A., Owens, T. J., Gurrola, H., Ritsema, J. and Langston, C. A. (2000). Seismic evidence for a deep upper mantle thermal anomaly beneath east Africa. Geology, 28(7), 599-602. https://doi.org/10.1130/0091-7613(2000)28<599:SEFADU>2.0.CO;2

Olivotos, S., Niedermann, S., Flügel, T., Mouslopoulou, V., Merchel, S., Cotterill, F., Bookhagen, B., Gärtner, A., Rugel, G., Scharf, A., Nadeau, M.-J. and Seiler, M. (2021). Quaternary landscape evolution in a tectonically active rift basin (paleo-lake Mweru, south-central Africa). Geomorphology, 381, 107669. https://doi.org/10.1016/j.geomorph.2021.107669

Omenda, P., Ebinger, C., Nelson, W., Delvaux, D., Cumming, W., Marini, L., Halldórsson, S., Varet, J., Árnason, K., Ruempker, G. and Alexander, K. (2016). Characteristics and important factors that influence the development of geothermal systems in the western branch of East African Rift System. In 6th African Rift Geothermal Conference 2016.

Pascovici, G., Dewald, A., Heinze, S., Fink, L., Müller-Gatermann, C., Schiffer, M., Feuerstein, C., Pfeiffer, M., Jolie, J., Thiel, S. and Zell, K. O. (2013). A new beam profile monitor and time of flight system for CologneAMS. Nuclear Instruments and Methods in Physics Research Section B: Beam Interactions with Materials and Atoms, 294, 410-415. https://doi.org/10.1016/j.nimb.2012.04.026

Perron, J. T. and Royden, L. (2012). An integral approach to bedrock river profile analysis. Earth Surface Processes and Landforms, 38(6), 570-576. https://doi.org/10.1002/esp.3302

Philbrick, S. S. (1970). Horizontal configuration and the rate of erosion of Niagara Falls. Geological Society of America Bulletin 81, 3723–3732.

Porada, H. and Berhorst, V. (2000). Towards a new understanding of the Neoproterozoic-Early Palaeozoic Lufilian and northern Zambezi Belts in Zambia and the Democratic Republic of Congo. Journal of African Earth Sciences, 30(3), 727-771. https://doi.org/10.1016/S0899-5362(00)00049-X

Putnam, A. E., Schaefer, J. M., Barrell, D. J. A., Vandergoes, M., Denton, G. H., Kaplan, M. R., Finkel, R. C., Schwartz, R., Goehring, B. M. and Kelley, S. E. (2010). In situ cosmogenic ^{10}Be production-rate calibration from the Southern Alps, New Zealand. Quaternary Geochronology, 5(4), 392-409. https://doi.org/10.1016/j.quageo.2009.12.001

Raymo, M. E. and Ruddiman, W. F. (1992). Tectonic forcing of late Cenozoic climate. Nature, 359(6391), 117-122. https://doi.org/10.1038/359117a0

Reeves, C. V. (1972). Rifting in the Kalahari? Nature, 237(5350), 95-96. https://doi.org/10.1038/237095a0

Ring, U. (1994). The influence of preexisting structure on the evolution of the Cenozoic Malawi rift (East African rift system). Tectonics, 13(2), 313-326. https://doi.org/10.1029/93TC03188

Rosenbloom, N. A. and Anderson, R. S. (1994). Hillslope and channel evolution in a marine terraced landscape, Santa Cruz, California. Journal of Geophysical Research: Solid Earth, 99(B7), 14013-14029. https://doi.org/10.1029/94JB00048

Rugel, G., Pavetich, S., Akhmadaliev, S., Baez, S. M. E., Scharf, A., Ziegenrücker, R. and Merchel, S. (2016). The first four years of the AMS-facility DREAMS: Status and developments for more accurate radionuclide data. Nuclear Instruments and Methods in Physics Research Section B: Beam Interactions with Materials and Atoms, 370, 94-100. https://doi.org/10.1016/j.nimb.2016.01.012

Saillard, M., Hall, S. R., Audin, L., Farber, D. L., Regard, V. and Hérail, G. (2011). Andean coastal uplift and active tectonics in southern Peru: ^{10}Be surface exposure dating of differentially uplifted marine terrace sequences (San Juan de Marcona, ~15.4°S). Geomorphology, 128(3-4), 178-190. https://doi.org/10.1016/j.geomorph.2011.01.004

Saria, E., Calais, E., Stamps, D. S., Delvaux, D. and Hartnady, C. J. H. (2014). Present-day kinematics of the East African Rift. Journal of Geophysical Research: Solid Earth, 119(4), 3584-3600. https://doi.org/10.1016/0301-9268(84)90032-9

Sartégou, A., Bourlès, D. L., Blard, P.-H., Braucher, R., Tibari, B., Zimmermann, L., Leanni, L., Aumaître, G. and Keddadouche, K. (2018). Deciphering landscape evolution with karstic networks: A Pyrenean case study. Quaternary Geochronology, 43, 12-29. https://doi.org/10.1016/j.quageo.2017.09.005

Scheingross, J. S. and Lamb, M. P. (2017). A mechanistic model of waterfall plunge pool erosion into bedrock. Journal of Geophysical Research: Earth Surface, 122(11), 2079-2104.

Schildgen, T., Dethier, D. P., Bierman, P. and Caffee, M. (2002). ^{26}Al and ^{10}Be dating of late Pleistocene and Holocene fill terraces: a record of fluvial deposition and incision, Colorado Front Range. Earth Surface Processes and Landforms, 27(7), 773-787. https://doi.org/10.1002/esp.352

Schimmelpfennig, I., Benedetti, L., Garreta, V., Pik, R., Blard, P. H., Burnard, P., Bourlès, D., Finkel, R., Ammon, K. and Dunai, T. (2011). Calibration of cosmogenic ^{36}Cl production rates from Ca and K spallation in lava flows from Mt. Etna (38ºN, Italy) and Payun Matru (36ºS, Argentina). Geochimica et Cosmochimica Acta, 75(10), 2611-2632. https://doi.org/10.1016/j.gca.2011.02.013

Schlische, R. W., Young, S. S., Ackermann, R. V. and Gupta, A. (1996). Geometry and scaling relations of a population of very small rift-related normal faults. Geology, 24(8), 683-686. https://doi.org/10.1130/0091-7613(1996)024<0683:GASROA>2.3.CO;2

Schlüter, T. (1997). Geology of East Africa. In: Bender, F., Jacobshagen, V. and Lüttig, G. (Eds.), Beiträge zur Regionalen Geologie der Erde, Band 27. Gebrüder Borntraeger, Berlin, Stuttgart, 484 pp.

Schultz, R. A., Soliva, R., Fossen, H., Okubo, C. H. and Reeves, D. M. (2008). Dependence of displacement–length scaling relations for fractures and deformation bands on the volumetric changes across them. Journal of Structural Geology, 30(11), 1405-1411. https://doi.org/10.1016/j.jsg.2008.08.001

Schwanghart, W. and Scherler, D. (2014). TopoToolbox 2–MATLAB-based software for topographic analysis and modeling in Earth surface sciences. Earth Surface Dynamics, 2(1), 1-7. doi:10.5194/esurf-2-1-2014

Schwarzer, J., Misof, B., Ifuta, S. N. and Schliewen, U. K. (2011). Time and origin of cichlid colonization of the lower Congo rapids. Plos One, 6(7), e22380. https://doi.org/10.1371/journal.pone.0022380

Sebagenzi, M. N. and Kaputo, K. (2002). Geophysical evidences of continental break up in the southeast of the Democratic Republic of Congo and Zambia (Central Africa). EGU Stephan Mueller Spec. Publ. Series, 2, 193-206.

Seidl, M. A., Weissel, J. K. and Pratson, L. F. (1996). The kinematics and pattern of escarpment retreat across the rifted continental margin of SE Australia. Basin Research, 8(3), 301-316. https://doi.org/10.1046/j.1365-2117.1996.00266.x

Seiler, M., Anjar, J., Værnes, E., Nadeau, M. J. and Scognamiglio, G. (2018). First ^{10}Be measurements at Trondheim 1 MV AMS. Nuclear Instruments and Methods in Physics Research Section B: Beam Interactions with Materials and Atoms, 437, 123-129. https://doi.org/10.1016/j.nimb.2018.08.013

Shudofsky, G. N. (1985). Source mechanisms and focal depths of East African earthquakes using Rayleigh-wave inversion and body-wave modelling. Geophysical Journal International, 83(3), 563-614. https://doi.org/10.1111/j.1365-246X.1985.tb04328.x

Shuman, B., Henderson, A. K., Colman, S. M., Stone, J. R., Fritz, S. C., Stevens, L. R., Power, M. J. and Whitlock, C. (2009). Holocene lake-level trends in the Rocky Mountains, USA. Quaternary Science Reviews, 28(19-20), 1861-1879. https://doi.org/10.1016/j.quascirev.2009.03.003

Stamps, D. S., Calais, E., Saria, E., Hartnady, C., Nocquet, J. M., Ebinger, C. J. and Fernandes, R. M. (2008). A kinematic model for the East African Rift. Geophysical Research Letters, 35(5), L05304. https://doi.org/10.1029/2007GL032781

Stock, G. M., Anderson, R. S. and Finkel, R. C. (2004). Pace of landscape evolution in the Sierra Nevada, California, revealed by cosmogenic dating of cave sediments. Geology, 32(3), 193-196. https://doi.org/10.1130/G20197.1

Stone, J. O. (2000). Air pressure and cosmogenic isotope production. Journal of Geophysical Research: Solid Earth, 105(B10), 23753-23759. https://doi.org/10.1029/2000JB900181

Storchak, D. A., Harris, J., Brown, L., Lieser, K., Shumba, B. and Di Giacomo, D. (2020). Rebuild of the Bulletin of the International Seismological Centre (ISC)—part 2: 1980–2010. Geoscience Letters, 7(1), 1-21.

Strecker, M. R., Blisniuk, P. M. and Eisbacher, G. H. (1990). Rotation of extension direction in the central Kenya Rift. Geology, 18(4), 299-302. https://doi.org/10.1130/0091-7613(1990)018<0299:ROEDIT>2.3.CO;2

Šujan, M., Lačný, A., Braucher, R., Magdolen, P., Aumaître, A. T. G., Bourlès, D. and Keddadouche, K. (2017). Early Pleistocene age of fluvial sediment in the Stará Garda Cave revealed by ^{26}Al/^{10}Be burial dating: implications for geomorphic evolution of the Malé Karpaty Mts. (Western Carpathians). Acta Carsologica, 46(2-3), 251-264..

Symoens, J. J. (1963). Le Parc National de L'Upemba. Son histoire on intérêt. In Colloque sur les problèmes biogéographiques du Parc National de L'Upemba, 6, 43-55.

Tack, L., Fernandez-Alonso, M., Trefois, P., Lavreau, J. and Cailteux, J. L. H. (2003). New data raise new questions on the regional geology of the Katanga Province as figured on the 1974 Geological Map (1/2000000) of the Democratic Republic of Congo (DRC). In Proterozoic Base Metal Deposits of Western Gondwana. 3rd IGCP-450 Conference and Guide Book of the Field Workshop, Lumbumbashi, Congo, 78-82.

Tack, L., Wingate, M. T. D., De Waele, B., Meert, J., Belousova, E., Griffin, B., Tahon, A. and Fernandez-Alonso, M. (2010). The 1375 Ma "Kibaran event" in Central Africa: Prominent emplacement of bimodal magmatism under extensional regime. Precambrian Research, 180(1-2), 63-84. https://doi.org/10.1016/j.precamres.2010.02.022

Thieme, J.G. (1971). The Geology of Musonda Falls Area, Explanation of Sheet 1028, SE Quarter. Geological Survey of Zambia, Report No. 32, 25.

Thomas, D. S. G. and Shaw, P. A. (1990). The deposition and development of the Kalahari Group sediments, Central Southern Africa. Journal of African Earth Sciences (and the Middle East), 10(1-2), 187-197. https://doi.org/10.1016/0899-5362(90)90054-I

Tiercelin, J. J. and Lezzar, K. E. (2002). A 300 million years history of rift lakes in Central and East Africa: an updated broad review. In: The East African great lakes: limnology, palaeolimnology and biodiversity. Springer, Dordrecht, 3-60. https://doi.org/10.1007/0-306-48201-0_1

Tiercelin, J. J., Chorowicz, J., Bellon, H., Richert, J. P., Mwanbene, J. T. and Walgenwitz, F. (1988). East African Rift System: offset, age and tectonic significance of the Tanganyika-Rukwa-Malawi intracontinental transcurrent fault zone. Tectonophysics, 148(3-4), 241-252. https://doi.org/10.1016/0040-1951(88)90133-3

Tinkler, K. J., Pengelly, J. W., Asselin, G. and Parkins, W. G. (1994). Postglacial recession of Niagara Falls in relation to the Great Lakes. Quaternary Research, 42, 20–29. https://doi.org/10.1006/qres.1994.1050

Torabi, A. and Berg, S. S. (2011). Scaling of fault attributes: A review. Marine and Petroleum Geology, 28(8), 1444-1460. https://doi.org/10.1016/j.marpetgeo.2011.04.003

Trauth, M. H., Maslin, M. A., Deino, A. and Strecker, M. R. (2005). Late Cenozoic moisture history of East Africa. Science, 309(5743), 2051-2053. https://doi.org/10.1126/science.1112964

Trauth, M. H., Maslin, M. A., Deino, A. L., Junginger, A., Lesoloyia, M., Odada, E. O., Olago, D. O., Olaka, L.A., Strecker, M. R. and Tiedemann, R. (2010). Human evolution in a variable environment: the amplifier lakes of Eastern Africa. Quaternary Science Reviews, 29(23-24), 2981-2988. https://doi.org/10.1016/j.quascirev.2010.07.007

Tucker, G. E. (2004). Drainage basin sensitivity to tectonic and climatic forcing: implications of a stochastic model for the role of entrainment and erosion thresholds. Earth Surface Processes and Landforms 29 (2), 185–205.

Unrug, R. (1984). The mid-Proterozoic Mporokoso Group of northern Zambia: stratigraphy, sedimentation and regional position. Precambrian Research, 24(2), 99-121.

Unrug, R. (1988). Mineralization controls and source of metals in the Lufilian fold belt, Shaba (Zaire), Zambia, and Angola. Economic Geology, 83(6), 1247-1258.

van der Beek, P., Pulford, A. and Braun, J. (2001). Cenozoic landscape development in the Blue Mountains (SE Australia): lithological and tectonic controls on rifted margin morphology. The Journal of Geology, 109(1), 35-56. https://doi.org/10.1086/317963

van der Merwe, P.D., Cotterill, F.P.D., Kandziora, M., Watters, B.R., Nagy, B., Genade, T., Flügel, T.J., Svendsen D. and Bellstedt, D. U. (2021). Genomic Fingerprints of Palaeogeographic History: The tempo and mode of Rift tectonics across tropical Africa has shaped the diversification of the killifish genus *Nothobranchius* (Teleostei: Cyprinodontiformes). Molecular phylogenetics and evolution, 158, 106988. https://doi.org/10.1016/j.ympev.2020.106988

Van Daele, J., Hulsbosch, N., Dewaele, S. and Muchez, P. (2020). Metamorphic and metasomatic evolution of the Western Domain of the Karagwe-Ankole Belt (Central Africa). Journal of African Earth Sciences, 41-42. https://doi.org/10.1016/j.jafrearsci.2020.103783

Van Heijst, M. W. I. M. and Postma, G. (2001). Fluvial response to sea-level changes: a quantitative analogue, experimental approach. Basin Research, 13(3), 269-292. https://doi.org/10.1046/j.1365-2117.2001.00149.x

Vermeesch, P. (2007). CosmoCalc: An Excel add-in for cosmogenic nuclide calculations. Geochemistry, Geophysics, Geosystems, 8(8). https://doi.org/10.1029/2006GC001530

Villeneuve, M. (1987). Géologie du synclinal de l'Itombwe (Zaïre oriental) et le problème de l'existence d'un sillon plissé pan-africain. Journal of African Earth Sciences (1983), 6(6), 869-880.

Villeneuve, M., Gärtner, A., Kalikone, C., Wazi, N., Hofmann, M. and Linnemann, U. (2019). U-Pb ages and provenance of detrital zircon from metasedimentary rocks of the Nya-Ngezie and Bugarama groups (DR Congo): A key for the evolution of the Mesoproterozoic Kibaran-Burundian Orogen in Central Africa. Precambrian Research, 328, 81-98.

von Blanckenburg, F., Hewawasam, T. and Kubik, P. W. (2004). Cosmogenic nuclide evidence for low weathering and denudation in the wet, tropical highlands of Sri Lanka. Journal of Geophysical Research: Earth Surface, 109(F3), F03008. https://doi.org/10.1029/2003JF000049

Von Engeln, O. D. (1940). A particular case of knickpunkte. Annals of the Association of American Geographers, 30(4), 268-271. https://doi.org/10.2307/2560885

Walsh, J. J. and Watterson, J. (1988). Analysis of the relationship between displacements and dimensions of faults. Journal of Structural Geology, 10(3), 239-247. https://doi.org/10.1016/0191-8141(88)90057-0

Walsh, J. J. and Watterson, J. (1991). Geometric and kinematic coherence and scale effects in normal fault systems. Geological Society, London, Special Publications, 56(1), 193-203. https://doi.org/10.1144/GSL.SP.1991.056.01.13

Watterson, J., Walsh, J. J., Gillespie, P. A. and Easton, S. (1996). Scaling systematics of fault sizes on a large-scale range fault map. Journal of Structural Geology, 18(2-3), 199-214. https://doi.org/10.1016/S0191-8141(96)80045-9

Weissel, J. K. and Seidl, M. A. (1998). Inland propagation of erosional escarpments and river profile evolution across the southeast Australian passive continental margin. Geophysical Monograph-American Geophysical Union, 107, 189-206.

Wells, D. L. and Coppersmith, K. J. (1994). New empirical relationships among magnitude, rupture length, rupture width, rupture area, and surface displacement. Bulletin of the Seismological Society of America, 84(4), 974-1002.

Wendorff, M. (2005). Evolution of Neoproterozoic–Lower Palaeozoic Lufilian arc, Central Africa: a new model based on syntectonic conglomerates. Journal of the Geological Society, 162(1), 5-8. https://doi.org/10.1144/0016-764904-085

Wesnousky, S. G. (2008). Displacement and geometrical characteristics of earthquake surface ruptures: Issues and implications for seismic-hazard analysis and the process of earthquake rupture. Bulletin of the Seismological Society of America, 98(4), 1609-1632. https://doi.org/10.1785/0120070111

Whipple, K. X. (2004). Bedrock rivers and the geomorphology of active orogens. Annu. Rev. Earth Planet. Sci., 32, 151-185. https://doi.org/10.1146/annurev.earth.32.101802.120356

Whipple, K. X. and Tucker, G. E. (1999). Dynamics of the stream-power river incision model: Implications for height limits of mountain ranges, landscape response timescales, and research needs. Journal of Geophysical Research: Solid Earth, 104(B8), 17661-17674. https://doi.org/10.1029/1999JB900120

Whipple, K. X., Snyder, N. P. and Dollenmayer, K. (2000). Rates and processes of bedrock incision by the Upper Ukak River since the 1912 Novarupta ash flow in the Valley of Ten

Thousand Smokes, Alaska. Geology, 28(9), 835-838. https://doi.org/10.1130/0091-7613(2000)28<835:RAPOBI>2.0.CO;2

Williamson, P. G. (1978). Evidence for the major features and development of Rift Palaeolakes in the Neogene of East Africa from certain aspects of Lacustrine Mollusc assemblages. Geological Society, London, Special Publications, 6(1), 507-527. https://doi.org/10.1144/GSL.SP.1978.006.01.35

Wobus, C. W., Whipple, K. X. and Hodges, K. V. (2006). Neotectonics of the central Nepalese Himalaya: Constraints from geomorphology, detrital $^{40}Ar/^{39}Ar$ thermochronology, and thermal modeling. Tectonics, 25(4). https://doi.org/10.1029/2005TC001935

Wohl, E. E. (1998). Bedrock channel morphology in relation to erosional processes. Geophysical Monograph-American Geophysical Union, 107, 133-152.

Young, R. W. (1985). Waterfalls: form and process. Zeitschrift für Geomorphologie N.F. Supplementband, 55, 81–85.

Appendix

Table A1: Quartz sample mass for ^{10}Be and ^{26}Al analyses and complete ^{9}Be carrier data

Name	Sample mass (g)	^{9}Be Carrier (g)	^{9}Be Carrier Concentration (μg g^{-1})
KUN01	44.54826	0.10007	3025 ± 9
KUN02	47.01686	0.10044	3025 ± 9
KUN03	45.91840	0.10029	3025 ± 9
KUN04	47.83346	0.10048	3025 ± 9
KUN05	46.89865	0.10015	3025 ± 9
KUN06	47.29090	0.10054	3025 ± 9
KUN07	46.13279	0.10033	3025 ± 9
LUM02	8.37028	0.15233	2511 ± 30
LUM03	24.9194	0.15323	2511 ± 30
NTU01	25.01740	0.13840	2511 ± 30
NTU02	25.6097	0.14768	2511 ± 30
NTU03	25.38520	0.13680	2511 ± 30
MUM01	24.96690	0.14310	2511 ± 30
MUM02	18.52987	0.13998	2511 ± 30
MUM03	26.01750	0.13910	2511 ± 30
MUM04	25.10300	0.13660	2511 ± 30
LUP01	24.91710	0.13710	2511 ± 30
LUO01	9.00696	0.17192	2511 ± 30
LUO02	24.48905	0.15914	2511 ± 30
LUZ01	23.40937	0.15767	2511 ± 30
LUZ02	24.67661	0.16047	2511 ± 30
ME04	25.02553	0.14423	2511 ± 30
ME05	25.15299	0.14757	2511 ± 30
ME06	22.54816	0.14406	2511 ± 30
ME09	22.66307	0.14481	2511 ± 30
MWE01	20.60960	0.14818	2511 ± 30
LUV01	27.10013	0.15828	2511 ± 30
LUV02	18.40597	0.15852	2511 ± 30
LUV03	19.17790	0.22190	770
LUV04	24.30359	0.15813	2511 ± 30

Name	Sample mass (g)	^{9}Be Carrier (g)	^{9}Be Carrier Concentration (μg g^{-1})
LUV05	24.67255	0.15954	2511 ± 30
LUF01	12.17660	0.22190	770
LUF02	11.53790	0.22250	770
LUF03	9.59545	0.19370	770
LUF04	22.65260	0.22180	770
LUF05	19.04010	0.22100	770
LUF06	24.84143	0.15812	2511 ± 30

Table A2: Complete ^{9}Be and Al blank carrier data.

Name	^{9}Be Carrier (g)	^{9}Be Carrier Concentration (μg g^{-1})	Al Carrier (g)	Al Carrier Concentration (mg l^{-1})
SOBL1	0.10034	3025 ± 9	0.99197	1000.5
SOBL2	0.13408	2511 ± 30	0.22000	10,000
SOBL3	0.14953	2511 ± 30	0.09884	10,000
SOBL5	0.15223	2511 ± 30	0.09897	10,000
SOBL6	0.14481	2511 ± 30	0.09256	10,000
SOBL7	0.22150	770	1.02	985

Table A3: Complete Ne data set including ^{4}He results for stepwise heating extractions of quartz samples. Problematic measurements with lower ^{21}Ne/^{20}Ne ratio than the crushing extractions (see Table AXX) are indicated with an asterisk (*). Totals for ^{21}Ne$_{ex}$ do not include the 1200°C step.

Samples	T	^{4}He	^{20}Ne	^{22}Ne/^{20}Ne	^{21}Ne/^{20}Ne	^{21}Ne$_{ex}$
	(°C)	(10^{-8} cm^{3} g^{-1})	(10^{-12} cm^{3} g^{-1})	(10^{-2})	(10^{-2})	(10^{6} atoms g^{-1})
KUN01	400	0.702	126.3	10.387	0.381	1.67
0.70372 g		*±0.035*	*±6.5*	*±0.064*	*±0.012*	*±0.21*
	600	19.14	974	10.278	0.4034	18.87
		±0.96	*±49*	*±0.025*	*±0.0058*	*±0.97*
	800	20.9	480	10.382	0.3594	3.62
		±1.0	*±24*	*±0.055*	*±0.0062*	*±0.45*
	1200	5.19	8.32	12.06	1.107	1.7335
		±0.26	*±0.69*	*±0.34*	*±0.063*	*±0.0069*
	Total	45.9	1589	10.327	0.392	24.2
		±1.4	*±55*	*±0.023*	*±0.0042*	*±1.1*
KUN02	400	0.0936	58.8	10.3	0.3561	0.392
0.70452 g		*±0.0049*	*±3.1*	*±0.12*	*±0.0077*	*±0.065*
	600	6.22	772	10.277	0.4169	17.77
		±0.31	*±39*	*±0.029*	*±0.0063*	*±0.84*
	800	9.9	496	10.364	0.3887	7.66
		±0.50	*±25*	*±0.048*	*±0.0062*	*±0.49*
	1200	7.05	11	11.54	0.801	1.389
		±0.35	*±0.78*	*±0.19*	*±0.053*	*±0.082*
	Total	23.26	1338	10.321	0.4069	25.81
		±0.68	*±46*	*±0.025*	*±0.0044*	*±0.84*
KUN03	400	0.0926	30.5	10.29	0.325	<0.02
0.71082 g		*±0.0047*	*±1.7*	*±0.17*	*±0.015*	-
	600	9.97	724	10.325	0.4302	19.24
		±0.50	*±37*	*±0.040*	*±0.0048*	*±0.73*
	800	26.1	747	10.333	0.3766	9.09
		±1.3	*±38*	*±0.047*	*±0.0076*	*±0.85*
	1200	17.42	8.14	11.46	1.145	1.778
		±0.87	*±0.67*	*±0.48*	*±0.061*	*±0.066*
	Total	53.6	1510	10.334	0.4054	28.33
		±1.6	*±53*	*±0.030*	*±0.0045*	*±0.90*

Sample	T (°C)	^{4}He (10^{-8} cm^{3} g^{-1})	^{20}Ne (10^{-12} cm^{3} g^{-1})	^{22}Ne/^{20}Ne (10^{-2})	^{21}Ne/^{20}Ne (10^{-2})	^{21}Ne$_{ex}$ (10^{6} atoms g^{-1})
KUN04	400	0.1261	50.5	10.22	0.319	<0.16
0.71320 g		*±0.0065*	*±2.7*	*±0.21*	*±0.013*	-
	600	9.2	822	10.254	0.4274	21.22
		±0.46	*±42*	*±0.021*	*±0.0057*	*±0.88*
	800	20.7	672	10.348	0.3736	7.64
		±1.0	*±34*	*±0.033*	*±0.0048*	*±0.53*
	1200	15.29	8.86	11.54	1.249	2.185
		±0.77	*±0.69*	*±0.38*	*±0.072*	*±0.087*
	Total	45.3	1553	10.301	0.4053	28.9
		±1.3	*±54*	*±0.020*	*±0.0038*	*±1.0*
KUN05	400	0.0631	10.91	10.61	0.344	0.037
0.70838 g		*±0.0034*	*±0.72*	*±0.22*	*±0.030*	*±0.044*
	600	11.26	458	10.308	0.4688	16.98
		±0.56	*±23*	*±0.028*	*±0.0092*	*±0.74*
	800	28.9	481	10.353	0.4107	10.20
		±1.5	*±25*	*±0.061*	*±0.0065*	*±0.52*
	1200	21.6	8.04	11.65	1.23	1.93
		±1.1	*±0.56*	*±0.31*	*±0.11*	*±0.12*
	Total	61.8	958	10.345	0.4446	27.22
		±1.9	*±34*	*±0.034*	*±0.0057*	*±0.90*
KUN06	400	0.0031	2.48	10.48	0.348	0.011
0.70560 g		*±0.0013*	*±0.48*	*±0.54*	*±0.070*	*±0.023*
	600	4.33	383	10.218	0.4103	8.05
		±0.22	*±20*	*±0.046*	*±0.0093*	*±0.54*
	800	22.8	900	10.291	0.4014	16.79
		±1.1	*±48*	*±0.058*	*±0.0044*	*±0.77*
	1200	24	32.4	10.83	0.509	1.53
		±1.2	*±1.8*	*±0.18*	*±0.028*	*±0.13*
	Total	51.1	1318	10.283	0.4065	24.85
		±1.6	*±52*	*±0.042*	*±0.0041*	*±0.94*
KUN07	400	0.801	97.6	10.312	0.41	2.06
0.70564 g		*±0.040*	*±5.0*	*±0.082*	*±0.018*	*±0.24*
	600	17.13	746	10.277	0.4212	18.03
		±0.86	*±38*	*±0.064*	*±0.0054*	*±0.76*
	800	24.4	511	10.35	0.3825	7.03
		±1.2	*±26*	*±0.059*	*±0.0073*	*±0.57*
	1200	6.65	9.72	11.89	1.516	3.10
		±0.33	*±0.74*	*0.16*	*±0.071*	*±0.10*
	Total	49	1364	10.318	0.4137	27.12
		±1.5	*±46*	*±0.042*	*±0.0043*	*±0.88*

Samples	T (°C)	^{4}He (10^{-8} cm^{3} g^{-1})	^{20}Ne (10^{-12} cm^{3} g^{-1})	^{22}Ne/^{20}Ne (10^{-2})	^{21}Ne/^{20}Ne (10^{-2})	^{21}Ne$_{ex}$ (10^{6} atoms g^{-1})
LUM02	400	3.53	117.4	10.231	0.379	1.57
0.69856 g		*±0.18*	*±6.1*	*±0.066*	*±0.016*	*±0.28*
	600	59.8	917	10.224	0.3886	14.6
		±3.0	*±47*	*±0.051*	*±0.0078*	*±1.3*
	800	51.5	470	10.311	0.3654	4.57
		±2.6	*±24*	*±0.042*	*±0.0054*	*±0.57*
	1200	9.22	10.13	10.95	1.214	2.41
		±0.47	*±0.77*	*±0.34*	*±0.073*	*±0.11*
	Total	124.1	1515	10.256	0.3862	20.8
		±4.0	*±53*	*±0.034*	*±0.0052*	*±1.5*
LUM03 #1	400	0.0333	9.69	10.3	0.376	0.051
0.70986 g		*±0.0020*	*±0.71*	*±0.28*	*±0.047*	*±0.061*
	600	15.59	612	10.291	0.3992	7.08
		±0.78	*±31*	*±0.025*	*±0.0094*	*±0.90*
	800	36.1	713	10.35	0.3775	4.12
		±1.8	*±36*	*±0.020*	*±0.0058*	*±0.76*
	1200	16.36	17.6	11.26	0.746	1.83
		±0.83	*±1.1*	*±0.20*	*±0.039*	*±0.10*
	Total	68.1	1352	10.335	0.3921	11.2
		±2.1	*±48*	*±0.016*	*±0.0053*	*±1.2*
LUM03 #2	<400	0.34	41.6	10.63	0.624	3.00
0.70788 g		*±0.017*	*±3.7*	*±0.34*	*±0.036*	*±0.24*
	<600	4.63	233	10.23	0.463	6.72
		±0.23	*±19*	*±0.13*	*±0.022*	*±0.76*
	<660	6.35	357	10.24	0.42	6.13
		±0.32	*±30*	*±0.11*	*±0.013*	*±0.73*
	~800	3.69	111.5	10.38	0.402	1.37
		±0.18	*±9.5*	*±0.16*	*±0.018*	*±0.28*
	1200	3.03	42.5	10.54	0.454	1.12
		±0.15	*±3.7*	*±0.21*	*±0.025*	*±0.21*
	Total	18.04	786	10.29	0.443	17.2
		±0.46	*±37*	*±0.07*	*±0.010*	*±1.1*

Samples	T (°C)	^{4}He (10^{-8} cm^{3} g^{-1})	^{20}Ne (10^{-12} cm^{3} g^{-1})	^{22}Ne/^{20}Ne (10^{-2})	^{21}Ne/^{20}Ne (10^{-2})	^{21}Ne$_{ex}$ (10^{6} atoms g^{-1})
LUP01	400	0.631	28.6	10.28	0.31	<0.12
0.71090 g		*±0.032*	*±1.6*	*±0.22*	*±0.020*	-
	600	103	657	10.248	0.4129	17.74
		±5.2	*±33*	*±0.038*	*±0.0042*	*±0.90*
	800	278	723	10.306	0.3594	9.15
		±14	*±37*	*±0.020*	*±0.0034*	*±0.86*
	1200	42	8.73	12.73	2.48	5.07
		±2.1	*±0.69*	*±0.31*	*±0.17*	*±0.21*
	Total	424	1417	10.294	0.3963	26.9
		±15	*±50*	*±0.021*	*±0.0032*	*±1.2*
MUM01 #1	400*	0.482	10.3	10.05	0.321	-
0.70288 g		*±0.024*	*±0.75*	*±0.32*	*±0.040*	-
	600	17.18	1285	10.332	0.4247	18.3
		±0.86	*±66*	*±0.037*	*±0.0042*	*±1.5*
	800	18.01	572	10.367	0.4078	5.57
		±0.90	*±29*	*±0.056*	*±0.0054*	*±0.71*
	1200	2.47	7.62	10.65	1.46	2.228
		±0.13	*±0.76*	*±0.38*	*±0.11*	*±0.087*
	Total	38.1	1875	10.342	0.4232	23.9
		±1.3	*±72*	*±0.031*	*±0.0034*	*±1.7*
MUM02 #1	400	0.285	106.4	10.2	0.3667	0.35
0.69716 g		*±0.014*	*±5.5*	*±0.15*	*±0.0048*	*±0.11*
	600	15.11	1318	10.34	0.4301	26.78
		±0.76	*±67*	*±0.033*	*±0.0052*	*±1.56*
	800	27.4	690	10.396	0.3974	7.96
		±1.4	*±35*	*±0.036*	*±0.0049*	*±0.75*
	1200	8.13	9.5	10.48	1.057	1.793
		±0.41	*±0.72*	*±0.39*	*±0.048*	*±0.063*
	Total	50.9	2124	10.352	0.4191	35.1
		±1.6	*±76*	*±0.025*	*±0.0037*	*±1.7*
MUM03 #1	400	0.351	92	10.203	0.3253	-
0.70854 g		*±0.018*	*±5.1*	*±0.074*	*±0.0092*	-
	600	19.82	851	10.295	0.4331	17.96
		±0.99	*±47*	*±0.088*	*±0.0046*	*±0.99*
	800	29.7	536	10.381	0.4021	6.85
		±1.5	*±29*	*±0.056*	*±0.0061*	*±0.64*
	1200	19.9	6.56	10.67	2.09	3.06
		±1.0	*±0.63*	*±0.39*	*±0.16*	*±0.12*
	Total	69.8	1486	10.322	0.4226	24.8
		±2.1	*±55*	*±0.055*	*±0.0037*	*±1.2*

Samples	T (°C)	^{4}He (10^{-8} cm^{3} g^{-1})	^{20}Ne (10^{-12} cm^{3} g^{-1})	^{22}Ne/^{20}Ne (10^{-2})	^{21}Ne/^{20}Ne (10^{-2})	^{21}Ne$_{ex}$ (10^{6} atoms g^{-1})
MUM04 #1	400	0.398	84.4	10.33	0.3705	<0.25
0.70816 g		*±0.020*	*±4.7*	*±0.13*	*±0.0093*	-
	600	15.25	736	10.414	0.4703	19.5
		±0.77	*±40*	*±0.051*	*±0.0067*	*±1.1*
	800	18.78	527	10.397	0.4187	6.67
		±0.94	*±29*	*±0.046*	*±0.0053*	*±0.66*
	1200	4.59	12.93	10.58	0.992	2.16
		±0.24	*±0.92*	*±0.22*	*±0.063*	*±0.12*
	Total	39	1360	10.404	0.4491	26.2
		±1.2	*±50*	*±0.034*	*±0.0044*	*±1.3*
MUM01 #2	<400	0.0517	9.46	10.71	0.366	<0.13
0.70594 g		*±0.0034*	*±0.85*	*±0.55*	*±0.053*	-
	400	4.9	242	10.349	0.489	7.66
		±0.25	*±13*	*±0.070*	*±0.013*	*±0.52*
	600	12.77	624	10.368	0.4834	18.7
		±0.64	*±32*	*±0.060*	*±0.0096*	*±1.1*
	800	7.29	179	10.48	0.4307	2.85
		±0.36	*±11*	*±0.11*	*±0.0074*	*±0.26*
	1000	6.05	33.2	10.63	0.541	1.51
		±0.30	*±2.2*	*±0.20*	*±0.038*	*±0.18*
	Total	31.06	1088	10.393	0.4767	29.3
		±0.83	*±36*	*±0.043*	*±0.0065*	*±1.3*
MUM02 #2	400	0.074	20.3	10.45	0.403	0.27
0.71192 g		*±0.0041*	*±1.3*	*±0.33*	*±0.049*	*±0.13*
	600	7.14	533	10.299	0.516	23.1
		±0.36	*±27*	*±0.074*	*±0.012*	*±1.1*
	800	17.66	598	10.31	0.433	12.63
		±0.88	*±30*	*±0.085*	*±0.0078*	*±0.85*
	1200	6.01	15.9	11	0.819	1.99
		±0.30	*±1.1*	*±0.56*	*±0.075*	*±0.17*
	Total	30.9	1167	10.317	0.4756	36.0
		±1.0	*±40*	*±0.056*	*±0.0071*	*±1.4*

Samples	T (°C)	^{4}He (10^{-8} cm^{3} g^{-1})	^{20}Ne (10^{-12} cm^{3} g^{-1})	^{22}Ne/^{20}Ne (10^{-2})	^{21}Ne/^{20}Ne (10^{-2})	^{21}Ne$_{ex}$ (10^{6} atoms g^{-1})
MUM02 #2	400	0.074	20.3	10.45	0.403	0.27
0.71192 g		*±0.0041*	*±1.3*	*±0.33*	*±0.049*	*±0.13*
	600	7.14	533	10.299	0.516	23.1
		±0.36	*±27*	*±0.074*	*±0.012*	*±1.1*
	800	17.66	598	10.31	0.433	12.63
		±0.88	*±30*	*±0.085*	*±0.0078*	*±0.85*
	1200	6.01	15.9	11	0.819	1.99
		±0.30	*±1.1*	*±0.56*	*±0.075*	*±0.17*
	Total	30.9	1167	10.317	0.4756	36.0
		±1.0	*±40*	*±0.056*	*±0.0071*	*±1.4*
MUM03 #2	400	0.222	37.4	10.57	0.373	0.19
0.70878 g		*±0.011*	*±2.1*	*±0.18*	*±0.029*	*±0.15*
	600	10.15	464	10.31	0.512	19.64
		±0.51	*±24*	*±0.12*	*±0.010*	*±0.89*
	800	17.09	430	10.36	0.444	10.34
		±0.85	*±22*	*±0.11*	*±0.0076*	*±0.62*
	1200	3.67	11.44	10.94	0.767	1.267
		±0.18	*±0.93*	*±0.32*	*±0.056*	*±0.085*
	Total	31.1	943	10.35	0.4786	15.1
		±1.0	*±33*	*±0.08*	*±0.0063*	*±1.1*
MUM04 #2	400	0.254	40.6	10.5	0.464	1.01
0.70530 g		*±0.013*	*±2.3*	*±0.21*	*±0.034*	*±0.19*
	600	6.55	431	10.417	0.5338	18.80
		±0.33	*±22*	*±0.082*	*±0.0093*	*±0.83*
	800	11.76	408	10.36	0.454	9.03
		±0.59	*±21*	*±0.10*	*±0.012*	*±0.82*
	1200	4.02	20.4	10.69	0.567	1.07
		±0.20	*±1.4*	*±0.33*	*±0.061*	*±0.17*
	Total	22.58	900	10.401	0.4952	28.8
		±0.71	*±31*	*±0.061*	*±0.0075*	*±1.2*

Samples	T (°C)	^{4}He (10^{-8} cm^{3} g^{-1})	^{20}Ne (10^{-12} cm^{3} g^{-1})	^{22}Ne/^{20}Ne (10^{-2})	^{21}Ne/^{20}Ne (10^{-2})	^{21}Ne$_{ex}$ (10^{6} atoms g^{-1})
LUO01	Total	31.06	1088	10.393	0.4767	29.3
0.70724 g		*±0.83*	*±36*	*±0.043*	*±0.0065*	*±1.3*
	400	3.58	141.5	10.45	0.553	5.44
		±0.18	*±7.3*	*±0.12*	*±0.019*	*±0.44*
	600	7.27	310	10.52	0.566	12.98
		±0.36	*±16*	*±0.065*	*±0.016*	*±0.86*
	~900	5.68	154.5	10.573	0.5197	4.56
		±0.28	*±8.1*	*±0.089*	*±0.0094*	*±0.32*
	1250	0.502	0.32	8.9	9.2	0.764
		±0.025	$^{+0.46}_{-0.32}$	*±7.6*	$^{+\infty}_{-6.0}$	*±0.069*
	Total	17.07	614	10.511	0.554	23.0
		±0.49	*±19*	*±0.049*	*±0.012*	*±1.0*
LUO02	600	22.9	493	10.557	0.559	26.0
0.70536 g		*±1.1*	*±26*	*±0.075*	*±0.011*	*±1.2*
	800	30.2	346	10.428	0.415	4.88
		±1.5	*±19*	*±0.057*	*±0.010*	*±0.65*
	1000	6.41	4.73	11.36	1.09	0.947
		±0.32	*±0.58*	*±0.45*	*±0.15*	*±0.089*
	1250	4.81	0.39	13	9.2	0.95
		±0.24	$^{+0.55}_{-0.39}$	*±4.3*	$^{+\infty}_{-6.1}$	*±0.10*
	Total	64.3	844	10.51	0.507	30.9
		±1.9	*±32*	*±0.050*	*±0.010*	*±1.3*
NTU01	400	0.1466	20.3	10.28	0.328	<0.20
0.70766 g		*±0.0075*	*±1.3*	*±0.35*	*±0.040*	-
	600	23.6	1307	10.1	0.3759	15.5
		±1.2	*±70*	*±0.065*	*±0.0059*	*±1.4*
	800	27.9	1470	10.179	0.3405	3.4
		±1.4	*±79*	*±0.048*	*±0.0067*	*±1.6*
	950	1.863	8.26	10.41	0.622	0.659
		±0.093	*±0.70*	*±0.62*	*±0.075*	*±0.083*
	1250	1.257	0.13	21	26	0.874
		±0.063	$^{+0.46}_{-0.13}$	$^{+\infty}_{-10}$	$^{+\infty}_{-21}$	*±0.075*
	Total	54.8	2810	10.144	0.3589	18.9
		±1.8	*±110*	*±0.040*	*±0.0063*	*±2.1*

Samples	T	^{4}He	^{20}Ne	^{22}Ne/^{20}Ne	^{21}Ne/^{20}Ne	^{21}Ne$_{ex}$
	(°C)	(10^{-8} cm^3 g^{-1})	(10^{-12} cm^3 g^{-1})	(10^{-2})	(10^{-2})	(10^6 atoms g^{-1})
NTU02	400	0.0658	16.7	10.39	0.375	0.14
0.70646 g		*±0.0035*	*±1.1*	*±0.57*	*±0.043*	*±0.10*
	600	8.31	722	10.204	0.4361	17.85
		±0.42	*±37*	*±0.068*	*±0.0064*	*±0.92*
	800	9.83	1126	10.198	0.3641	6.0
		±0.49	*±58*	*±0.058*	*±0.0070*	*±1.3*
	1250	3.08	6.29	11.49	1.83	2.52
		±0.15	*±0.62*	*±0.39*	*±0.16*	*±0.13*
	Total	21.29	1871	10.206	0.3969	24.0
		±0.66	*±69*	*±0.044*	*±0.0051*	*±1.6*
NTU03	400	0.362	49.2	10.28	0.387	0.14
0.70704 g		*±0.018*	*±2.7*	*±0.17*	*±0.015*	*±0.13*
	600	15.25	867	10.155	0.406	6.8
		±0.76	*±45*	*±0.052*	*±0.012*	*±2.0*
	800*	19.88	949	10.166	0.3464	-
		±0.99	*±49*	*±0.047*	*±0.0075*	-
	1250	9.59	14.8	10.79	1.014	2.54
		±0.48	*±1.0*	*±0.30*	*±0.075*	*±0.16*
	Total	45.1	1880	10.169	0.3802	6.9
		±1.3	*±67*	*±0.034*	*±0.0068*	*±2.0*
LUV01	400*	0.898	80.5	10.25	0.42	-
0.70856 g		*±0.045*	*±4.2*	*±0.19*	*±0.024*	-
	600	12.64	387	10.262	0.596	2.48
		±0.63	*±20*	*±0.052*	*±0.013*	*±0.77*
	800	15.89	158.9	10.457	0.594	0.93
		±0.80	*±8.3*	*±0.080*	*±0.020*	*±0.45*
	1200	19.52	7.71	11.49	1.13	1.16
		±0.98	*±0.65*	*±0.41*	*±0.13*	*±0.13*
	Total	48.9	634	10.324	0.58	3.41
		±1.4	*±22*	*±0.045*	*±0.010*	*±0.90*

Samples	T (°C)	^{4}He (10^{-8} cm^{3} g^{-1})	^{20}Ne (10^{-12} cm^{3} g^{-1})	^{22}Ne/^{20}Ne (10^{-2})	^{21}Ne/^{20}Ne (10^{-2})	^{21}Ne$_{ex}$ (10^{6} atoms g^{-1})
LUV02	400*	0.495	72.5	10.27	0.411	-
0.70860 g		*±0.025*	*±3.8*	*±0.10*	*±0.018*	-
	600	10.96	364	10.243	0.587	1.49
		±0.55	*±19*	*±0.091*	*±0.014*	*±0.78*
	800	15.88	159.8	10.4	0.599	1.18
		±0.79	*±8.5*	*±0.15*	*±0.014*	*±0.35*
	1200	10.51	4.96	11.89	1.31	0.980
		±0.53	*±0.55*	*±0.58*	*±0.16*	*±0.094*
	Total	37.8	601	10.302	0.575	2.67
		±1.1	*±21*	*±0.069*	*±0.010*	*±0.85*
LUV04	400*	0.332	69.1	10.29	0.408	-
0.71032 g		*±0.023*	*±5.0*	*±0.23*	*±0.024*	-
	600	6.17	388	10.291	0.598	2.75
		±0.43	*±28*	*±0.045*	*±0.010*	*±0.69*
	800	6.62	162	10.43	0.617	1.97
		±0.46	*±12*	*±0.11*	*±0.018*	*±0.44*
	1200	3.84	18.6	10.86	0.544	-
		±0.27	*±1.5*	*±0.28*	*±0.064*	-
	Total	16.96	638	10.343	0.581	4.72
		±0.69	*±31*	*±0.047*	*±0.008*	*±0.82*
LUV05	400*	0.651	82.5	10.25	0.462	-
0.70844 g		*±0.046*	*±6.0*	*±0.16*	*±0.022*	-
	600	6.9	368	10.31	0.598	2.6
		±0.48	*±26*	*±0.10*	*±0.019*	*±1.0*
	800	5.81	165	10.46	0.594	0.99
		±0.41	*±12*	*±0.10*	*±0.024*	*±0.57*
	1200	4.31	6.33	10.92	1.209	1.083
		±0.30	*±0.73*	*±0.31*	*±0.094*	*±0.070*
	Total	17.67	622	0.008	10.34	3.6
		±0.70	*±29*	*±0.07*	*±0.013*	*±1.2*
LUF06	400*	0.144	30.6	10.27	0.33	-
0.70704 g		*±0.010*	*±2.3*	*±0.27*	*±0.055*	-
	600	20.7	378	10.339	0.572	0.01
		±1.4	*±27*	*±0.082*	*±0.012*	*±0.72*
	800	22.2	317	10.366	0.597	2.16
		±1.6	*±23*	*±0.076*	*±0.013*	*±0.65*
	1200	13.64	10.03	10.76	1.03	1.24
		±0.96	*±0.97*	*±0.44*	*±0.095*	*±0.13*
	Total	56.7	736	0.001	10.354	2.17
		±2.3	*±36*	*±0.055*	*±0.009*	*±0.97*

Table A4: Complete Ne data set for crushing extractions of quartz samples.

Sample	^{4}He (10^{-8} cm^{3} g^{-1})	^{20}Ne (10^{-12} cm^{3} g^{-1})	^{22}Ne/^{20}Ne (10^{-2})	^{21}Ne/^{20}Ne (10^{-2})
KUN01	0.311	408	10.253	0.3253
1.01906 g	*±0.016*	*±21*	*±0.039*	*±0.0067*
KUN03	0.1633	411	10.284	0.3376
1.00074 g	*±0.0082*	*±22*	*±0.036*	*±0.0049*
KUN07	0.32	426	10.275	0.3294
0.99382 g	*±0.016*	*±23*	*±0.042*	*±0.0039*
LUM03	0.572	383	10.354	0.3559
1.02114 g	*±0.029*	*±20*	*±0.046*	*±0.0055*
LUP01	1.898	297	10.291	0.3121
0.97376 g	*±0.095*	*±16*	*±0.043*	*±0.0078*
MUM01	0.684	444	10.284	0.3716
0.99934 g	*±0.034*	*±23*	*±0.058*	*±0.0073*
LUM01	1.78	552	10.245	0.3292
1.03420 g	*±0.089*	*±28*	*±0.045*	*±0.0070*
MUM02	0.605	470	10.26	0.3545
1.00158 g	*±0.049*	*±41*	*±0.16*	*±0.0060*
LUO01	0.902	283	10.335	0.41
0.98696 g	*±0.045*	*±15*	*±0.071*	*±0.011*
NTU01	0.549	1109	10.131	0.3319
0.96956 g	*±0.027*	*±59*	*±0.042*	*±0.0046*
LUO02	0.517	432	10.256	0.3619
1.00488 g	*±0.026*	*±23*	*±0.062*	*±0.0094*
NTU02	0.226	894	10.139	0.3441
0.98644 g	*±0.011*	*±46*	*0.066*	*±0.0052*
NTU03	1.053	223	10.281	0.377
1.00658 g	*±0.053*	*±12*	*±0.060*	*±0.012*
LUV01	0.284	151	10.321	0.567
1.00704 g	*±0.020*	*±11*	*±0.064*	*±0.015*
LUV04	0.227	168	10.33	0.579
1.03144 g	*±0.016*	*±12*	*±0.11*	*±0.017*
LUF06	0.387	258	10.384	0.571
1.00342 g	*±0.019*	*±14*	*±0.056*	*±0.011*

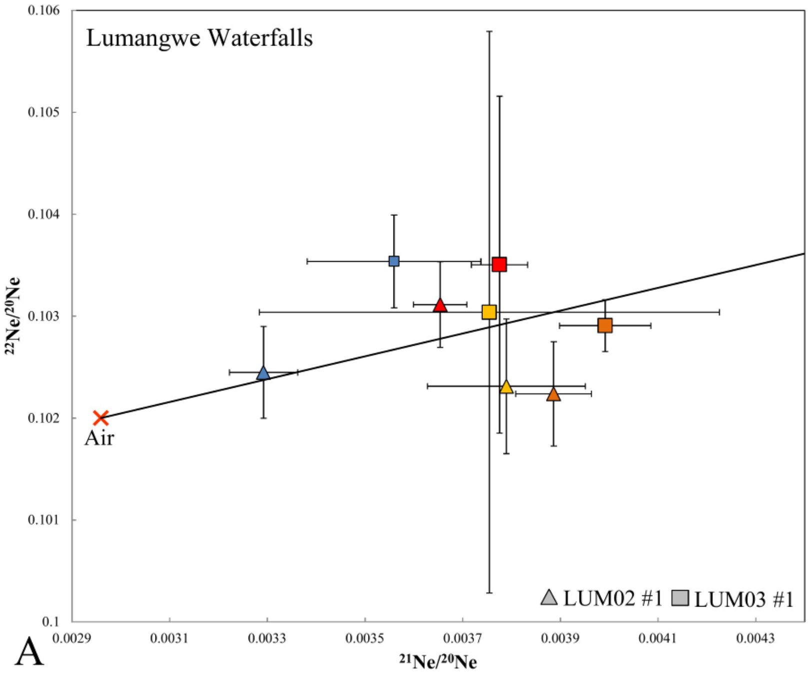
Lumangwe Waterfalls
^{22}Ne/^{20}Ne
0.106
0.105
0.104
0.103
0.102
0.101
0.1
Air
△ LUM02 #1
☐ LUM03 #1
0.0029
0.0031
0.0033
0.0035
0.0037
0.0039
0.0041
0.0043
^{21}Ne/^{20}Ne
A

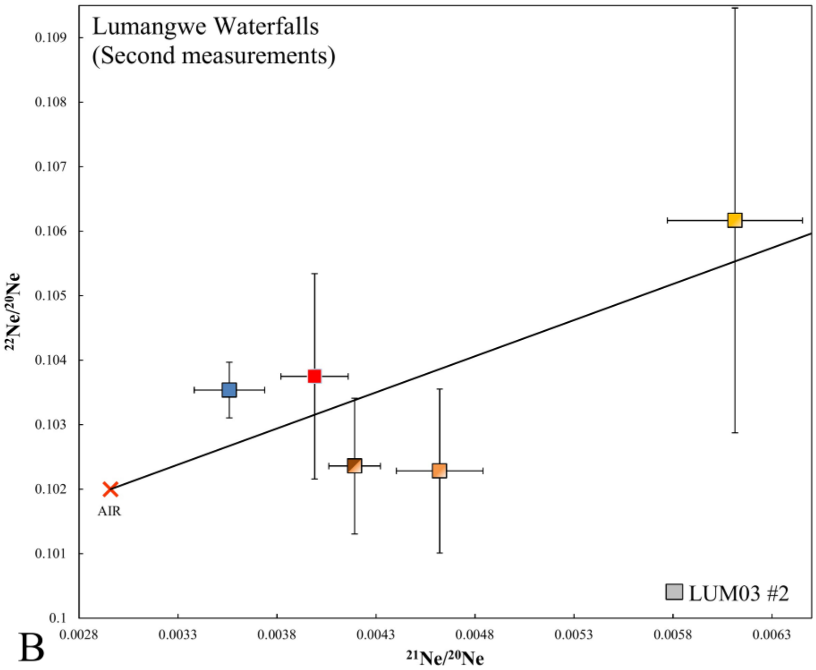
Lumangwe Waterfalls
(Second measurements)
^{22}Ne/^{20}Ne
0.109
0.108
0.107
0.106
0.105
0.104
0.103
0.102
0.101
0.1
AIR
☐ LUM03 #2
0.0028
0.0033
0.0038
0.0043
0.0048
0.0053
0.0058
0.0063
^{21}Ne/^{20}Ne
B

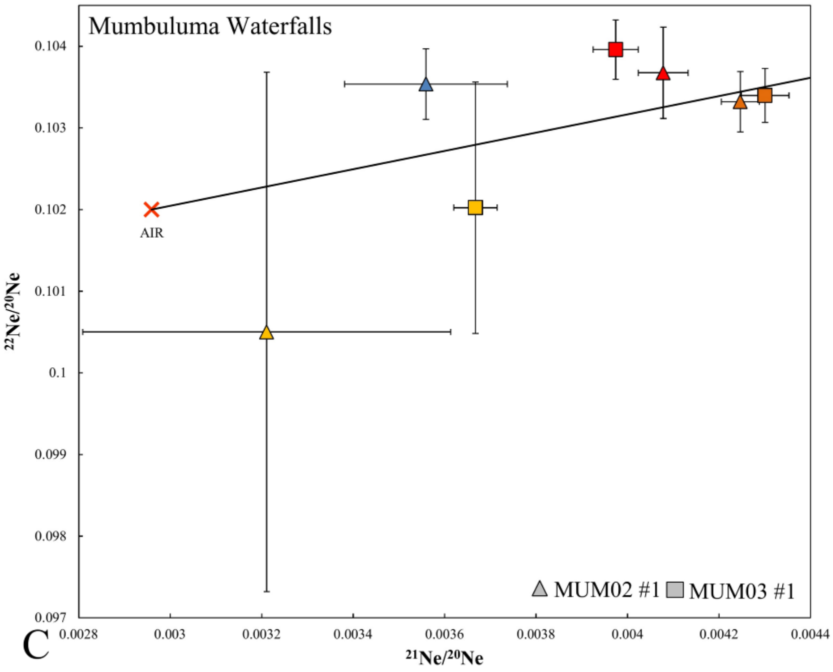
Mumbuluma Waterfalls
0.104
0.103
0.102
0.101
0.1
0.099
0.098
0.097
AIR
^{22}Ne/^{20}Ne
△ MUM02 #1 ◻ MUM03 #1
C
0.0028
0.003
0.0032
0.0034
0.0036
0.0038
0.004
0.0042
0.0044
^{21}Ne/^{20}Ne

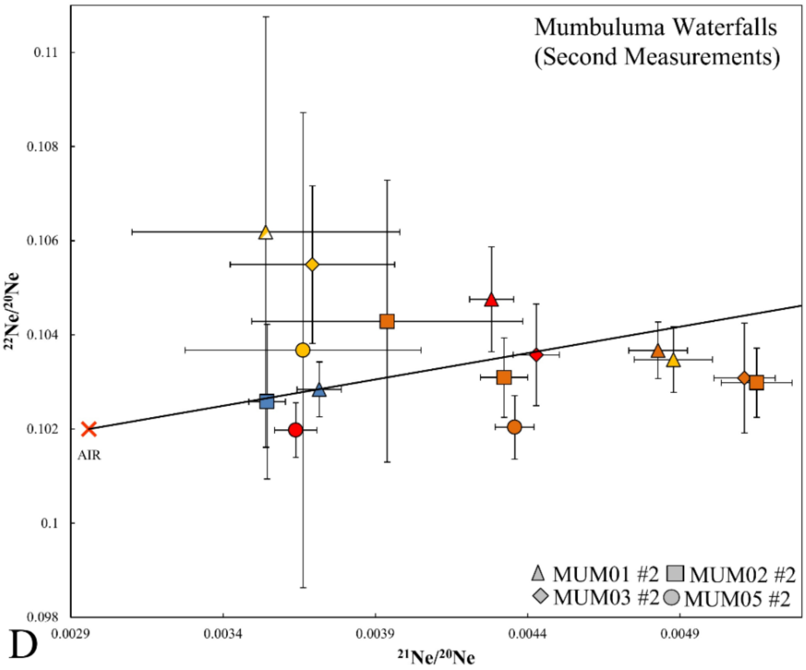
Mumbuluma Waterfalls
(Second Measurements)
0.11
0.108
0.106
0.104
0.102
0.1
0.098
AIR
^{22}Ne/^{20}Ne
△ MUM01 #2 ◻ MUM02 #2
◇ MUM03 #2 ○ MUM05 #2
D
0.0029
0.0034
0.0039
0.0044
0.0049
^{21}Ne/^{20}Ne

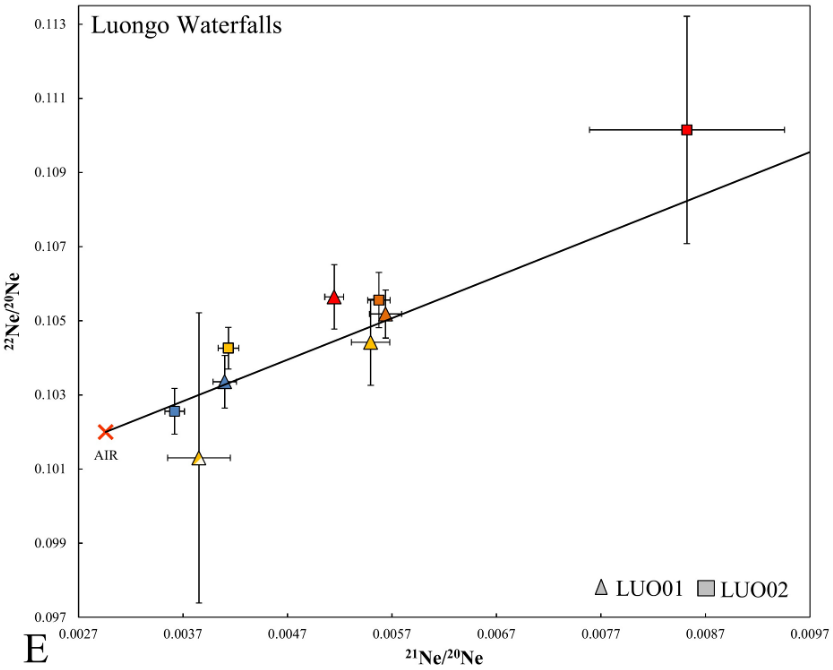
Luongo Waterfalls
0.113
0.111
0.109
0.107
0.105
0.103
0.101
0.099
0.097
$^{22}Ne/^{20}Ne$
AIR
△ LUO01
□ LUO02
0.0027
0.0037
0.0047
0.0057
0.0067
0.0077
0.0087
0.0097
$^{21}Ne/^{20}Ne$

E

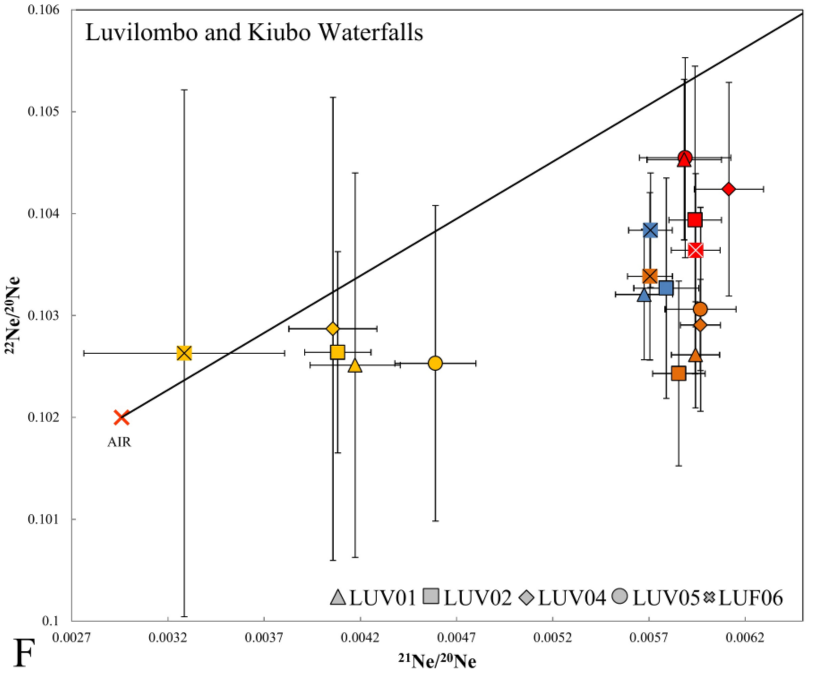
Luvilombo and Kiubo Waterfalls
0.106
0.105
0.104
0.103
0.102
0.101
0.1
$^{22}Ne/^{20}Ne$
AIR
△LUV01
□LUV02
◇LUV04
○LUV05
✖LUF06
0.0027
0.0032
0.0037
0.0042
0.0047
0.0052
0.0057
0.0062
$^{21}Ne/^{20}Ne$

F

Figure A1: Neon three-isotope diagrams showing ^{21}Ne/^{20}Ne versus ^{22}Ne/^{20}Ne. Colors indicate different heating steps (yellow: 400°C, orange: 600°C, red: 800°C; 1200°C data would plot out of the field shown). In a few cases, samples piled up in the crucible and did not reach the nominal temperatures, such measurements are shown in diagonally divided colors (yellow/white: <400°C, orange/white: <600°C, brown/yellow: <660°C). Crushing extractions are shown in blue. The air value is indicated with a red cross. The spallation line is the mixing line between air and cosmogenic Ne (Niedermann et al., 1993). A) Lumangwe Waterfall #1 (LUM02, LUM03); B) Lumangwe Waterfall #2 (LUM03); C) Mumbuluma I Waterfalls #1 (MUM02, MUM03); D) Mumbuluma I Waterfalls #2 (MUM01, MUM02, MUM03, MUM04); E) Mumbuluma II Waterfall (LUO01, LUO02); F) Luvilombo Waterfalls (LUV01, LUV02, LUV04, LUV05) and Kiubo Waterfalls (LUF06).

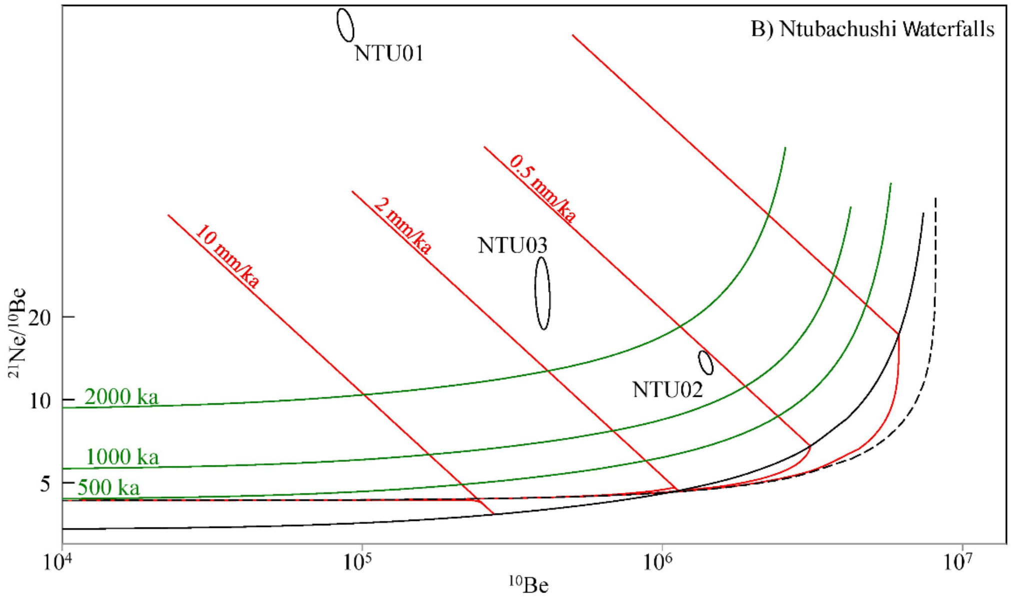

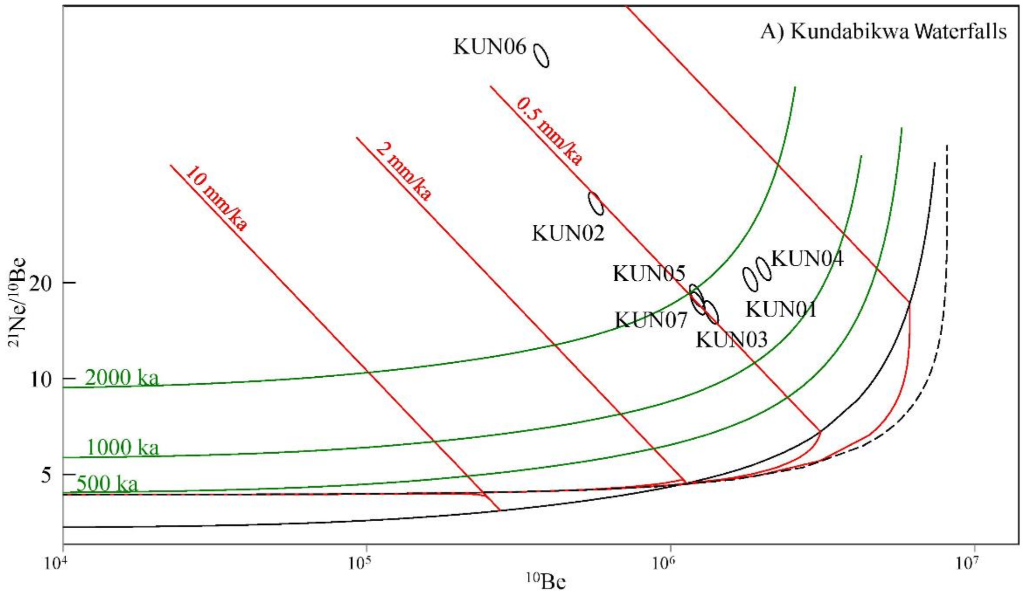

Figure A2: Examples of two-nuclide diagrams showing ^{10}Be concentrations (atoms/g, corrected for total shielding and scaled to common elevation) versus ^{21}Ne/^{10}Be ratios for some Group A samples. The black solid line indicates the “steady state denudation line” and the black dashed line shows the “constant exposure line” (e.g. Lal, 1991). Red lines show the temporal evolution of data at constant denudation rates and subsequent burial. Green lines indicate duration of burial under the assumption that samples were first exposed and later completely buried until present. Samples are indicated with black error ellipses (1σ shown). a) Kundabikwa Waterfalls; b) Ntumbachushi Waterfalls.